



THE UNIVERSITY OF QUEENSLAND
AUSTRALIA

**Process Investigation of Incremental Sheet Forming: The Evolution
Towards Multi-Pass Deformation Design**

Zhaobing Liu

{Bachelor of Engineering}

{Master of Engineering}

A thesis submitted for the degree of Doctor of Philosophy at

The University of Queensland in 2014

School of Mechanical and Mining Engineering

Abstract

Incremental sheet forming (ISF) is a promising sheet metal forming technology with high potential to shape complex three-dimensional parts. It is suitable for rapid prototyping as well as low volume production. The advantages of ISF technology are flexible, short product development time, inexpensive die/tooling and high formability in comparison to conventional sheet forming technologies. Although many contributions have been made on the development of ISF technology, unsatisfactory forming quality still hampers its use in industrial applications. The work in this thesis focuses on the development of ISF in terms of process investigation on formability, forming force, geometric accuracy, forming time and surface quality, multi-pass ISF modelling and its validation including SPIF (single point incremental forming with no forming die) multi-pass deformation design and AMINO TPIF (two point incremental forming with full forming die) multi-pass deformation design, which form two main parts of this thesis.

The work in the first part of this thesis is focused on the process investigation including process formability, forming forces, geometric accuracy, forming time and surface quality. In particular, tensile tests were carried out to characterize the mechanical properties of AA7075-O aluminium alloy sheets with three different thicknesses. **(i) Process formability.** Groove tests were performed to evaluate the process formability in terms of the effect of tool type and size. Furthermore, the effects of tool path types with different incremental steps on the maximum forming angle as well as the successful forming height were evaluated to clarify their influences on process formability during a cone-forming process. Additionally, a fracture forming limit diagram was developed to give the design limits for strain. **(ii) Forming forces.** A finite element (FE) model was developed to evaluate the forming forces, strain behaviour and thickness distribution with a groove test using different forming tools. Experimental tests were then performed to validate the FE results. Additionally, the trends in forming forces were also analysed considering the influences of different draw angles, sheet thicknesses, step-down sizes and sheet orientation during a cone and pyramid forming process. **(iii) Geometric accuracy.** A study on the effect of step-down size on geometric accuracy was implemented, which is of great importance in design and control of a tool path to improve the forming quality. **(iv) Forming time.** Design of experiments (DOE) together with the Taguchi method was used to investigate the effects of process parameters (step over (the distance the forming tool moves over the

part surface to generate a spiral tool path), feed rate, sheet thickness and tool diameter) on forming time. It was concluded that the most significant process parameter influencing forming time is the step over followed by the feed rate. **(v) Surface roughness.** Surface integrity was evaluated during a groove test in terms of rolling and sliding forming tools. Microscopic observations of the surface topography revealed that a rolling tool tip produced better surface integrity as compared with a sliding tool, wherein, distinct scratch patterns in the tool traverse direction were evident. Design of experiments (DOE) together with response surface methodology (RSM) was used to investigate the effects of process parameters (step-down size, feed rate, sheet thickness and tool diameter) on surface roughness. An empirical model has been established for the overall surface roughness (tool-sheet contact surface roughness and non-contact surface roughness) prediction of a part formed by SPIF. Sheet thickness was found to be the most influential forming variable on the overall surface roughness followed by the step down. Furthermore, the influence of sheet metal roll marks on surface roughness were also examined and discussed.

The work in the second part of this thesis is focused upon multi-pass ISF modelling and validation. A common technical problem encountered in ISF is the non-uniform thickness distribution of formed parts; particularly excessive thinning on severely sloped regions. This may lead to fracture and limit the process formability. Design of multi-stage deformation passes (intermediate shapes or preforms) before the final part, is a desirable and practical way to control material flow in order to obtain a more uniform thickness distribution and avoid forming failure. **(i) SPIF multi-pass deformation design.** An empirical trial-and-error method was first proposed for SPIF multi-pass deformation design in which three forming strategies and their combinations have been evaluated in terms of the process formability. The results showed that the forming strategy using more material in the forming as well as the addition of a small amount of bending can greatly improve the formability. **(ii) AMINO TPIF multi-pass deformation design.** It is noted that there is lack of analytical modelling for multi-pass ISF design in literature. A systematic methodology incorporating two analytical models (**M1** and **M2**) for AMINO TPIF multi-pass deformation design considering the predicted thickness strains given the design geometry was developed based on shear deformation and the strain compensation mechanism. The feasibility of the proposed closed-loop design methodology was validated by finite element analysis (FEA) and experimental tests. The results revealed that a more uniform thickness strain distribution can be derived using **M2**. The occurrence of the highest strains can be

delayed in the intermediate stages and the flow of material is allowed into the deformed region, thereby allowing a compressive deformation state to develop and enabling steeper shapes to be formed. Therefore, the process formability can be enhanced via the proper design of deformation passes. Additionally, the generalization of simple shapes to complex shapes using the developed multi-pass design methodology has also been performed. The interaction of different tool paths on material thinning of the final part given the same multi-pass design was evaluated and analysed. A method for multi-pass tool path generation to further improve the process formability was then recommended.

The work in this thesis explores various aspects of ISF research, although the most important contribution focuses on the multi-pass ISF modeling and its validation, which greatly enhances the process formability and obtains more uniform thickness distributions of final products. This provides an insight into the future development and implementation of ISF technology.

Declaration by author

This thesis is composed of my original work, and contains no material previously published or written by another person except where due reference has been made in the text. I have clearly stated the contribution by others to jointly-authored works that I have included in my thesis.

I have clearly stated the contribution of others to my thesis as a whole, including statistical assistance, survey design, data analysis, significant technical procedures, professional editorial advice, and any other original research work used or reported in my thesis. The content of my thesis is the result of work I have carried out since the commencement of my research higher degree candidature and does not include a substantial part of work that has been submitted to qualify for the award of any other degree or diploma in any university or other tertiary institution. I have clearly stated which parts of my thesis, if any, have been submitted to qualify for another award.

I acknowledge that an electronic copy of my thesis must be lodged with the University Library and, subject to the General Award Rules of The University of Queensland, immediately made available for research and study in accordance with the *Copyright Act 1968*.

I acknowledge that copyright of all material contained in my thesis resides with the copyright holder(s) of that material. Where appropriate I have obtained copyright permission from the copyright holder to reproduce material in this thesis.

Publications during candidature

Published Papers

- A. Liu, Z.B.**, Li, Y.L., Meehan, P.A., 2013. Experimental investigation of mechanical properties, formability and force measurement for AA7075-O aluminium alloy sheets formed by incremental forming. *International Journal of Precision Engineering and Manufacturing* 14(11), 1891-1899.
- B. Li, Y.L., Liu, Z.B.**, Lu, H.B., Daniel, W.J.T., Meehan, P.A., 2014. Experimental study and efficient prediction on forming forces in incremental sheet forming. *Advanced Materials Research* 939, 313-321.
- C. Li, Y.L., Liu, Z.B.**, Daniel, W.J.T., Meehan, P.A., 2014. Simulation and experimental observations of effect of different contact interfaces on the incremental sheet forming process. *Materials and Manufacturing Processes* 29(2), 121-128.
- D. Lu, H.B., Li, Y.L., Liu, Z.B.**, Liu, S., Meehan, P.A., 2014. Study on step depth for part accuracy improvement in incremental sheet forming process. *Advanced Materials Research* 939, 274-280.
- E. Liu, Z.B.**, Li, Y.L., Daniel, W.J.T., Meehan, P.A., 2014. Taguchi optimization of process parameters for forming time in incremental sheet forming process. *Materials Science Forum* 773-774, 137-143.
- F. Liu, Z.B.**, Liu, S., Li, Y.L., Meehan, P.A., 2014. Modelling and optimization of surface roughness in incremental sheet forming using a multi-objective function. *Materials and Manufacturing Processes* 29(7), 808-818.
- G. Liu, Z.B.**, Li, Y.L., Meehan, P.A., 2013. Vertical wall formation and material flow control for incremental sheet forming by revisiting multistage deformation path strategies, *Materials and Manufacturing Processes* 28(5), 562-571.

- H. Liu, Z.B., Meehan, P.A., Bellette, P.A., 2011. Thickness distribution and forming strategy analysis for two point incremental forming with a male die. *Advanced Materials Research* 337, 452-455.
- I. Liu, Z.B., Li, Y.L., Daniel, W.J.T., Meehan, P.A., 2014. An analytical model for deformation path design in multistage incremental sheet forming process. *Advanced Materials Research* 939, 245-252.
- J. Liu, Z.B., Daniel, W.J.T., Li, Y.L., Liu, S., Meehan, P.A., 2014. Multi-pass deformation design for incremental sheet forming: Analytical modeling, finite element analysis and experimental validation. *Journal of Materials Processing Technology* 214(3), 620-634.
- K. Liu, Z.B., Li, Y.L., Meehan, P.A., 2014. Tool path strategies and deformation analysis in multi-pass incremental sheet forming process. *International Journal of Advanced Manufacturing Technology*, 75(1-4), 395-409.
- L. Li, Y.L., Liu, Z.B., Lu, H.B., Daniel, W.J.T., Liu, S., Meehan, P.A., 2014. Efficient force prediction for incremental sheet forming and experimental validation. *International Journal of Advanced Manufacturing Technology* 73(1-4), 571-587.

Publications included in this thesis

Chapter 4

4.1 Process Investigation

A. Liu, Z.B., Li, Y.L., Meehan, P.A., 2013. Experimental investigation of mechanical properties, formability and force measurement for AA7075-O aluminium alloy sheets formed by incremental forming. *International Journal of Precision Engineering and Manufacturing* 14(11), 1891-1899.

Contributor	Statement of contribution
Author Z.B. Liu (Candidate)	Designed experiments (80%) Wrote and edited the paper (85%)
Author Y.L. Li	Designed experiments (10%)

	Wrote and edited paper (0%)
Author P.A. Meehan	Designed experiments (10%) Wrote and edited the paper (15%)

B. Li, Y.L., **Liu, Z.B.**, Lu, H.B., Daniel, W.J.T., Meehan, P.A., 2014. Experimental study and efficient prediction on forming forces in incremental sheet forming. *Advanced Materials Research* 939, 313-321.

Contributor	Statement of contribution
Author Y.L. Li	Designed experiments (70%) Wrote and edited the paper (75%)
Author Z.B. Liu (Candidate)	Designed experiments (10%) Wrote and edited paper (5%)
Author H.B. Lu	Designed experiments (5%) Wrote and edited paper (5%)
Author W.J.T. Daniel	Designed experiments (5%) Wrote and edited the paper (5%)
Author P.A. Meehan	Designed experiments (10%) Wrote and edited the paper (10%)

C. Li, Y.L., **Liu, Z.B.**, Daniel, W.J.T., Meehan, P.A., 2013. Simulation and experimental observations of effect of different contact interfaces on the incremental sheet forming process. *Materials and Manufacturing Processes* 29(2), 121-128.

Contributor	Statement of contribution
Author Y.L. Li	Designed experiments (65%) Wrote and edited the paper (80%)
Author Z.B. Liu (Candidate)	Designed experiments (15%) Wrote and edited paper (5%)
Author W.J.T. Daniel	Designed experiments (10%) Wrote and edited the paper (5%)
Author P.A. Meehan	Designed experiments (10%) Wrote and edited the paper (10%)

D. Lu, H.B., Li, Y.L., Liu, Z.B., Liu, S., Meehan, P.A., 2014. Study on step depth for part accuracy improvement in incremental sheet forming process. *Advanced Materials Research* 939, 274-280.

Contributor	Statement of contribution
Author H.B. Lu	Designed experiments (70%) Wrote and edited the paper (75%)
Author Y.L. Li	Designed experiments (10%) Wrote and edited paper (5%)
Author Z.B. Liu (Candidate)	Designed experiments (10%) Wrote and edited paper (5%)
Author S. Liu	Designed experiments (0%) Wrote and edited the paper (5%)
Author P.A. Meehan	Designed experiments (10%) Wrote and edited the paper (10%)

E. Liu, Z.B., Li, Y.L., Daniel, W.J.T., Meehan, P.A., 2014. Taguchi optimization of process parameters for forming time in incremental sheet forming process. *Materials Science Forum* 773-774, 137-143.

Contributor	Statement of contribution
Author Z.B. Liu (Candidate)	Designed experiments (75%) Wrote and edited the paper (85%)
Author Y.L. Li	Designed experiments (10%) Wrote and edited paper (0%)
Author W.J.T. Daniel	Designed experiments (5%) Wrote and edited the paper (5%)
Author P.A. Meehan	Designed experiments (10%) Wrote and edited the paper (10%)

F. Liu, Z.B., Liu, S., Li, Y.L., Meehan, P.A., 2014. Modelling and optimization of surface roughness in incremental sheet forming using a multi-objective function, *Materials and Manufacturing Processes* 29(7), 808-818.

Contributor	Statement of contribution
Author Z.B. Liu (Candidate)	Designed experiments (80%) Wrote and edited the paper (80%)

Author S. Liu	Designed experiments (5%) Wrote and edited paper (10%)
Author Y.L. Li	Designed experiments (5%) Wrote and edited the paper (0%)
Author P.A. Meehan	Designed experiments (10%) Wrote and edited the paper (10%)

4.2 Multi-Pass ISF Modelling and Its Validation

G. Liu, Z.B., Li, Y.L., Meehan, P.A., 2013. Vertical wall formation and material flow control for incremental sheet forming by revisiting multi-stage deformation path strategies, *Materials and Manufacturing Processes* 28(5), 562-571.

Contributor	Statement of contribution
Author Z.B. Liu (Candidate)	Designed experiments (80%) Wrote and edited the paper (85%)
Author Y.L. Li	Designed experiments (10%) Wrote and edited paper (0%)
Author P.A. Meehan	Designed experiments (10%) Wrote and edited the paper (15%)

H. Liu, Z.B., Meehan, P.A., Bellette, P.A., 2011. Thickness distribution and forming strategy analysis for two point incremental forming with a male die. *Advanced Materials Research* 337, 452-455.

Contributor	Statement of contribution
Author Z.B. Liu (Candidate)	Designed experiments (80%) Wrote and edited the paper (80%)
Author P.A. Meehan	Designed experiments (10%) Wrote and edited paper (10%)
Author P.A. Bellette	Designed experiments (10%) Wrote and edited the paper (10%)

I. Liu, Z.B., Li, Y.L., Daniel, W.J.T., Meehan, P.A., 2014. An analytical model for deformation path design in multistage incremental sheet forming process. *Advanced Materials Research* 939, 245-252.

Contributor	Statement of contribution
Author Z.B. Liu (Candidate)	Designed experiments (75%) Wrote and edited the paper (85%)
Author Y.L. Li	Designed experiments (5%) Wrote and edited paper (0%)
Author W.J.T. Daniel	Designed experiments (10%) Wrote and edited the paper (5%)
Author P.A. Meehan	Designed experiments (10%) Wrote and edited the paper (10%)

J. Liu, Z.B., Daniel, W.J.T., Li, Y.L., Liu, S., Meehan, P.A., 2014. Multi-pass deformation design for incremental sheet forming: Analytical modeling, finite element analysis and experimental validation. *Journal of Materials Processing Technology* 214(3), 620-634.

Contributor	Statement of contribution
Author Z.B. Liu (Candidate)	Designed experiments (75%) Wrote and edited the paper (80%)
Author W.J.T. Daniel	Designed experiments (10%) Wrote and edited the paper (5%)
Author Y.L. Li	Designed experiments (5%) Wrote and edited the paper (0%)
Author S. Liu	Designed experiments (0%) Wrote and edited the paper (5%)
Author P.A. Meehan	Designed experiments (10%) Wrote and edited the paper (10%)

K. Liu, Z.B., Li, Y.L., Meehan, P.A., 2014. Tool path strategies and deformation analysis in multi-pass incremental sheet forming process. *International Journal of Advanced Manufacturing Technology* 75(1-4), 395-409.

Contributor	Statement of contribution
Author Z.B. Liu (Candidate)	Designed experiments (80%) Wrote and edited the paper (90%)
Author Y.L. Li	Designed experiments (10%) Wrote and edited paper (0%)

Author P.A. Meehan	Designed experiments (10%) Wrote and edited the paper (10%)
--------------------	--

Contributions by others to the thesis

My principle supervisor Paul Meehan provided extensive assistance with drafting and revision of this thesis so as to contribute to the interpretation.

Statement of parts of the thesis submitted to qualify for the award of another degree

None.

Acknowledgements

I would like to thank my principal supervisor A/Prof. Paul A. Meehan for his excellent guidance, great support and encouragement during the course of my candidature. You provided me the opportunity to participate in this interesting research project.

To my co-supervisor Dr. Bill Daniel, thank you very much for your enlightening guidance and suggestions, especially those regarding the multi-pass modelling issues. I am also grateful for your precious time to revise my papers and the advice on how to improve them.

I would also like to express my gratitude and thanks to the following people:

- Yanle Li and Haibo Lu for their assistance in setting up experiments.
- Dr. Paul Bellette and Dr. Sheng Liu for their valuable suggestions on the experiments and data analysis.
- Michael Elford, Geoff Weakley, Sara Eastwood, Gui Wang and Matthew Dargusch for their technical support.

The financial support provided by the Australian Research Council (ARC), Boeing Research & Technology – Australia (BRTA) and QMI Solutions are greatly acknowledged. Many thanks are also given to the University of Queensland for providing me a UQ International Scholarship (UQI) to accomplish my study.

Finally, I would like to express my sincere gratitude to my parents for their understanding, encouragement and endless love during the course of my study in Australia.

Keywords

incremental sheet forming, multi-pass, prediction, thickness strain, optimization, aluminium, formability, forming force, geometric accuracy, surface roughness

Australian and New Zealand Standard Research Classifications (ANZSRC)

ANZSRC code: 091399, Mechanical Engineering not elsewhere classified, 20%

ANZSRC code: 091307, Numerical Modelling and Mechanical Characterisation, 30%

ANZSRC code: 091006, Manufacturing Processes and Technologies, 50%

Fields of Research (FoR) Classification

FoR code: 0913, Mechanical Engineering, 50%

FoR code: 0910, Manufacturing Engineering, 50%

Table of Contents

Chapter 1 Introduction	1
1.1 Background and Motivation.....	1
1.1.1 Incremental Sheet Forming Technology.....	2
1.1.2 Research Motivation.....	4
1.2 Scope and Objectives of This Thesis.....	8
1.3 Thesis Outline.....	10
Chapter 2 Literature Review	12
2.1 Deformation Mechanisms and Process Formability.....	12
2.1.1 Deformation Mechanisms.....	12
2.1.1.1 Membrane Analysis.....	12
2.1.1.2 Shear Deformation.....	13
2.1.1.3 Bending under Tension.....	14
2.1.1.4 The ‘Noodle’ Theory.....	15
2.1.2 Investigation of Forming Limits.....	16
2.1.2.1 Fracture Forming Limit Diagrams.....	16
2.1.2.2 Formability Indicators - Maximum Forming Angle and Fracture Depth....	19
2.1.3 Increased Process Capability.....	20
2.1.4 Summary.....	22
2.2 Forming Forces.....	23
2.2.1 Effects of Process Parameters on Forming Forces.....	23
2.2.2 Force Prediction.....	24
2.2.3 Force-Based Failure Prediction.....	25
2.2.4 Summary.....	25
2.3 Forming Efficiency.....	26
2.3.1 Summary.....	26
2.4 Geometric Accuracy.....	26
2.4.1 Prediction for Geometric Accuracy - Empirical and FE Modeling.....	27
2.4.2 Methods for Enhanced Geometric Accuracy.....	28
2.4.3 Summary.....	29
2.5 Surface Finish.....	29
2.5.1 Effects of Process Parameters on Surface Finish.....	29

2.5.2 Predictive Modelling for Surface Finish.....	30
2.5.3 Summary.....	30
2.6 Multi-Pass Deformation Design and Tool Path Generation.....	31
2.6.1 Thinning and Fracture.....	31
2.6.2 Multi-Pass Deformation Design.....	33
2.6.3 Tool Path Generation and Optimization.....	37
2.6.3.1 Tool Path Generation.....	37
2.6.3.2 Tool Path Optimization.....	39
2.6.4 Summary.....	41
2.7 Conclusions.....	42
Chapter 3 Methodology.....	43
3.1 Process Investigation - Optimization Methodologies.....	43
3.1.1 Taguchi Method.....	43
3.1.2 Response Surface Methodology.....	45
3.2 SPIF Multi-Pass Deformation Design.....	48
3.2.1 Simplified Deformation Analysis for Qualitative Comparison between Single-Stage Forming and Multi-Stage Forming.....	51
3.2.2 Simplified Deformation Analysis for Qualitative Comparison between Multi-Stage Forming Strategies.....	52
3.3 AMINO TPIF Multi-Pass Deformation Design.....	54
3.3.1 Modeling Methodology for Closed-Loop Deformation Pass Design.....	54
3.3.1.1 Single-Pass Deformation Model - Shear Deformation.....	54
3.3.1.2 Developed Open-Loop Multi-Pass Deformation Models.....	55
3.3.1.3 Methodology for Closed-Loop Multi-Stage Deformation Pass Design.....	62
3.3.2 Finite Element Modeling.....	63
3.3.3 Multi-Pass Tool Path Generation Strategies.....	65
3.4 Experimental Equipment and Validation Methodology.....	68
3.4.1 The AMINO DLNC-PC ISF Machine.....	69
3.4.2 Simplified Load Cell for Force Measurement.....	70
3.4.3 Laser Scanner.....	70
3.4.4 Profilometer.....	71
3.4.5 Tensile Test Machine.....	72

Chapter 4 Results.....	73
4.1 Overview of Papers for Process Investigation: Process Formability, Forming Forces, Geometric Accuracy, Forming Time and Surface Roughness.....	73
4.1.1 Process Formability and Forming Forces.....	73
4.1.2 Geometric Accuracy.....	75
4.1.3 Forming Time.....	76
4.1.4 Surface Roughness.....	76
4.2 Overview of Papers for Multi-Pass ISF Modeling and Its Validation.....	77
4.2.1 SPIF Multi-Pass Deformation Design.....	77
4.2.2 AMINO TPIF Multi-Pass Deformation Design.....	78
Paper A.....	83
Liu, Z.B. , Li, Y.L., Meehan, P.A.	
Experimental investigation of mechanical properties, formability and force measurement for AA7075-O aluminium alloy sheets formed by incremental forming	
International Journal of Precision Engineering and Manufacturing 2013, Volume: 14(11), Pages: 1891-1899.	
Paper B.....	93
Li, Y.L., Liu, Z.B. , Lu, H.B., Daniel, W.J.T., Meehan, P.A.	
Experimental study and efficient prediction on forming forces in incremental sheet forming	
Advanced Materials Research 2014, Volume: 939, Pages: 313-321.	
Paper C.....	103
Li, Y.L., Liu, Z.B. , Daniel, W.J.T., Meehan, P.A.	
Simulation and experimental observations of effect of different contact interfaces on the incremental sheet forming process	
Materials and Manufacturing Processes 2014, Volume: 29(2), Pages: 121-128.	
Paper D.....	112
Lu, H.B., Li, Y.L., Liu, Z.B. , Liu, S., Meehan, P.A.	
Study on step depth for part accuracy improvement in incremental sheet forming process	
Advanced Materials Research 2014, Volume: 939, Pages: 274-280.	
Paper E.....	120
Liu, Z.B. , Li, Y.L., Daniel, W.J.T., Meehan, P.A.	

Taguchi optimization of process parameters for forming time in incremental sheet forming process

Materials Science Forum 2014, Volume 773-774, Pages 137-143.

Paper F.....128

Liu, Z.B., Liu, S., Li, Y.L., Meehan, P.A.

Modelling and optimization of surface roughness in incremental sheet forming using a multi-objective function

Materials and Manufacturing Processes 2014, Volume: 29(7), Pages: 808-818.

Paper G.....141

Liu, Z.B., Li, Y.L., Meehan, P.A.

Vertical wall formation and material flow control for incremental sheet forming by revisiting multi-stage deformation path strategies

Materials and Manufacturing Processes 2013, Volume: 28(5), Pages: 562-571.

Paper H.....153

Liu, Z.B., Meehan, P.A., Bellette, P.A.

Thickness distribution and forming strategy analysis for two point incremental forming with a male die

Advanced Materials Research 2011, Volume: 337, Pages: 452-455.

Paper I.....158

Liu, Z.B., Li, Y.L., Daniel, W.J.T., Meehan, P.A.

An analytical model for deformation path design in multistage incremental sheet forming process

Advanced Materials Research 2014, Volume: 939, Pages: 245-252.

Paper J.....167

Liu, Z.B., Daniel, W.J.T., Li, Y.L., Liu, S., Meehan, P.A.

Multi-pass deformation design for incremental sheet forming: Analytical modeling, finite element analysis and experimental validation

Journal of Materials Processing Technology 2014, Volume: 214(3), Pages: 620-634.

Paper K.....183

Liu, Z.B., Li, Y.L., Meehan, P.A.

Tool path strategies and deformation analysis in multi-pass incremental sheet forming process

International Journal of Advanced Manufacturing Technology 2014, Volume: 75(1-4), Pages: 395-409.

Chapter 5 Conclusions and Future Work.....198
5.1 Thesis Contributions.....201
5.2 Suggestions for Future Work.....203

References.....205

Appendix I.....218

Appendix II.....219

List of Figures

Fig.1.1. Sheet metal components: (a) automobile hood [Amino website]; (b) 1:2.5 scale model of a bullet train nose [Amino website]; (c) a medical part - ankle support [Ambrogio et al. (2005)].....	2
Fig.1.2. Various sheet metal parts manufactured by ISF: (a)-(b) [Jeswiet et al. (2005d)]; (c) [Ambrogio et al. (2004b)]; (d) [Schafer and Schraft (2005)]; (e) [Duflou et al. (2008b)]; (f) a human face made by QMI solutions.....	3
Fig.1.3. ISF configurations: (a) single point incremental forming (Paper A); (b) two point incremental forming (Paper A).....	4
Fig.1.4. Forming Limit Curve (both traditional and non-traditional curves) for 1.21 mm thick AA1050-O forming of pyramids in SPIF (Filice et al. (2002)).....	5
Fig.1.5. Equipment for ISF: (a) Conventional milling machine upgraded and used for ISF [Jeswiet et al. (2005a)]; (b) Specifically-built Amino ISF machine; (c) Industrial robot used for ISF (Schafer and Schraft (2005)).....	6
Fig.1.6. (a) Illustration of the sine law in 2D and 3D (Bambach (2010)); (b) An example of thickness prediction by the sine law (Junk (2003)).....	8
Fig.2.1. Illustration of 'noodle' theory in SPIF as compared to conventional forming:(a) Stretching the string at the free end; (b) material localization at a single location on the string; (c) Fracture at location of material localization; (d) Stretching the string by Δ_s at location Δ_c from the free end; (e) continuous material localization along length of the string; (f) elongation to a greater length without fracture (Malhotra et al. (2012)).....	15
Fig.2.2. Forming Limit Curve (both traditional and non-traditional curves) for 1.21 mm thick AA1050-O forming of pyramids in SPIF (Filice et al. (2002)).....	16
Fig.2.3. Configuration for ISF with stretch forming (Taleb Araghi et al. (2009)).....	21
Fig.2.4. Single-pass SPIF wall thickness profile for the 70° cone (Young and Jeswiet (2004)).....	32
Fig.2.5. Thinning band observed on the 70° cone (Young and Jeswiet (2004)).....	32
Fig.2.6. Multi-stage forming strategy in Hirt et al. (2004).....	34
Fig.2.7. Multi-stage SPIF strategy for producing a cylindrical cup with vertical walls (Skjoedt et al. (2010)).....	35
Fig.2.8. Material extrusion phenomenon in multi-pass SPIF (Paper G).....	35
Fig.2.9. Determination of corrected points (Hirt et al. (2004)).....	40
Fig.2.10. Closed-loop feedback control (Allwood et al. (2009)).....	41

Fig.3.1. Membership functions for internal tool-sheet contact surface roughness SR_i and external non-contact surface roughness SR_e	48
Fig.3.2. Forming strategies: (a) Strategy A: incremental part diameter; (b) Strategy B: incremental draw angle; (c) Strategy C: incremental part height and draw angle.....	49
Fig.3.3. Mechanism explanation: (a) comparison of single-stage forming and multi-stage forming, and (b) comparison of strategy B and strategy C.....	50
Fig.3.4. Mechanism of shear deformation.....	54
Fig.3.5. Illustration of model two in detail.....	60
Fig.3.6. Systematic methodology for closed-loop multi-stage deformation pass design (ζ is a very small number).....	63
Fig.3.7. Simplified FE modeling for TPIF.....	64
Fig.3.8. The designed tool path with three adjustable parameters-ramp angle, start point and travel direction.....	66
Fig.3.9. The AMINO ISF machine used for experiments.....	68
Fig.3.10. Simplified load cell for the force measurement.....	69
Fig.3.11. Laser scanner.....	70
Fig.3.12. Taylor-Hobson Surtronic 3+ Profilometer.....	71
Fig.3.13. Specimen shape for uniaxial tensile tests (drawing unit: mm, thickness unit: inch)	72
Fig.3.14. INSTRON 5584 universal testing machine.....	72
Fig.4.1(Fig.1). Specimen shape for uniaxial tensile test (Unit: mm).....	(1892)84
Fig.4.2(Fig.2). INSTRON 5584 universal testing machine.....	(1892)84
Fig.4.3(Fig.3). True stress-true strain curves for AA7075-O aluminium alloy sheets with 1.02 mm thickness.....	(1893)85
Fig.4.4(Fig.4). True stress-true strain curves for AA7075-O aluminium alloy sheets with 1.60 mm thickness.....	(1893)85
Fig.4.5(Fig.5). True stress-true strain curves for AA7075-O aluminium alloy sheets with 2.54 mm thickness.....	(1893)85
Fig.4.6(Fig.6). Benchmark- a truncated cone.....	(1893)85
Fig.4.7(Fig.7). The Amino ISF machine used for experiments.....	(1893)85
Fig.4.8(Fig.8). Details of incremental forming and illustration of incremental steps (step over and step down).....	(1894)86
Fig.4.9(Fig.9). Design of tool paths to test formability for truncated cones: (a) spiral tool path and (b) z-level tool path (α is the draw angle).....	(1894)86

Fig.4.10(Fig.10). Influence of spiral and z-level tool paths on formability vs the draw angle α (1894)86

Fig.4.11(Fig.11). Influence of the z-level tool path with different incremental steps on formability vs the draw angle α (1895)87

Fig.4.12(Fig.12). The comparison of effects of spiral and z-level tool paths with incremental steps on formability vs the draw angle α (1895)87

Fig.4.13(Fig.13). Fracture forming limit diagram-experimental strains for truncated cones with different draw angles (z-level path with 0.2 mm step-over size). The solid points correspond to maximum and minimum major true strains..... (1895)87

Fig.4.14(Fig.14). Sensor for the force measurement.....(1896)88

Fig.4.15(Fig.15). Influence of three different draw angles on resultant forces with 1.6 mm sheet thickness, spiral tool path with 0.5 mm step-over size and 15 mm tool radius for AA 7075-O sheets (Cracks happen in the cases with draw angles 65° and 70°).....(1896)88

Fig.4.16(Fig.16). Influence of three different draw angles on resultant forces with 1.6 mm sheet thickness, z-level tool path with 0.5 mm step-over size and 15 mm tool radius for AA 7075-O sheets (Cracks happen in the cases with draw angles 65° and 70°).....(1896)88

Fig.4.17(Fig.17). Slopes for force curves after force peak values for both spiral and z-level tool paths.....(1896)88

Fig.4.18(Fig.18). Investigated benchmark shape and z-level tool path: (a) pyramidal shape (b) z-level tool path.....(1897)89

Fig.4.19(Fig.19). Three-axis forces for the truncated pyramid of draw angle 55° with 2.54 mm sheet thickness, z-level tool path with 0.5 mm step-down size and 15 mm tool radius for AA 7075-O sheets: (a) the whole forming process (b) one small time period with one typical lap in transition region (c) one small time period with one typical lap in steady region.....(1897)89

Fig.4.20(Fig.20). The influence of sheet thickness and step-down size on vertical forming force of truncated pyramid with 55° draw angle in SPIF: (a) the relationship of sheet thickness and step-down size with maximum vertical forces (b) the comparison of the maximum vertical forces in nine experiments.....(1898)90

Fig.4.21(Fig.21). Forming results with different sheet orientations (a) 0 degree; (b) 45 degree.....(1898)90

Fig.4.22(Fig.22). Vertical forming forces for two sheet orientations (0 degree and 45 degree) with 0.5 mm step-down size and 15 mm tool radius for AA 7075-O sheet (T=thickness).....(1898)90

Fig.4.23(Fig.1). Incremental sheet forming on Amino machine.....	(315)95
Fig.4.24(Fig.2). Sketch of ISF experimental parameters and a case study made from AA 7075 -O of 1.6 mm in thickness.....	(315)95
Fig.4.25(Fig.3). Three force components (F_x , F_y and F_z) versus forming time and a detailed view for two cycles during forming a cone.....	(317)97
Fig.4.26(Fig.4). Vertical force trend with the varying of wall angle (fracture parts are marked).....	(317)97
Fig.4.27(Fig.5). Variations of forming forces with different wall angles.....	(318)98
Fig.4.28(Fig.6). Formed depth with different wall angles.....	(318)98
Fig.4.29(Fig.7). Vertical force trend with the varying of step down size (fracture parts are marked).....	(319)99
Fig.4.30(Fig.8). Variations of forming forces with different step down sizes.....	(319)99
Fig.4.31(Fig.9). Comparison between MATLAB model and experimental values...	(320)100
Fig.4.32(Figure 1). Incremental sheet forming on Amino machine.....	(122)104
Fig.4.33(Figure 2). Four different tools and tool path that were utilised in the experiments	(122)104
Fig.4.34(Figure 3). FE model of the ISF process in LS-DYNA. Reference elements 1-4 marked.....	(123)105
Fig.4.35(Figure 4). Vertical and horizontal force with a tool of 30 mm in diameter and the absolute value of the ratios between two components.....	(123)105
Fig.4.36(Figure 5). Variations of failure depth of the groove test with tools different in diameter. (RD represents rolling direction and TD for transverse direction).....	(124)106
Fig.4.37(Figure 6). Failure types of sheets formed with different tools. (a. monodirectional; b. bidirectional failure; c. scanning electron micrograph of the onset of fracture and the cross section).....	(124)106
Fig.4.38(Figure 7). Force comparison between simulated and experimental results	(125)107
Fig.4.39(Figure 8). Distributions of major strain predicted by LS-DYNA with different size tools at the depth of 21 mm.....	(125)107
Fig.4.40(Figure 9). Effective plastic strain evolution of four elements in a groove forming process with 30 mm diameter tool.....	(125)107
Fig.4.41(Figure 10). Thickness distribution predicted by LS-DYNA with different size tools. Reference elements 1-4 marked.....	(126)108

Fig.4.42(Figure 11). Surface topography examined by SEM for sheets formed with different tools along the directions indicated by arrows: (a) hemispherical tool; (b) ball tool.....(126)108

Fig.4.43(Figure 12). Border zone of the contracted and non-contracted area with ball tool.....(126)108

Fig.4.44(Fig.1). Process principle of SPIF: step depth (ΔZ) is the vertical distance between two neighbouring contours.....(275)113

Fig.4.45(Fig.2). AMINO[®] DLNC-PC ISF Machine.....(276)114

Fig.4.46(Fig.3). (a) Cross-sectional comparison among deformed profiles and the target profile; (b) Error distribution of deformed parts.....(277)115

Fig.4.47(Fig.4). Diagram of tool marks on the inner part face.....(278)116

Fig.4.48(Fig.5). Surface morphology of deformed parts in surface quality test: (a) $\Delta Z = 1.1$ mm; (b) $\Delta Z = 0.6$ mm; (c) $\Delta Z = 0.1$ mm(278)116

Fig.4.49(Fig.6). (a) Part fracture in formability test ($\Delta Z = 0.1$ mm); (b) Formed depth of parts in formability test.....(279)117

Fig.4.50(Fig.1). Amino ISF machine.....(138)121

Fig.4.51(Fig.2). The formability test - a truncated cone with curvature generatrix...(138)121

Fig.4.52(Fig.3). The nine formed truncated cones according to Taguchi design.....(140)123

Fig.4.53(Fig.4). Graph showing factor effects for S/N ratio.....(141)124

Fig.4.54(Fig.1). Surface topography in SPIF: (a) internal tool-sheet contact surface; (b) external non-contact surface (shape: a 45° cone, step-down:0.5 mm, feed rate:1000 mm/min, tool diameter:10 mm, sheet thickness(AA7075-O): 1.02 mm).....(809)129

Fig.4.55(Fig.2). Evolution of internal tool-sheet contact surface roughness with a tool diameter of 12.7 mm influenced by different step-down sizes [7].....(810)130

Fig.4.56(Fig.3). Illustration of surface characteristics in detail.....(810)130

Fig.4.57(Fig.4). Optical image for roll marks on AA7075-O sheets with a thickness of 1.02 mm..... (810)130

Fig.4.58(Fig.5). An example of tested pyramidal shapes with 55° draw angle illustrating measured regions and directions parallel and perpendicular to roll mark direction..(810)130

Fig.4.59(Fig.6). Definition of R_a(811)131

Fig.4.60(Fig.7). Membership functions for internal tool-sheet contact surface roughness SR_i and external non-contact surface roughness SR_e [16].....(811)131

Fig.4.61(Fig.8). The Amino ISF machine for experiments.....(812)132

Fig.4.62(Fig.9). Taylor-Hobson Surtronic 3+ Profilometer.....(812)132

Fig.4.63(Fig.10). Measured results of internal and external surface roughness. Note: Sd, Fr, St and Td are defined as step down, feed rate, sheet thickness and tool diameter(813)133

Fig.4.64(Fig.11). Optical images for experimental sample 17: (a) internal roughness-region A; (b) internal roughness-region B;(c) external roughness-region A;(d) external roughness-region B.....(814)134

Fig.4.65(Fig.12). 3D response surface showing the effect of factors step down (X_1) and sheet thickness (X_3) on the overall surface roughness with the constant feed rate (X_2) of 5000 mm/min: (a) tool diameter (X_4) =15 mm; (b) tool diameter (X_4) =20 mm; (c) tool diameter (X_4) =25 mm.....(815)135

Fig.4.66(Fig.13). 3D response surface showing the effect of factors feed rate (X_2) and tool diameter (X_4) on the overall surface roughness with the constant step down (X_1) of 0.5 mm: (a) sheet thickness (X_3)=1.02 mm; (b) sheet thickness (X_3)=1.60 mm; (c) sheet thickness (X_3)=2.54 mm.....(816)136

Fig.4.67(Fig.14). 3D response surface showing the effect of factors feed rate (X_2) and tool diameter (X_4) on the overall surface roughness with the constant sheet thickness (X_3) of 1.60 mm: (a) step down (X_1)=0.2 mm; (b) step down (X_1)=0.5 mm; (c) step down (X_1)=0.8 mm.....(817)137

Fig.4.68(Fig.15). Optimization results: (a) multi-objective function with single-objective desirability function; (b) desirability function with multiple responses.....(817)137

Fig.4.69(FIGURE 1). Single point incremental forming (SPIF) [1,5].....(563)142

Fig.4.70(FIGURE 2). Two point incremental forming (SPIF) [1,5].....(563)142

Fig.4.71(FIGURE 3). Strategy A: incremental part diameter.....(563)142

Fig.4.72(FIGURE 4). strategy B: incremental part draw angle.....(563)142

Fig.4.73(FIGURE 5). Strategy C: incremental part height and draw angle.....(564)143

Fig.4.74(FIGURE 6). Amino ISF machine at the University of Queensland.....(564)143

Fig.4.75(FIGURE 7). Description of z-level tool path adopted in the experiments...(565)144

Fig.4.76(FIGURE 8). Investigated geometry: a cylindrical cup with vertical wall (unit=mm)(565)144

Fig.4.77(FIGURE 9). Mechanism explanation: (a) strategy B and (b) comparison of strategy B and strategy C.....(566)145

Fig.4.78(FIGURE 10). Obtained experimental shapes for different strategies and strategic combinations.....(567)146

Fig.4.79(FIGURE 11). Crack morphology caused by meridional tensile stress:

(a) initial draw angle 40° and (b) initial draw angle 50°	(568)147
Fig.4.80(FIGURE 12). Forming defects for strategic combination A+B: (a) initial draw angle 40° and (b) initial draw angle 50°	(569)148
Fig.4.81(FIGURE 13). Thickness distribution along wall height for different strategies and strategic combinations with two initial draw angles: (a) IDA= 40° and (b) IDA=50° (IDA=Initial draw angle)	(569)148
Fig.4.82(FIGURE 14). Comparison of biggest differences on thickness measurement between the same strategic combinations A+C, A+B, strategies C and B with initial draw angles 40° and 50°	(570)149
Fig.4.83(Fig.1). Configuration of two point incremental forming with a male die.....	(453)154
Fig.4.84(Fig.2). The method to obtain preform shape and path generation simulation	(455)156
Fig.4.85(Fig.3). ISF machine.....	(455)156
Fig.4.86(Fig.1). Mechanism of shear deformation.....	(247)160
Fig.4.87(Fig.2). Simplified FE modelling for TPIF	(247)160
Fig.4.88(Fig.3). The Amino ISF machine used for experiments.....	(248)161
Fig.4.89(Fig.4). (a) Hemisphere with 50 mm radius; (b) thickness strain distribution	(249)162
Fig.4.90(Fig.5). (a) Deformation paths; (b) predicted thickness strain distribution for deformation path one and two obtained from the model (a quarter section of the part)	(249)162
Fig.4.91(Fig.6). Thickness strain distribution with X and Y sections of deformation path one: X section (rolling direction); (b) Y section (transverse direction).....	(250)163
Fig.4.92(Fig.7). Thickness strain distribution with X and Y sections of deformation path two: (a) X section (rolling direction); (b) Y section (transverse direction).....	(251)164
Fig.4.93(Fig.8). Thickness strain distribution with X and Y sections of the final shape formed by single-stage and designed multi-stage forming: (a) X section (rolling direction); (b) Y section (transverse direction)	(251)164
Fig.4.94(Fig.9). Traces of material points in SPIF and TPIF [2]	(252)165
Fig.4.95(Fig.1). Mechanism of shear deformation.....	(622)169
Fig.4.96(Fig.2). Illustration of model two in detail.....	(623)170
Fig.4.97(Fig.3). Systematic methodology for closed-loop multi-stage deformation pass design (ζ is a very small number).....	(624)171
Fig.4.98(Fig.4). Simplified FE modelling for TPIF.....	(624)171

Fig.4.99(Fig.5). True stress-true strain curves for AA7075-O aluminium alloy sheets with 1.016 mm thickness.....	(625)172
Fig.4.100(Fig.6). Z-level milling tool path for hemisphere: ramp angle=10°	(625)172
Fig.4.101(Fig.7). An approach to importing the tool path into the FE model.....	(625)172
Fig.4.102(Fig.8). The Amino ISF machine used for experiments.....	(625)172
Fig.4.103(Fig.9). Hemisphere with 50 mm radius.....	(626)173
Fig.4.104(Fig.10). Designed deformation passes (intermediate shapes) and final shape: (a) M1 ; and M2	(627)174
Fig.4.105(Fig.11). Multi-stage deformation passes obtained from the developed models (a quarter section of the part): (a) M1 ; (b) M2 . (Vertical solid line indicates the position of minimum intermediate thickness strains.).....	(628)175
Fig.4.106(Fig.12). The predicted thickness strain distribution obtained from the developed models (a quarter section of the part): (a) M1 ; (b) M2 . (Vertical solid line indicates the position of minimum intermediate thickness strains.).....	(628)175
Fig.4.107(Fig.13). Kinematics of material points in ISF: (a) results in Bambach (2010); (b) results in this study.....	(628)175
Fig.4.108(Fig.14). The movement of material point evidenced by FEM results (thickness strain distribution).....	(630)177
Fig.4.109(Fig.15). Thickness strain distribution in the case of deformation pass one for M1 and M2 : (a) M1 -X section; (b) M2 -X section; (c) M1 -Y section; (b) M2 -Y section....	(631)178
Fig.4.110(Fig.16). Thickness strain distribution in the case of deformation pass two for M1 and M2 : (a) M1 -X section; (b) M2 -X section; (c) M1 -Y section; (b) M2 -Y section....	(632)179
Fig.4.111(Fig.17). Thickness strain distribution in the case of final shape for single-stage forming and multi-stage (M1 and M2) forming: (a) Single-stage and M1 -X section; (b) Single-stage and M2 -X section; (c) Single-stage and M1 -Y section; (d) Single-stage and M2 -Y section.....	(633)180
Fig.4.112(Fig.18). Geometric accuracy comparison between designed shape and manufactured shape by multi-stage forming (M2).....	(633)180
Fig.4.113(Fig.1). The designed tool path with three adjustable parameters-ramp angle, start point and travel direction.....	(3)185
Fig.4.114(Fig.2). Simplified FE modeling for TPIF.....	(3)185
Fig.4.115(Fig.3). The AMINO ISF machine used for experiments.....	(4)186
Fig.4.116(Fig.4). Designed shapes: (a) ellipsoidal cup (symmetric shape); (b) free-form shape (asymmetric shape).....	(5)187

Fig.4.117(Fig.5). Deformation pass design for ellipsoidal cup (MATLAB meshes)....	(6)188
Fig.4.118(Fig.6). Deformation pass design for asymmetric free-form shape (MATLAB meshes).....	(6)188
Fig.4.119(Fig.7). Comparison of thickness strain distributions for ellipsoidal cup (Single-pass forming vs. Test No.2 in multi-pass forming).....	(8)190
Fig.4.120(Fig.8). Influence of ramp angle (RA) on thickness strain distribution of the final shape.....	(8)190
Fig.4.121(Fig.9). Influence of start point (SP) on thickness strain distribution of the final shape (RA=20°).....	(9)191
Fig.4.122(Fig.10). Influence of travel direction (TD) on thickness strain distribution of the final shape.....	(9)191
Fig.4.123(Fig.11). Material flow analysis by FEA (thickness strain distribution).....	(10)192
Fig.4.124(Fig.12). Illustration of tool path start points relative to final part region (top view) with steep angles (Angle increases as the color changes from blue to red).....	(12)194
Fig.4.125(Fig.13). Evolution of thickness strains for the maximum thinning point in the final part of multi-pass forming (No.1) during the FEM simulation.....	(13)195
Fig.4.126(Fig.14). Comparison of thickness strain distributions (Single-pass forming vs. Test No.1 in multi-pass forming).....	(14)196
Fig.4.127(Fig.15). Drawings for asymmetric free-form shape (Unit: mm).....	(15)197

List of Tables

Table 4.1(Table 1). Chemical composition (% wt) for AA7075-O aluminum alloy sheets	(1892)84
Table 4.2(Table 2). Mechanical properties for AA7075-O aluminum alloy sheets with three different thicknesses.....	(1892)84
Table 4.3(Table 3). Strength coefficient K and strain-hardening exponent n for AA7075-O sheets with three different thicknesses.....	(1893)85
Table 4.4(TABLE 1). Experimental design for different wall angles.....	(315)95
Table 4.5(TABLE 2). Experimental design for different step down sizes.....	(316)96
Table 4.6(Table 1). Experimental parameters design for groove test.....	(122)104
Table 4.7(Table 2). Mechanical properties for 7075-O aluminium sheet.....	(123)105
Table 4.8(Table 1). Parameter settings of experiments on step depth.....	(276)114
Table 4.9(Table 1). Mechanical properties for AA 7075-O.....	(138)121
Table 4.10(Table 2). Process parameters and their levels studied.....	(139)122
Table 4.11(Table 3). Orthogonal array L9 (3^4) of the experimental runs.....	(140)123
Table 4.12(Table 4). Experimental results for forming time and S/N ratio.....	(140)123
Table 4.13(Table 5). S/N response table for forming time.....	(141)124
Table 4.14(Table 6). ANOVA table for effect of different forming time.....	(141)124
Table 4.15(Table 7). Results of confirmatory tests at optimal level $A_3B_3C_3D_2$	(142)125
Table 4.16(Table 1). Independent factors and coded levels for response surface...(812)	132
Table 4.17(Table 2). Box-Behnken design for four factors and observed response(813)	133
Table 4.18(Table 3). Results of ANOVA for overall surface roughness (from Minitab)	(814)134
Table 4.19(TABLE 1). Parameter values for different stages.....	(564)143
Table 4.20(TABLE 2). Mechanical properties for AA7075-O sheets with 1.6 mm thickness	(565)144
Table 4.21(TABLE 3). Experimental results for strategies and strategic combinations for cylindrical cup formation (H_F means fracture happens at this height).....	(568)147
Table 4.22(TABLE 4). Comparison of formability prediction and experimental results for initial draw angle 40°	(568,1381)151
Table 4.23(Table 1). Mechanical properties of AA 7075-O aluminium alloy sheets with 1.016 mm thickness.....	(248)161
Table 4.24(Table 2). Designed parameters for deformation paths in the model.....	(249)162

Table 4.25(Table 3). Comparison of formability between single-stage and designed multi-stage forming.....	(250)163
Table 4.26(Table 4). Comparison of minimum thickness strain between model prediction, FE simulation and experiments.....	(251)164
Table 4.27(Table 1). Mechanical properties of AA 7075-O aluminium alloy sheets with 1.016 mm thickness.....	(625)172
Table 4.28(Table 2). Determined parameters for multi-stage deformation passes in M1 and M2	(626)173
Table 4.29(Table 3). Comparison of the formability between the single-stage forming and the proposed multi-stage forming.....	(629)176
Table 4.30(Table 4). Comparison of the minimum thickness strains between the single-stage forming and the proposed closed-loop multi-stage forming.....	(629)176
Table 4.31(Table 1). Tensile test results of AA7075-O aluminum alloy sheets with 1.016 mm and 1.6 mm thicknesses for three directions.....	(4)186
Table 4.32(Table 2). Mechanical properties of AA7075-O aluminum alloy sheets with 1.016 mm and 1.6 mm thicknesses.....	(4)186
Table 4.33(Table 3). Determined parameters in multi-pass deformation design for designed shapes.....	(5)187
Table 4.34(Table 4). Tool path parameters designed in multi-pass forming for ellipsoidal cup.....	(7)189
Table 4.35(Table 5). Comparison of the formability for ellipsoidal cup between single-pass forming and multi-pass forming.....	(7)189
Table 4.36(Table 6). Tool path parameters designed in multi-pass forming for the asymmetric free-form shape.....	(12)194
Table 4.37(Table 7). FEM results (Avg:75%) for maximum thinning points in single-pass forming and multi-pass forming.....	(13)195

List of Abbreviations used in the thesis

2D	Two dimensional
3D	Three dimensional
ADSIF	Accumulative double sided incremental forming
ANOM	Analysis of means
ANOVA	Analysis of variance
CAD	Computer-aided design
CAE	Computer-aided engineering
CAM	Computer-aided manufacturing
CI	Confidence interval
CL	Cutter location
CNC	Computer numerically controlled
DOE	Design of experiments
DSIF	Double sided incremental forming
FEA	Finite element analysis
FEM	Finite element method
FFLDs	Fracture forming limit diagrams
FLC	Forming limit curve
FLDs	Forming limit diagrams
ISF	Incremental sheet forming
MARS	Multivariate adaptive regression splines
MDF	Medium density fiberboard
MK	Marciniak-Kuczynski
RD	Rolling direction
PSO	Particle swarm optimization
RSM	Response surface methodology
SEM	Scanning electron microscope
S/N	Signal-to-noise
SPF	Super plastic forming
SPIF	Single point incremental forming
STL	Stereolithography
TD	Transverse direction
TPIF	Two point incremental forming
TTS	Through thickness shear

Chapter 1 Introduction

The work presented in this thesis is focused on the development of incremental sheet forming (ISF) technology, mainly including two aspects: process investigation, and multi-pass ISF modeling and its validation. The benefit of this research is expected to facilitate the manufacture of complex 3D sheet components, such as aircraft fairings, fan blades and vehicle panels. This chapter summarises the materials presented in the appended papers, which form the basis of this PhD thesis. A general introduction is provided to introduce the current ISF research and the motivation of this thesis.

1.1 Background and Motivation

Sheet metal forming technology is an essential part of modern industry, which allows for the production of high quality products with complex geometries at low manufacturing costs. Nowadays, in the automotive, aerospace and biomedical industries, an increasing demand has emerged for rapid prototyping, and customized small-volume production of diverse sheet metal products, see examples in Fig.1.1. However, sheet metal forming is still mainly characterized by conventional, complicated and cost intensive forming processes like deep drawing, hot forming, super plastic forming (SPF) and hydroforming. These forming techniques show drawbacks which include high costs, long industrialisation phases and high energy consumption rates. Therefore, a new sheet forming technology is necessary to create flexible forming facilities without specialised expensive dies, capable of producing small to medium volume complex shapes with generic tooling.

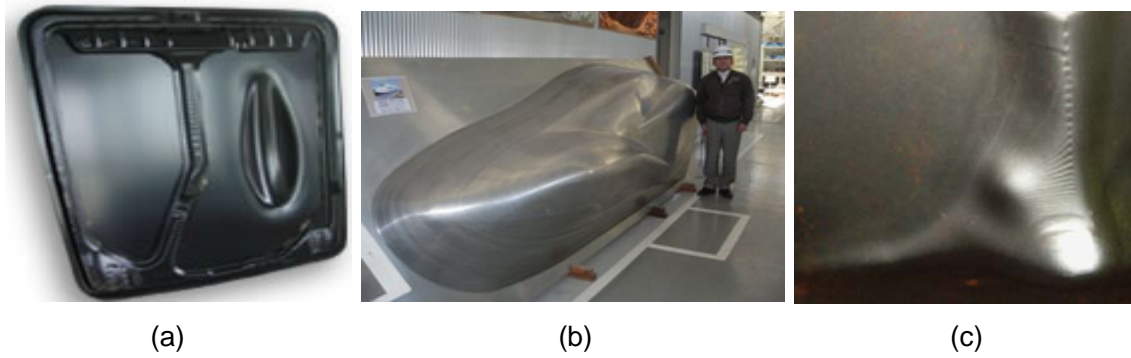


Fig.1.1. Sheet metal components: (a) automobile hood [Amino website]; (b) 1:2.5 scale model of a bullet train nose [Amino website]; (c) a medical part - ankle support [Ambrogio et al. (2005)].

In the past two decades, incremental sheet forming technology (ISF) has been developed to overcome the drawbacks mentioned above. ISF has potential advantages of increased flexibility, cost reduction, minimised energy consumption and a speed up in the industrialisation phase.

1.1.1 Incremental Sheet Forming Technology

Incremental sheet forming (ISF) is characterized in the field of metal forming processes, as a novel forming technology which enables the fabrication of 3-D complex parts, see examples in Fig.1.2. By using ISF it is possible to manufacture most of the typical geometries obtained by deep drawing and stamping although this process is different from conventional deep drawing and stamping processes.

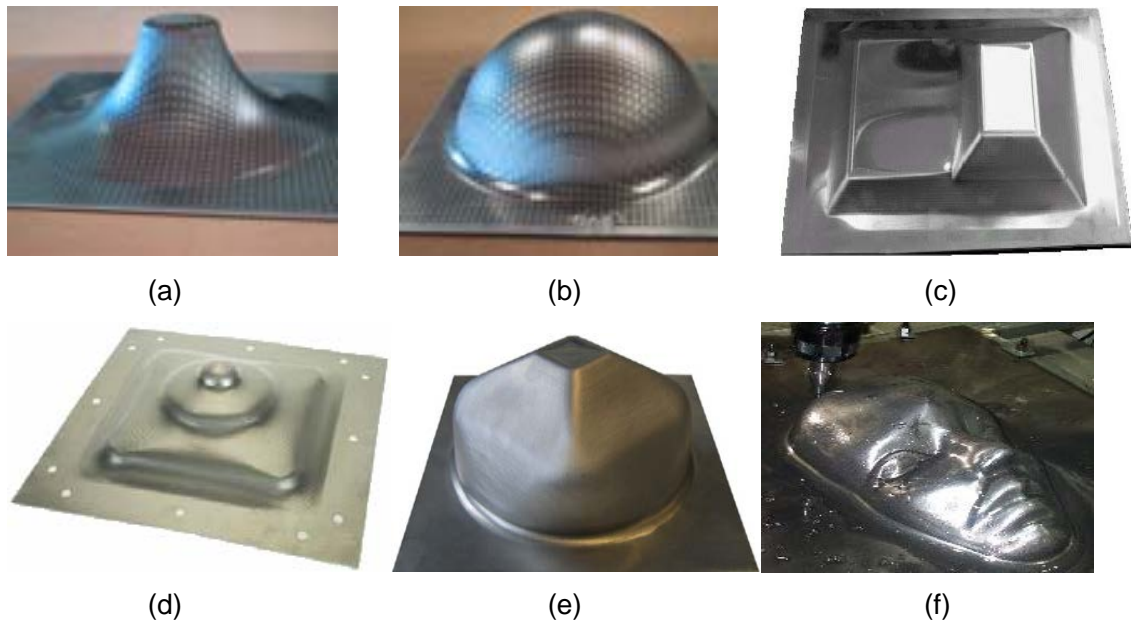
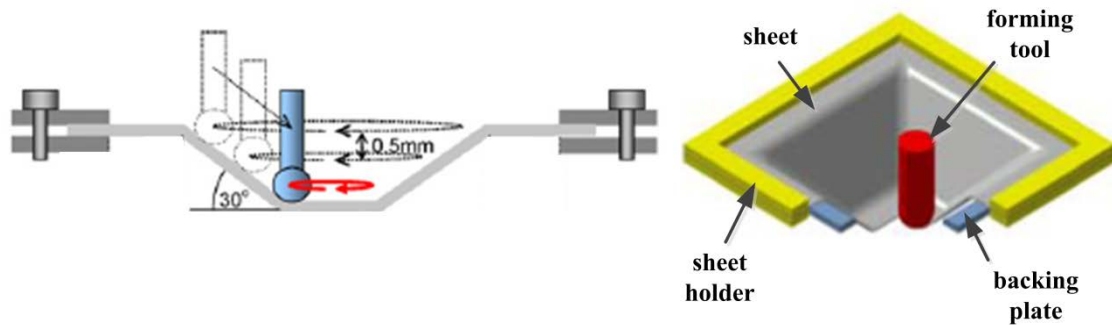


Fig.1.2. Various sheet metal parts manufactured by ISF: (a)-(b) [Jeswiet et al. (2005d)]; (c) [Ambrogio et al. (2004b)]; (d) [Schafer and Schraft (2005)]; (e) [Duflou et al. (2008b)]; (f) a human face made by QMI solutions.

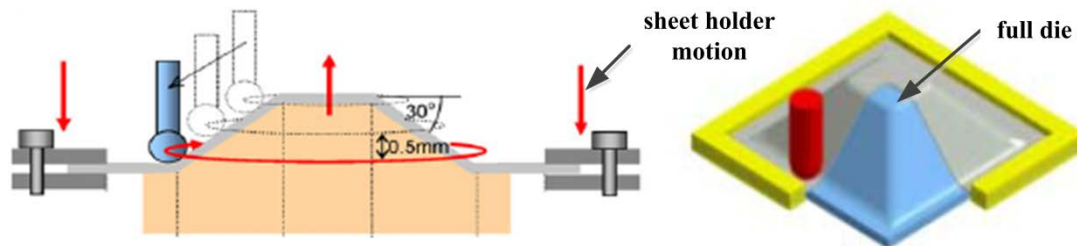
The forming of sheet metal parts is achieved by the generation of successive and localized deformations on the sheet surface until the addition of all the small deformations reaches the final desired shape of the part. Compared with traditional forming processes, this technology allows the dramatic reduction of tooling costs such as no need for expensive dies or punches as well as the costs associated with the manufacture of metallic parts. However, due to its incremental deformation nature, the forming process involves a long travel of forming tool movement. Therefore, it is only suitable for small-batch production of sheet metal parts.

The ISF process can be mainly categorized into two types: single point incremental forming (SPIF) without a forming die and two point incremental forming (TPIF) with a partial or full forming die. The rudimentary illustrations of the types are shown in Fig.1.3(a) and Fig.1.3(b), respectively. The characteristic feature of SPIF is that a part is shaped by the movement of a forming tool which has a single point contact with the sheet metal. The sheet is clamped with a sheet holder which remains at a constant height. In most cases, with the purpose to improve forming accuracy in the transition zone between the flange

and the forming geometry, a backing plate is utilized underneath the sheet. For TPIF, a partial or full positive die is required to provide more control of the sheet deformation and enhance the part accuracy through the forming process. The movement of the sheet holder can be adjusted by the hydraulic actuator with the aim of keeping the sheet metal in the exact working position.



(a) Single point incremental forming



(b) Two point incremental forming

Fig.1.3. ISF configurations: (a) single point incremental forming (**Paper G**); (b) two point incremental forming (**Paper G**).

1.1.2 Research Motivation

Advantages of ISF: In the past decade, ISF has attracted interests in the academic community as well as the industrial sector because of its striking advantages over traditional sheet forming processes such as deep drawing and stamping. These are summarized as follows:

- Higher formability: As seen in Fig.1.4, forming limit curve (FLC) in SPIF has a negative slope and is above the one in conventional forming. The

maximum forming strains to be achieved in SPIF are much higher than that in conventional forming.

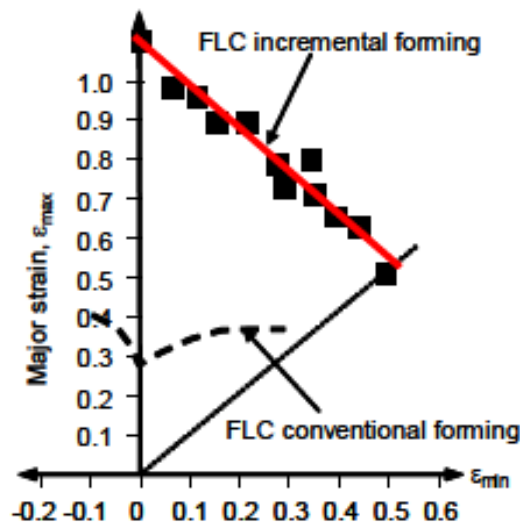
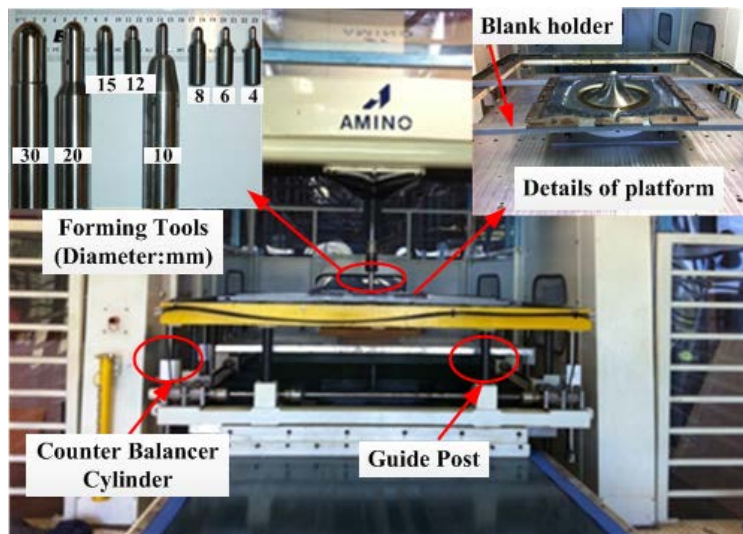


Fig.1.4. Forming Limit Curve (both traditional and non-traditional curves) for 1.21 mm thick AA1050-O forming of pyramids in SPIF (Filice et al. (2002)).

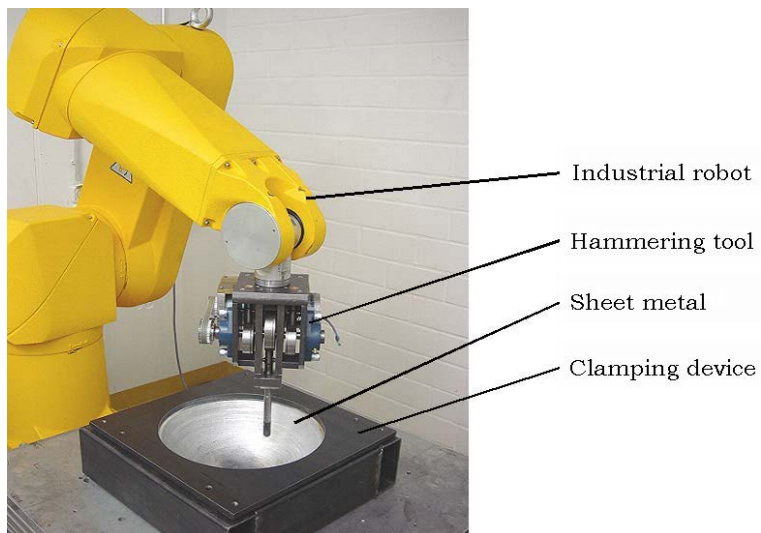
- Lower forming forces: Compared to conventional forming processes, the forming forces are much lower due to the localization of deformation in the tool-sheet contact region. This means that forming forces do not necessarily increase with a part size since they are mainly influenced by several process parameters related to contact conditions, such as the forming tool size, the sheet thickness, the material type and the step-down size.
- Flexible equipment with low-cost tooling: In ISF, one forming tool can manufacture an infinite variety of 3D shapes. Fig.1.5 shows the equipment used for ISF. The first one (Fig.1.5(a)) is updated from a conventional milling machine. The second one (Fig.1.5(b)) is a specifically-built AMINO ISF machine. The third one (Fig.1.5(c)) is an industrial robot used for ISF. As shown in the embedded picture in Fig.1.5(b), tooling is also quite simple for a typical ISF process. In SPIF, tooling can be reduced to a simple rig. In TPIF, forming dies can be made of low-cost materials (wood, plastics, etc.). This makes ISF economically and ecologically favourable for small volume production compared to deep drawing and stamping.



(a) Conventional milling machine upgraded and used for ISF.



(b) Specifically-built AMINO ISF machine.



(c) Industrial robot used for ISF.

Fig.1.5. Equipment for ISF: (a) Conventional milling machine upgraded and used for ISF (Jeswiet et al. (2005a)); (b) Specifically-built Amino ISF machine; (c) Industrial robot used for ISF (Schafer and Schraft (2005)).

- Control of material flow: The material flow can be controlled by using multi-pass forming strategies. Process formability in ISF can be further improved. Additionally, the final part with more uniform thickness distribution would be achieved.

These advantages have made ISF as a potential and promising sheet forming technology to be developed. However, there are still some limitations in ISF that hamper the extensive industrial applications, which will be discussed in the next section.

Limitations of ISF: The limitations of ISF are listed and discussed as follows:

- Process limits: Broadly speaking, process limits can be divided into three aspects, i.e. geometric accuracy at the macroscopic level, surface finish at the microscopic level and excessive thinning.
 - Geometric accuracy. This is a key concern for ISF researchers. Geometric deviations can be observed after unclamping and trimming due to residual stresses as well as springback effects.
 - Surface finish. This is regarded as a weak point in ISF compared to traditional forming processes. Several process parameters, such as step-down size, tool diameter and sheet thickness, determine the surface roughness of final parts.
 - Excessive thinning and fracture. The sine law, as one of the simplest geometrical models in ISF is widely used to predict the sheet thickness of a final part. It relates the initial thickness t_0 to the final thickness t_1 given a wall angle α , see Fig.1.6:

$$t_1 = t_0 \sin(90^\circ - \alpha) \quad (1.1)$$

Experiments show that most sheet materials fail due to fracture induced by excessive thinning when forming a part feature with

wall angles between 60° and 70° . This restriction narrows the range of geometries that can be produced by ISF.

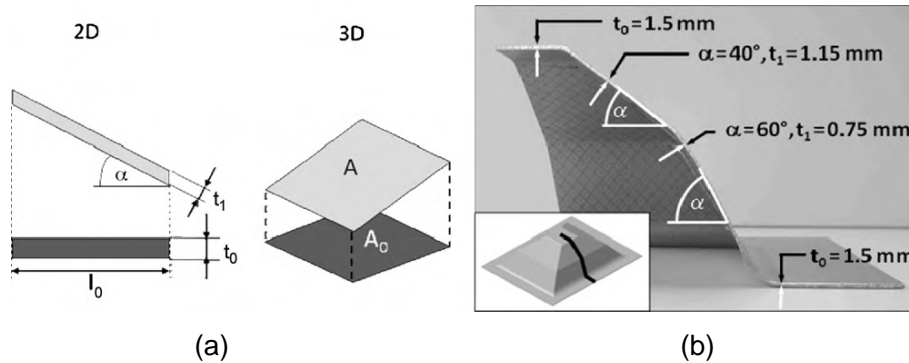


Fig.1.6. (a) Illustration of the sine law in 2D and 3D (Bambach (2010)); (b) An example of thickness prediction by the sine law (Junk (2003)).

- Process efficiency: It is only suitable for small-batch production because of its incremental localized deformation feature inducing relative long forming time.

The limitations discussed above bring some challenges to the extensive industrial applications of ISF. This motivates the on-going researches on the development of ISF being a feasible technology on an industrial scale.

1.2 Scope and Objectives of This Thesis

The focus of this thesis has been mainly directed to two aspects: process investigation, and multi-pass ISF modeling and its validation.

Specifically the major objectives of this thesis have been to:

- Process investigation:

(1) Process formability:

Investigate the effects of process parameters (tool path types, incremental steps, forming tool types) on process formability.

(2) Forming forces:

Investigate the effects of process parameters (part draw angle, sheet thickness, step-down size and sheet orientation) on forming forces. These results are expected to form the basis of the development of a forming force prediction model in the further research.

(3) Geometric accuracy:

Investigate the effect of step-down size on geometric accuracy. These results are expected to form the basis of a future closed-loop control study in the ISF process.

(4) Forming time:

Perform a quantitative design of experiments (Taguchi method) to analyse the effects of process parameters (step over, feed rate, sheet thickness and tool diameter) on forming time and determine the optimal parameters to optimize it.

(5) Surface roughness:

Develop an empirical model with response surface methodology to predict and optimize surface roughness taking into account the influences of relevant process parameters (step-down size, feed rate, sheet thickness and tool diameter). The impact of sheet roll mark orientation on surface roughness is also investigated.

● Multi-pass ISF modeling and its validation:

(1) SPIF multi-pass deformation design to improve process formability and obtain thickness distribution:

- i. Develop an empirical trial-and-error method for deformation pass design.
- ii. Develop a simplified analytical model for formability prediction.

- iii. Perform experimental validation for the empirical design and formability prediction.

(2) AMINO TPIF multi-pass deformation design to improve process formability and obtain thickness distribution:

- i. Develop analytical models for deformation pass design to improve process formability and control material flow.
- ii. Develop FE models to simulate and analyse the actual AMINO TPIF multi-pass forming process in terms of the multi-pass deformation design via analytical models.
- iii. Perform experimental validation for the analytical designs and FE predictions.
- iv. Generalize the developed multi-pass design methodology from simple to complex geometries.
- v. Investigate different tool path generation strategies and their interactions on material thinning and process formability in multi-pass forming.

1.3 Thesis Outline

This thesis can be divided into 5 chapters including this introduction chapter. The results are presented as a collection of published papers grouped in chapter 4. These papers were all completed during the candidature, either as the first author or a co-author, and provide readers with an account for how the research progressed and how the findings of each paper contributes to the development of ISF technology. A summary of the remaining chapters is provided as follows:

Chapter 2 provides a comprehensive review on the state of the art in ISF. The review is divided into six aspects, including methods for deformation mechanisms and process formability, forming forces, forming efficiency, geometric accuracy, surface finish, and multi-pass deformation design and tool path generation.

In Chapter 3, the major methodologies used in this thesis are introduced.

Chapter 4 provides an overview of the results in papers included in this thesis. Six papers are grouped to represent the results for the researches on process formability, forming forces, geometric accuracy, forming time and surface roughness. Five papers are incorporated to illustrate the results for multi-pass ISF modelling and its validation.

Chapter 5 summarises the research in this thesis and provides an outline for future work which discusses possible pathways for further exploring ISF technology.

Chapter 2 Literature Review

This chapter presents a detailed literature review of the state of the art in ISF research including six aspects which are categorized into process mechanism and formability, forming forces, forming efficiency, geometric accuracy, surface finish, multi-pass deformation design and tool path generation. This shall allow for a statement of where the research performed in this thesis contributes to the body knowledge on the development of ISF technology.

2.1 Deformation Mechanisms and Process Formability

This section presents an overview of deformation mechanisms found in literature that are suggested to explain the enhanced formability in ISF. Then, the results concerning the characterization of forming limits are reviewed. Finally, methods to enhance process formability in the literature are discussed.

2.1.1 Deformation Mechanisms

ISF process mechanics are fully characterized by localized plastic deformation, which occurs in a small area between the tool and the sheet metal. In ISF, strains can be obtained well above the forming limit curve (FLC) that is applicable to traditional sheet forming processes like deep drawing and stretching. Understanding of deformation and fracture mechanics in ISF has a great importance for improving formability and extending applicability in the manufacturing industry. There are efforts to explain deformation mechanisms of the ISF process through theoretical analysis and experimental evidence. Several mechanisms have been discussed in full detail in a review paper (Emmens and Boogaard (2009a)). This section only provides a brief review on deformation mechanisms in literature.

2.1.1.1 Membrane Analysis

Silva et al. (2008a) presented a closed-form analytical model for SPIF, which was established based on membrane analysis and the experimental

observation of the smear-mark interference between the tool and the surface of the sheet. The likely mode of material failure at the transition zone between the inclined wall and the corner radius of the sheet was examined. They concluded that cracks in SPIF are claimed to be induced by meridional tensile stresses and not by in-plane shearing stresses. However, they further pointed out that strain hardening and anisotropy are not taken into consideration and bending effects are only indirectly included in the analysis. Following this line, Martins et al. (2008) analysed formability limits of the process by combining the proposed membrane analysis with ductile damage mechanics. An explanation to the increased formability compared to conventional stamping and deep drawing operations was provided through the utilization of fracture forming limit diagrams based on the onset of fracture instead of conventional forming limit diagrams which are based on the onset of necking.

2.1.1.2 Shear Deformation

Shear deformation is believed to be one of the major deformation modes in the ISF process. Much research in the literature has been performed to prove its existence and its influence on process formability.

Allwood et al. (2007) presented that through-thickness shear can affect formability by modeling the SPIF process with the finite element method. The authors demonstrated the significant through-thickness shear (TTS) occurring in the direction parallel to tool motion. It was explained that material on the top surface of the sheet metal tends to move in the direction of the tool displacement because of friction. However, shear perpendicular to the tool direction could not be explained directly by the aspects of friction due to the direction of the tool path. They suggested two alternative explanations: (i) rotation of the tool; and (ii) the tool pushes material downwards while it is moving in descending contours over the inclined wall. The effect of rotation of the tool in shear can be eliminated by investigating of locking off the rotation of the tool.

Jackson and Allwood (2009) continued the previous work by experimentally examining the deformation mechanism through forming of copper sheets with both TPIF and SPIF approaches. They concluded that the deformation mechanisms for both SPIF and TPIF are increasing stretching and shear in the radial-axial plane (perpendicular to tool direction) and shear in the tool direction. Shear in the tool direction, which is likely to be a result of friction between the tool and work-piece, is the most significant strain component. Increasing stretching and shear perpendicular to the tool direction account for differences between the sine law and measured wall thickness for SPIF and TPIF. Shear both parallel and perpendicular to the tool direction is the main distinction between the deformation mechanisms of SPIF or TPIF and pressing.

In Eyckens (2010), the phenomenon of plastic shearing of sheet metal in a plane containing the sheet normal direction (TTS) has been studied in the SPIF process. Strong proof of its existence has been provided on the basis of three different methods: (i) Finite element modeling strategy; (ii) A direct experimental measurement method; (iii) Texture measurements. Furthermore, an extended Marciniak-Kuczynski (MK) model was utilized to predict localized necking in SPIF process. This model is applicable to monotonic loading conditions that do not only consist of in-plane stretching, but also simultaneous through-thickness shearing. The formability predictions of this model showed that TTS can delay the onset of necking under monotonic loading. This delay is similar to the one in the onset of necking under a biaxial stretching mode in conventional forming process.

2.1.1.3 Bending under Tension

Bending under tension can create large stable deformations in sheet metal, which has been proposed as a mechanism operating in ISF. It is postulated that in a relatively large area around the punch, the punch penetration induces a tensile membrane force in the sheet, while close to the punch, the sheet bends around the punch and bends back. Emmens and Boogaard (2009b) pointed out that the stress field around the punch is quite complex, including double bending, so that the direct measurement of membrane forces is almost

impossible. Therefore, they performed the continuous bending under tension test (CBT) to study the aspect of localized deformation in ISF. The results showed that the enhanced formability created by CBT will increase with increasing sheet thickness and decreasing punch radius.

2.1.1.4 The 'Noodle' Theory

Malhotra et al. (2012) used a developed fracture model combined with finite element analysis to predict forming forces, thinning and the occurrence of fracture in SPIF. They concluded that fracture in SPIF is controlled by both local bending and shear. The local nature of deformation in SPIF is the root cause for increased formability as compared to conventional forming. They further proposed a so-called 'noodle' theory, as illustrated in Fig.2.1, to explain the increased formability in SPIF. It was shown that the inherently local nature of deformation in SPIF allows the generation of a larger region of unstable, but not fractured, material before actual failure occurs. This deformed region has the ability to share some of the deformation in the subsequent passes of the tool.

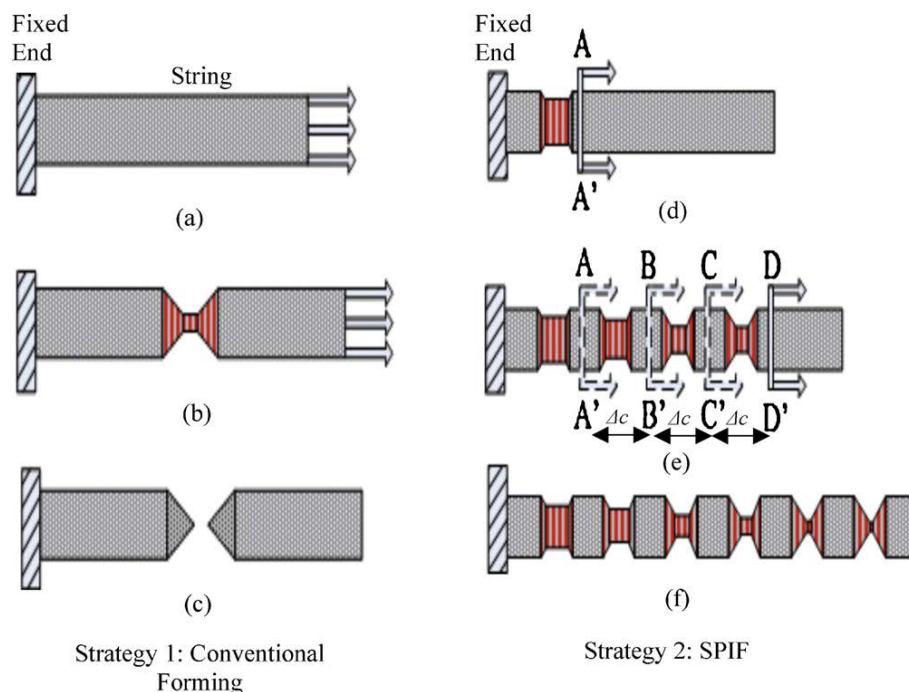


Fig.2.1. Illustration of 'noodle' theory in SPIF as compared to conventional forming:(a) Stretching the string at the free end; (b) material localization at a single location on the string; (c) Fracture at location of material localization; (d) Stretching the string by Δs at

location Δc from the free end; (e) continuous material localization along length of the string; (f) elongation to a greater length without fracture (Malhotra et al. (2012)).

2.1.2 Investigation of Forming Limits

In ISF, forming limits can be generally tested and characterized by fracture forming limit diagrams as well as maximum forming angle and fracture depth.

2.1.2.1 Fracture Forming Limit Diagrams

Forming limit diagrams (FLDs) are traditionally used as one of the tools to determine if the material with a particular thickness can be successfully formed by a deep drawing process. It expresses the maximum strains that can be achieved before necking begins. However, as necking formation is suppressed in ISF, the strains obtained in ISF are much higher than those predicted by traditional FLDs which are applicable to a deep drawing process or a stretching process as shown in Fig.2.2. Therefore, the so-called fracture forming limit diagrams (FFLDs) which are also called non-traditional FLDs in earlier work of ISF research, have been used to characterize the formability in ISF. Much work has been performed in literature to determine FFLDs.

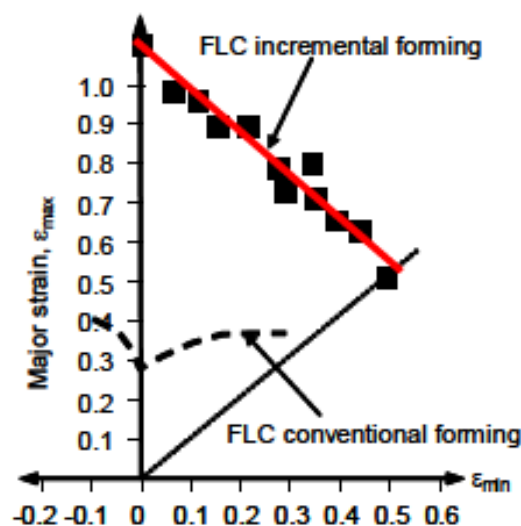


Fig.2.2. Forming Limit Curve (both traditional and non-traditional curves) for 1.21 mm thick AA1050-O forming of pyramids in SPIF (Filice et al. (2002)).

Earlier work performed by Shim and Park (2001) showed that the forming limit diagram in ISF is quite different from that in conventional forming. It appears to be a straight line with a negative slope in the positive region of the minor strain in FLD. The experimental tests further revealed that cracks are likely to occur at the corners due to greater deformation at a corner than that along a part side. Kim and Park (2002) studied the effect of process parameters (tool type, tool size, friction at the interface between tool and sheet, and sheet anisotropy) on formability by experiments and FEM analysis. Non-traditional FLDs were determined by experiments in terms of the variation of each parameter. It was found that the formability can be enhanced when a ball tool of 10 mm diameter is used with a small feed rate and a little friction. Additionally, the formability differs according to the direction of the tool movement due to the sheet anisotropy. Further tests were performed to investigate the formability compared to stretching and deep drawing processes by forming complex shapes in Park and Kim (2003). Non-traditional FLDs were used to compare the strains in ISF with those obtained by stretching and deep drawing. They concluded that it is possible to form complicated shapes with sharp corners or edges using TPIF because the plane-strain mode of deformation becomes dominant compared to SPIF.

Filice et al. (2002) investigated the material formability in ISF under different strain conditions. The results indicated that local stretching is the dominant deformation mode in ISF. The obtained non-traditional forming limit curve has a linear shape with a negative slope in the positive minor strain side of the non-traditional FLD which is similar to the findings in Shim and Park (2001). Fratini et al. (2004) studied the major strain at fracture in non-traditional FLD in plane strain conditions for different materials. The influence of the main material parameters on formability was investigated through a statistical analysis. The results indicated that material formability in SPIF increases as the strain hardening coefficient and the percentage elongation increase. Similar work was also conducted by Hussian et al. (2009), in which the effect of mechanical properties of material upon the formability was revisited by employing a variety of materials with hardening exponents ranging from 0.04 to 0.53. The same parameter (the major strain at fracture in non-traditional FLD) was used to

represent the formability. An empirical model was established to investigate the influence of the proposed formability indicator, i.e., reduction in area at tensile fracture, on the formability.

Non-traditional FLDs were also developed for incremental forming of aluminium sheets using SPIF by Jeswiet and Young (2005c). Five shapes were tested to define the forming limits. It was found that strains of more than 300 percent can be achieved for all shapes. Ham and Jeswiet (2007) used Box-Behnken experimental design to determine the effect of five process factors (material type, material thickness, shape, step size and tool size) on the maximum forming angle, effective stain, major and minor strains. The results showed that material type has the greatest effect on formability followed by the shape. Forming limits were further presented in terms of non-traditional FLDs.

Silva et al. (2008b) extended their previous closed-form analytical model into a theoretical framework to investigate the different modes of deformation in SPIF. In addition, the formability limits of SPIF in terms of ductile damage mechanics were also studied. It was found that necking in SPIF is suppressed unlike conventional sheet forming. Traditional FLDs that give the loci of necking strains are not relevant to limits in SPIF. Instead, FFLDs should be employed to evaluate the overall formability of the process. Silva et al. (2009) further compared the deformation mechanics of SPIF (distribution of stresses and strains) obtained from the analytical model with numerical estimates derived from finite element modelling. Additionally, the forming limits determined by the analytical model were compared with experimental values. It was shown that the agreement between analytical, finite element and experimental results is good. Silva et al. (2011) revisited the previously established analytical model and proposed a unified view on formability limits and development of fracture by considering the influence of tool radius. They concluded that the stabilizing effect of dynamic bending under tension with large tool radius seems to be capable of raising the forming limit curve in order to ensure localization by necking. The stabilizing effect with small tool radius is not sufficient to ensure localization and the failure mechanism will change in order to promote fracture with suppression of necking.

2.1.2.2 Formability Indicators - Maximum Forming Angle and Fracture Depth

It is recognized that the maximum formability in ISF can be described by the maximum forming angle. The forming angle is related to the sine law. As the forming angle approaches a maximum, the thickness reduction reaches a minimum value where fracture occurs as a consequence. Capece Minutolo et al. (2007) carried out experimental tests to evaluate the maximum forming angle of truncated pyramids and cones by SPIF. Finite element analysis was also used to evaluate the limits of the process with regard to the geometry of the manufacturing product. The results showed that the maximum forming angles for truncated pyramids and cones are 63° and 66° , respectively. Ham and Jeswiet (2006) conducted a design of experiments (DOE) to investigate the effect of process parameters (material thickness, step size and tool size) on forming angle. It was found that step-down size has little effect on the maximum forming angle, whereas the material thickness, tool size and the interaction of material thickness and tool size have a significant effect on the maximum forming angle.

A method was developed to test the thinning limits of sheet metals by SPIF (see details in Hussain et al. (2007a), (2007b), (2007c), (2007d), (2008a) and (2008b)). The idea was to form an axisymmetric part with a generatrix varying its slopes until a crack occurred. The thinning limits obtained from the parts formed at fixed slopes were found to be lower than those obtained from parts with varying slopes with depths. In order to acquire the lowest possible thinning, the forming of parts at fixed slopes was recommended. In this case, the thickness distribution on a part also follows the sine law.

Another geometric formability indicator is the fracture depth. If the maximum forming angle of a part is lower than the critical angle then the final shape can be achieved. It is also true that a part with forming angles higher than the critical one can be formed for a small height. Filice (2006a) developed a phenomenology-based approach for modelling material thinning and formability by manufacturing a cylindrical cup. It was observed that a severe slope can be

safely manufactured for short components. For this reason, if the wall slope angles to be manufactured are always lower than the critical one, the product can be realized without any problem; otherwise, different strategies need to be implemented to improve formability by changing process parameters. Ambrogio et al. (2011) used a neural network to predict the maximum forming depth of parts by taking into account the geometry variability (changing the wall slopes), which gives a valuable contribution in terms of predictive evaluation of the process when the geometrical complexity of the part increases.

2.1.3 Increased Process Capability

In order to further enhance process formability, several hybrid configurations for ISF have been developed in recent years. A review paper by Taleb Araghi et al. (2011) discussed two hybrid process combinations for ISF, i.e., ISF with stretch forming (ISF+SF) and laser-assisted ISF (Laser+ISF).

Fig.2.3 shows the configuration of ISF with stretch forming. A preform is created first by stretch forming. A subsequent ISF process is used to complete the forming of features like corrugations or grooves that are not formed by stretch forming. As discussed in Taleb Araghi et al. (2009), the advantages of “ISF+SF” have three aspects: (i) process time can be shortened; (ii) a more homogeneous sheet thickness distribution could be achieved and therefore formability could be improved; (iii) residual stresses created by cyclic bending deformation in ISF could be reduced and therefore geometric accuracy is expected to be improved.

The development of “Laser+ISF” aims at introducing local heating to form Ti and Mg alloy sheets which typically show limited formability at room temperatures (see examples in Duflou et al. (2007a), (2008a) and Göttmann et al. (2011)). The main advantages of “Laser+ISF” are expected to be: (i) increased formability of sheet materials that are hardly formed at room temperatures; (ii) increased geometric accuracy.

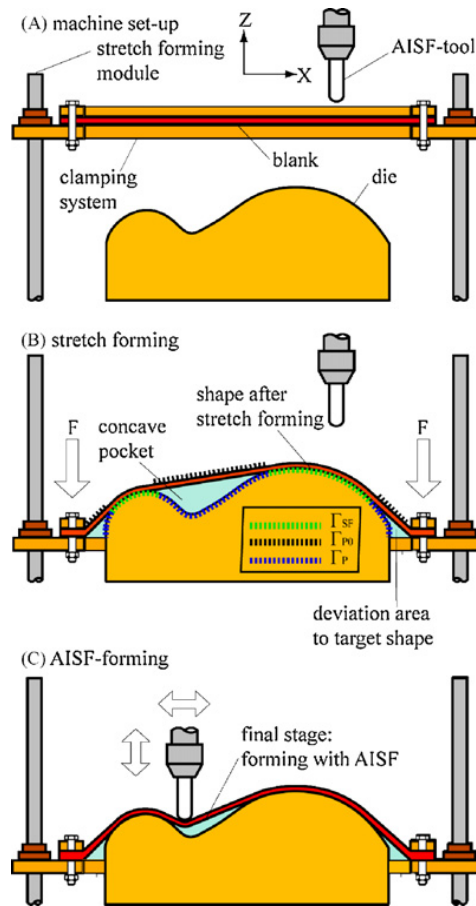


Fig.2.3. Configuration for ISF with stretch forming (Taleb Araghi et al. (2009)).

As the cost of set-up for laser-assistant ISF is high, Fan et al. (2008) and (2010) developed an electric heating system to assist with local heating of sheets. The suitability of the developed device was examined by forming three hard-to-form sheet metals, i.e., AZ31 magnesium, $\text{TiAl}_2\text{Mn}_{1.5}$ titanium, and Ti-6Al-4V titanium sheets. All the investigated materials were successfully formed by means of electric heating. In Ambrogio et al. (2008), the authors investigated the incremental forming of magnesium alloys. The analysis of process suitability was implemented through the evaluation of material formability and the assessment of the role of the most important process parameters. Experiments were carried out at the varying of temperatures designed by DOE. They concluded that a dramatic formability enhancement can be achieved by forming magnesium alloys in warm conditions. Furthermore, Ambrogio et al. (2012) proposed a simple and effective electric heating system based on Joule's effect. The incremental forming workability windows were drawn for each investigated material plotting the allowable forming angle as a function of the supplied heating energy. These maps can be used by the process analysts as a suitable

tool to optimally design the process when a given forming angle has to be considered in manufacturing of lightweight components. In terms of microstructure of formed parts, the results showed a different grain distribution due to both electrical heating and induced strain, directly dependent on material properties.

Research on the effect of elevated tool rotational speeds on process capability has also been conducted. In particular, Park et al. (2010) used the rotational tool to accelerate plastic deformation of magnesium forming using SPIF. During the rotational incremental forming process, a large amount of heat is naturally generated in the contact area due to friction energy at the tool-specimen interface and plastic deformation energy by shear deformation. This local heat generation accelerates the plastic deformation and increases the formability of sheet material. Buffa et al. (2013) also investigated the approach to enhancing the material formability through a localized sheet heating by elevating tool rotational speeds. Three materials, i.e., AA1050-O, AA 1050-H24, and AA6082-T2 were tested. A significant increase in material formability was observed. Additionally, new formability curves have been developed based on varying of the utilized rotational speeds.

Palumbo and Brandizzi (2012) further combined two approaches (electric static heating and high tool rotation) with the aim to increase the process formability of titanium alloy (Ti6Al4V) forming. The case study showed that the combination of the two approaches was a feasible solution for manufacturing hard-to-form materials like Ti alloys. Additionally, the tool rotation speed has a positive effect on stabilizing the necking, thus allowing higher levels of stretching to be reached.

2.1.4 Summary

It is recognized that the ISF process involves a complex combination of deformation modes (shear, bending and stretching). Previous results have shown that the dominant deformation mode will change with process parameters (such as step down size) changes. Although several individual

methods have been developed in the literature to explain the deformation mechanism, there is still no unified analytical model to describe the existing results. This is a challenge for future ISF research. In addition, simplified and efficient hybrid ISF configurations still need to be further developed so as to improve the process capability and extend the practical applications of ISF.

2.2 Forming Forces

The review paper by Jeswiet et al. (2005b) pointed out that potential users of ISF are often concerned about forming forces that are generated during forming. The forces required for forming have consequences in the design of tooling and fixtures, and also the machinery used. In addition, forces can be seen as a critical quantity to monitor the forming process, prevent failure, implement on-line control and process optimization (Duflou et al. (2007b), Aerens et al. (2010), Henrard et al. (2011), Mirnia and Dariani (2012), Bahloul et al. (2013), Ambrogio et al. (2006), Filice et al. (2006b), Petek et al. (2009), and Fiorentino (2013)).

2.2.1 Effects of Process Parameters on Forming Forces

Duflou et al. (2007b) investigated the effects of four process parameters (tool diameter, vertical depth increment, part wall angle and sheet thickness) on the forces during SPIF. The resultant force will increase as the vertical step size, tool diameter, wall angle or sheet thickness increase. They also pointed out that the slope of the resultant force curve after the peak value can be seen as a forming failure prediction indicator.

Bahloul et al. (2013) presented a Box-Behnken experimental design to determine the effects of wall angle, step size, material thickness and tool size on the sheet thinning rate and the maximum forming forces in the SPIF process. They concluded that the wall angle and the initial sheet thickness are the most influential parameters on the above two responses. Furthermore, an optimization procedure, based on a genetic algorithm, was implemented to find the optimal solutions with the aim of optimizing the sheet thinning rate and the maximum forming forces.

2.2.2 Force Prediction

Aerens et al. (2010) presented an approach for the prediction of SPIF forces based on experimental results as well as analytical relations derived from finite element results. They also reported that the derived model can be used to compute an approximate value for the force for any material, based on the knowledge of the tensile strength only.

Henrard et al. (2011) studied the force prediction by finite element simulations during SPIF process. The forming of two cones was simulated with two finite element (FE) codes and several constitutive laws (an elastic-plastic law coupled with various hardening models). The parameters in those material laws were identified using several combinations of a tensile test, shear tests, and an inverse modelling approach taking into account a test similar to the incremental forming process. They pointed out that the type of finite element, the constitutive law and the identification procedure for the material parameters have an influence on force prediction. Additionally, it was confirmed that a detailed description of the behaviour occurring across the thickness of the metal sheet is crucial for an accurate force prediction by FE simulations.

Mirnia and Dariani (2012) used the upper-bound approach to studying the deformation zone of single point incremental forming of truncated cones. The velocity field and the dissipated power of the process are achieved using an assumed deformation zone and streamlines defined by Bezier curves. The tangential force acting on the tool is attained by optimizing the presented upper-bound solution. They also investigated influences of the effective parameters including vertical pitch, initial thickness, tool diameter, and wall angle on the tangential force and the predicted equivalent strain. A strain hardening law is utilized to consider the work hardening behaviour of sheet metals. The comparison showed an appropriate agreement between experimental and predicted tangential forces.

2.2.3 Force-Based Failure Prediction

Some researchers proposed force-based methods to predict part failure and control the forming process. In particular, Ambrogio et al. (2006) and Filice et al. (2006b) developed an approach to detecting the failure during incremental forming. This approach is based on the analysis of the trend of the forming force. For a typical cone forming process, the forming force usually increases until it reaches a peak and then decreases before reaching a steady state. They pointed out that the curve gradient after the peak can be assumed as a critical indicator to detect the forming failure. Furthermore, a failure prevention strategy was implemented for setting up an effective process parameter correction to reduce failure risk and increase formability.

Petek et al. (2009) proposed an autonomous on-line system for fracture identification during ISF process, which is based on the shape analysis of the forming force time series using skewness and statistical estimators. The results showed that the system works effectively with different material types, material thicknesses and product shapes.

Fiorentino (2013) presented a criterion to predict the forming fracture in TPIF, which uses forming forces, process parameters, and two different material constants to estimate a reference stress acting on the sheet compared with the ultimate strength of the material. The results showed that it is suitable for online control and is able to explain the influence of the step-down size on the formability of the material.

2.2.4 Summary

In terms of forming forces, further research work can be focused on the following aspects. Firstly, the influence of process parameters (such as tool path types, material properties) on forming forces should be further clarified so as to understand the forming process mechanism. Secondly, efficient and simplified analytical modelling could be developed to predict the forming forces (tangential, radial and vertical directions) so as to potentially estimate the

process forming formability and prevent forming failure in the design stage. Thirdly, an on-line force-based control system would be established to further enhance the process formability and possibly optimise the forming quality.

2.3 Forming Efficiency

Due to the long travel of tool movement, forming efficiency (forming time) in ISF is one of the major concerns for practical production.

Sarraji et al. (2012) studied process forming time in ISF in terms of the effects of four different process parameters (tool diameter, step down size, feed rate and support type). By using Taguchi analysis with design of experiments (DOE) and analysis of variance (ANOVA), the effects of these four process parameters and their combinations were investigated to optimize parameter levels with the aim to minimize forming time. The analysis results showed that the most influential parameter on forming time is step down size followed by feed rate and then tool diameter.

2.3.1 Summary

Further research can be performed on the simultaneous optimization of forming time together with other process quality outputs such as surface roughness and geometric accuracy taking into account the effects of the most relevant process parameters.

2.4 Geometric Accuracy

Geometric accuracy has been a key concern for ISF developers. Allwood et al. (2010) summarized three definitions of geometric accuracy in ISF process, i.e., (a) clamped accuracy, (b) unclamped accuracy, and (c) final accuracy. It is noted that the degradation in unclamped accuracy and final accuracy is mainly due to residual stresses.

They developed an idea of cutting slots and tabs to form a partially cut-out blank with the aim to improve geometric accuracy. However, the experimental results showed that the use of partial cut-outs had very little effect, and the use of a stiff backup plate was far more significant in improving accuracy compared to the use of partial cut-outs. Micari et al. (2007) discussed the factors influencing geometric accuracy in SPIF. They pointed out that the shape and dimensional error can be reduced using suitable strategies, including two main categories: the use of different types of support and optimised tool trajectories.

2.4.1 Prediction for Geometric Accuracy - Empirical and FE Modeling

Ambrogio et al. (2004a) discussed and analysed the geometric accuracy of SPIF by using an effective experimental technique. Moreover, an FE model was developed to predict the shape after forming. A preliminary study of the design of trajectories to increase the geometric accuracy was also performed. A significant improvement in terms of product precision was obtained. Ambrogio et al. (2007) focused on the investigation of the influence of process parameters on geometric accuracy through a reliable statistical analysis. The statistical models were established to predict material spring-back. The prediction results were further used to improve the geometric accuracy taking into account a simple case study. Ambrogio et al. (2013) proposed a robust design of incremental sheet forming by the Taguchi method with the aim to modify the tool path in order to improve the thickness distribution of the final part. A robust FEM model was used to simulate the forming process and the best process settings were determined to simultaneously minimize the maximum thinning and the shape geometrical error.

Han et al. (2013) developed a coupled artificial neural networks and finite element model to simulate and predict spring-back responses to changes in process parameters. Then, a particle swarm optimization algorithm was used to optimize the weights and thresholds of the neural network model. The results have shown that a more accurate prediction of spring-back can be achieved using the FEM-PSONN model.

Essa and Hartley (2011) used numerical modelling to investigate the influence of different strategies on process precision. In particular, a finite element model has been used to investigate the effects of a backing plate, a supporting kinematic tool and tool path modification in the final stage. The results showed that the backing plate can minimise the sheet bending near to the initial tool contact location. The additional kinematic tool can reduce spring-back; and the extension of the tool path across the base of the sheet will eliminate the pillow effect. The cumulative effect of introducing these strategies to the process showed an improvement in the overall accuracy of the profile and in the thickness distributions of the final product.

Guzmán et al. (2012) analysed the geometric inaccuracy by forming a two-slope SPIF pyramid with two different depths using finite element simulations. They concluded that the main shape deviations come from elastic strains due to structural elastic bending, plus a minor contribution of localized spring-back. They recommended that a feasible tool path can be designed to further eliminate these deviations induced by elastic strains.

2.4.2 Methods for Enhanced Geometric Accuracy

Geometric accuracy can be also increased by using a multi-stage ISF design. Bambach et al. (2009) suggested that multi-stage forming yields reduced deviations compared to single-stage forming, which is verified by the forming of a pyramidal benchmark part as well as a fender section. However, the improved geometric accuracy achieved by multi-stage forming will be lost if an ensuing trimming operation is performed without stress-relief annealing. Therefore, a combination of multi-stage forming, stress-relief annealing and trimming is recommended to further enhance the accuracy of the final part.

Other approaches have been also developed to improve process accuracy, such as ISF with stretch forming, laser-assisted ISF, and electric hot incremental forming, see discussions in Section 2.1.3.

2.4.3 Summary

Although great efforts have been made on the investigation of geometric accuracy, there are still some challenges that need to be dealt with in the future research. First, numerical modelling should be further developed to accurately predict the geometric deviations, especially the spring-back prediction. Second, a tool path based on-line control would be implemented to compensate the geometric deviations. The influence of process parameters related to the tool path control (such as step down size) on geometric accuracy should be clarified. Third, a combination of forming methods can be incorporated with ISF to further reduce the geometric deviations.

2.5 Surface Finish

As a critical product quality constrain, surface roughness is regarded as a weak point in incremental sheet forming. It is of great importance to identify the impact of forming parameters on the surface roughness and optimize the surface finish at the production stage.

2.5.1 Effects of Process Parameters on Surface Finish

Hagan and Jeswiet (2004) performed surface roughness tests and analysed the influence of several forming variables, such as step-down size and spindle speed, on surface roughness. They concluded that the surface finish can be viewed as a resultant of large-scale waviness created by the tool path and small-scale roughness induced by large surface strains. With step-down sizes decreasing, the morphology of surfaces transforms from waviness to strict roughness without waviness.

Powers et al. (2010) investigated the surface metrology through a SPIF case analysis. The effect of sheet rolling mark direction and analysis direction on surface topology in SPIF considering two process variables (feed rate and forming direction) was first studied. The results showed that surface roughness R_z is greater with rolling marks perpendicular to the forming orientation.

Lasunon et al. (2013) assessed the effects of three process parameters on the surface roughness in SPIF by a factorial design. The results showed that wall angle, depth increment and its interaction play an important role on the surface roughness, while feed rate has little effect.

2.5.2 Predictive Modelling for Surface Finish

Durante et al. (2010) described a model for evaluating the roughness both in terms of amplitude and spacing depending on three parameters: the slope angle, the vertical step and the tool radius. Analytical and experimental results were compared in terms of surface roughness in SPIF. The roughness values R_a , R_z , and the mean spacing between profile peaks were evaluated as the output of the models. The prediction and experimental results showed that a good agreement can be achieved with an error below 10%.

Hamilton et al. (2010) investigated the influences of tool feed rates and spindle rotation at high speeds during forming on the non-contact side roughness (i.e. orange peel effect). A model for the orange peel prediction in SPIF was established, which provided some guidelines for the improvement of external surface quality by choosing desirable process parameters during forming.

2.5.3 Summary

Although some research has been performed on the investigation of effects of process parameters on surface roughness and predictive modelling, little research has been focused on the evaluation of overall surface roughness. In addition, the impact of roll mark orientation of metal sheets on surface roughness should be clarified when the surface roughness measurement is carried out along the step down direction. Although this aspect has been considered in Powers et al. (2010), the effect of more than two process factors was not taken into account, which may limit the findings. The study is needed to further investigate and clarify this aspect by taking more process factors and both internal and external surfaces into consideration.

2.6 Multi-Pass Deformation Design and Tool Path Generation

A common technical problem encountered in ISF is the non-uniform thickness distribution of formed parts; particularly excessive thinning occurring on severely sloped regions. This may lead to fracture and limit process formability. The focus in this section is on the review of the state of the art of multi-pass ISF design and tool path generation strategies in the literature which are used to avoid process fracture and increase formability.

2.6.1 Thinning and Fracture

The sine law, as one of the simplest geometrical models in ISF, is widely utilized by ISF researchers to predict the sheet thickness as shown in Eq.(1.1) and Fig.1.6. It assumes that the forming process is a pure projection of material points along the forming direction from the start to the end configuration. It predicts the thickness quite well in low strain situations. However, as part draw angle tends to 90° , the final sheet thickness would be zero. So the sine law has a limitation to predict thickness results when applied to this situation, but it reflects a decreasing trend on thickness distribution. Bambach (2010) has developed a kinematic geometrical model to predict the sheet thickness which obtains more accurate results compared with the sine law. This is because the kinematic model reproduces the sine law on flat surfaces and corrects it in curved areas. But it also has some limitations, i.e., bending effects are neglected and cannot be directly applied to multi-stage tool path strategies.

Non-uniform thickness distribution has been observed during cone forming in Young and Jeswiet (2004) as shown in Fig.2.4. The measurements indicated that the initial deformation is due to bending with subsequent deformation possibly being due to shear and/or stretching. In particular, the sheet thins first, reaching the maximum thinning point. Then, the material thickens until it stabilizes at an approximate thickness of 0.38 mm and remains at this value for the remainder of the cone's surface. The uniform thickness zone of the cone's wall profile is thinner than the predicted value of the sine law.

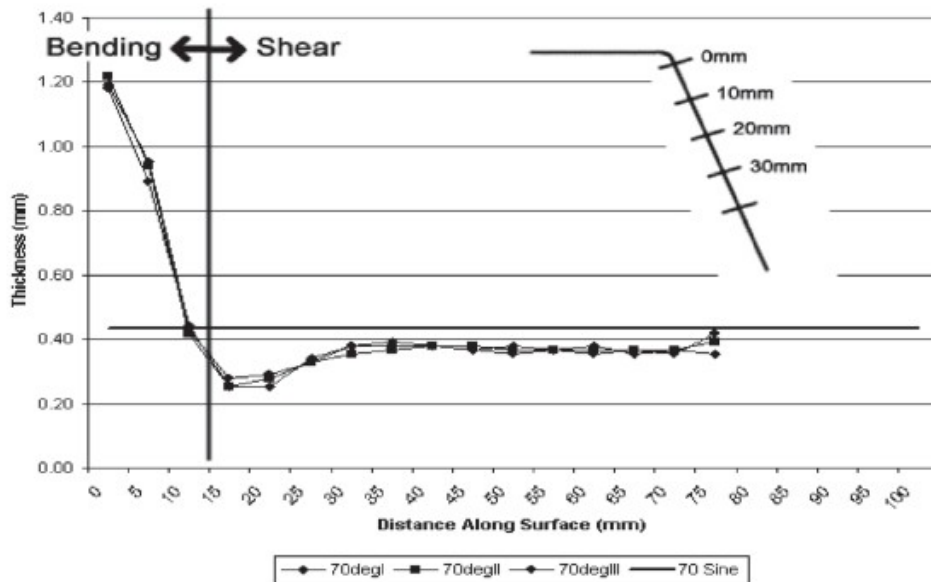


Fig.2.4. Single-pass SPIF wall thickness profile for the 70° cone (Young and Jeswiet (2004)).

Fig.2.5 shows a thinning band, occurring from the position 15 mm to 30 mm along the part wall. It shows a sign of localized necking, similar to what is found in a uniaxial tensile test. This observed thinning band matches the failures witnessed, indicating thinning is dramatic at high draw angles of parts, and can be seen as a precursor of failure. However, the sine law and the kinematic geometrical model developed in Bambach (2010) cannot predict this thinning band.

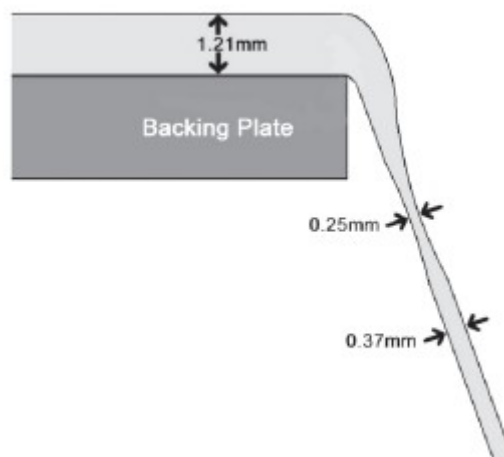


Fig.2.5. Thinning band observed on the 70° cone (Young and Jeswiet (2004)).

In order to avoid excessive thinning and therefore failures as discussed above, the available material elsewhere in a part could be used to compensate the

thinning band zone in order to avoid failure. Multi-pass deformation design (preforms or intermediate shapes) provides such an opportunity to control material flow and alter final thickness distribution.

2.6.2 Multi-Pass Deformation Design

Kim and Yang (2000) proposed a double-pass forming method to improve formability for the ISF process. This method is based on shear deformation using a means of equalizing the thickness strain distribution across the surface of a part to design intermediate shapes in order to get uniform thickness distribution of a final part. This paper presents the first attempt towards a model-based deformation pass design. However, it is only suitable for two-stage forming (preform and final geometry). For the manufacture of more complex parts, more forming stages are needed. Therefore, this approach does not provide a general solution to multi-pass deformation design in ISF.

Apart from the above model-based multi-pass ISF design, there are also various experimental trial-and-error approaches developed to achieve complex shapes. Iseki and Naganawa (2002) developed a multi-stage strategy using spherical and cylindrical rollers to form a vertical wall surface of rectangular shallow shapes. The multi-stage incremental forming comprises three operations: bulging with a spherical roller, right-angle-forming and flattening with cylindrical rollers. An approximate deformation analysis for thickness strain distributions and the maximum bulging height of the rectangular panel was also provided.

Young and Jeswiet (2004) proposed a double-pass SPIF strategy to form a cone with a steep draw angle. This strategy introduces bending in the first pass forming with the aim to encourage the undeformed sheet in the flange area to bend downwards over the backing plate and into the part. It helps alleviate the thinning band seen from 15 mm to 30 mm along the wall surface as shown in Fig.2.5.

Duflou et al. (2008b) developed a multi-pass ISF strategy to redistribute the material from the previously unformed base of the part to the side wall and manufactured parts with vertical walls without failure. The final thinning in multi-pass forming can exceed the maximum thickness reductions in single-pass forming, which means a formability increase.

Hirt et al. (2004) described a modified multi-stage forming strategy, as seen in Fig.2.6, to produce a pyramid with a steep angle (81°) using TPIF. In this forming strategy, a preform with a shallow wall angle 45° is first produced and then a number of stages follow in which the motion of the forming tool alternates from upward to downward. 7-12 intermediate stages with an increase in angle of 3° or 5° are needed to produce this pyramid.

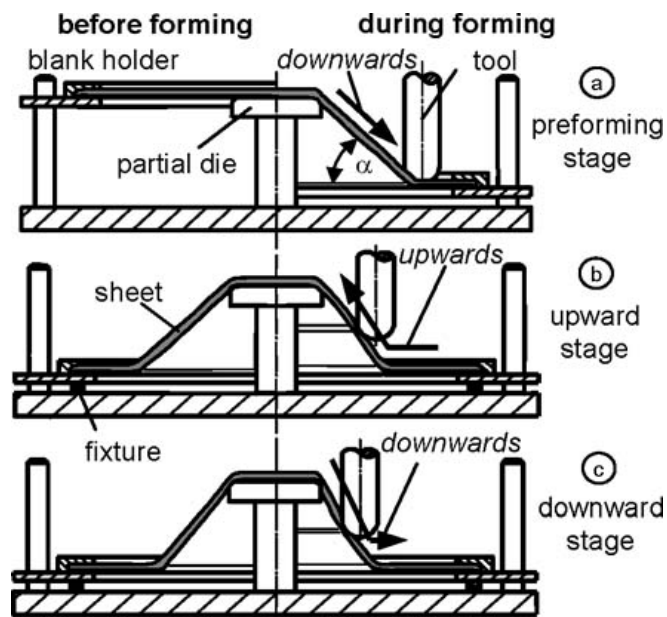


Fig.2.6. Multi-stage forming strategy in Hirt et al. (2004).

Similar to the multi-stage design idea in Hirt et al. (2004), Skjoedt et al. (2010) made use of five stages (four intermediate stages) to produce a cylindrical cup with vertical walls using SPIF. It is noted that all stages, apart from the first, were performed with the tool moving either downwards or upwards, see Fig.2.7. They indicated that tool paths going upwards imply more biaxial strains than downward tool paths, which are closer to plane strain conditions. Furthermore,

an improved multi-stage SPIF strategy was presented in order to eliminate the unwanted material extrusion phenomenon, see Fig.2.8.

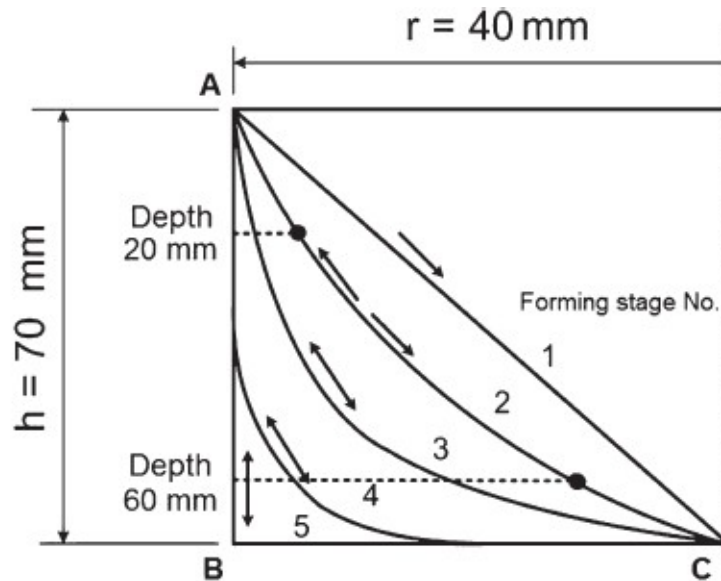


Fig.2.7. Multi-stage SPIF strategy for producing a cylindrical cup with vertical walls (Skjoedt et al. (2010)).



Fig.2.8. Material extrusion phenomenon in multi-pass SPIF (**Paper G**).

Malhotra et al. (2011a) attributed the aforementioned material extrusion phenomenon (also called stepped features) to a result of accumulated rigid body translation during the deformation of intermediate shapes. They developed analytical formulations to predict the rigid body translation and then generated a new mixed tool path to achieve a smoother component base by using a combination of in-to-out and out-to-in tool paths for each intermediate shape. However, finite element simulations are needed to perform every time to calibrate the model constants when the material type or sheet thickness of the

blank is changed. Xu et al. (2012) extended the work in Malhotra et al. (2011a) by relating the material constants in analytical formulations to the yield stress and the sheet thickness of the blank. Therefore, the required number of prior FEA simulations is reduced to only six for arbitrary material types and thicknesses, which is a significant addition to the prior work.

Manco et al. (2011) discussed the effect of tool trajectories in terms of final thickness distribution and formability. The advantages and disadvantages of single-pass forming and three different forming strategies have been compared and analysed by manufacturing the same shape and evaluating the thickness distributions. It was concluded that formability can be conveniently enhanced with a proper multi-stage deformation design by involving as much material as possible from a theoretical point of view.

Cui and Gao (2010) proposed three multi-pass strategies to produce flanged parts. It was shown that increasing the part diameter in small steps, named as strategy (a), to achieve the final part is proved to be an effective way to improve the formability of flanges and avoid the occurrence of the thinning band.

Although a multi-pass forming strategy benefits the increase of formability, it is still uncertain how material flows between intermediate and final forming stages. A FE model for a double-pass forming was developed by Li et al. (2012a) to simulate the actual forming process. Compared to single-pass forming, the results indicated that more uniform thickness distribution in double-pass forming can be achieved, which benefits from the increase of the total plastic deformation zone. Additionally, Li et al. (2013) made an attempt to produce a complex part - a car taillight bracket with a nearly straight wall region and a groove region. In order to avoid cracks and wrinkles in the two aforementioned critical regions, a multi-pass forming strategy, based on a regional division idea was proposed. It was found that an intermediate surface which is geometrically closer to the final part can obtain better forming quality.

Zhang et al. (2013) developed an FEM-based multi-stage SPIF method, which treats the SPIF process as hydro-bulging forming. The intermediate surfaces

obtained from the FEM results can be used for the tool path generation. They also pointed out that the kinematics trajectory of material flowing is a curve in multi-stage ISF which depends on the intermediate surfaces and the tool kinematics strategy. In addition, it was concluded that the kinematics direction of surface points are not the normal direction of intermediate surface points.

2.6.3 Tool Path Generation and Optimization

In addition to multi-pass deformation design, tool path generation and optimization is another significant research direction, which influences forming limits, geometric accuracy, surface quality, thickness distribution, and forming time. A number of attempts have been made to investigate the effect of tool path generation (Malhotra et al. (2010), (2011b), (2012a), Lu et al. (2013), Li et al. (2012b), Liu et al. (2004), Zhu et al. (2011)) and its optimization (Rauch et al. (2009), Attanasio et al. (2008), Behera et al. (2013), Azaouzi and Lebaal (2012), Attanasio et al. (2006)) on the quality of manufactured parts.

2.6.3.1 Tool Path Generation

Two different methods have been used to generate the tool paths for ISF in literature: (i) tool path generation using commercial computer aided manufacturing (CAM) softwares (Suresh et al. (2013)), (ii) tool path generation using specifically developed algorithms (Liu et al. (2004), Zhu et al. (2011), Malhotra et al. (2010), (2011b), (2012a), Lu et al. (2013), Li et al. (2012b)). There are mainly two kinds of tool paths used in ISF process, i.e. contour (z-level) tool path and spiral tool path. For a contour tool path, deformation is biaxial at the start and end points of each contour and is close to plane strain in between. Fracture tends to occur at the start and end points of each contour compared to the rest of the contour being formed. Additionally, a contour tool-path leaves stretch marks at the transition points between contours and creates force peaks. Instead, a spiral tool path is continuous with incremental descent of the tool distributed over the entire surface of the part. The advantage is that no obvious marks are generated by step down.

Earlier work performed by Liu et al. (2004) was focused on contour tool path generation based on STL files of a designed geometry. Most commercial CAM softwares do not provide the capability of generating the spiral tool path for complex geometries. Considering the merits of spiral tool paths, great efforts have been dedicated to the investigation of 3D spiral tool path generation. A spiral tool-path generation method with constant scallop height for ISF was proposed based on a triangular mesh model in Zhu et al. (2011). Malhotra et al. (2010) developed an automatic 3D spiral tool path generation method for SPIF that uses the knowledge of local geometry and treats the geometric accuracy and scallop heights as constraints to minimize the forming time. However, this methodology does not account for formability as a constraint for the generation of optimum tool paths as forming integrity is an essential prerequisite to the quality of a fabricated part. Furthermore, Zhu and Li (2013) proposed a new cutter contact surface modelling algorithm based on the non-equidistant offset, which can be adapted to the sheet thickness variation so as to guarantee a reasonable gap between the forming tool and support. Additionally, a spiral tool path generation algorithm was introduced taking into account the scallop height in both the z-axis direction and circumferential rotation direction so that a smoother surface can be obtained.

Lu et al. (2013) presented a new feature-based tool path generation algorithm. Three case studies were provided in order to obtain a better understanding of the forming mechanism using a new tool path generation method. The results demonstrated that better surface quality, better geometric accuracy and shorter forming time can be achieved.

Malhotra et al. (2011b) proposed a tool path strategy for double sided incremental forming (DSIF), which uses two identical tools on each side of the sheet to improve geometric accuracy compared to SPIF. A significant improvement in the geometry of the formed part wall can be achieved. However, they also pointed out that the loss of contact of the bottom tool during forming leads to the process degenerating into SPIF. Furthermore, Malhotra et al. (2012a) developed an Accumulative Double Sided Incremental Forming (ADSIF) strategy for DSIF in which both the tools are under displacement control and the

tool path is generated completely a priori from the CAD geometry. It was noted that contact between both tools and the sheet are maintained at all times during the forming process. The geometric accuracy achieved with ADSIF is considerably better than those with SPIF and DSIF tool paths.

Li et al. (2012b) presented a tool path generation method for ISF based on an STL model but with defects by adopting the thought of generating cutter-location data directly from cutter-contact data. Various tool shapes and types of tool paths can be applied and generated according to different ISF requirements. The new algorithms have been implemented and integrated into a specific CAM module. The effectiveness and robustness of this tool path generation method has been validated by experiments.

2.6.3.2 Tool Path Optimization

Tool path optimization can be categorized into two research directions: (i) off-line tool path optimization, (ii) on-line tool path optimization.

Most of the research is focused on off-line tool path optimization with regards to the effects of process parameters related to a tool path on the quality of final products. This is because the automated on-line feedback control of forming processes is very difficult to achieve due to the very slow process model solution times which arise from the non-linearity of the process deformation on past forming history (Allwood et al. (2009)). In particular, Attanasio et al. (2008) investigated two types of contour tool paths in a TPIF process, in which the first one was generated with a constant incremental depth and the other was created with a constant scallop height. The optimized tool paths were generated using a commercial 3D CAD-CAM software. Better geometric accuracy and surface quality can be obtained when both parameters (incremental depth and scallop height) are set as low values. Behera et al. (2013) used Multivariate Adaptive Regression Splines (MARS) to predict the formed surface in SPIF. Using MARS predictions, compensated single pass tool paths were generated with the aim to bring down the average geometric deviations. Azaouzi and Lebaal (2012) used finite element analysis along with response surface method

and sequential quadratic programming to determine the optimal forming tool path. An asymmetric part was tested. The results showed that the manufacturing time can be reduced and homogenous thickness distribution can be achieved. Attanasio et al. (2006) presented experimental optimization of the tool path in TPIF with the aim to produce an automotive component with the best dimensional accuracy, the best surface quality and the lowest sheet thinning. The experimental tests demonstrated that to reach good results in terms of surface quality, geometric accuracy and thickness of the final part, it is important to use a tool path with a variable step depth depending on the part geometry, and to correctly set the value of both the maximum step depth and the scallop height. Meier et al. (2009) and Belchior et al. (2013) focused on the development of robot-based incremental sheet forming. Off-line tool path compensation strategy was used to plan the corrected path trajectories so that the accuracy of the final geometry can be greatly improved. Hirt et al. (2004) developed a general correction algorithm to improve geometric accuracy based on tool path optimisation. A component was first produced and then measured with the format of cloud of points. The deviation vector from each measured point to the corresponding target point is compensated to generate the trial point, see Fig.2.9.

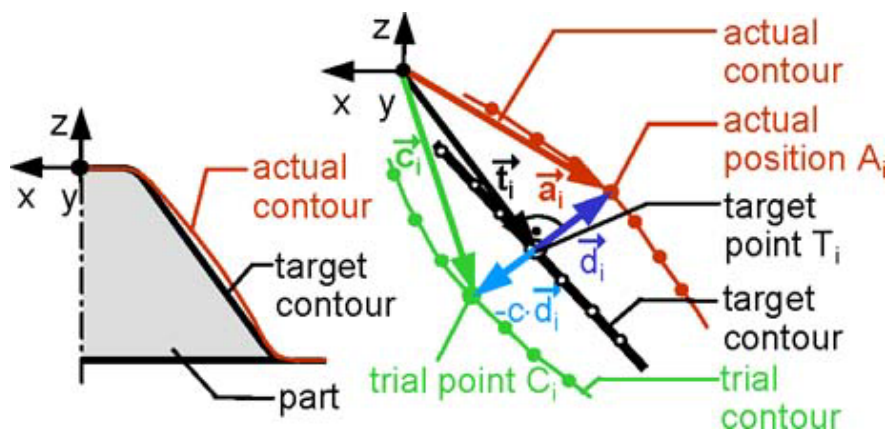


Fig.2.9. Determination of corrected points (Hirt et al. (2004)).

Attempts were also made to investigate on-line tool path optimization. Rauch et al. (2009) first discussed the effects of forming strategies and other programming related parameters on part accuracy and process implementation. They pointed out that the basic CAM tool paths are not suitable to carry out ISF

applications. Therefore, the implementation of intelligent CAM programmed tool paths was proposed, which adapts and optimizes the tool paths during the manufacturing of a part based on process data evaluations. Allwood et al. (2009) placed an on-line stereovision camera under the work-piece to implement feedback control of part forming using SPIF as shown in Fig.2.10. This feedback control is used to adjust the tool path through an optimisation algorithm using a piece-wise linear model of process behaviour based on deviations around a pre-planned tool path. The results have shown that parts can be produced within ± 0.2 mm of a target shape. However, this approach has so far been applied only to simple part geometries.

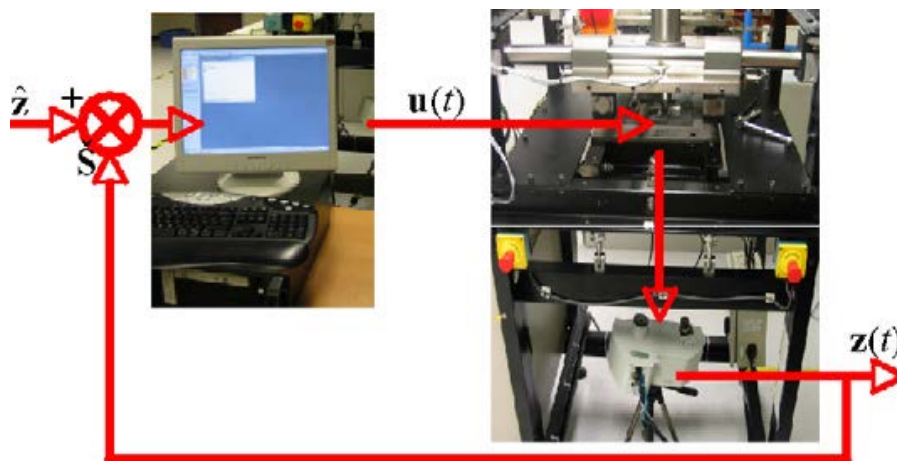


Fig.2.10. Closed-loop feedback control (Allwood et al. (2009)).

2.6.4 Summary

The above review of recent studies shows that most of the previous work on the multi-pass deformation design is based on the trial-and-error method. However, there is still lack of the analytical analysis to predict the formability between different multi-pass deformation strategies with the trial-and-error method. Additionally, as opposed to the trial-and-error method, analytical deformation pass design is needed to quantitatively control the material flow so as to improve the process formability and obtain more uniform thickness distribution of the final parts. Furthermore, different strategies for tool path generation in multi-pass forming have not been fully investigated yet. This point should be clarified because the interactions between different tool paths adopted in multi-

pass forming also has an important influence on thickness distribution and process formability.

2.7 Conclusions

This chapter provides a comprehensive review of the state of the art of ISF technology, including all research aspects. Research contributions and challenges in each aspect are highlighted based on the relevant studies reported in the literature. Dealing with these challenges is of great importance to implement extensive industrial applications of ISF. However, this thesis is mainly focused on two broad aspects: forming process investigation and the evolution toward multi-pass ISF modeling and its validation. First, a comprehensive understanding of the influences of process parameters is still necessary to clarify the forming process mechanism and optimise it. Furthermore, it is noted that, despite advances in multi-pass ISF deformation design, there still remains a lack of analytical modeling to design multiple deformation passes as well as a deep understanding of the material flow mechanism in multi-pass forming. In addition, a simplified analytical analysis is still lacking to explain why multi-pass forming has higher formability than single-pass forming and why different multi-pass strategies have different formability. This thesis addresses these limitations by performing a detailed experimental investigation to understand the forming process mechanism in terms of the effects of process parameters on process formability, forming forces, geometric accuracy, forming time and surface roughness. Then, a simplified analytical analysis has been proposed for formability prediction in a SPIF multi-pass process. Additionally, a closed-loop multi-pass deformation design methodology for TPIF has also been developed to improve the process formability and obtain more uniform thickness distributions of final products, which is backed up by FEA and experimental validation. The corresponding methodologies and results will be provided in the following chapters.

Chapter 3 Methodology

This chapter provides a summary of the most important methodologies used in this thesis for process investigation, and multi-pass ISF modeling and its validation. More specifically, section 3.1 mainly introduces the optimization methodologies used for ISF process investigation. Section 3.2 provides a SPIF multi-pass deformation design methodology, in which a simplified qualitative analysis for the formability prediction of the multi-stage cylindrical cup forming is provided. In section 3.3, AMINO TPIF multi-pass deformation design is introduced. The modeling methodology for the closed-loop deformation pass design has been detailed, followed by the finite element modelling methodology and multi-pass tool path generation strategies. Section 3.4 provides an overview of experimental equipment and validation methodologies. More details can be also found in the attached papers in chapter 4.

3.1 Process Investigation - Optimization Methodologies

Two process optimization methodologies (Taguchi method and response surface methodology) have been used as part of this thesis to investigate the influence of process parameters on the forming process (forming time in **Paper E** and surface roughness in **Paper F**). A brief overview of the methodologies is provided and more details can be found in **Papers E and F**.

3.1.1 Taguchi Method

Taguchi methods are statistical methods developed by Genichi Taguchi to improve the quality of manufactured goods by minimizing the quality loss with one of the objective functions of “the-nominal-the-best”, “the-larger-the-better”, or “the-smaller-the-better” depending on the experimental objective. The Taguchi method uses an orthogonal array to organize the parameters affecting the process and the levels at which they should be varied. Instead of having to test all possible combinations like the factorial design, the Taguchi method tests pairs of combinations. This allows for the efficient collection of the necessary data to determine which factors most affect the product quality with a minimum

amount of experimentation. The general design steps involved in the Taguchi method are given as follows:

1. Define the process objective, or more specifically, a target value for a performance measure of the process;
2. Determine the design parameters affecting the process. Parameters are variables within the process that affect the performance measure set above;
3. Create orthogonal arrays for the parameter design indicating the number of and conditions for each experiment;
4. Conduct the experiments and select the optimum level of process parameters through ANOVA analysis;
5. Perform a confirmation test to verify the optimal process parameters.

The Taguchi optimization procedure starts with the selection of an orthogonal array. The minimum number (N_{\min}) of runs in the array can be determined as follows:

$$N_{\min} = (L-1)F + 1, \quad (3.1)$$

where L and F is the number of levels and the number of factors, respectively. In this thesis, four process parameters (step over, feed rate, sheet thickness and tool diameter) are chosen as factors to study their effect on forming time. Three levels are defined for each of the factors (see Table 2 in **Paper E**). Calculated by Eq.(3.1), L_9 orthogonal array is selected (see Table 3 in **Paper E**). The signal-to-noise ratio (S/N) is originally defined as the ratio of the signal to the random noise. In Taguchi designs, the S/N ratio represents a measure of robustness used to identify the controllable factors (step over, feed rate, sheet thickness and tool diameter) that reduce the variability in a product or a process by minimizing the effects of uncontrollable factors (loading and unloading time which refer to the time for the movement of the machine table with workpiece or the deformed product to or away from the machine working zone). Higher values of the S/N ratio indicate the controllable factor settings that can minimize the effects of the uncontrollable factors. Therefore, the S/N ratio is a quality control indicator in which it reflects the influence of changing any process parameters on the performance of the process. Different S/N ratios can be chosen depending on the goal of the experiment. A S/N ratio of the-smaller-the-

better as defined in Taguchi et al. (2005) is chosen because the objective is to minimize the output value (forming time) and the target is zero. This can be calculated as

$$\eta = -10 \log \left(\frac{1}{n} \sum_{i=1}^n y_i^2 \right), \quad (3.2)$$

where η is the S/N ratio, n is the number of experiments taken in one test run, y_i indicates the dimensionless output at the i th experiment with respect to one unit measure.

3.1.2 Response Surface Methodology

As described in a review paper (Bezerra et al. (2008)), response surface methodology (RSM) is a collection of mathematical and statistical techniques based on the fit of empirical models to the experimental data, which must describe the behaviour of a data set with the objective of making statistical previsions. It can be well applied when a response or a set of responses of interest are influenced by several variables (process parameters). The objective is to simultaneously optimize the levels of these variables to attain the best system performance.

Before applying the RSM methodology, it is necessary to choose an experimental design that will define which experiments should be carried out in the experimental region being studied. There are some experimental matrices for this purpose. Experimental designs for first-order models can be used when the data set does not present curvature. However, to approximate a response function to experimental data that cannot be described by linear functions, experimental designs for quadratic response surfaces should be used, such as three-level factorial, Box-Behnken, central composite, and Doehlert designs.

The stages in the application of RSM as an optimization technique are as follows:

- (1) The selection of independent variables of major effects on the process and the delimitation of the experimental region, according to the objective the study and the experience of the researcher;
- (2) The choice of the experimental design and carrying out the experiments according to the selected experimental matrix;
- (3) The mathematic-statistical treatment of the obtained experimental data through the fit of a polynomial function;
- (4) The evaluation of the model's fitness;
- (5) The verification of the necessity and possibility of performing a displacement in direction to the optimal region;
- (6) Obtaining the optimum values for each studied variable.

The models which can be used in RSM are a linear model or a second-order model. In most situations, the responses present a curvature feature. Therefore, to evaluate the curvature, the second-order model must be used. The second-order polynomial model which contains all the linear, square and linear by linear interaction terms can be described below:

$$Y = \beta_0 + \sum_{i=1}^n \beta_i X_i + \sum_{i=1}^n \beta_{ii} X_i^2 + \sum_{i=1}^n \sum_{j=2, i < j}^n \beta_{ij} X_i X_j, \quad (3.3)$$

where n is the number of variables, Y is the predicted response surface function, β_0 is the model constant, β_i is the slope or linear effect of the input factor X_i , β_{ii} is the quadratic effect of input factor X_i and β_{ij} is the linear by linear interaction effect between the input factor X_i and factor X_j .

In this thesis, Box-Behnken design was adopted to evaluate the model parameters in Eq.(3.3) because it can handle non-symmetrical variables. The most significant reason for using a Box-Behnken design is the ability to do testing in positions which are not at the limit of the process. For a Box-Behnken design, its principal characteristics are:

- (1) An experiment number is required according to $N = 2n(n-1) + c$, where n is the number of variables and c is the number of the central points;

(2) All variable levels have to be adjusted on at three levels (-1, 0, +1) with equally spaced intervals between these levels.

As described in **Paper F**, a total of 27 experiments have been employed to evaluate the effects of four main independent factors (step-down size, feed rate, sheet thickness and tool diameter) in a single point incremental forming process on surface roughness.

The original RSM is only limited to single response optimization. In order to minimize the internal surface roughness SR_i and the external surface roughness SR_e simultaneously, a simple modification to evaluate the overall surface response for multi-objective performance has been adopted in **Paper F**. As shown in Fig.3.1, this method utilizes the membership functions μ_α and μ_β as weighting factors attached to each of the objective functions,

$$\mu_\alpha = 1 - \frac{SR_i}{SR_{i,max}}, \quad (3.4)$$

$$\mu_\beta = 1 - \frac{SR_e}{SR_{e,max}}, \quad (3.5)$$

where $SR_{i,max}$ and $SR_{e,max}$ are the maximum values of internal surface roughness SR_i and external surface roughness SR_e assumed based on the experimental measurements. The simultaneous optimization of SR_i and SR_e requires the minimization of the shaded area as shown in Fig.3.1. Then, the multi-objective function for the overall surface roughness $SR_{overall}$ is defined as,

$$SR_{overall} = \frac{1}{2}SR_i(1 - \mu_\alpha) + \frac{1}{2}SR_e(1 - \mu_\beta). \quad (3.6)$$

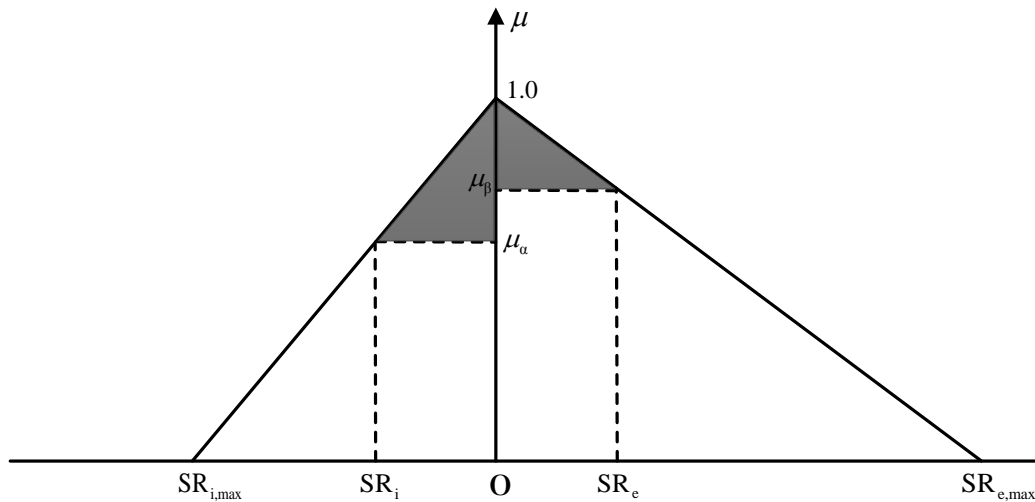


Fig.3.1. Membership functions for internal tool-sheet contact surface roughness SR_i and external non-contact surface roughness SR_e .

3.2 SPIF Multi-Pass Deformation Design

Cui and Gao (2010) proposed three multi-stage forming strategies for hole-flanging manufacture. Formability was evaluated and analysed in terms of the comparison of the proposed forming strategies. Enlightened by the multi-stage design ideas in Cui and Gao (2010), **Paper G** revisited multi-stage deformation path strategies for single point incremental forming (SPIF) with the purpose of controlling material flow (improve sheet thickness distribution) and forming a vertical wall surface for cylindrical cups. The novelty is bending deformation and more material allocation in the forming are both considered in the multi-stage forming design to improve the formability compared to the forming strategies proposed in Cui and Gao (2010). More specifically, three basic multi-stage deformation path strategies have been proposed, that is, A. incremental part diameter; B. incremental draw angle; C. incremental part height and draw angle (see Fig.3.2). Those strategies and their combinations have been evaluated in terms of the process formability and compared in order to understand the material allocation mechanism and optimise the multi-stage forming process. Approximate analysis models have been proposed to qualitatively compare the formability between single-stage and multi-stage forming processes, and strategies B and C in multi-stage forming. The motivation is to provide an efficient simplified means of predicting the relative success of different forming

strategies. The approaches and derivations of the developed models are briefly introduced in this section (see **Paper G** for full details).

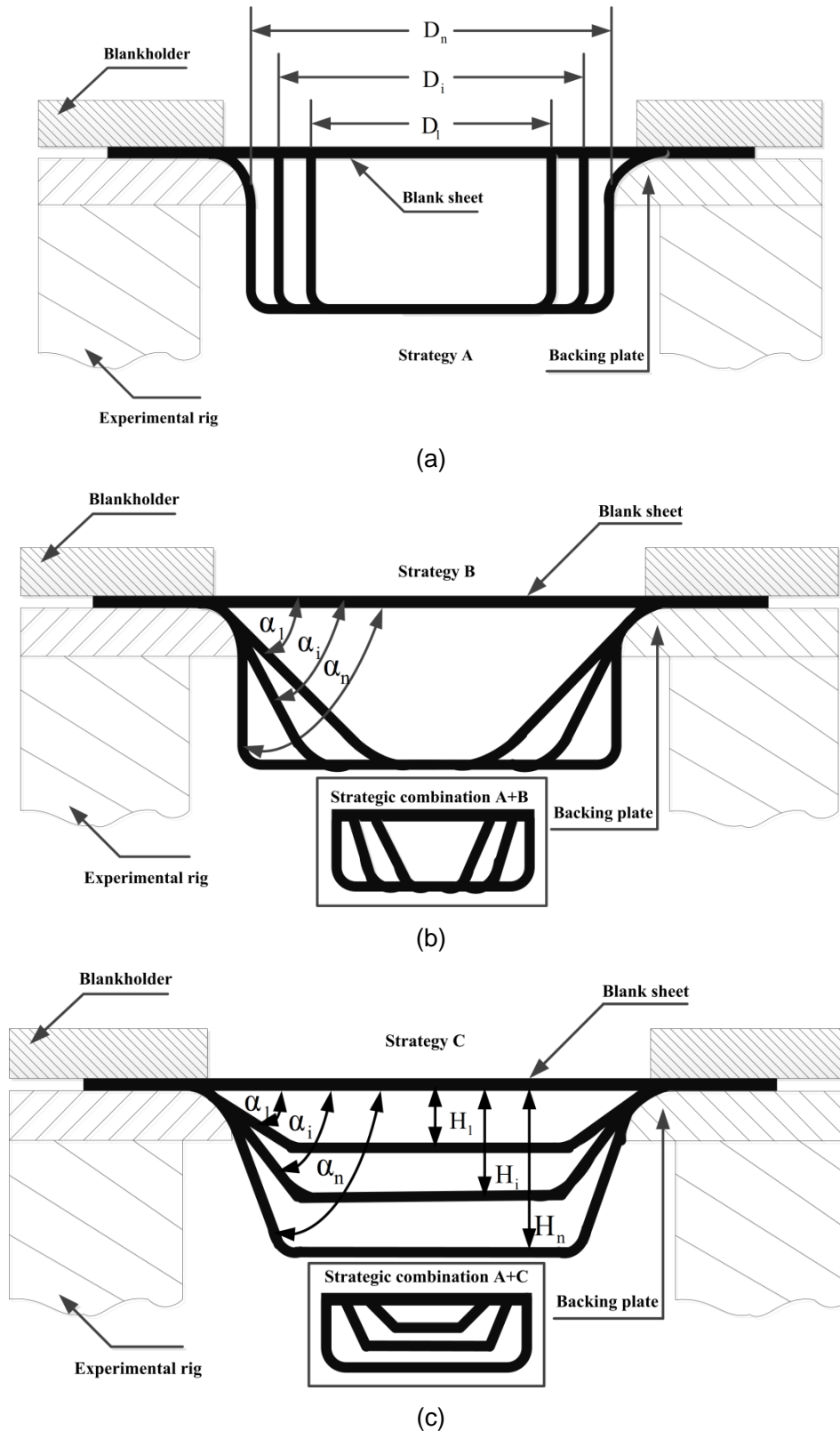


Fig.3.2. Forming strategies: (a) Strategy A: incremental part diameter; (b) Strategy B: incremental draw angle; (c) Strategy C: incremental part height and draw angle.

Li and Hu (2012) gave a brief explanation why the multi-stage deformation path strategy can lead to less thickness thinning according to the plain-strain deformation mechanism. Using a similar approach, the deformation mechanism has been approximately analysed between single-stage and multi-stage forming processes, and between strategies B and C in multi-stage forming, respectively. Geometrical relations for the analytical analysis are expressed in Fig.3.3.

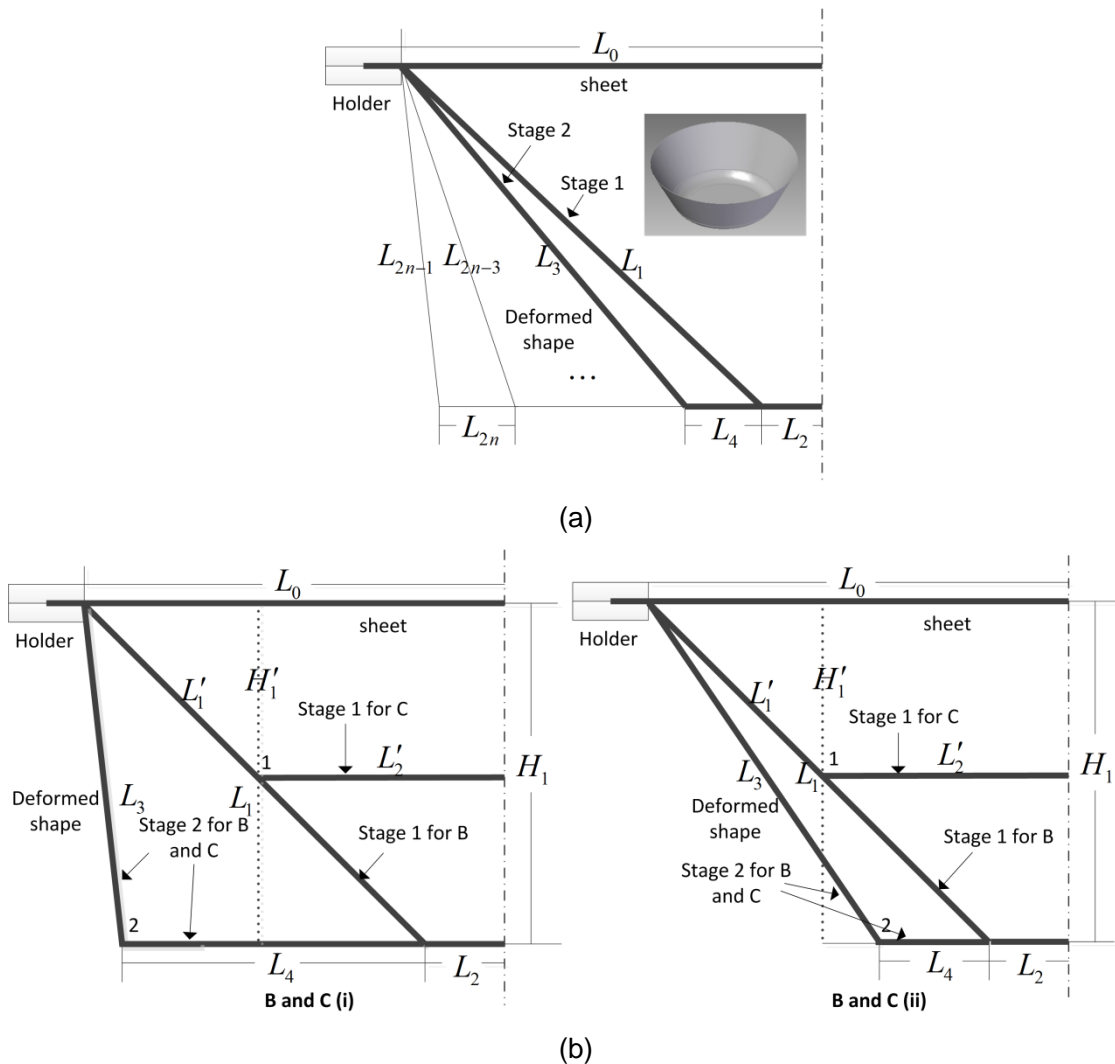


Fig.3.3. Mechanism explanation: (a) comparison of single-stage forming and multi-stage forming, and (b) comparison of strategy B and strategy C.

In this study, the analysis is simplified for qualitative purposes based on the following assumptions:

- a) thickness strain deformation only occurs in shear (sloped) sections;
- b) deformation is due to shear only;

- c) incremental deformations in multi-stage forming may be superposed to provide a total strain measure for the qualitative comparison of different forming strategies.
- d) The purpose of the following analysis is to provide only a qualitative comparison of the forming strategies. More detailed quantitative analysis is recommended for future research.

3.2.1 Simplified Deformation Analysis for Qualitative Comparison between Single-Stage Forming and Multi-Stage Forming

For Fig.3.3(a), take the first two multi-stages (Stages 1 and 2) for instance, the forming target is the sloped wall section L_3 . It is noted that the sheared section length formed after stage 1 is $L_0 - L_2$ from an initial length L_1 and then becomes $L_3 + L_4$ after stage 2. Therefore the principle strain due to shear only in multi-stage forming ε_M , can be expressed as,

$$\varepsilon_M = \ln \frac{L_1}{L_0 - L_2} + \ln \frac{L_3 + L_4}{L_1} = \ln \frac{L_3 + L_4}{L_0 - L_2}. \quad (3.7)$$

In contrast, for the single-stage forming process, the final sheared wall section length formed is only L_3 from an initial section length $L_0 - L_2 - L_4$. Therefore the principal strain due to shear only, ε_S , can be expressed as,

$$\varepsilon_S = \ln \frac{L_3}{L_0 - L_2 - L_4}. \quad (3.8)$$

Using Eqs. (3.7) and (3.8) and then,

$$\varepsilon_M - \varepsilon_S = \ln \frac{L'L_3 + L'L_4}{L'L_3 + L_3L_4}, \quad (3.9)$$

where $L' = L_0 - L_2 - L_4$. From Fig.3.3(a), the geometrical relationship $L_3 > L'$ holds and using Eq.(3.9) it is shown that,

$$\varepsilon_M < \varepsilon_S. \quad (3.10)$$

Eq.(3.10) shows that the principal strain due to shear only in multi-stage deformation path strategies is smaller than that in the single-stage forming process, which means less thinning is involved in the multi-stage forming process. Therefore, its formability is expected to be higher than that of the single-stage forming process.

3.2.2 Simplified Deformation Analysis for Qualitative Comparison between Multi-Stage Forming Strategies

The comparison of the formability between strategies B and C is investigated in a similar manner to the previous subsection. Two possible incremental geometries need to be considered as shown in Fig.3.3(b) where; (i), a larger final incremental draw angle is chosen with the corner 2 moving further away from the section centre than its previous stage position 1 such that $L_0 - L'_2 < L_4 < L_0 - L_2$ and (ii), a smaller final incremental draw angle is chosen with the corner 2 moving closer to the section centre than its previous stage position 1 such that $0 < L_4 \leq L_0 - L'_2$. Also, according to the design parameters (see Table 1 in **Paper G**) and the geometrical relationship in Fig.3.3(b), the following conditions hold,

$$H_1 = 2H'_1, \quad (3.11)$$

$$L_1 = 2L'_1. \quad (3.12)$$

For strategy B, in both cases (i) and (ii), the sheared section length formed after stage 1 is L_1 from an initial length $L_0 - L_2$ and then becomes $L_3 + L_4$ after stage 2. Hence the principal strain due to shear only can be derived as,

$$\varepsilon_B = \ln \frac{L_3 + L_4}{L_0 - L_2}. \quad (3.13)$$

For strategy C, the two cases need to be considered separately:

(i) The sheared section length formed after stage 1 is L'_1 from an initial length $L_0 - L'_2$ and then becomes $L_3 + L_4 - (L_0 - L'_2)$ after stage 2. Therefore, the principal strain due to shear only, ε_C , can be obtained as,

$$\varepsilon_C = \ln \frac{L_3 + L_4 - (L_0 - L'_2)}{L_0 - L'_2}. \quad (3.14)$$

Therefore, using Eqs.(3.13), (3.14) and the geometrical constraints of (i), it holds

$$\varepsilon_B - \varepsilon_C = \ln \frac{L_3 + L_4}{2[L_3 + L_4 - (L_0 - L'_2)]} < \ln \frac{L_3 + L_4}{L_3 + L_3}. \quad (3.15)$$

In this case, the difference in strain is dependent on the shape and size of the final geometry. In particular, if $L_4 \leq L_3$, then $\varepsilon_B < \varepsilon_C$; otherwise the relative size of the geometrical parameters needs to be known.

(ii) The sheared section length formed after stage 1 is L'_1 from an initial length $L_0 - L'_2$ and then becomes L_3 after stage 2 from an intermediate length $L'_1 + L'_2 - (L_2 + L_4)$. Therefore, the principal strain due to shear only, ε_C , can be obtained as,

$$\varepsilon_C = \ln \frac{L'_1}{L_0 - L'_2} + \ln \frac{L_3}{L'_1 + L'_2 - (L_2 + L_4)}. \quad (3.16)$$

Therefore, using Eqs.(3.13), (3.16) and the geometrical constraints of (ii), it holds

$$\begin{aligned} \varepsilon_B - \varepsilon_C &= \ln \frac{L_3 + L_4}{L_0 - L_2} - \ln \frac{L'_1}{L_0 - L'_2} - \ln \frac{L_3}{L'_1 + L'_2 - (L_2 + L_4)} \\ &= \ln \frac{L_3 + L_4}{L_0 - L_2} - \ln \frac{L'_1 + L'}{L_0 - L_2 - L_4} - \ln \frac{L'_1(L_0 - L'_2) + L'L'_1}{L'_1(L_0 - L'_2) + L'(L_0 - L'_2)} - \ln \frac{L_3}{L'_1 + L'} \quad (3.17) \\ &= \ln \frac{L_3(L_0 - L_2 - L_4) + L_4(L_0 - L_2 - L_4)}{L_3(L_0 - L_2 - L_4) + L_4L_3} - \ln \frac{L'_1(L_0 - L'_2) + L'L'_1}{L'_1(L_0 - L'_2) + L'(L_0 - L'_2)} \\ &< 0, \end{aligned}$$

where $L' = L'_2 - (L_2 + L_4)$, and the following geometrical relationships from the sine law have been utilised; $L'_1 > L_0 - L'_2$ and $L_3 > L_0 - L_2 - L_4$.

Therefore,

$$\varepsilon_B < \varepsilon_C. \quad (3.18)$$

According to the design parameters in **Paper G**, it is noted that case (ii) was satisfied so that strategy C would lead to more thickness reduction compared to strategy B considering the above approximate analysis. Therefore, the introduction of strategy C has a negative influence on the proper control for material flow. This will explain why strategic combinations including strategy C cause fracture earlier than the others. These theoretical predictions have been compared with experimental results (see the results in **Paper G**).

3.3 AMINO TPIF Multi-Pass Deformation Design

3.3.1 Modeling Methodology for Closed-Loop Deformation Pass Design

Kim and Yang (2000) proposed a double-pass forming method to improve the formability for the ISF process. This method is based on shear deformation using the predicted thickness strain distribution to design deformation passes (intermediate shapes) in order to improve the formability and get a uniform thickness distribution of a final part. Although there was an analytical model developed by Kim and Yang (2000), it is only suitable for two-stage forming. For the manufacture of more complex parts (as shown in **Paper G**), more forming stages are needed. In view of this, two analytical models have been developed in this thesis for the closed-loop multiple deformation pass design based on the shear deformation assumption (see **Papers I** and **J** for full details). The subsequent sections provide an overview of the developed approaches as well as the derivations of the models.

3.3.1.1 Single-Pass Deformation Model - Shear Deformation

An arbitrary designed part can be discretized by triangular elements. Based on the shear deformation, x and y coordinates are the same for both initial and final configurations. Fig.3.4 illustrates the 3D shear deformation for one sheared triangular element in a part.

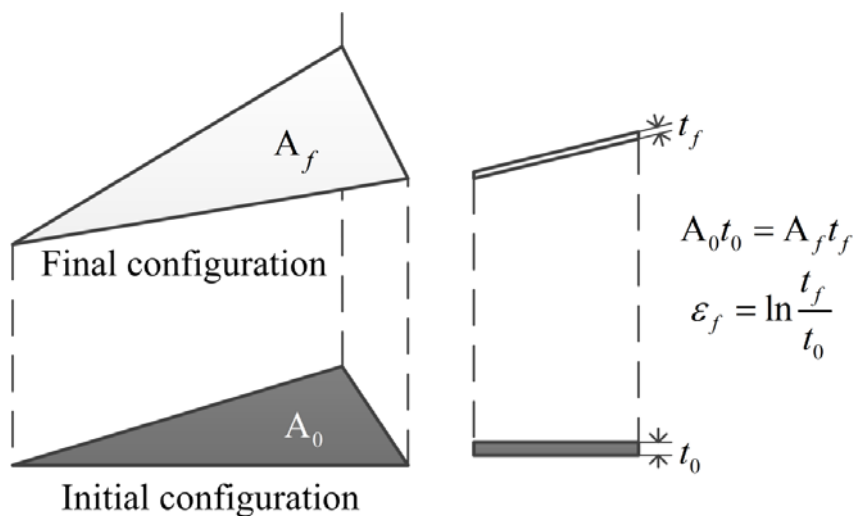


Fig.3.4. Mechanism of shear deformation.

Based on the assumption of volume constancy, the thickness strain can be calculated in the following equation,

$$\varepsilon_f = \ln \frac{t_f}{t_0} = \ln \frac{A_0}{A_f}, \quad (3.19)$$

where ε_f is the thickness strain in one element in the final configuration. t_0 and t_f are the initial and final thickness in one element. A_0 and A_f are the initial and final areas in one element, which can be calculated by x , y , z coordinates.

In this way, the thickness strains of all elements on the designed part can be approximately estimated, which are the input of the developed multi-pass deformation models. It is worth mentioning that the shear deformation assumption in this single-pass model can be relaxed. In fact, the deformation mechanism can be shear and/or stretching, or a combination of any of these as long as the centroidal plane of a sheet does not displace horizontally, which would result in the same thickness relationship compared to the pure shear assumption. However, in order to develop a simple and efficient model for multi-pass design, the shear deformation is still used to calculate the intermediate thickness strains in the following multi-pass modeling process.

3.3.1.2 Developed Open-Loop Multi-Pass Deformation Models

It is noted that the aim of the development of two models is to improve the process forming limits. The underlying hypothesis of the two models can be summarized as follows:

- (i) The use of intermediate stages in the forming process will delay the occurrence of the highest strains to larger perimeter area, and therefore allow steeper shapes to be formed than would be possible by using single-pass forming.
- (ii) By forming a wider area than the perimeter of the shape, it is possible to:
 - Avoid discontinuities in the intermediate thickness strains, and therefore allow steeper shapes to be formed than would be possible

by using single-pass forming;

- Allow the flow of material into the deformed region, thereby allowing a compressive deformation state to develop and enabling steeper shapes to be formed than would be possible in single-pass forming.

The first model (**M1**) has been developed to test the first of the above points, whilst the second model (**M2**) has been developed to test all three of the above points.

Within the modeling process, it is assumed that the deformation mode is only based on shear deformation and the material properties need not be considered in this case. The following modeling process involves two aspects: (i) devise intermediate thickness strains in the corresponding intermediate passes given the thickness strains of the designed part predicted by the single-pass model; (ii) determine the intermediate passes (intermediate shapes) based on the intermediate thickness strains.

In order to control the material flow and obtain the uniform thickness distribution, the forming in the localised region of a part requiring severe shear deformation (with higher magnitude of thickness strains) to achieve the final form should be delayed by compensating with less shear deformation (with lower magnitude of thickness strains) in the multi-stage passes. In other words, the occurrence of the highest thickness strains will be delayed using intermediate stages in the forming, and therefore steeper shapes are allowed to be formed than would be possible by using single-pass forming. The part regions with less shear deformation (with lower magnitude of thickness strains) should be kept close to the final shape in the deformation passes in order to reduce the occurrence of forming defects. On this basis, two analytical models are developed to design multi-stage deformation passes by calculating and compensating the intermediate thickness strains in each multi-stage deformation pass given a final part.

- **Model One (M1)**

In this model, it is assumed that only the material in the final part region is used in the forming. The global average thickness strain of the final part is used to compensate the strain in the severely sloped region of the final part in the intermediate stages. The local thickness strain of the final part is used to estimate the intermediate shape in the non-severely sloped region of the final part.

The intermediate thickness strain for each triangular element i (from **1** to **N**) of the final part in the corresponding deformation pass can be determined as follows:

A loop calculation applies to the following two equations until all the intermediate thickness strains of triangular elements ($i=1:N$) are calculated.

For the severely deformed region of the final part, i.e. $\varepsilon_f(i) \leq \varepsilon_{Gavg}$, the intermediate thickness strains can be calculated as,

$$\varepsilon_{int}(i) = a_1(m) * \varepsilon_{Gavg} - b_1(m) * \frac{\varepsilon_f(i) - \varepsilon_{min}}{\varepsilon_{max} - \varepsilon_{min}} * \varepsilon_{Gavg}. \quad (3.20)$$

For the non-severely deformed region of the final part, i.e. $\varepsilon_f(i) > \varepsilon_{Gavg}$, the intermediate thickness strains can be calculated as,

$$\varepsilon_{int}(i) = a_2(m) * \varepsilon_f(i) - b_2(m) * \frac{\varepsilon_f(i) - \varepsilon_{min}}{\varepsilon_{max} - \varepsilon_{min}} * \varepsilon_f(i), \quad (3.21)$$

where $\varepsilon_{min} = \min[\varepsilon_f(1), \varepsilon_f(2), \dots, \varepsilon_f(n)]$, $\varepsilon_{max} = \max[\varepsilon_f(1), \varepsilon_f(2), \dots, \varepsilon_f(n)]$,

$$\varepsilon_{Gavg} = \frac{\sum_{j=1}^n \varepsilon_f(i)}{n}. \quad (3.22)$$

$\varepsilon_f(i)$ is the thickness strain in element i of the final part, and $\varepsilon_{int}(i)$ is the intermediate thickness strain in element i of the deformation pass. $a_1(m)$, $a_2(m)$, $b_1(m)$, and $b_2(m)$ are parameters which need to be tuned to determine the intermediate thickness strain and (m) is the index of the intermediate stage ($m=1:M$). M denotes the number of intermediate passes.

It is worth mentioning that all these thickness strains in the above model are negative, i.e. ε_{min} and ε_{max} corresponding to the maximum and minimum magnitudes, respectively. Eq.(3.20) applies when the **local thickness strain** $\varepsilon_f(i)$ in the final shape has a higher magnitude than that of the **global average thickness strain** ε_{Gavg} . The first term of the right side in this equation scales the **global average thickness strain** ε_{Gavg} in the final shape to estimate an intermediate shape (deformation pass). This would have uniform thickness strain. However, this is corrected by the second term, which gives the most deformed triangular element in the final shape (with ε_{min}) this average thickness strain, but reduces the magnitude of thickness strain induced in triangular elements which have a higher magnitude of the thickness strain. This delays the forming of the regions to be stretched the most. If $b_1(m) = a_1(m)$, then the least deformed triangular element in the final shape (with ε_{max}) has $\varepsilon_{int} = 0$. Similarly, when the **local thickness strain** $\varepsilon_f(i)$ in the final shape has a lower magnitude than that of the **global average thickness strain** ε_{Gavg} , then Eq.(3.21) applies. In this case, in the right side of Eq.(3.21), the first term scales the **local thickness strain** ε_f in the final shape to estimate an intermediate shape, more closely reflecting the final shape. The second term corrects this so that if $b_2(m) = a_2(m)$, then again no reduction in the thickness strain occurs at a triangular element with the minimum thickness change in the final shape. However, the magnitude of thickness strain at the intermediate stage is reduced to zero (delaying forming), where the final shape has the maximum thickness strain (minimum thickness strain magnitude). $b_1(m) = a_1(m)$ and $b_2(m) = a_2(m)$ gives consistent results where $\varepsilon_f = \varepsilon_{Gavg}$.

Once all the intermediate thickness strains are derived in the deformation passes by the model developed, the second aspect as discussed above is to determine the positions of all triangular elements given these intermediate thickness strains in order to construct the deformation passes (intermediate shapes). Due to the shear assumption, the z coordinate of the unknown node in each triangular element can be achieved recursively. The positions of

corresponding elements (three nodes in one element) can be imported to a CAD software to build the deformation passes (intermediate shapes). Then, the tool path generation can be implemented based on the determined deformation passes (intermediate shapes) using Siemens NX CAM 7.5 software (more details can be found in Section 2.4 in **Paper J**).

- **Model Two (M2)**

Bambach (2010) discussed the deformation mechanism of ISF (SPIF and TPIF) by tracing the material points during forming (see Fig.14(a) in Section 3.1 in **Paper J**). It is found that the movement of material points is from outside to inside (“pull material in” deformation) in TPIF, which results in a “compression” mode in TPIF compared with a stretching mode in SPIF. In the multi-stage forming process, deformation passes (intermediate shapes) can be devised to encompass the final shape and provide the additional material, thereby allowing for manufacturing more complex parts than that in SPIF.

Taking into account the discussion above, model two (**M2**) is developed, which is a modified model based on **M1**. In this model, the additional material around the final part is incorporated in the multi-stage forming. It is noted that, by forming a wider area than the perimeter of the design shape, it is possible to

- Avoid discontinuities in the intermediate thickness strains, and therefore allow steeper shapes to be formed than would be possible by using single-pass forming.
- Allow the flow of material into the deformed region, thereby allowing a compressive deformation state to develop and enabling steeper shapes to be formed than would be possible in single-pass forming.

The **local weighted average thickness strain** is proposed to compensate the thickness strain in the severely sloped region instead of the **global average thickness strain** in Eq.(3.14) in the intermediate passes. The **local thickness strain** in the final part is used to estimate the intermediate shape in the non-

severely sloped region. An illustration of **M2** is shown in Fig.3.5 and the details are presented as follows:

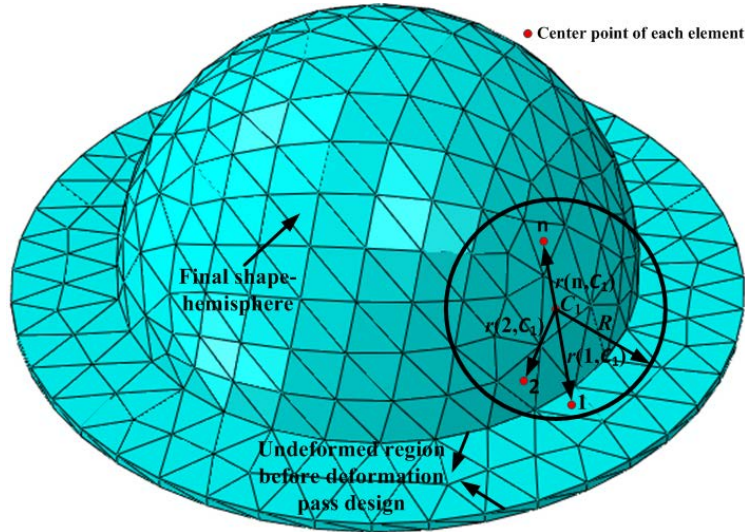


Fig.3.5. Illustration of model two in detail.

Consider the center point j (from C_1 to C_N) of each triangular element and its neighbour i (from 1 to n) with $r(i, j) \leq R$.

The first loop calculation applies to Eqs.(3.23)-(3.25) to determine $\varepsilon_{Wavg}(i, j)$ until all the neighbours ($i=1:n$) of center point j of the triangular element are calculated.

$$r(i, j) = \sqrt{(\bar{x}_{i,j} - \bar{x}_j)^2 + (\bar{y}_{i,j} - \bar{y}_j)^2 + (\bar{z}_{i,j} - \bar{z}_j)^2}, \quad (3.23)$$

$$d_{disfac}(i, j) = 1.0 - \alpha * \frac{r(i, j)}{R}, \quad (3.24)$$

$$\varepsilon_{Wavg}(i, j) = \varepsilon_f(i, j) * d_{disfac}(i, j). \quad (3.25)$$

Then, $\varepsilon_{Lavg}(j)$ can be derived from Eq.(3.26)

$$\varepsilon_{Lavg}(j) = \frac{\sum_{i=1}^n \varepsilon_{Wavg}(i, j)}{\sum_{i=1}^n d_{disfac}(i, j)}. \quad (3.26)$$

Next, for the severely deformed region of the final part, i.e. $\varepsilon_f(j) \leq \varepsilon_{Gavg}$ (region in the final part) or $\varepsilon_f(j) = 0$ (additional material region outside the final part), the intermediate thickness strain can be calculated as,

$$\varepsilon_{int}(j) = a_1(m) * \varepsilon_{Lavg}(j) - b_1(m) * \frac{\varepsilon_f(j) - \varepsilon_{min}}{\varepsilon_{max} - \varepsilon_{min}} * \varepsilon_{Lavg}(j). \quad (3.27)$$

For the non-severely deformed region of the final part, i.e. $\varepsilon_f(j) > \varepsilon_{Gavg}$, the intermediate thickness strain can be calculated as,

$$\varepsilon_{int}(j) = a_2(m) * \varepsilon_f(j) - b_2(m) * \frac{\varepsilon_f(j) - \varepsilon_{min}}{\varepsilon_{max} - \varepsilon_{min}} * \varepsilon_f(j). \quad (3.28)$$

The second loop calculation applies to all Eqs.(3.23)-(3.28) above until all the triangular elements ($j=C_1:C_N$) are calculated. Where $r(i, j)$ is the radius between the center point j and its neighbour i . R is the radius, which defines the size of the region over which the thickness strains of neighbour elements are averaged. \bar{x} , \bar{y} and \bar{z} represent the arithmetic average of corresponding coordinates in an element. $d_{disfac}(i, j)$ is the distance factor for the i th neighbor element, which linearly decreases with the distance to the center point j . α is an adjustable slope parameter, which changes the influence of the distance on the weighted average thickness strain. $\varepsilon_{Wavg}(i, j)$ is the weighted average thickness strain for the i th neighbor element. $\varepsilon_{Lavg}(j)$ is the local weighted average thickness strain for local element j . Other expressions are defined in **M1**.

Because **M2** allocates more undeformed material involved in the multi-stage deformation pass design (allow the flow of material into the deformed region in the actual TPIF process, thereby allowing a compressive deformation state to develop and enabling steeper shapes to be formed), it improves the process formability and achieves a more uniform thickness strain distribution compared to **M1**, in which only the material in the final part region is used. In addition, **M2** substitutes the global average thickness strain ε_{Gavg} in Eq.(3.20) for the local weighted average thickness strain $\varepsilon_{Lavg}(i)$ in Eq.(3.27), which can provide a more smooth estimate of the deformation transition period from the initial state to the final shape to compensate the severely sloped regions (avoid discontinuities in the intermediate thickness strains, and therefore allow steeper shapes to be formed). In **M2**, the other settings are the same as in **M1**.

3.3.1.3 Methodology for Closed-Loop Multi-Stage Deformation Pass Design

In this subsection, a systematic methodology for multi-stage deformation pass design is proposed based on the deformation pass models developed previously. In this methodology, the thinning rate is set as a forming target to optimize the design of multi-stage deformation passes in order to increase the possibilities of successful forming and control the material flow to achieve more uniform thickness strain distributions on the final part.

Due to the volume conservation during forming, the relationship between thickness strains of multi-stage deformation passes and the final part can be expressed as,

$$\varepsilon_1 + \varepsilon_2 + \dots + \varepsilon_n = \varepsilon_f, \quad (3.29)$$

where ε_i is the thickness strain of the i th forming stage ($i=1,2,\dots,n$) and ε_f is the final thickness strain of the formed part. The deformation defects are not considered here. Taking the thickness thinning rate into consideration, Eq.(3.29) can be expressed as follows, see Li et al. (2012a):

$$\ln(1-T_1) + \ln(1-T_2) + \dots + \ln(1-T_n) = \ln(1-T_0), \quad (3.30)$$

where T_i is the thickness thinning rate of the i th deformation pass ($i=1,2,\dots,n$) and T_0 is the total thickness thinning rate. By assuming $T_1 = T_2 = \dots = T_n = \bar{T}$, the total number of forming stages needed can be approximately estimated as follows:

$$n_e = \frac{\ln(1-T_0)}{\ln(1-\bar{T})}. \quad (3.31)$$

The systematic methodology for multi-stage deformation pass design is proposed as described in Fig.3.6. The desired maximum total thinning rate and the maximum average thinning rate for all forming stages are set to estimate the number of needed forming stages. Then, the maximum thinning rate for each forming stage is designed given the average thinning rate and the corresponding thickness strain is calculated. The predicted minimum thickness strain for each deformation pass is calculated by tuning the parameters in the

deformation models until the error between the predicted value and the designed value is smaller than a predefined value. Finally, the deformation passes (intermediate shapes) can be determined.

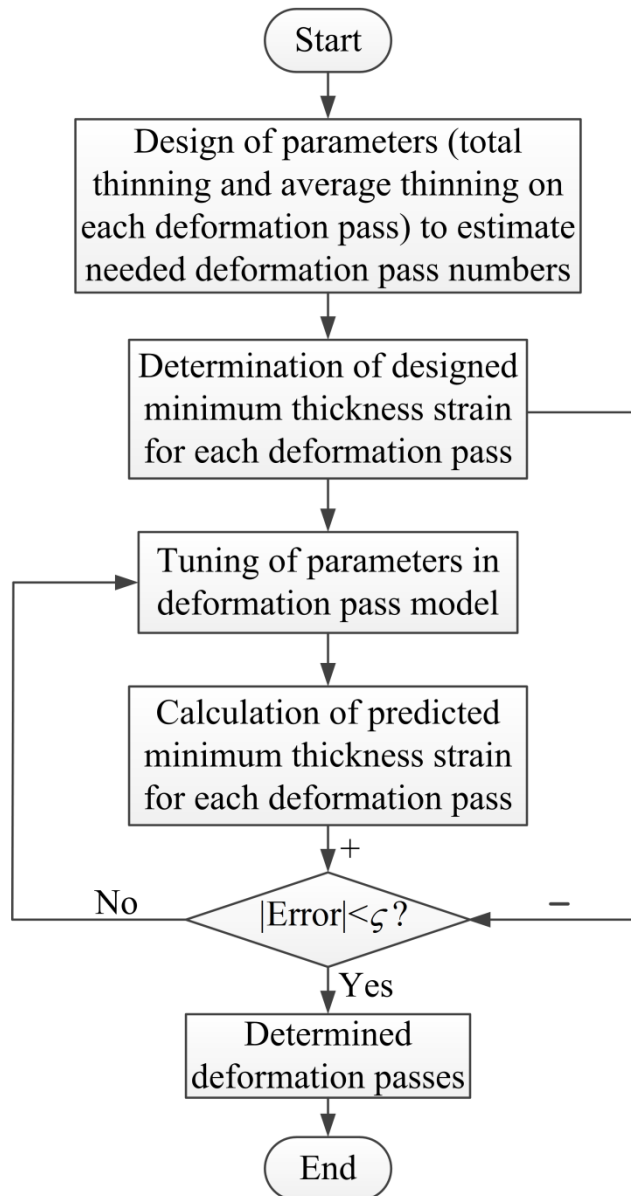


Fig.3.6. Systematic methodology for closed-loop multi-stage deformation pass design (ζ is a very small number).

3.3.2 Finite Element Modeling

This section briefly introduces the finite element modeling methodology used in this thesis for the incremental sheet forming process, especially the multi-pass TPIF process. More details can be found in **Papers C, I, J and K**.

A simplified FE model was developed to simulate the forming process for TPIF using ABAQUS[®]/Explicit software 6.11, as seen in Fig.3.7 (**Papers I, J and K**). The full forming die can be changed to an arbitrary designed 3D shape to perform the TPIF simulation and other configurations (such as forming tool and sheet metal) can be kept unchanged, which can mimic the real AMINO forming process. More details of the modelling are introduced as follows.

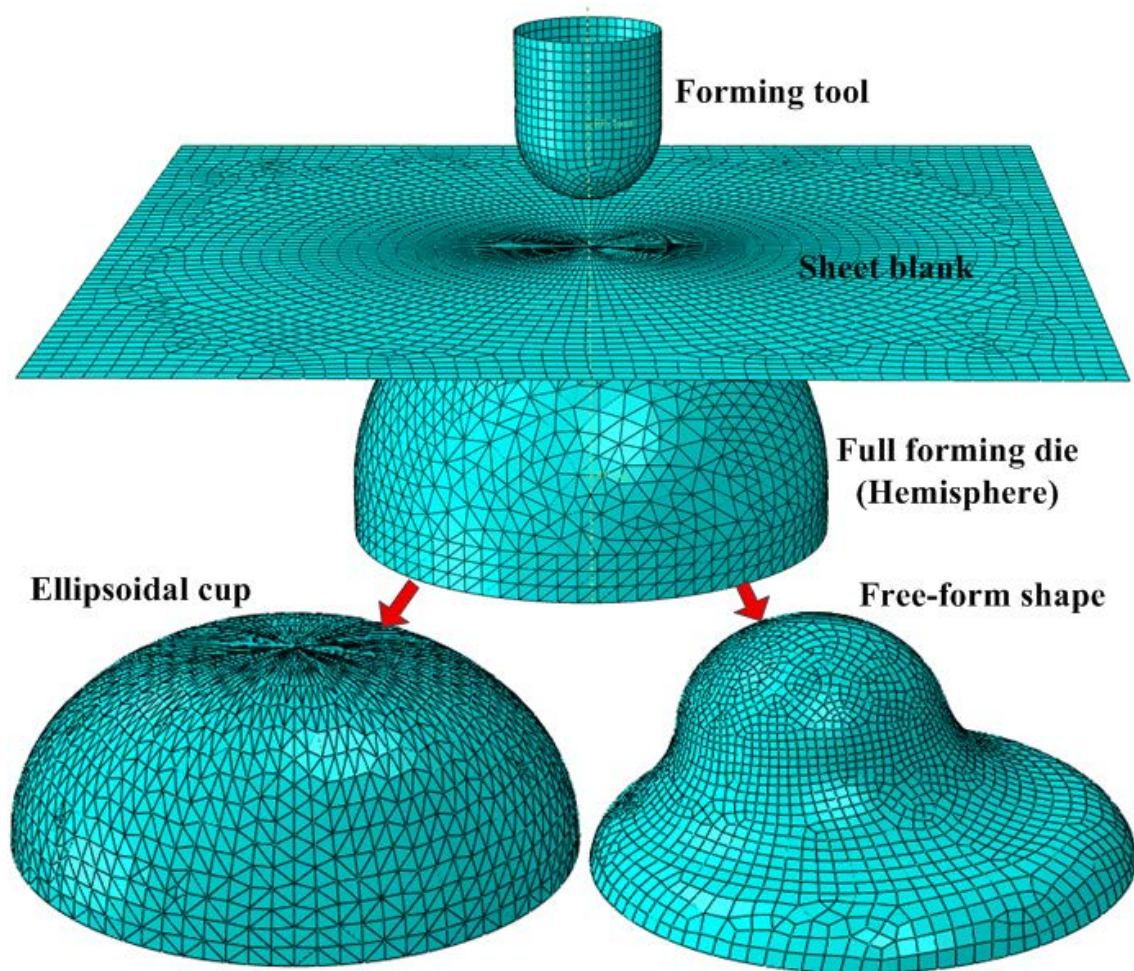


Fig.3.7. Simplified FE modeling for TPIF.

In this model, it is assumed that the material is isotropic and elastic strains after forming are neglected. Additionally, the process deformation is homogeneous. The periphery of the sheet blank is rigidly clamped and endures a constant pressure to mimic the movement of the hydraulic actuator in the real AMINO ISF machine. To reduce the size of the FE model, smaller sheets can be used in the simulations, which are determined based on the sizes of forming benchmarks. These appear to not influence the simulation results. The blank is

considered as a deformable body and is discretized with shell elements S4R, which are reduced integration elements with one integration point in the plane and five integration points through the thickness. The size of each shell element is 4mm. The forming tool and die are modeled using rigid surface elements R3D4 with sizes of 2mm and 4mm, respectively. The friction behavior is modeled using the Coulomb friction law with a friction coefficient of 0.1 between the blank and the forming tool and a friction coefficient of 0.8 between the blank and the forming die. The mass scaling factor is set to be 500. For the multi-pass forming, the designed intermediate shapes and the final shape are all formed against the final-shaped forming die.

Note that the FE model for TPIF can be easily simplified to simulate the SPIF process in which the full forming die needs to be removed and the boundary nodes can be fixed to constrain the movement of the sheet blank. In order to increase the stiffness around the initial forming region, a backing plate is sometimes used and modelled as a rigid body. More details can be found in **Paper C**, in which the LS-DYNA software was used to model the SPIF process.

3.3.3 Multi-pass Tool Path Generation Strategies

Tool path generation is one of the key topics in ISF development. Note that the shape to be manufactured is determined only by the tool movement, which has infinite possible paths to realize the same shape. Therefore, there is scope to control material flow during forming using different tool path strategies. The research in multi-pass forming can be directed towards two aspects: (i) deformation pass design (intermediate shapes or preforms); and (ii) corresponding tool path generation. The first aspect looks for the appropriate intermediate deformation shapes to enhance the forming quality by reallocating material concerning the characteristics of the designed shape. The second aspect is to realize the deformation passes and the final shape by determining suitable tool paths so as to further improve the forming quality. Our previous results have revealed that deformation passes (intermediate shapes or preforms) have an overall influence on material flow during an ISF forming process. The appropriate preform (intermediate shape) design can greatly

improve the process formability and enhance the final product quality. In addition, tool path generation representing different deformation passes and the final part in multi-pass forming also plays a role on the final product quality (such as thickness distribution, formability, etc.). On this point, the interaction of different tool paths in intermediate forming passes and the final part on material thinning has not been widely investigated yet. A guideline for tool path generation given the same multi-pass design is needed to further improve the forming quality of the final product. This section presents a strategy for tool path generation in a multi-pass deformation design which aims to clarify the interaction between the intermediate and the final tool paths on material thinning. More details can be found in **Paper K**.

Siemens NX CAM 7.5 software is utilized to define the tool paths given the CAD models for designed intermediate passes and the final part. A z-level tool path with a ramp angle is adopted in the multi-pass forming process, see Fig.3.8.

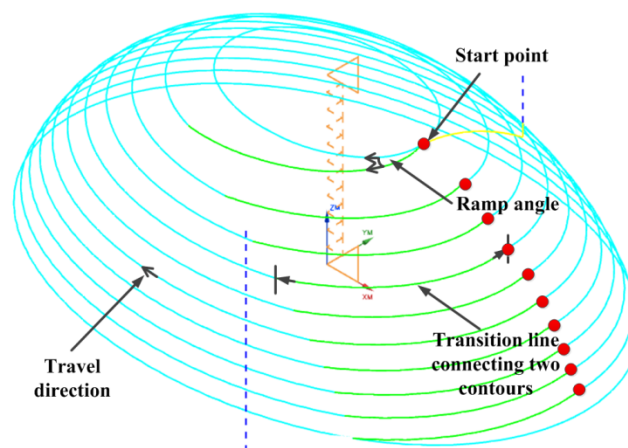


Fig.3.8. The designed tool path with three adjustable parameters-ramp angle, start point and travel direction.

The in-out downward movement of the tool is defined and the connection between two levels can be adjusted by the ramp angle, which guarantees that the tool path is continuous and leaves no obvious marks on the part surface. It is worth mentioning that the tool path devised in this study is quite similar to the tool path used in Strategy 2 in Rauch et al. (2009). In fact, this kind of tool path is a generalized tool path and more like a combination of tool paths in Strategies 1, 2 and 3. Specifically, when the ramp angle is set to be 90° , a tool

path similar to that in Strategy 1 can be obtained. Otherwise, when the ramp angle tends to 0° , a spiral-shape tool path more similar to that in Strategy 3 can be derived. It is noted that several process parameters involved in the forming process can influence the final product quality. Since these have been investigated in the previous work, this paper focuses on the most relevant tool path parameters in the multi-pass forming process and the other parameters (such as feed rate, tool diameter, etc.) are deliberately set as constants. In particular, the step-down size has been fully investigated in the previous work (**Paper A**), where it was shown that a larger step-down size can increase the process formability while a smaller one can be used to detail local characteristics of the manufactured shape and improve the forming quality. Hence this parameter will be set as a constant in multi-pass forming of this study.

Conversely, three parameters, that have not been widely investigated yet; ramp angle, start point and travel direction in a tool path, are studied in terms of their influence on material thinning, as they are relevant to the control of multi-pass tool path generation. All three parameters are assumed to influence the material allocation in multi-pass forming. More specifically, start point refers to the beginning position of each path contour. In this case, all start points can be determined by the first start point as shown in Fig.3.8 and for simplicity, in the following discussion, the start point refers to the first start point of a tool path. Its position is designed in forming passes and the final shape relative to the geometric feature of the final part and is expected to influence material thickness distribution. Ramp angle can change the length of transition line between two consecutive path contours, which is also expected to have an effect on material thinning. The change of travel direction tends to cancel out the unbalanced material flow during forming, and so is expected to obtain more symmetric thickness strain distribution in the final part.

3.4 Experimental Equipment and Validation Methodology

In this section, an overview of the experimental equipment and validation methodology used in this thesis is introduced. More details can be found in the **Papers A-L**.

3.4.1 The AMINO DLNC-PC ISF Machine

For the experimental investigations performed in this thesis, an AMINO[®] DLNC-PC incremental forming machine was used. Its detailed features can be seen in Fig.3.9. This machine is specifically built for the ISF process, which is a three-axis CNC machine with a maximum workspace of 2100×1450×500 mm³ and can exert maximum forces of 3.0 kN in Z axis and 1.5 kN in X axis and Y axis. The maximum feed rate in X axis and Y axis is 6000 mm/min and 1000 mm/min in Z axis.

For SPIF, the sheet is clamped in a blank holder, which is kept at a constant height. Whilst, for TPIF, four guide posts constrain the blank holder to move only in vertical direction. The motions of the blank holder can be controlled by six counter balancer cylinders. In the experiments, the default forming feed rate is recommended to be 4000 mm/min and the forming down pressure is set to be 0.015 MPa. In a multi-pass TPIF process, the designed intermediate shapes and the final shape are all formed against the final-shaped wooden die.

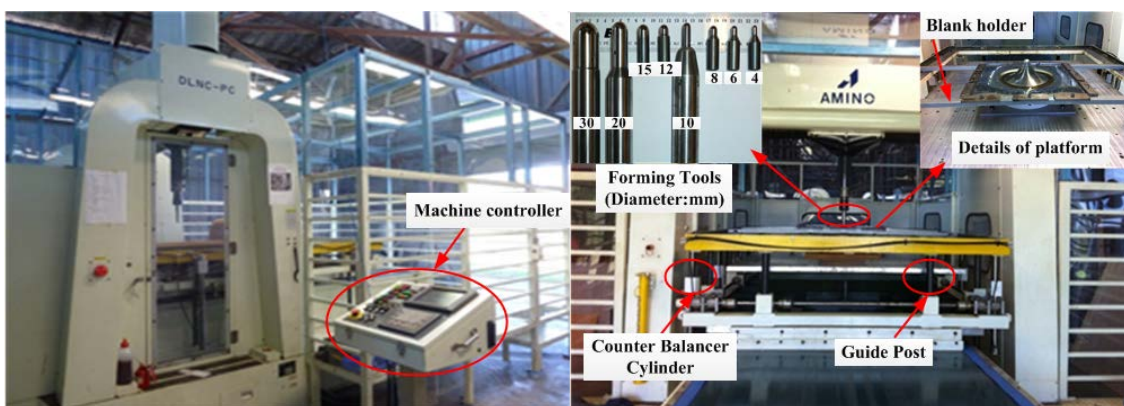


Fig.3.9. The AMINO ISF machine used for experiments.

In the experiments, the forming tools with different radii ranging from 2 mm-15 mm can be used, which are a series of machined bars with a Tungsten Carbide ball segment soldered to the end. The tool radius that has to be chosen in the experiments depends on the smallest radius of the part. Before forming, lubricant oil (Shell Tellus Oil 68) was sprayed on the blank to reduce the friction between the forming tool and the sheet metal.

3.4.2 Simplified Load Cell for Force Measurement

In this thesis, the force measurement was implemented using a specially designed simplified load cell mounted on a forming tool with 15 mm radius as seen in Fig.3.10, which has three full Wheatstone bridges. Each bridge is configured by four strain gauges and designed to measure one of the three orthogonal forces: two bending directions, and one axial direction. Before taking any measurements, the strain gauges were calibrated twice in all three directions by applying a known force. The calibrated system shows an approximate linear relation between the strain and the output voltage. During the forming process, strains transmitted from the sensor were first input into the NI USB-9237(Bridge and Strain Measurement Module), which provides a USB interface for four channels of 24-bit half/full-bridge analog input, and then connected to the laptop computer in order to record the strain signals using NI LabVIEW software. Finally, the recorded strains were converted to 3-axis forces according to the calibration relation between forces and corresponding strains.



Fig.3.10. Simplified load cell for the force measurement.

3.4.3 Laser Scanner

After forming, the geometric accuracy of the part can be measured for comparison with the designed CAD model by the VIVID 9i non-contact 3D laser scanner (Fig.3.11), which provides high-speed and high-precision 3D measurement of dies, cast and forged products, and stamped and plastic-molded products with an accuracy of $\pm 50\mu\text{m}$.



Fig.3.11. Laser scanner.

Before scanning, the part needs to be painted with the quick drying Spotcheck[®] SKD-S2 Non-Halogenated Solvent Developer to avoid the influence of light reflection. If the part is very big, several scans have to be performed and reference coded markers should be made on the scanned surface. Once each VIVID 9i scan is captured, the 3D data can be automatically aligned and merged according to the reference markers. Then, the VIVID 9i can read the target data and place the scans in the correct orientation.

3.4.4 Profilometer

The surface roughness measurements were implemented using a portable, self-contained instrument (Taylor-Hobson Surtronic 3+ Profilometer in Fig.3.12). The measurement process and operation is controlled from a wipe-clean membrane touch key panel, via 'walk through' menu selections. It is usable on horizontal,

vertical or inclined surfaces. According to the ISO standard, non-periodic roughness profile evaluation can be conducted with a high-pass Gaussian filter. For the measurement work in this thesis, the sampling length, evaluation length and calculated resolution were set to be 0.8 mm, 4 mm and 0.01 μm , respectively.



Fig.3.12. Taylor-Hobson Surtronic 3+ Profilometer.

3.4.5 Tensile Test Machine

In order to obtain the mechanical properties of the investigated aluminium sheets, uniaxial tension tests were performed on samples which have been cut in the directions of 0°, 45° and 90° with respect to the rolling direction. The dimensions of the specimen shape were shown in Fig.3.13. The tensile tests were carried out using an INSTRON 5584 universal testing machine equipped with an extensometer with a gauge length of 50mm, see Fig.3.14. Through the tensile tests, the basic mechanical properties such as yield stress, and ultimate tensile strength for different directions of the aluminium sheets were obtained. The material flow behavior, in the sheet plane, was characterized on the base of the true stress-true strain curves for three orientations in 0°, 45° and 90° with respect to the rolling direction. Through these curves, certain anisotropic flow behavior in the sheet plane for each thickness is revealed. The true stress-true strain curves can be fit by the Hollomon power law:

$$\bar{\sigma} = K \bar{\epsilon}^n, \quad (3.32)$$

where K is the strength coefficient and n is the strain-hardening exponent. $\bar{\sigma}$ and $\bar{\epsilon}$ are the flow stress and the plastic strain, respectively. The obtained corresponding material parameters can be used in finite element simulations.

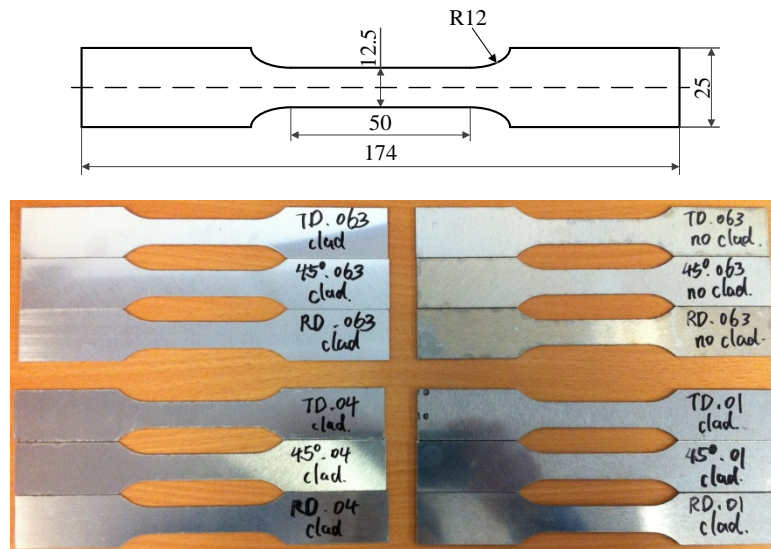


Fig.3.13. Specimen shape for uniaxial tensile tests (drawing unit: mm, thickness unit: inch).



Fig.3.14. INSTRON 5584 universal testing machine.

Chapter 4 Results

This chapter first provides an overview of the results in papers included in this thesis. Then, the detailed results are presented as a collection of published papers, mainly grouped in two aspects according to the main objectives of this thesis.

4.1 Overview of Papers for Process Investigation: Process Formability, Forming Forces, Geometric Accuracy, Forming Time and Surface Roughness

4.1.1 Process Formability and Forming Forces

In **Paper A**, (*Liu, Z.B., Li, Y.L., Meehan, P.A., 2013. Experimental investigation of mechanical properties, formability and force measurement for AA7075-O aluminium alloy sheets formed by incremental forming. International Journal of Precision Engineering and Manufacturing 14(11), 1891-1899*), an experimental campaign is presented to investigate AA7075-O aluminum alloy sheet forming using single point incremental forming (SPIF) technology and understand the forming process mechanism. Firstly, tensile tests were carried out to characterize the mechanical properties of AA7075-O sheets with three different thicknesses. Then, the effects of tool path types with different incremental steps on the maximum part draw angle and the successful part height were evaluated to clarify the formability. Additionally, a fracture forming limit diagram was developed to give the design limits for strain. Finally, the trends in forming forces were analyzed considering the influence of different draw angles, sheet thicknesses, step-down sizes and sheet orientations. Experimental results showed that formability is affected by the part draw angle and incremental steps of the tool path. However, the likelihood of successful forming also depends on other geometrical design parameters such as the part height. In addition, the influences of process parameters on tool forces provide further insights into the deformation mechanics of AA7075-O sheets. The slope of the force curve after

the peak value can be identified as a forming failure prediction indicator regardless of the tool path types when using a truncated cone as a benchmark. Also the influence of sheet orientations on forming forces was investigated in SPIF. The vertical forming force is found to be smaller in a sheet orientation 45° to the rolling direction than that of a sheet orientation 0° for three different sheet thicknesses due to the smaller strain hardening values found in the sheet orientation 45° .

In **Paper B**, (Li, Y.L., **Liu, Z.B.**, Lu, H.B., Daniel, W.J.T., Meehan, P.A., 2014. *Experimental study and efficient prediction on forming forces in incremental sheet forming. Advanced Materials Research 939, 313-321*), forces during the cone forming process with different wall angles and step down sizes were recorded and compared. Different force trends were identified and discussed with reference to bending and strain hardening mechanics. Influences of different parameters on the process formability were also qualified which would benefit the design process. An efficient predictive model based on upper-bound approach was applied for the tangential force prediction in this case. Predicted tangential forces were then compared with the experimental results showing relatively good agreement. The limits of the proposed model were also identified and the potential of future improvements were suggested.

In **Paper C**, (Li, Y.L., **Liu, Z.B.**, Daniel, W.J.T., Meehan, P.A., 2014. *Simulation and experimental observations of effect of different contact interfaces on the incremental sheet forming process. Materials and Manufacturing Processes, 29(2), 121-128*), the effect of tool type and size on the formability and surface integrity is studied in SPIF. Experimental tests were carried out on aluminum sheets of 7075-O to create a straight groove with four different tools (ϕ 30 mm, ϕ 25.4 mm, ϕ 20 mm and ϕ 10 mm). One tool indenter was fitted with a roller ball (ϕ 25.4 mm) while the other three were sliding indenters. The contact force, friction and failure depth were evaluated. A finite element (FE) model of the process was set up in an explicit code LS-DYNA and the strain behavior and thickness distribution with different tools were evaluated and compared with the experimental results. This study provides important insights into the relatively

high formability observed in the ISF process. Microscopic observations of the surface topography revealed that a rolling tool tip produced better surface integrity as compared with a sliding tool tip, wherein, distinct scratch patterns in the tool traverse direction were evident.

4.1.2 Geometric Accuracy

In **Paper D**, (Lu, H.B., Li, Y.L., **Liu, Z.B.**, Liu, S., Meehan, P.A., 2014. *Study on step depth for part accuracy improvement in incremental sheet forming process. Advanced Materials Research 939, 274-280*), a comprehensive investigation is provided on step depth; a critical process variable in ISF process, and to demonstrate that this variable is of great importance in the design and control of a tool path. Several experiments were conducted to investigate its influence on the part quality of the formed parts, including geometric accuracy, part surface quality and process formability. The results showed that a smaller step depth leads to better geometric accuracy and part surface quality in ISF process. Parts deformed with a large step depth cannot reach the required level both in geometric accuracy and surface quality but too small a step depth value should also be avoided with regard to the process formability, especially when producing parts with large wall angles. Also, the forming time will increase as the step depth decreases. A trade-off among geometric accuracy, part surface quality, process formability and forming time should be made in the design and control of tool paths and the first two aspects should be considered as priorities. It is clearly suggested that there is an optimum value of step depth in the ISF path design; for instance 0.7mm presented in the case. Further research on the optimization of step depth should be included in the design of an advanced ISF control system. Additionally, the control of tool path should be developed for the part accuracy improvement and design time reduction for new parts in the ISF process.

4.1.3 Forming Time

In **Paper E**, (*Liu, Z.B., Li, Y.L., Daniel, W.J.T., Meehan, P.A., 2014. Taguchi optimization of process parameters for forming time in incremental sheet forming process. Materials Science Forum 773-774, 137-143*), forming time is studied by investigating the effects of four distinctive process parameters (step over, feed rate, sheet thickness and tool diameter). An effective analysis tool, Taguchi method together with the design of experiment (DOE) and analysis of variance (ANOVA), is utilized to study the effects of the four process parameters on forming time and further to optimize parameter combinations in order to minimize forming time. Using these techniques, experimental results showed that the step over of the spiral tool path is the most important process parameter affecting forming time followed by the feed rate. Sheet thickness and tool diameter have little effect on forming time. The comparison between the prediction of optimized parameter combination and the confirmation test result has further demonstrated the effectiveness of the proposed method. It is worth noting that the results of this study will indicate a further direction on how to optimize process parameters to find a balance between forming efficiency (forming time) and forming quality (forming accuracy and surface roughness).

4.1.4 Surface Roughness

In **Paper F**, (*Liu, Z.B., Liu, S., Li, Y.L., Meehan, P.A., 2014. Modelling and optimization of surface roughness in incremental sheet forming using a multi-objective function. Materials and Manufacturing Processes 29(7), 808-818*), a systematic methodology for modelling and optimization of surface roughness in ISF is proposed. The quantitative effects of four parameters (step down, feed rate, sheet thickness and tool diameter) on surface roughness are investigated using the response surface methodology (RSM) with Box-Behnken design. The multi-objective function is used to evaluate the overall surface roughness in terms of the tool-sheet contact surface roughness, i.e. internal surface roughness and the non-contact surface roughness i.e. external surface roughness. Then, the overall surface roughness is minimized using a single-

objective desirability function with the aim of simultaneous minimization of both internal surface roughness and external surface roughness. The average surface roughness (R_a) on each surface is measured along the tool-path step-down direction taking the impact of sheet roll marks into account. The measurement results are fitted to a second-order polynomial model describing the inherent relationships between the four factors and the evaluated overall surface roughness. The optimal conditions for the minimization of overall surface roughness are determined as step down (0.39 mm), feed rate (6000 mm/min), sheet thickness (1.60 mm) and tool diameter (25 mm), respectively. These predicted values are further verified by a validation experiment. This study shows that the Box-Behnken design with multi-objective function can be efficiently applied for modelling and optimization of the overall surface roughness in ISF.

4.2 Overview of Papers for Multi-Pass ISF Modeling and Its Validation

4.2.1 SPIF Multi-Pass Deformation Design

In **Paper G**, (*Liu, Z.B., Li, Y.L., Meehan, P.A., 2013. Vertical wall formation and material flow control for incremental sheet forming by revisiting multi-stage deformation path strategies, Materials and Manufacturing Processes 28(5), 562-571*), multi-stage deformation path strategies for single point incremental forming (SPIF) are revisited with the purpose of controlling material flow (improve sheet thickness distribution) and forming a vertical wall surface for cylindrical cups. It is noted that stretching and thinning are two main deformation modes during SPIF. How to control material flow in an optimal way is a key point for successful forming. Multi-stage incremental forming shows more advantages than single-stage forming, especially dealing with shapes with steep walls. In the paper, three basic multi-stage deformation path strategies have been proposed, that is, A. incremental part diameter; B. incremental draw angle; C. incremental part height and draw angle. Those strategies and their combinations have been evaluated in terms of the process formability and

compared in order to understand the material allocation mechanism and optimise the multistage forming process. In addition, approximate plane-strain analysis models have been given to provide formability predictions between single-stage and multi-stage strategies, and between strategies B and C, respectively. The prediction results show good agreement with the experimental results. It is demonstrated that the strategic combination A+B is the optimal way to achieve the forming target. However, the multi-stage design in this paper is still based on the trial-and-error method, although the allocation of more material close to the critical part region facilitates the likelihood of successful forming.

4.2.2 AMINO TPIF Multi-Pass Deformation Design

In **Paper H**, (*Liu, Z.B., Meehan, P.A., Bellette, P.A., 2011. Thickness distribution and forming strategy analysis for two point incremental forming with a male die. Advanced Materials Research 337, 452-455*), the geometrical model, sine law, is introduced for predicting the thickness distribution of a final part. The forming procedures for the multi-stage TPIF are then detailed, which is the basics for the experimental investigations in the following papers.

In **Paper I**, (*Liu, Z.B., Li, Y.L., Daniel, W.J.T., Meehan, P.A., 2014. An analytical model for deformation path design in multistage incremental sheet forming process. Advanced Materials Research 939, 245-252*), different from the trial-and-error method proposed in **Paper G**, an analytical model for designing multi-stage deformation paths and predicting the thickness strain distribution is proposed based on shear deformation and strain compensation idea. The aim is to achieve a uniform thickness distribution of formed parts and particularly eliminate the excessive thinning on severely sloped regions, which may lead to the part fracture and limit the process formability. The feasibility of the proposed model is validated by the finite element analysis (FEA) and experimental tests in terms of the comparison of prediction, simulation and experimental results on the thickness strain distribution and the process formability. However, because only the material in the final part region is considered in the multi-pass design,

the results show the process formability has not been enhanced compared with the single-stage forming. The possible reason has been discussed.

In **Paper J**, (*Liu, Z.B., Daniel, W.J.T., Li, Y.L., Liu, S., Meehan, P.A., 2014. Multi-pass deformation design for incremental sheet forming: Analytical modeling, finite element analysis and experimental validation. Journal of Materials Processing Technology 214(3), 620-634*), following the method proposed in **Paper I**, a systematic methodology incorporating two analytical models (**M1** and **M2**) for closed-loop multi-pass deformation design considering the predicted thickness strains given the design geometry is developed based on shear deformation and the strain compensation mechanism. In particular, two analytical models (**M1** and **M2**) are developed considering; the global average thickness strain and only the material in the final part region used in the forming (**M1**), and the local weighted average thickness strain and the additional material around the final part region used in the forming (**M2**), respectively. It is noted that the idea of more material allocated to the steep regions during multi-pass forming coincides with the results (strategy B) in **Paper G** and is also evidenced by the experiments in which the movement of material points has been traced. The feasibility of the proposed design methodology was validated by finite element analysis (FEA) and experimental tests. The results revealed that a more uniform thickness strain distribution can be derived using **M2**, in which more material has been devised in the multi-pass design. The occurrence of the highest strains can be delayed in the intermediate stages and the flow of material is allowed into the deformed region, thereby allowing a compressive deformation state to develop and enabling steeper shapes to be formed. Therefore, the process formability is enhanced via the analytical design of deformation passes.

In **Paper K**, (*Liu, Z.B., Li, Y.L., Meehan, P.A., 2014. Tool path strategies and deformation analysis in multi-pass incremental sheet forming process. International Journal of Advanced Manufacturing Technology, 75(1-4), 395-409*), the work of **Paper J** has been extended to clarify three points using finite element simulations and experiments: (i) generalization of simple shapes to

complex shapes using the developed multi-pass design methodology; (ii) interaction of different tool paths on material thinning of the final part given the same multi-pass design; (iii) material flow mechanism in multi-pass forming. The FEM and experimental results confirmed that the developed multi-pass design methodology can be applied to the forming of more complex shapes. Three parameters, which are relevant to the control of multi-pass tool path generation, have been evaluated in terms of their influence on material thinning. It is concluded that ramp angle shows little influence on material thinning. Changes in travel direction can balance the thickness strain distribution so that material twisting phenomenon can be eliminated to some extent. The tool path start point in multi-pass forming is the most important controllable parameter to reduce material thinning of the final part compared to the other two parameters (ramp angle and travel direction). The maximum material thinning and the thickness strain distribution can be controlled by deliberately changing the tool path start points in multi-pass forming so as to further improve the process formability. It is suggested that the multi-pass tool path start points should be distributed as evenly as possible and the tool path in pass one can start around the final part region with steep angles. However, the reasons behind these findings still need to be further clarified in the future work so as to facilitate the multi-pass design. The inward in-plane material flow mechanism has been evidenced by FEA given the proposed multi-pass design. It appears to cause a compressive deformation state and therefore allows steeper shapes to be formed. This clarifies the reason why multi-pass forming can achieve increases in the process formability compared to single-pass forming.

4.1 Process Investigation: Process Formability, Forming Forces, Geometric Accuracy, Forming Time and Surface Roughness

4.1.1 Process Formability and Forming Forces

Paper A

**Experimental investigation of mechanical properties,
formability and force measurement for AA7075-O
aluminium alloy sheets formed by incremental forming**

Liu, Z.B., Li, Y.L., Meehan, P.A.

International Journal of Precision Engineering and Manufacturing

2013, Volume: 14(11), Pages: 1891-1899.

Experimental Investigation of Mechanical Properties, Formability and Force Measurement for AA7075-O Aluminum Alloy Sheets Formed by Incremental Forming

Zhaobing Liu^{1#}, Yanle Li¹, and Paul Anthony Meehan¹

¹ School of Mechanical and Mining Engineering, The University of Queensland, Brisbane St Lucia, QLD 4072, Australia
Corresponding Author / E-mail: z.liu7@uq.edu.au, TEL: +61-7-336-53885, FAX: +61-7-336-54799

KEYWORDS: Incremental sheet forming, Mechanical properties, Aluminum 7075-O, Formability, Force measurement

Incremental sheet forming (ISF) has demonstrated its high potential to shape complex three-dimensional components without using specific tooling, thus enabling product customization, cost reduction and efficiencies. This paper presents an experimental campaign to investigate AA7075-O aluminum alloy sheet forming using single point incremental forming (SPIF) technology and understand the forming process mechanism. Firstly, tensile tests were carried out to characterize the mechanical properties of AA7075-O sheets with three different thicknesses. Then, the effects of tool path types with different incremental steps on the maximum part draw angle and the successful part height were evaluated to clarify the formability. Additionally, a fracture forming limit diagram was developed to give the design limits for strain. Finally, the trends in forming forces were analyzed considering the influence of different draw angles, sheet thicknesses, step-down sizes and sheet orientations. Experimental results showed that formability is affected by the part draw angle and incremental steps of the tool path. However, the likelihood of successful forming also depends on other geometrical design parameters such as the part height. In addition, the influences of process parameters on tool forces provide further insights into the deformation mechanics of AA7075-O sheets. The slope of the force curve after the peak value can be identified as a forming failure prediction indicator regardless of the tool path types when using a truncated cone as a benchmark. Also the influence of sheet orientations on forming forces was investigated in SPIF. The vertical forming force is found to be smaller in a sheet orientation 45 to the rolling direction than that of a sheet orientation 0 for three different sheet thicknesses.

Manuscript received: January 25, 2013 / Accepted: September 14, 2013

1. Introduction

The 7xxx series aluminum alloys have been widely utilized as structural materials due to their attractive comprehensive properties, such as low density, high strength, ductility, toughness and resistance to fatigue.¹⁻³ The 7075 aluminum alloy is one of the highest strength alloys and is typically used as aircraft structures. The 7075 aluminum alloy sheets, in O temper condition, have practical and wide industrial application due to their higher formability compared with the other temper conditions. For many applications, AA7075-O sheets are required to deform in various kinds of 3D shells. In industry, the cost of forming is high for processes such as deep drawing or stamping where specialized tooling is needed for a specific 3D designed shape. However, applications in fields such as rapid prototyping and customized products require small-batch production, so the high cost tooling is disadvantageous. The inception of incremental sheet forming

(ISF) has provided a solution, which is quite flexible, suitable for small-batch production, and no high-cost tooling is required.⁴⁻¹⁶ The development of ISF began in the 1990s in Japan.⁴ Since then, this technology has gained great attention in Europe and North America, and many efforts have been made to push it towards industrial applications.⁹ Basically, there are two variations of incremental sheet forming, single point incremental forming (SPIF) and two point incremental forming (TPIF). In single point incremental forming, the tool deforms the sheet metal into the concave shape without any dies while in two point incremental forming, the tool moves on the convex sheet surface with a positive die. The blank holder is moved by the hydraulic actuator in order to firmly maintain the sheet metal in the proper working position.

Comprehensive reviews have been provided on the development of ISF in the past decades.^{9,10} It is noted that the tool path defines the component geometry. So, the influence of different tool paths with

different incremental steps on formability is worth further investigating. Filice et al. discussed the material formability in incremental forming, in which a spiral tool path was proposed to form a truncated cone shape.¹¹ They concluded that incremental forming is characterized by local stretching deformation mechanics which determines a linear forming limit curve with a negative slope in the first quadrant. Young et al. pointed out that the maximum draw angle for SPIF could be defined to evaluate part formability.¹² Experimental tests were performed to determine specific values for two kinds of aluminum alloys (3003-O and 5754-O). Durante et al. performed experimental campaigns to deform AA7075-T0 sheets.¹³ They found that formability decreases with the increase of tool diameter and the angular step, which is evaluated by measuring the maximum forming angle for truncated cones. However, the comparison between two kinds of tool paths (spiral and z-level) with different incremental steps has not been made in terms of formability.

Forming force is one of the important quantities required to understand the deformation mechanics in ISF. Dufloy et al. investigated the influence of four process parameters (vertical step size, tool diameter, geometrical wall angle and sheet thickness) as well as the lubrication and the geometry of the part on the forming forces.¹⁴ It was concluded that within the explored limits, vertical step size has the least significant impact and can therefore be increased without great penalty, in favor of lower part production times. Jackson et al. compared the forming forces between sandwich panel incremental forming and aluminum incremental forming.¹⁵ The influence of tool radius and vertical pitch on tool force was highlighted. They concluded that vertical force increases approximately linearly with tool radius for both materials. Jeswiet et al. found that tool force usually evolves to a peak value and then stabilizes to a steady state when manufacturing a part with a constant wall angle.¹⁶

The scope of this paper is mainly focused on incremental forming of AA7075-O aluminum sheets. Uniaxial tensile tests were performed on AA7075-O sheets with three different thicknesses to characterize some basic material properties. Then, two aspects are investigated in this paper. Firstly, formability has been evaluated in order to clarify the influence of different kinds of tool paths with different incremental steps. The maximum draw angle can be seen as a simple formability indicator. However, the likelihood of successful forming also depends on other geometric design parameters such as the part height. A safety formability region is given in view of different tool paths and incremental steps. Moreover, the fracture forming limit diagram is derived to further characterize the material formability. Secondly, the influences of process parameters on tool forces have been revisited to give further insights into the deformation mechanics of AA7075-O sheets. In particular, the influence of sheet orientations on forming forces has been considered for the first time in this study.

2. Material Characterization and Mechanical Behavior

In this section, AA7075 O-temper aluminum alloy sheets were investigated with three different thicknesses (1.02 mm, 1.60 mm and 2.54 mm). The chemical composition for AA7075-O sheets is presented in Table 1. In order to obtain the mechanical properties, uniaxial

tension tests were performed on samples which have been cut in the directions of 0°, 45° and 90° with respect to the rolling direction. The dimensions of the specimen shape are shown in Fig. 1. The tensile tests were carried out using INSTRON 5584 universal testing machine equipped by extensometer with a gauge length of 50 mm, see Fig. 2.

Through the tensile tests, the basic mechanical properties such as yield stress, ultimate tensile strength for different directions were obtained as presented in Table 2.

The material flow behavior, in the sheet plane, was characterized on the base of the true stress-true strain curves for three orientations in 0°, 45° and 90° with respect to the rolling direction. They are presented in Figs. 3~5. Through these curves, certain anisotropic flow behavior in the sheet plane for each thickness is revealed. It is shown that anisotropy

Table 1 Chemical composition (% wt) for AA7075-O aluminum alloy sheets

Si	Fe	Cu	Mn	Mg	Cr	Zn	Ti	Al
0.08	0.12	1.7	0.01	2.5	0.19	5.7	0.04	Balance

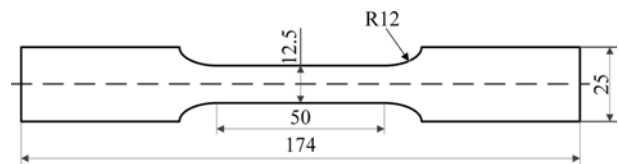


Fig. 1 Specimen shape for uniaxial tensile test (Unit: mm)



Fig. 2 INSTRON 5584 universal testing machine

Table 2 Mechanical properties for AA7075-O aluminum alloy sheets with three different thicknesses

Material	Orientation	Y	UTS	EI	E
1.02 mm	Rolling (0°)	88	190	17	69
	Diagonal (45°)	88	191	18	71
	Transverse (90°)	91	192	14	70
1.60 mm	Rolling (0°)	91	199	20	70
	Diagonal (45°)	91	196	22	69
	Transverse (90°)	94	202	19	70
2.54 mm	Rolling (0°)	93	190	19	70
	Diagonal (45°)	95	200	22	70
	Transverse (90°)	97	203	21	72

Note: Y is yield stress at 0.2% yield [MPa], UTS is ultimate tensile strength [MPa], EI is elongation [%] and E is young's modulus [Gpa].

becomes a little more obvious as the sheet thickness increases. But, overall, it represents a rather weak anisotropic behavior for the investigated sheets. The true stress-true strain curves can be fit by the Hollomon power law

$$\sigma = K\epsilon^n \tag{1}$$

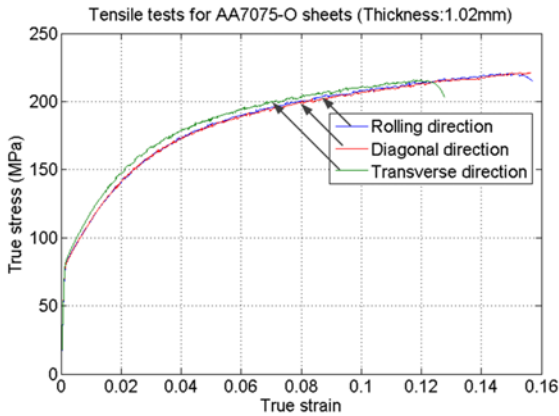


Fig. 3 True stress-true strain curves for AA7075-O aluminum alloy sheets with 1.02 mm thickness

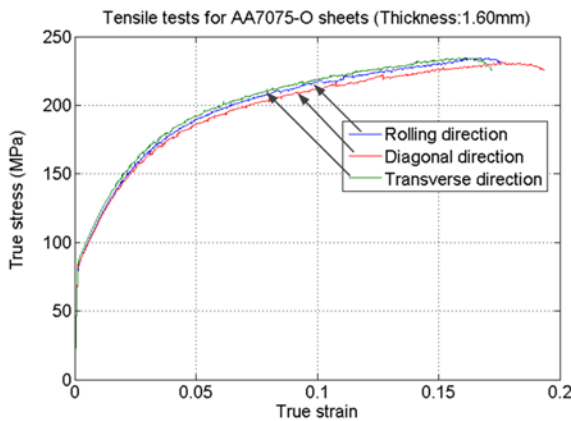


Fig. 4 True stress-true strain curves for AA7075-O aluminum alloy sheets with 1.60 mm thickness

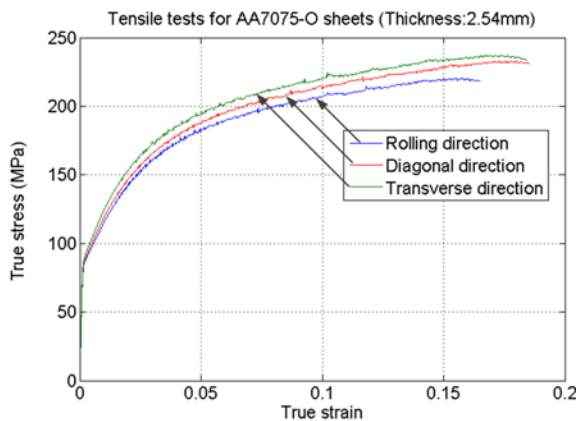


Fig. 5 True stress-true strain curves for AA7075-O aluminum alloy sheets with 2.54 mm thickness

where K is the strength coefficient and n is the strain-hardening (or work-hardening) exponent. The corresponding parameters are presented in Table 3.

3. Formability

In ISF, the formability is much higher than the conventional forming processes such as deep drawing and stamping. In many ISF research papers,^{9,12,13} the draw angle can be seen as a formability indicator, because this quantity has a close relationship with the sine law which is widely used to estimate the thickness distribution as a plane strain model. In this section, the maximum draw angle is used as an indicator to estimate the formability of AA7075-O sheets with 1.6 mm thickness considering the influence of different tool paths with different incremental steps. A truncated cone is selected as the benchmark as

Table 3 Strength coefficient K and strain-hardening exponent n for AA7075-O sheets with three different thicknesses

Material	Orientation	K	n
1.02 mm	Rolling (0°)	351.2	0.2301
	Diagonal (45°)	349.5	0.2294
	Transverse (90°)	361.3	0.2300
1.60 mm	Rolling (0°)	361.2	0.2276
	Diagonal (45°)	343.9	0.2176
	Transverse (90°)	361.3	0.2224
2.54 mm	Rolling (0°)	341.2	0.2202
	Diagonal (45°)	349.4	0.2181
	Transverse (90°)	353.4	0.2190

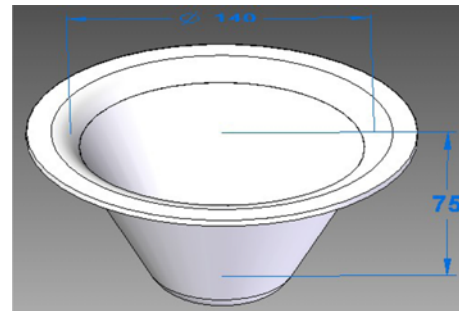


Fig. 6 Benchmark-a truncated cone



Fig. 7 The Amino ISF machine used for experiments

shown in Fig. 6. The size of AA7075-O sheet is 300 mm×300 mm. The tool radius is 15 mm and feed rate was set to 4000 mm/min. In order to increase the rigidity between the forming area and the sheet flange, a backing plate is utilized underneath the sheet metal. Before forming, lubricant oil-Shell Tellus Oil 68 was sprayed on the blank. The tool paths were generated by Siemens NX 7.0. Fig. 7 shows the Amino ISF machine used for the experiments.

Fig. 8 shows the details of incremental forming and the illustration of incremental steps. It is noted that step over is the adjustable quantity to generate the spiral tool path in Siemens NX software. For the investigated truncated cone with the constant draw angle, step over and step down are directly related based on simple trigonometric relationship. In order to make comparison clear, step over is used here to generate two kinds of tool paths (spiral and z-level) to control the downward movement of the forming tool and investigate their influence on formability. The spiral tool path in Fig. 9(a) is continuous with an incremental descent of the tool distributed over the entire surface of a part, which can be adjusted by changing the step over. The advantage of this tool path is that no marks occur at step down. Z-level tool path in Fig. 9(b) is defined by fixed vertical increments between consecutive discrete contours. Previous studies⁹ have shown that for a z-level tool path, deformation is biaxial at the starting and end points of each contour, and is close to plane strain in between. It has been observed that the tendency for fracture at the start and end points of each contour is higher as compared with when the rest of the contour is being formed. Compared with the spiral tool path, the z-level tool path can leave stretch marks at the transition points between layers and create force peaks. It is noted that tool path defines the forming

geometry. So, is there any difference in formability when different tool paths are adopted to deform the same part? How is the formability affected by different incremental steps of tool paths? These questions will be answered based on experimental tests in the following discussion.

3.1 Influence of tool path and step-down size on formability

In the first test, in order to investigate the influence of the spiral tool path and the z-level tool path on formability, step over was set to be a constant value 0.5 mm for both tool paths. A series of truncated cones were formed with draw angles 60°, 61°, 62°, 63°, 64°, 65° and 70° to evaluate the formability. The experimental results are presented in Fig. 10. It can be seen that under the same step-over size, there is no noticeable difference on formability between the spiral tool path and the z-level tool path. Formability is greatly affected by the draw angle of the truncated cone. However, the likelihood of successful forming also depends on the cone height. As can be seen, draw angles 62° and 63° are the formability boundary for successful forming of the truncated cone. Taking the cone height into consideration, a safety formability region is identified as shown in Fig. 10. Areas A+B are the safety formability zone for the spiral path compared with the area B for the z-level path.

In the second test, emphasis is laid on evaluating the influence of the z-level tool path with different incremental steps on formability. The experimental results are shown in Fig. 11. It is concluded that formability is higher for a larger step over (0.5 mm as compared to 0.2 mm) based on the experimental results. However, because only two step-down sizes were tested, more tests involving a wide range of step down sizes need to be performed to further demonstrate this conclusion in the future. In addition, a safety formability region is drawn in Fig. 11. The area B is the safety formability zone for z-level tool path with 0.2 mm step-over size. The area A shows the quantitative formability difference between 0.5 mm step-over size and 0.2 mm step-over size for the z-level tool path. Fig. 12 summarizes the comparison of effects of spiral and z-level tool paths with different incremental steps on formability.

3.2 Fracture forming limit diagram

In order to further investigate the formability, fracture forming limit

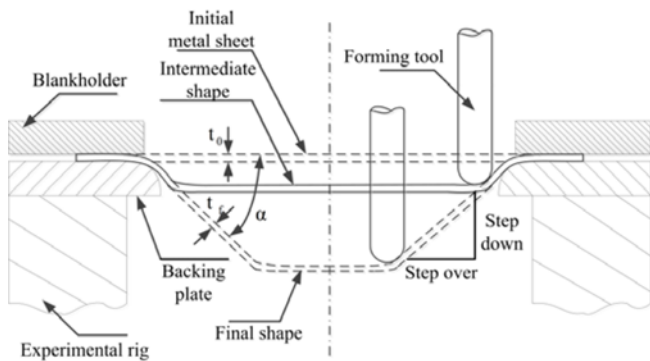


Fig. 8 Details of incremental forming and illustration of incremental steps (step over and step down)

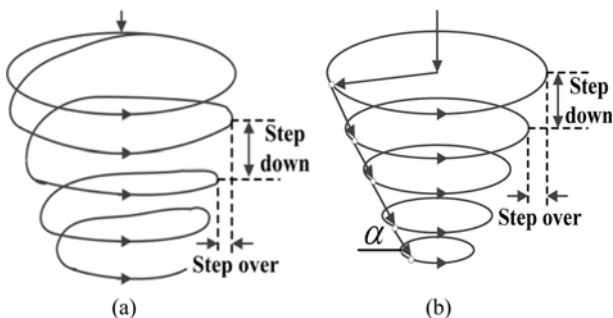


Fig. 9 Design of tool paths to test formability for truncated cones: (a) spiral tool path and (b) z-level tool path (α is the draw angle)

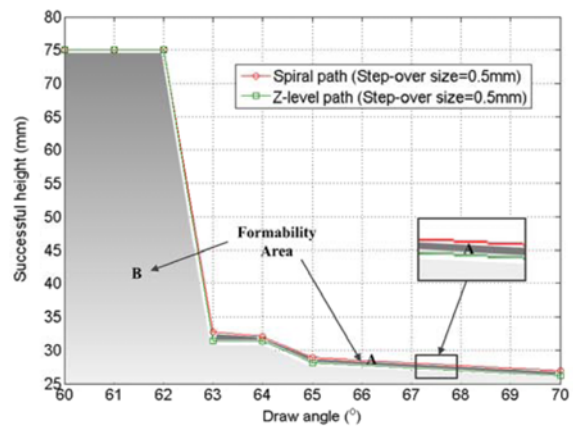


Fig. 10 Influence of spiral and z-level tool paths on formability vs the draw angle α

diagram was obtained as shown in Fig. 13. The results were obtained by measuring the experimental strains at several places along the crack for truncated cones with different draw angles in the case of z-level path with 0.2 mm step-over size. To measure the strains after deformation, circles with 5.5 mm initial diameter were drawn on the surface of the sheets before forming using 0.5-mm-thick oil-based blue pen. The line pitch was 0.5 mm and was already included in the size of the initial diameter of the circle. The size of the major and minor axis of the ellipses after the plastic deformation of the circles was measured and calculated based on the in-plane surface strains directly from

$$\varepsilon_1 = \ln\left(\frac{Y}{D}\right) \tag{2}$$

$$\varepsilon_2 = \ln\left(\frac{X}{D}\right) \tag{3}$$

where D is the initial diameter of the circle and X and Y are the corresponding measured major and minor axis of the ellipse.

As seen in Fig. 13, the measured major true strain for crack failure lies between 0.68 and 0.92 defining a fracture band for major true strain. The process designer can acquire an insight from this result and increase the product formability by properly choosing process parameters such as larger incremental step in the beginning of forming or choosing

multi-stage deformation path design.

4. Force Measurement

It is noted that the investigation of forming forces is one of the most important aspects to understand the deformation mechanism of ISF. Previous studies have mainly focused on the influences of process parameters on tool forces. In this section, emphasis is laid on the analysis of mechanics of forming AA7075-O sheets with three thicknesses (1.02 mm, 1.60 mm and 2.54 mm) through the force measurement. Forming forces are evaluated from three characteristics: (1) the influence of the draw angle and the tool path on resultant forming forces, (2) the influence of the sheet thickness and the step-down size of z-level tool path on forming forces, (3) the influence of sheet orientations on forming forces. It is worth noting that the third aspect has not been considered before in ISF.

In this study, the force measurement was implemented using a specially designed sensor mounted on a forming tool with 30 mm diameter as seen in Fig. 14, which has three full Wheatstone bridges. Each bridge is configured by four strain gauges and designed to measure one of the three orthogonal forces: two bending directions, and one axial direction. Before taking any measurements, the strain gauges were calibrated twice in all three directions by applying a known force. The calibrated system shows an approximate linear relation between strain and output voltage. During the forming process, strains transmitted from the sensor were first input into the NI USB-9237 (Bridge and Strain Measurement Module), which provides a USB interface for four channels of 24-bit half/full-bridge analog input, and then connected to the laptop computer in order to record the strain signals using NI LabVIEW software. Finally, the recorded strains were converted to 3-axis forces according to the calibration relation between forces and corresponding strains.

4.1 Influence of draw angle and tool path on forming forces

The influence of the part draw angle and the type of tool path on resultant forming forces was compared by forming truncated cones

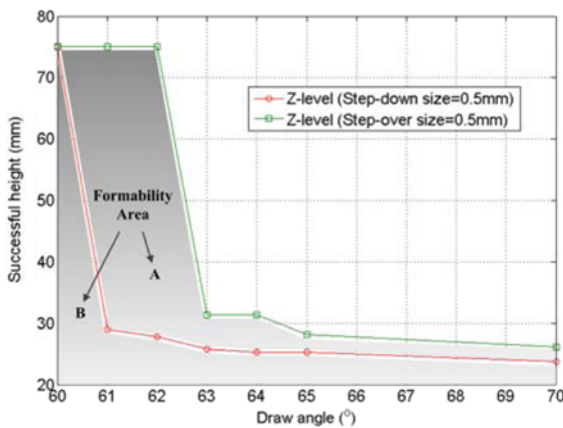


Fig. 11 Influence of the z-level tool path with different incremental steps on formability vs the draw angle α

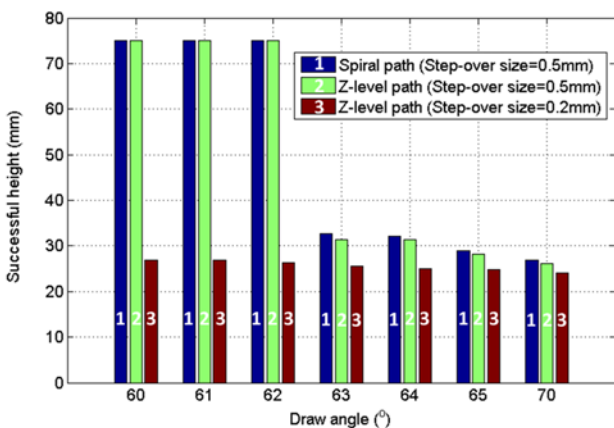


Fig. 12 The comparison of effects of spiral and z-level tool paths with incremental steps on formability vs the draw angle α

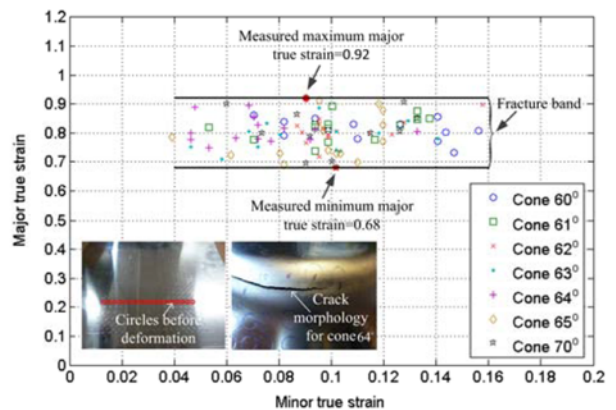


Fig. 13 Fracture forming limit diagram-experimental strains for truncated cones with different draw angles (z-level path with 0.2 mm step-over size) - The solid points correspond to maximum and minimum major true strains

with different draw angles (60° , 65° and 70°). AA7075-O sheet with 1.6 mm thickness was selected and the other experimental configuration is the same as described in the previous section. Fig. 15 shows the evolution of resultant forming forces with different draw angles for the spiral tool path. Different draw angles influence the formability. Only the truncated cone with the draw angle 60° was successfully formed. In this case, the trend of resultant force with forming time goes up first and then reaches a force peak and slightly decreases. After that the force increases again until the forming is finished. For the truncated cones with draw angles 65° and 70° , cracks happen before the forming goal is achieved. In these two cases, the resultant forces show the same trend as the case with the draw angle 60° in the initial stage (below 300 s). However, when the cracks appear, the forces drop down quickly. The crack for the draw angle 70° case happens earlier than the case with the draw angle 65° . In addition, as the draw angle increases, the peak force also increases in the initial stage.

Fig. 16 represents the evolution of resultant forming forces with different draw angles for the z-level tool path. Overall, the trend of resultant forming forces in Fig. 16 is quite similar to the force trend in Fig. 15. However, the maximum resultant forces in Fig. 16 are higher than those in Fig. 15 in the case with the same draw angle. In addition, the oscillation of the forces in Fig. 16 is more severe than the situations in Fig. 15. The reason is that the z-level tool path is not a continuous



Fig. 14 Sensor for the force measurement

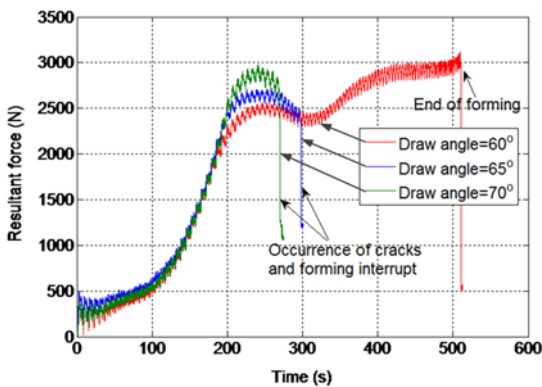


Fig. 15 Influence of three different draw angles on resultant forces with 1.6 mm sheet thickness, spiral tool path with 0.5 mm step-over size and 15 mm tool radius for AA 7075-O sheets (Cracks happen in the cases with draw angles 65° and 70°)

tool path. Large force peaks will occur at the transition points between two consecutive contours. Conversely, the spiral tool path is a continuous one and no transition points are involved, so the force evolution is smoother.

A geometry that is about to fail will experience an obvious force peak followed by a drop trend in force magnitude and then will develop fractures before achieving a minimum force level and slowly increasing again.¹⁴ Therefore, the slope of the force curve after the peak value may be seen as a forming failure prediction indicator. Some results have been obtained for AA3003-O sheets with the 1.2 mm thickness.¹⁴ In this study, the similar results have also been observed in terms of force slopes after peak values when using both spiral path and z-level path, seen in Figs. 15 and 16. Fig. 17 shows the calculated results of slopes for force curves after peak values for 1.6 mm thick AA7075-O sheets. It is noted that the slope decreases as the draw angle increases, which is in agreement with the previous results¹⁴ regardless of the types of the tool paths.

4.2 Influence of sheet thickness and step-down size of z-level tool path on forming forces

In this section, the influence of the sheet thickness and the step-down size of z-level tool path on forming forces was compared by

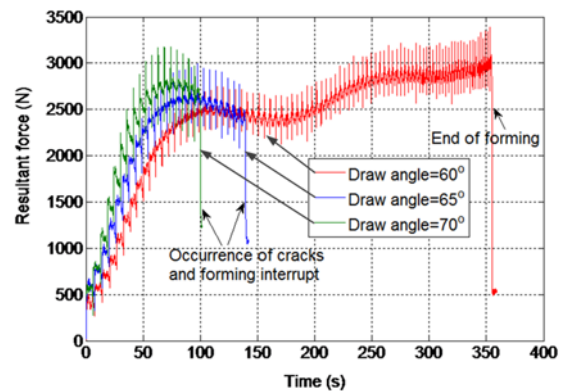


Fig. 16 Influence of three different draw angles on resultant forces with 1.6 mm sheet thickness, z-level tool path with 0.5 mm step-over size and 15 mm tool radius for AA 7075-O sheets (Cracks happen in the cases with draw angles 65° and 70°)

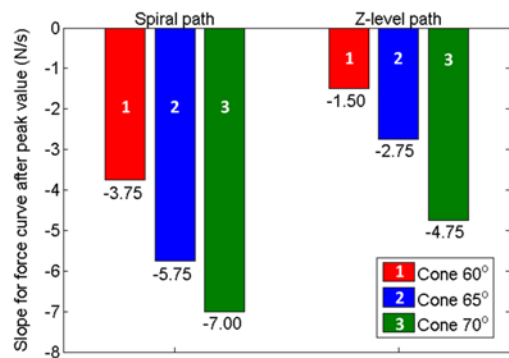


Fig. 17 Slopes for force curves after force peak values for both spiral and z-level tool paths

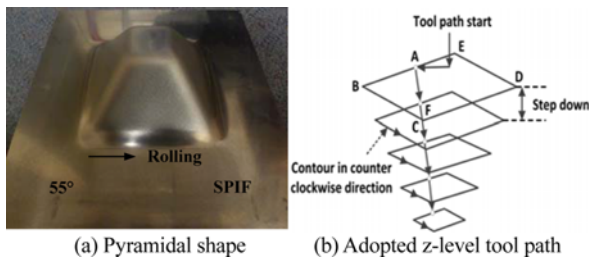
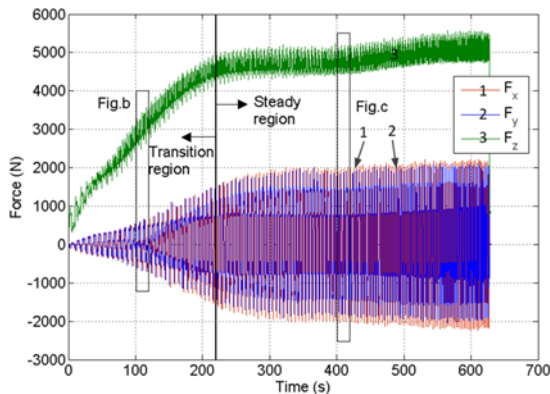
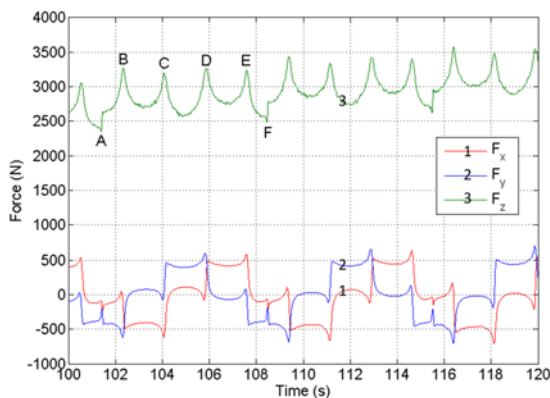


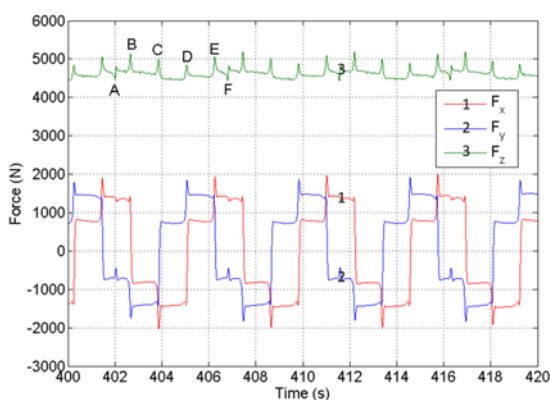
Fig. 18 Investigated benchmark shape and z-level tool path: (a) pyramidal shape (b) z-level tool path



(a) The whole forming process with three-axis forces



(b) One typical lap within a small time period in transition region



(c) One typical lap within a small time period in the steady region

Fig. 19 Three-axis forces for the truncated pyramid of draw angle 55° with 2.54 mm sheet thickness, z-level tool path with 0.5 mm step-down size and 15 mm tool radius for AA 7075-O sheets: (a) the whole forming process (b) one small time period with one typical lap in transition region (c) one small time period with one typical lap in steady region

forming pyramids using nine combinations of three sheet thicknesses (1.02 mm, 1.60 mm and 2.54 mm) and three step-down sizes (0.5 mm, 1.0 mm and 1.5 mm). Those pyramids, as shown in Fig. 18a, had a constant draw angle of 55° and a major base area of $140\text{ mm} \times 140\text{ mm}$. The size of sheet metal is $300\text{ mm} \times 300\text{ mm}$ and a square backing plate is utilized to increase rigidity between forming area and undeformed area. Other experimental parameters are the same as described in the previous sections. The tool movement can be described corresponding to points A-F shown in Fig. 18b. Firstly, the tool moves in the vertical direction with the desired pitch. Then, it moves along square path in the same direction. Once this square movement is finished, the tool moves and penetrates the sheet along the part surface and begins the next square movement.

Fig. 19(a) shows a time evolution of three-axial forces for a truncated pyramid of draw angle 55° with 2.54 mm sheet thickness and 0.5 mm step-down size. In all nine experiments, the shape of these curves is quite similar. So, the analysis is only focused on one case. The three-axial forces increase over the first initial period (approximate 220 s) and then the vertical force stabilizes to a relatively steady state. For x-axial and y-axial forces, they evolve in a periodic way but with almost the same amplitude. Fig. 19(b) shows a typical lap within a small time period in the transition region. As can be seen, points B, C, D and E are corresponding to four corners of the pyramid illustrated in Fig. 18(b). In the typical lap, four peaks of the vertical force can be observed corresponding to the four corners B, C, D and E. The trend of three-axis forming forces in the steady region in Fig. 19(c) is quite similar to that in the transition region.

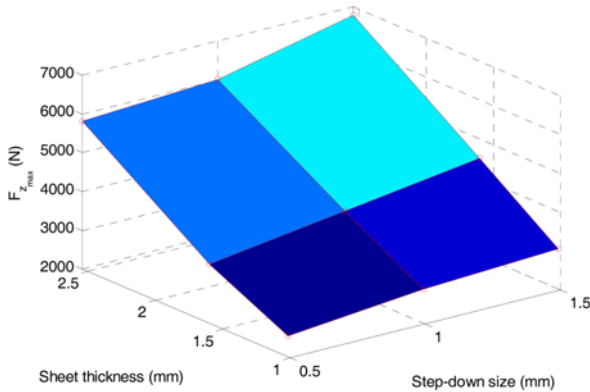
In order to compare all nine experiments, the maximum vertical forming force was plotted against the sheet thickness and the step-down size for each of the nine experiments on AA7075-O sheets in Fig. 20. Fig. 20(a) shows that the maximum vertical forming force increases in an approximately linear way with the sheet thickness. It also shows that the maximum vertical forming force increases as the step-down size increases. Fig. 20(b) represents the magnitude comparison of the maximum vertical forces in nine experiments. In these nine experiments, the biggest maximum vertical force is 6792.4 N with 2.54 mm thickness and 1.5 mm step-down size, which is a little more than twice that of the maximum vertical force (3038.8 N) in the case with 1.02 mm thickness and 1.5 mm step-down size. The similar trends can be also found in other cases. The explanation for this phenomenon would be that more deformation energy is required to deform thicker sheets. In addition, with bigger step-down size, more material is deformed in one step and more deformation energy is needed as well.

4.3 Influence of sheet orientation on vertical forming forces

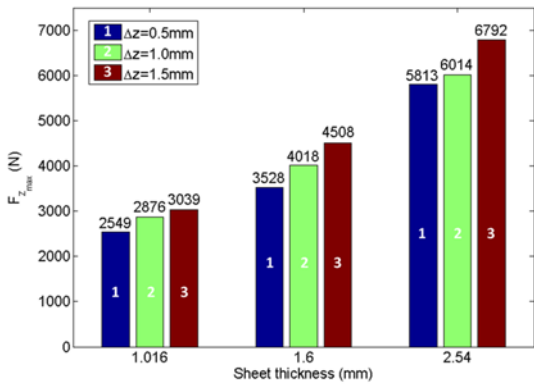
In this section, emphasis is laid on the influence of sheet orientation on vertical forming forces. The sheet was arranged at two orientations 0° and 45° by rotating the rolling direction when clamping the sheet. Fig. 21 shows the forming results with different sheet orientations.

Fig. 22 shows the vertical forming forces for sheet orientations 0° and 45° with 0.5 mm step-down size and 15 mm tool radius for three thicknesses. It is obvious that the vertical forces in the sheet orientation 45° are smaller than those in the sheet orientation 0° regardless of sheet thicknesses. This is due to the influence of different strain-hardening exponents in different orientations. The strain-hardening exponent is a

very significant parameter for sheet metal forming process.¹⁷ The higher its value, the greater will be the resistance of the material and the greater the absorption of strain, but the more force will be required to deform the material. Based on the calculated strain-hardening exponents with three directions for three different sheet thicknesses, the strain-hardening exponents in diagonal directions are smaller than those in rolling and transverse directions. This illustrates the reason why vertical forces in sheet orientation 45° are found to be smaller than those in the sheet orientation 0°.

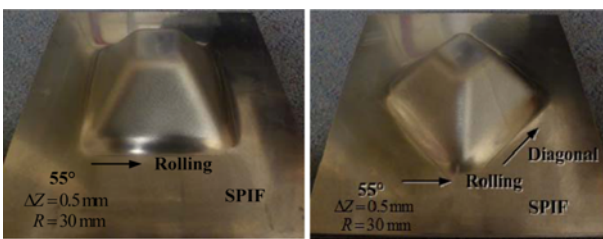


(a) The relationship of the sheet thickness and the step-down size with the maximum vertical forces



(b) The magnitude comparison of the maximum vertical forces in nine experiments

Fig. 20 The influence of sheet thickness and step-down size on vertical forming force of truncated pyramid with 55° draw angle in SPIF: (a) the relationship of sheet thickness and step-down size with maximum vertical forces (b) the comparison of the maximum vertical forces in nine experiments



(a) (b)

Fig. 21 Forming results with different sheet orientations (a) 0 degree (b) 45 degree

5. Conclusions

In this study, an experimental campaign has been carried out to deform AA7075-O aluminum alloy sheets by incremental forming. Basic material properties have been acquired to clarify the material behavior using tensile tests. Formability and forming forces are evaluated to understand the forming process mechanism. Some conclusions can be drawn as follows:

(1) The phenomenon of anisotropy increases as the sheet thickness increases. The strain-hardening exponent in diagonal direction is smaller than that in rolling direction and transverse direction for all three thicknesses.

(2) In terms of formability, spiral and z-level tool paths have no significant difference when forming the same part. For the z-level tool path, formability can increase as step-over (or step-down) size increases (0.2 mm vs 0.5 mm). However, more tests involving a wide range of step-over (step-down) sizes need to be performed to further demonstrate this conclusion in the future.

(3) The maximum draw angle can be considered as a formability indicator, but other geometrical design parameters, such as the part height, also play a role on formability. A safety formability zone has been given for the truncated cone forming. Furthermore, a fracture forming limit diagram has been derived to characterize the material formability. A fracture band was obtained with maximum major true strain (0.92) and minimum major true strain (0.68).

(4) For spiral and z-level tool paths, the overall trend of resultant force is similar. However, the evolution force curve for the spiral tool path is smoother than that for the z-level tool path. In addition, the slope of force curve after peak value can be seen as a forming failure prediction indicator. The slope decreases as the draw angle increases. This provides an approach to on-line control and failure detection of incremental forming.

(5) The maximum vertical force increases as the step-down size increases. In addition, the maximum vertical force increases in an approximately linear way with the increase in the sheet thickness. This is expected due to greater deformation forces. The measured biggest vertical force is 6792.4 N with 2.54 mm sheet thickness and 1.5 mm step-down size.

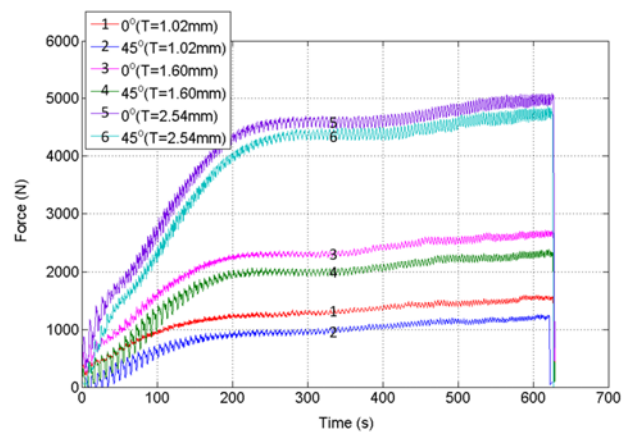


Fig. 22 Vertical forming forces for two sheet orientations (0 degree and 45 degree) with 0.5 mm step-down size and 15 mm tool radius for AA 7075-O sheet (T = thickness)

(6) The influence of sheet orientations on the forming force is first considered in incremental forming. Results have shown that the vertical force is found to be smaller in the sheet orientation 45° compared with that in the sheet orientation 0° due to the smaller strain-hardening exponents in diagonal directions.

This study provides a further insight into how to successfully deform 7075-O aluminum sheets into a 3D shell product by ISF. The process formability is not only affected by geometrical parameters (draw angle and part height), but also by different tool paths and incremental step-down sizes. In addition, forming force, as a process quantity, can be monitored to develop a closed-loop on-line control and failure detection system for product quality improvement. Vertical forming forces can be noticeably reduced when forming a part along the sheet diagonal direction due to the smaller strain-hardening exponent.

ACKNOWLEDGEMENT

This research was supported by the ARC Linkage Program, Boeing Research and Technology Australia and QMI Solutions in Australia. The authors are specifically grateful for the insights and assistance from Michael Elford BRTA and Sara Eastwood QMI.

REFERENCES

1. Tajally, M. and Emadoddin, E., "Mechanical and anisotropic behaviours of 7075 aluminum alloy sheets," *Materials and Design*, Vol. 32, No. 3, pp. 1594-1599, 2011.
2. Molladavoudi, H. R. and Djavanroodi, F., "Experimental study of thickness reduction effects on mechanical properties and spinning accuracy of aluminum 7075-O, during flow forming," *International Journal of Advanced Manufacturing Technology*, Vol. 52, No. 9-12, pp. 949-957, 2011.
3. Rikhtegar, F. and Ketabchi, M., "Investigation of mechanical properties of 7075 Al alloy formed by forward thixoextrusion process," *Materials and Design*, Vol. 31, No. 8, pp. 3943-3948, 2010.
4. Kitazawa, K., Wakabayashi, A., and Murata, K., "Metal flow phenomena in computerized numerically controlled incremental stretch-expanding of aluminum sheets," *Japanese Journal of Institute of Light Metals*, Vol. 46, No. 2, pp. 65-70, 1996.
5. Liu, Z. B., Li, Y. L., and Meehan, P. A., "Vertical wall formation and material flow control for incremental sheet forming by revisiting multistage deformation path strategies," *Materials and Manufacturing Processes*, Vol. 28, No. 5, pp. 562-571, 2013.
6. Manco, L., Filice, L., and Ambrogio, G., "Analysis of the thickness distribution varying tool trajectory in single-point incremental forming," *Proc. of the Institution of Mechanical Engineers Part B: Journal of Engineering Manufacture*, Vol. 225, No. 3, pp. 348-356, 2011.
7. Centeno, G., Silva, M. B., Cristino, V. A. M., Vallellano, C., and Martins, P. A. F., "Hole-flanging by incremental sheet forming," *International Journal of Machine Tools and Manufacture*, Vol. 59, pp. 46-54, 2012.
8. Dejardin, S., Thibaud, S., Gelin, J. C., and Michel, G., "Experimental investigations and numerical analysis for improving knowledge of incremental sheet forming process for sheet metal parts," *Journal of Materials Processing Technology*, Vol. 210, No. 2, pp. 363-369, 2010.
9. Jeswiet, J., Micari, F., Hirt, G., Bramley, A., Duflou, J., and Allwood, J., "Asymmetric single point incremental forming of sheet metal," *CIRP Annals - Manufacturing Technology*, Vol. 54, No. 2, pp. 88-114, 2005.
10. Emmens, W. C., Sebastiani, G., and Van den Boogaard, A. H., "The technology of Incremental Sheet Forming-A brief review of the history," *Journal of Materials Processing Technology*, Vol. 210, No. 8, pp. 981-997, 2010.
11. Filice, L., Fratini, L., and Micari, F., "Analysis of material formability in incremental forming," *CIRP Annals- Manufacturing Technology*, Vol. 51, No. 1, pp. 199-202, 2002.
12. Young, D. and Jeswiet, J., "Forming limit diagrams for single point incremental forming of aluminum sheet," *Proc. of the Institution of Mechanical Engineers Part B: Journal of Engineering Manufacture*, Vol. 219, No. 4, pp. 359-364, 2005.
13. Durante, M., Formisano, A., and Langella, A., "Observations on the influence of tool-sheet contact conditions on an incremental forming process," *Journal of Materials Engineering and Performance*, Vol. 20, No. 6, pp. 941-946, 2011.
14. Duflou, J. R., Tunçkol, Y., Szekeres, A., and Vanherck, P., "Experimental study on force measurements for single point incremental forming," *Journal of Materials Processing Technology*, Vol. 189, No. 1-3, pp. 65-72, 2007.
15. Jackson, K. P., Allwood, J. M., and Landert, M., "Incremental forming of sandwich panels," *Journal of Materials Processing Technology*, Vol. 204, No. 1-3, pp. 290-303, 2008.
16. Jeswiet, J., Duflou, J. R., and Szekeres, A., "Forces in single point and two point incremental forming," *Advanced Materials Research*, Vol. 6-8, pp. 449-456, 2005.
17. Folle, L. F., Netto, S. E. S., and Schaeffer, L., "Analysis of the manufacturing process of beverage cans using aluminum alloy," *Journal of Materials Processing Technology*, Vol. 205, No. 1-3, pp. 347-352, 2008.

4.1.1 Process Formability and Forming Forces

Paper B

Experimental study and efficient prediction on forming forces in incremental sheet forming

Li, Y.L., **Liu, Z.B.**, Lu, H.B., Daniel, W.J.T., Meehan, P.A.

Advanced Materials Research

2014, Volume: 939, Pages: 313-321.

Experimental Study and Efficient Prediction on Forming Forces in Incremental Sheet Forming

Yanle Li^{1, a}, Zhaobing Liu^{1, b}, Haibo Lu^{1, c}, W.J.T (Bill) Daniel^{1, d}
and Paul A. Meehan^{1, e}

¹School of Mechanical & Mining Engineering, University of Queensland, St Lucia, Brisbane, QLD 4072, Australia

^ayanle.li@uq.edu.au, ^bz.liu7@uq.edu.au, ^ch.lu2@uq.edu.au, ^dbilld@uq.edu.au, ^emeehan@uq.edu.au

Keywords: Incremental sheet forming, forming force, formability, prediction

Abstract. Incremental sheet forming (ISF) is a promising forming process in which complex 3D shapes are formed from a sheet of metal using a simple moving tool. The efficient prediction of contact forces in ISF is desirable to monitor the forming process, prevent failure, and implement on-line control and process optimization. However, traditional Finite Element (FE) simulation used for force prediction is significantly time-consuming for complex products. The purpose of this study is to investigate the ISF force prediction and characteristics under different forming conditions and build a potential efficient model.

In the present work, forces during the cone forming process with different wall angles and step down sizes were recorded and compared. Different force trends were identified and discussed with reference to bending and strain hardening mechanics. Influences of different parameters on designated formability were also qualified which should benefit the product design process. An efficient predictive model based on upper-bound approach was applied for force prediction in this case. Predicted tangential forces were then compared with the experimental results showing relatively good agreement. The limits of the proposed model were also identified and the potential of future improvements were suggested.

Introductions

Incremental Sheet Forming (ISF) technology is an emerging forming process ideal for rapid prototype and small batch production. In an ISF process, a flat metal sheet is gradually formed into the designed 3D shape using Computer Numerical Control (CNC)-controlled generic tool stylus. The process is highly flexibility such that complex shapes can be achieved with tool path programming and sometimes with the support of a die. Therefore, ISF was widely accepted as a promising forming process over conventional processes such as deep drawing and stamping [1-3] for small batch production. However, one of the dominant limits for the further development and commercialization of ISF technology is the limited geometrical accuracy of the final shape [4-6]. Although various strategies [7, 8] have been proposed to obtain a better product quality, a systematic understanding of the contact mechanics and further investigation on the forming force are essential to achieve this goal.

In ISF, the blank sheet is incrementally formed to its final shape via a small deformation zone in the vicinity of the forming tool, leading to lower forming forces than traditional processes, such as deep drawing. Additionally, unlike traditional forming processes, the size of the desired part does not affect the forming forces [9]. The characterization and prediction of the forming forces is essential for tool design and to determine the necessary power of the machine. The forming force also provides key insight into the deformation mechanics of the process. Filice and Ambrogio [10, 11] worked on the force measurement and analysis and classified the force trends of tangential force into three types: steady state force trends, polynomial force trends and monotonically decreasing force trends. It was also concluded that the force gradient after the peak can be effectively considered as a critical indicator to detect and prevent workpiece fracture. Therefore, forming force is a potential indicator for forming limits identification. Petek et al. [12] proposed an autonomous on-line system for fracture

identification and localization by analyzing the reaction force with skewness function. Another failure criterion presented by Fiorentino [13] is also based on force monitoring during the forming process. This approach was achieved by comparing the stresses acting on the material calculated from forming forces with the ultimate strength of the material. Additionally, G. Ingarao et al. [14] investigated recorded force data to calculate and evaluate the energy consumption required for the ISF process.

The lack of an efficient predictive force model limits the development of ISF technology in many aspects including on-line control, failure prevention and process optimization. Iseki [15] obtained the forming forces for the incremental forming of a pyramid using an approximated deformation analysis. Aerens et al. [16] studied the incremental forming of truncated cones with different materials using experimental and statistical analyses. They proposed regression formulae to predict the triple forming force components including axial, radial, and tangential components from input variables including wall angle, initial thickness, tool diameter, and vertical pitch. Finally, an approximate formula was deduced for predicting the axial component for forming any material based on the tensile strength only. Unlike other mentioned work for predicting the forming forces acting on the tool, Mirnia [17] proposed a new approach to predict the tangential force on a truncated cone using an assumed deformation zone and the upper-bound analysis. It was reported that the forces were in good agreement with those from the experimental work of Aerens et al. [16]. Nevertheless, this model can only predict tangential force and further experimental validation for different materials is needed.

In this paper, the following research tasks are tackled, and related results are reported:

- An accurate force measurement method was implemented on an ISF CNC machine. The trend of the forming force was identified and analyzed.
- The effects of wall angle and step down size on the forming forces and formability was investigated.
- A potential computationally efficient method to predict forming force for this case was investigated.

Experiments

To facilitate the study of the effect of product geometry and step down size on the forming force and formability, truncated cones with different wall angles are selected as the target shapes.

Equipment Setup. The forming tests have been performed on a state-of-the-art machine designed dedicated for the ISF process by Amino Corporation which can be numerical controlled by a FANUC controller (Fig. 1). The hemispherical tool with a diameter of 30 mm was used to deform the material. The tip of the tool is tungsten carbide and the body is made of K110 steel which was hardened and tempered to HRC60. The sheet material used in the present study was aluminum 7075-O sheet and has been cut into 300 mm × 300 mm in size with 1.016mm in thickness.

The forming forces acting on the forming tool have been measured continuously over time during the process. There are several ways to capture the forming force, such as the cantilever sensor designed by Jeswiet [18] and force dynamometer used by Duflou et al. [19]. In the present work, three full Wheatstone bridges have been designed and mounted on the 30 mm hemispherical tool. Each bridge was configured by four strain gauges and designed to measure one of the three orthogonal forces: two bending directions (F_x and F_y), and one axial direction (F_z). The strain gauges were calibrated twice in all three directions by applying a known force to get an accurate result. The calibrated system shows a rather linear relation between strain and output voltage.

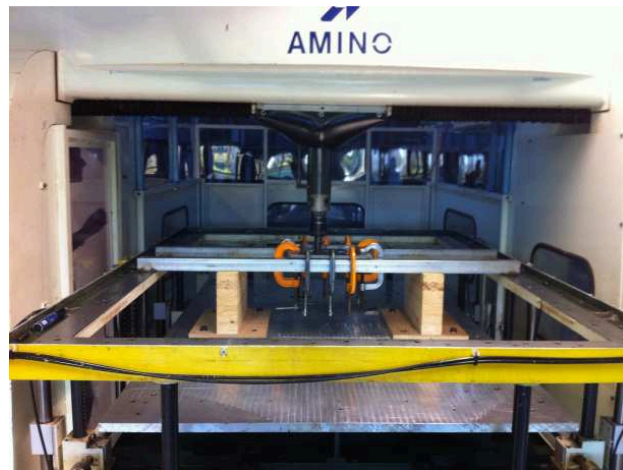


Fig. 1 Incremental sheet forming on Amino machine

Fig. 2 shows the experimental configuration and a case study of a truncated cone formed by Amino CNC machine. The truncated cones are formed in a stepwise way with many contours. The vertical distance between two consecutive contours is defined as step down (Δz). The angle between the deformed sheet to the horizontal plan is defined as wall angle (α).

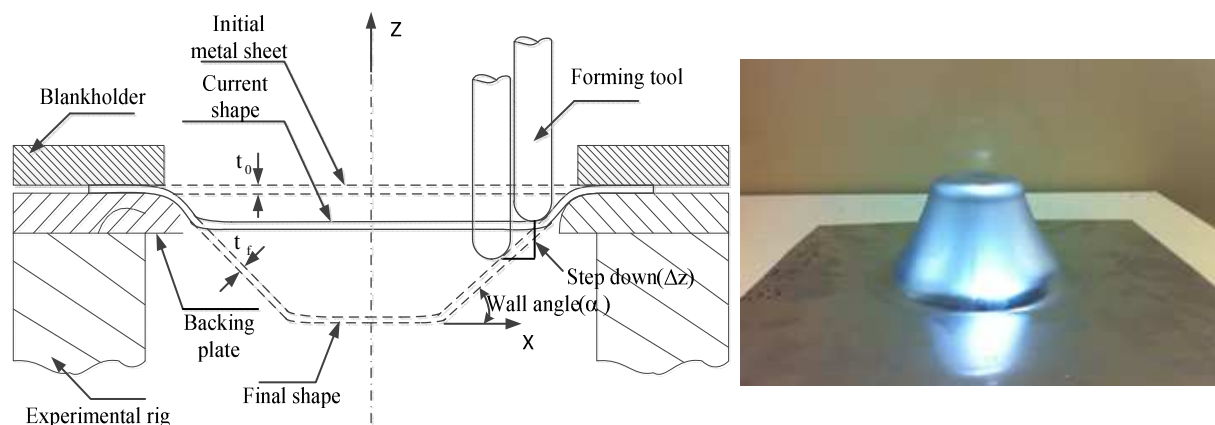


Fig. 2 Sketch of ISF experimental parameters and a case study made from Al 7075 of 1.6 mm in thickness.

Experimental Tests. Lubricant (oil-Shell Tellus Oil 68) was sprayed on the blank before forming to prevent excessive friction. A backing plate was utilized underneath the sheet in order to increase the rigidity between the forming area and sheet flange. The feed rate of forming tool was set to 4000 mm/min. For the tool path strategy, Z-level tool path with different vertical step-down size (Δz , the increment between two successive passes) were utilized. All the cones were designed with the same major diameter of 140 mm and smaller cone height should be defined for smaller inclination of the wall due to the geometric constraint. The tests were conducted until the crack of the sheet and the forming forces for all the three components (F_x , F_y and F_z) were recorded continuously during this process. The detailed tests parameters are listed in Table 1 and Table 2.

Table 1 Experimental design for different wall angles

Wall angle α (Degree)	Step down Δz (mm)	Tool diameter (mm)	Thickness (mm)	Feed rate (mm/min)	Designed height (mm)
30	0.5	30	1.6	4000	28
40	0.5	30	1.6	4000	40
50	0.5	30	1.6	4000	60
60	0.5	30	1.6	4000	75
62	0.5	30	1.6	4000	75

63	0.5	30	1.6	4000	75
65	0.5	30	1.6	4000	75
70	0.5	30	1.6	4000	75

Table 2 Experimental design for different step down sizes

Wall angle α (Degree)	Step down Δz (mm)	Tool diameter (mm)	Thickness (mm)	Feed rate (mm/min)	Designed height (mm)
60	0.1	30	1.6	4000	75
60	0.2	30	1.6	4000	75
60	0.3	30	1.6	4000	75
60	0.4	30	1.6	4000	75
60	0.5	30	1.6	4000	75
60	0.7	30	1.6	4000	75
60	1.0	30	1.6	4000	75

Efficient Model for Force Prediction

In this model, the upper-bound approach [17] is used to analysis the deformation behavior and predicts the tangential force of the truncated cone during ISF process. The deformation zone is estimated according to the tool path and tool radius and defined as Bezier curves which can be tailored by adjusting two presupposed parameters. The velocity field and the dissipated power of the process are then expressed with optimizable parameters. Then the tangential force is obtained by minimizing the dissipated power using upper-bound solution according to the assumptions made in literature [17]. This analytical model was recomposed and implemented using MATLAB. In order to confirm the performance of the recomposed efficient MATLAB model, the predicted tangential forces with different forming parameters were compared with the experimental results. The measured forces (F_x and F_y) need to be converted to tangential (F_t) and radial components (F_r) to make sure the comparison is effective. The same methodology presented in [16] are used here to achieve the conversion.

Results and Discussion

Force Trend in ISF. Fig. 3 presents the record of the three components forces all over the process versus time ($\alpha = 60^\circ$, $\Delta z = 0.5$ mm) with a detailed view in two steady segments on the top. In one cycle, F_x and F_y forces change in a sinusoidal way between their maximum and minimum values due to the current tool position relative to the global absolute axis around a contour of the truncated cone. In contrast with horizontal forces, vertical force only experienced some small fluctuations in the final steps caused by the Z-level tool path. The amplitude of the forces experienced an increasing trend during the first half process and tends to become steady for the rest of the process. This occurs due to a number of reasons. Firstly, the initial increase of the forming forces could be caused by the bending mechanism [11]. Then, with the build-up of the contact area between tool head and the sheet surface, the force required to deform the sheet also increased. Additionally, the following rise can be assigned to the continuous stretching of the material which has been examined by Allwood et al [20]. The stretching would result in the increase of the forming force caused by the strain hardening of the material. However, thinning of the material would reduce the magnitude of the force. Therefore, the later contour loops of the forming force are determined by the combined effects of strain hardening and thinning.

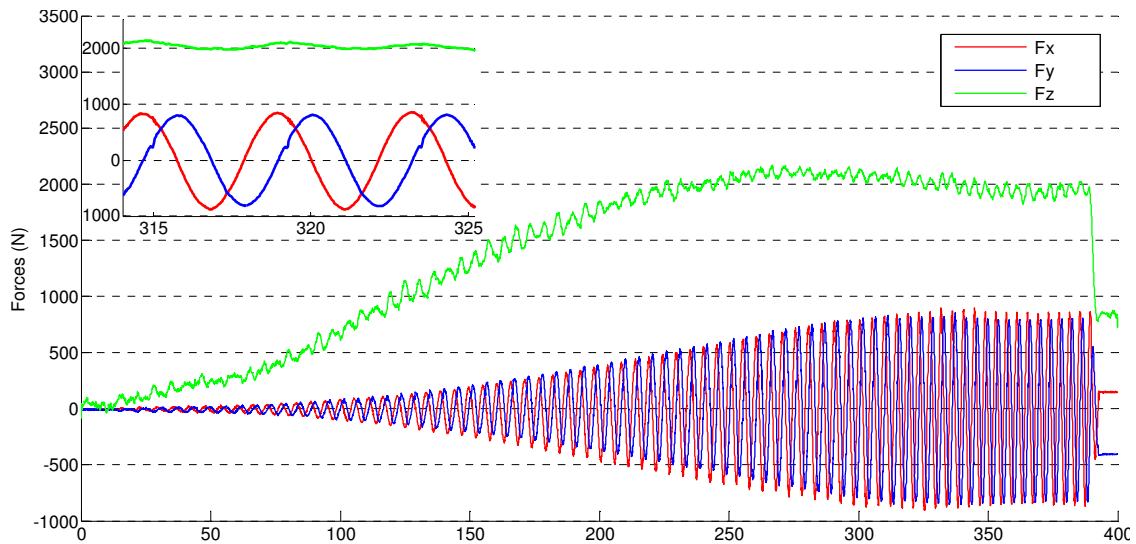


Fig. 3 Three force components (F_x , F_y and F_z) versus forming time and a detailed view for two cycles during forming a cone.

Effect of Wall Angle. To study the effect of wall angles on the forming force, the forming trends of vertical forces at the varying of wall angle from 30° to 70° are plotted in Fig. 4. For small wall angles under 60° , the vertical forces reach the turning point at the forming depth of around 30 mm and then keep rising slowly until the end of the process. The magnitudes of F_z for these cases at the same depth approximately have the same value. On the contrary, the force trends are recorded in a different fashion for wall angles larger than 60° . The forces quickly register their peak values at a depth of around 12 mm and then decrease monotonically towards process completion/failure. The achievements of steady conditions are delayed with small wall angles. This is because with a smaller wall angle, the sheet undergoes a longer bending mechanism before the occurrence of strain hardening. By carefully checking of these cases, one can concluded that if the material work hardening plays a dominant role to compensate sheet thinning, the force could remain steady and avoid fracture. Otherwise, if thinning prevails, the forces drop quickly which indicates the failure of the material. If appropriate statistical analysis can be performed to calculate the force gradient after peak value, this could possibly be considered as an effective indicator for failure prediction.

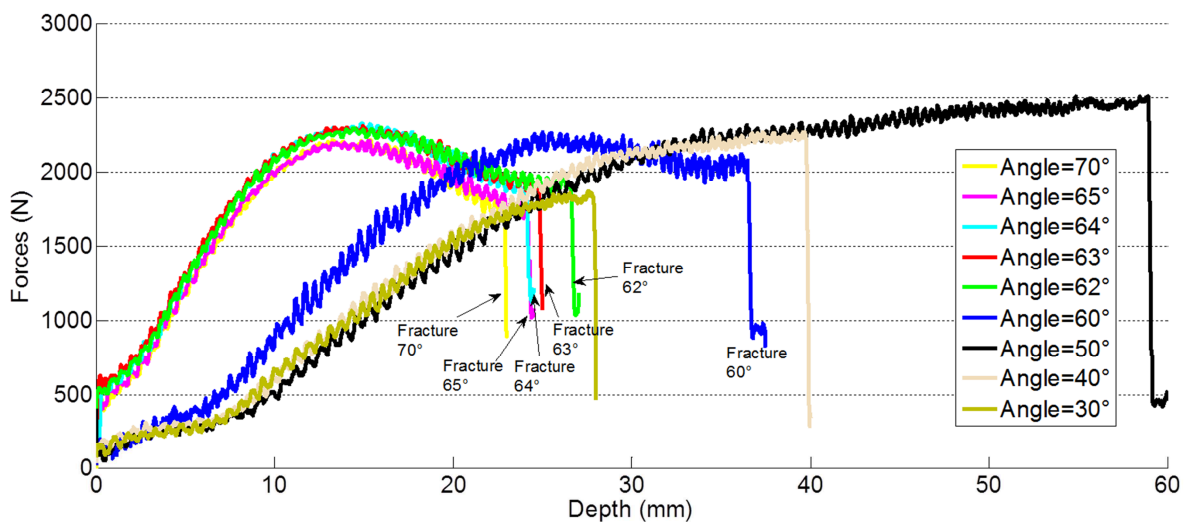


Fig. 4 Vertical force trend with the varying of wall angle (fracture parts are marked).

The variations of the peak values for forces in Y direction (F_{yp}) and vertical direction (F_{zp}) as a function of the wall angle (α) are shown in Fig. 5. It can be seen that with the increase of wall angle from 30° to 70° , F_{zp} has its maximum value when the cone with the angle of 50° is being formed.

Interestingly, if we plot the curve $(\alpha * \cos \alpha)$ scaled by an appropriate factor in the same figure, it can be found that the trend of F_{zp} is similar with curve $(\alpha * \cos \alpha)$. According to the sine law of sheet thinning [21], $\cos \alpha$ is used to calculate the wall thickness of the sheet after deformation. Therefore, it could be inferred that F_{zp} is positive proportional to the inclination of the wall angle and also the thickness of the deformed sheet metal. In the case of the horizontal force F_{yp} , a linear increase can be observed with the increase of wall angle. The equation of the linear regression and its coefficient of determination R^2 are also presented.

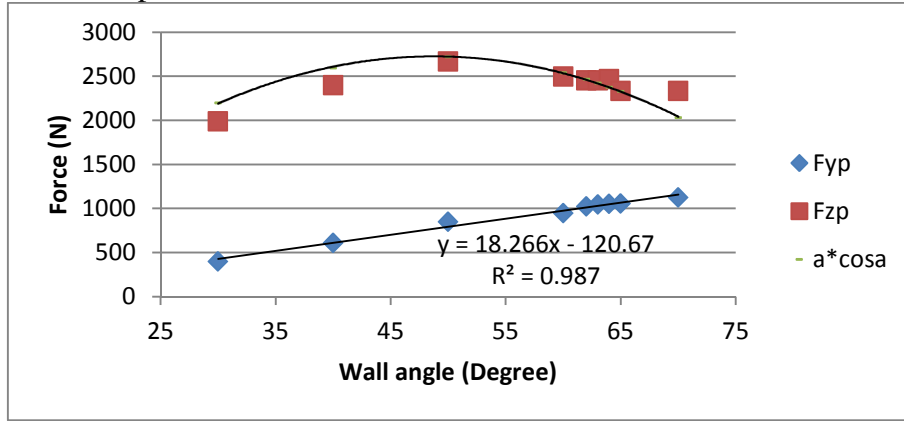


Fig. 5 Variations of forming forces with different wall angles.

The formability of the material can be assessed with various approaches [22, 23]. The traditional way is based on the measurement of the main strain values of a series of parts formed under different deformation conditions. Generally, the definition of forming limits in this way is time consuming and not economical. Moreover, forming limit in ISF would change if different process parameters are used. Therefore, the maximum formable wall angle or forming depth is used directly as an alternative way to evaluate the formability at a given forming condition in the current work. As listed in Table 1, the designed heights of the cones for 30°, 40° and 60° are 28 mm, 40 mm and 60 mm due to the limits of minor diameter, respectively. These three parts are formed successfully without fracture because the thinning of the sheet is relatively light under the forming limit of the material. With the increase of the wall angle from 60° to 70°, the achievable forming depth reduces slightly from 37.5 mm to 23 mm. These tests can provide useful information for preliminary design for the shape to avoid the risk of failure and improve the stability of the final product.

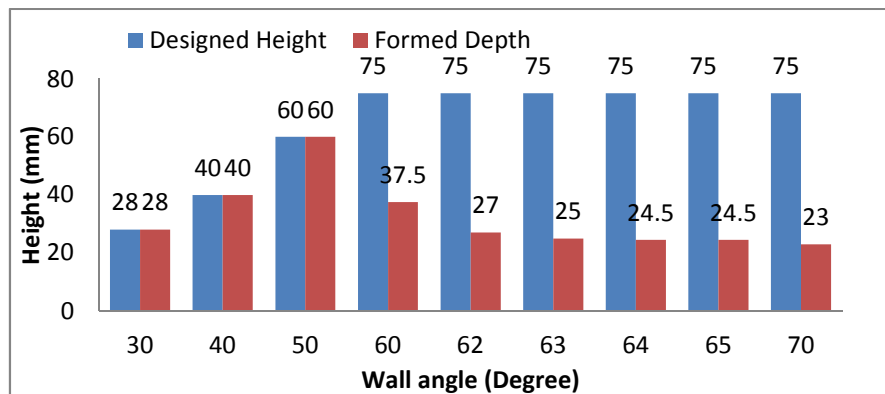


Fig. 6 Formed depth with different wall angles.

Effect of Step Down. A set of experiments has also been performed with different step down sizes (Δz) range from 0.1 mm to 1.0 mm. The evolution histories of the vertical force F_z at the varying of step down sizes are presented in Fig. 7. It can be noticed that at the former stage, the vertical forces for big Δz (0.7 and 1.0 mm) shows smaller values compared with forces with little step down sizes. However, after a depth of 40 mm, the F_z values present a limited decrease and then increase until the

part is successfully formed. From Fig. 7, we can see that only the parts with Δz of 0.7 and 1.0 mm are formed successfully and the fracture occurs earlier with lower step down size. This can be explained by the fact that smaller Δz values lead to closer tool punch passes. In particular, with small Δz , the amount of already hardened material which is deformed by the tool punch in each pass is higher; therefore, the stress required for the deformation raises. As a result of the higher stress state induced in the material, the sheet formability is reduced.

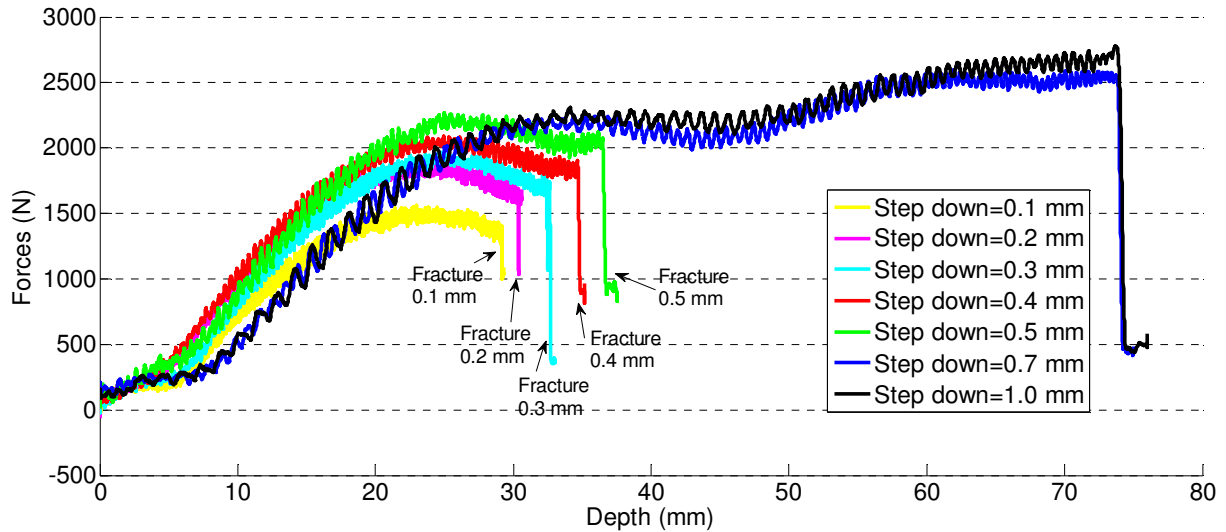


Fig. 7 Vertical force trend with the varying of step down size (fracture parts are marked).

The maximum values of F_{yp} and F_{zp} are plotted in Fig. 8. The figure shows that both F_{yp} and F_{zp} increase with step down size. More specifically, the relation between peak forces and Δz can be approximated as a linear function.

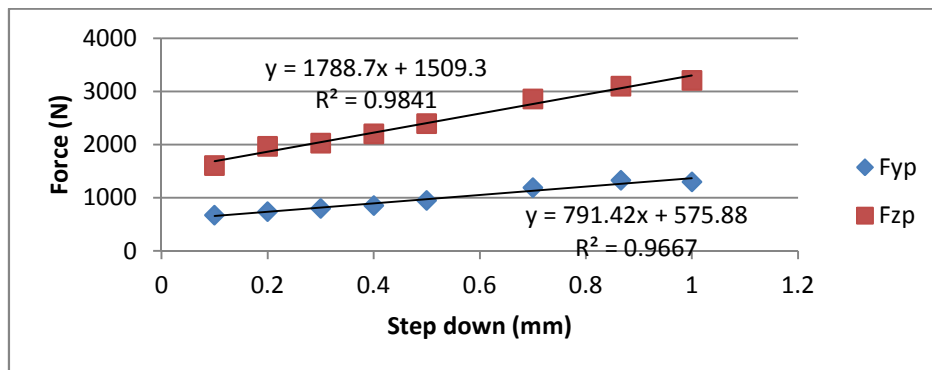


Fig. 8 Variations of forming forces with different step down sizes.

Comparison of the Modeling and Experimental Results

Tangential forces converted from measured results and the predicted values are plotted in Fig. 9. By comparison, the current model can provide good agreement with experimental results for the cases with small step down sizes (below 0.5 mm). The larger deviations for larger step down sizes may be due to the inherent limits existing in the present model. Firstly, the analytical model is based on the assumption that no material flow occurs in the radial direction. Therefore, only transverse shear strains of the deformed elements are considered and no stretching behavior is taken into account along the radial component. However, stretching which causes membrane strain is one of the significant mechanics in some experimental tests [24] and Finite Element simulations [25]. Secondly, the deformation zone is represented by Bezier curves which may be larger than the actual deformed area, resulting in the higher force value. Furthermore, the assumption that the non-contact regions of

the sheet are considered as rigid material may also cause the over prediction of the force. To provide further insight into these above limits, a complete strain analysis of the deformed region which includes membrane strains could be performed.

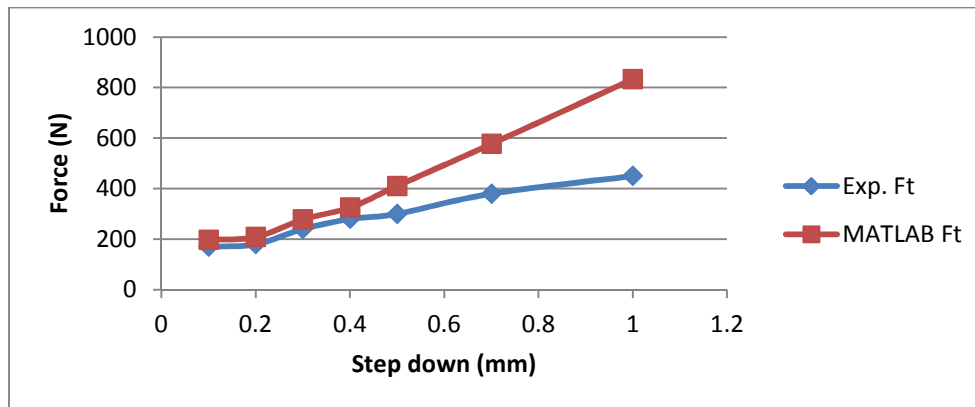


Fig. 9 Comparison between MATLAB model and experimental values.

Conclusion

- Forming forces have been successfully measured on a benchmark ISF case by means of strain gauges and provide useful information to understand the forming process. By analyzing the development of the force, it can be concluded that the forces are attributed to the bending effect of the sheet in the former stage but the combined effects of sheet thinning and strain hardening appear to be important in the second half of the process.
- From the experimental results, by varying wall angles from 30 ° to 70°, the maximum vertical force was observed for the cone with 50° wall angle; while the maximum horizontal forces F_{yp} present a linear growth with the increase of wall angle. Large values of step down size would cause the increase of both vertical and horizontal forces. In the investigated range, a small wall angle and big step down size should be selected to achieve a better formability in terms of forming depth.
- An efficient force prediction model based on upper-bound approach is presented and good agreement is achieved within a limited step down size compared with experimental results. The limitations of the current model are identified for future work.

Acknowledgements: The present work was supported by Australian Research Council (ARC) Linkage project.

References

- [1] J. Jeswiet, F. Micari, G. Hirt, A. Bramley, J. Duflou, J. Allwood, Asymmetric single point incremental forming of sheet metal, *Annals of CIRP—Manufacturing Technology*, 54 (2005) 623-649.
- [2] S.B.M. Echrif, M. Hrairi, *Research and Progress in Incremental Sheet Forming Processes, Materials and Manufacturing Processes*, 26 (2011) 1404-1414.
- [3] B.T. Araghi, A. Göttmann, M. Bambach, G. Hirt, G. Bergweiler, J. Diettrich, M. Steiners, A. Saeed-Akbari, Review on the development of a hybrid incremental sheet forming system for small batch sizes and individualized production, *Production Engineering*, 5 (2011) 393-404.
- [4] K. Essa, P. Hartley, An assessment of various process strategies for improving precision in single point incremental forming, *International Journal of Material Forming*, 4 (2011) 401-412.
- [5] F. Micari, G. Ambrogio, L. Filice, Shape and dimensional accuracy in Single Point Incremental Forming: State of the art and future trends, *Journal of Materials Processing Technology*, 191 (2007) 390-395.

- [6] J.R. Duflou, B. Lauwers, J. Verbert, Study on the Achievable Accuracy in Single Point Incremental Forming, in, Springer Berlin Heidelberg, Berlin, Heidelberg, 2007, pp. 251-262.
- [7] R. Malhotra, J. Cao, F. Ren, V. Kiridena, Z. Cedric Xia, N.V. Reddy, Improvement of Geometric Accuracy in Incremental Forming by Using a Squeezing Toolpath Strategy With Two Forming Tools, *Journal of Manufacturing Science and Engineering*, 133 (2011) 61019.
- [8] J.R. Duflou, J. Verbert, B. Belkassen, J. Gu, H. Sol, C. Henrard, A.M. Habraken, Process window enhancement for single point incremental forming through multi-step toolpaths, *CIRP Annals - Manufacturing Technology*, 57 (2008) 253-256.
- [9] P.A.F. Martins, N. Bay, M. Skjoedt, M.B. Silva, Theory of single point incremental forming, *CIRP Annals - Manufacturing Technology*, 57 (2008) 247-252.
- [10] L. Filice, G. Ambrogio, F. Micari, On-Line Control of Single Point Incremental Forming Operations through Punch Force Monitoring, *CIRP Annals - Manufacturing Technology*, 55 (2006) 245-248.
- [11] G. Ambrogio, L. Filice, F. Micari, A force measuring based strategy for failure prevention in incremental forming, *Journal of Materials Processing Technology*, 177 (2006) 413-416.
- [12] A. Petek, K. Kuzman, B. Suhač, Autonomous on-line system for fracture identification at incremental sheet forming, *CIRP Annals - Manufacturing Technology*, 58 (2009) 283-286.
- [13] A. Fiorentino, Force-based failure criterion in incremental sheet forming, (2013) 1-7.
- [14] G. Ingarao, G. Ambrogio, F. Gagliardi, R. Di Lorenzo, A sustainability point of view on sheet metal forming operations: material wasting and energy consumption in incremental forming and stamping processes, *Journal of Cleaner Production*, 29-30 (2012) 255-268.
- [15] H. Iseki, An approximate deformation analysis and FEM analysis for the incremental bulging of sheet metal using a spherical roller, *Journal of Materials Processing Technology*, 111 (2001) 150-154.
- [16] R. Aeren, P. Eyckens, A. Van Bael, J.R. Duflou, Force prediction for single point incremental forming deduced from experimental and FEM observations, *The International Journal of Advanced Manufacturing Technology*, 46 (2010) 969-982.
- [17] M.J. Mirnia, B.M. Dariani, Analysis of incremental sheet metal forming using the upper-bound approach, *Proceedings of the Institution of Mechanical Engineers, Part B: Journal of Engineering Manufacture*, (2012).
- [18] J.R.D. J. Jeswiet, Alexander Szekeres, Forces in Single Point and Two Point Incremental Forming, *Advanced Materials Research*, 6-8 (2005) 449-456.
- [19] J. Duflou, Y. Tunçkol, A. Szekeres, P. Vanherck, Experimental study on force measurements for single point incremental forming, *Journal of Materials Processing Tech*, 189 (2007) 65-72.
- [20] J. Allwood, D. Shouler, A.E. Tekkaya, The increased forming limits of incremental sheet forming processes, *Key Engineering Materials*, 344 (2007) 621-628.
- [21] B. Avitzur, C.T. Yang, Analysis of Power Spinning of Cones, *Journal of Engineering for Industry*, 82 (1960) 231.
- [22] R. Uppaluri, N. Venkata Reddy, P.M. Dixit, An analytical approach for the prediction of forming limit curves subjected to combined strain paths, *International Journal of Mechanical Sciences*, 53 (2011) 365-373.
- [23] M. Tisza, Preliminary Studies on the determination of FLD for single point incremental sheet metal forming, *Key Engineering Materials*, 504 (2012) 863-868.
- [24] M.B. Silva, P.S. Nielsen, N. Bay, P.A.F. Martins, Failure mechanisms in single-point incremental forming of metals, *The International Journal of Advanced Manufacturing Technology*, 56 (2011) 893-903.
- [25] C. Henrard, Numerical Simulations of the Single Point Incremental Forming Process, in, 2009.

4.1.1 Process Formability and Forming Forces

Paper C

Simulation and experimental observations of effect of different contact interfaces on the incremental sheet forming process

Li, Y.L., **Liu, Z.B.**, Daniel, W.J.T., Meehan, P.A.

Materials and Manufacturing Processes

2014, Volume: 29(2), Pages: 121-128.

Simulation and Experimental Observations of Effect of Different Contact Interfaces on the Incremental Sheet Forming Process

YANLE LI, ZHAOBING LIU, W.J.T. (BILL) DANIEL, AND P.A. MEEHAN

School of Mechanical & Mining Engineering, The University of Queensland, St Lucia, Brisbane, Australia

Incremental sheet forming (ISF) is a promising forming process perfectly suitable for manufacturing customized products with large plastic deformation by using a simple moving tool. Up to now, however, the effects of contact conditions at the sheet interface are not well understood. The aim of this work is to study the effect of tool type and size on the formability and surface integrity during the forming process. Experimental tests were carried out on aluminum sheets of 7075-O to create a straight groove with four different tools (ϕ 30, ϕ 25.4, ϕ 20 and ϕ 10 mm). One tool tip was fitted with a roller ball (ϕ 25.4 mm) while the other three were sliding tips. The contact force, friction and failure depth were evaluated. A finite element (FE) model of the process was set up in an explicit code LS-DYNA and the strain behavior and thickness distribution with different tools were evaluated and compared with the experimental results. This study provides important insights into the relatively high formability observed in the ISF process. Microscopic observations of the surface topography revealed that a rolling tool tip produced better surface integrity as compared with a sliding tool tip, wherein, distinct scratch patterns in the tool traverse direction were evident.

Keywords Deformation; Forces; Forming; Strain; Stresses.

INTRODUCTION

Incremental sheet forming (ISF) is a promising manufacturing process in which flat metal sheets are gradually formed into 3D shapes using a generic tool stylus only. By using this process, useable parts can be formed directly from computer-aided design (CAD) data with a minimum of specialized tooling; therefore, it has economic benefits for rapid prototyping production and for small quantity applications [1–3].

Over recent years, different kinds of studies have been conducted [2, 4–9] with emphasis on understanding, assessing and improving the formability in this forming process. Among them, straight groove tests have been performed by Kim and Park [10] and suggested as an appropriate method to evaluate the effects of process parameters on the formability for aluminum sheet. In this forming test, two characteristics of deformation can be achieved [10]. One is the deformation condition. Biaxial stretching deformation takes place at the starting and ending points of the straight line when the tool moves horizontally. As the forming depth increases, the deformation turns more into biaxial stretching. On the contrary, plane-strain stretching deformation occurs between the starting and ending points. Another important characteristic of ISF is the higher formability

achieved compared with other conventional sheet forming processes. As for deformation mechanics of ISF, stretching rather than vertical shearing appears to be the dominant mode of deformation in ISF according to recent published work by Silva [11] and Allwood [12]. Failure mechanics in ISF [13] were revisited recently and a much deeper insight on the influence of tool radius led to the proposal of a new understanding and assessing on formability limits and formation process of fracture. Minutolo [14], working on force analysis in the groove test, found that using a tool with a bigger diameter and higher drawing depth, higher forming forces and a different typology of failure can be observed. However, comparison between the results using ball (rolling) and hemispherical (sliding) tools were not conducted in this article. Kim [10] concluded that the ball tool is more effective than the hemispherical head tool in terms of formability by simply judging the value of $(\epsilon_{\text{major}} + \epsilon_{\text{minor}})$ [4] after deformation, without comparing the failure depth of two kinds of tools. Durante [15] and Hussain [16], working on the effect of tool/sheet contact conditions on the surface finish of the product, found that the lowest levels of surface roughness were obtained with sphere/sheet contact. Still, surface topography of the forming surface needs to be studied to deepen the knowledge in the effect of different contact conditions on this innovative sheet forming process.

In the present paper, the test to form a straight groove has been carried out and the effect of tool size, tool type and friction between tool and sheet was investigated. One of the few state-of-the-art ISF machines designed by Amino Corporation that allows mold based forming for a maximum

Received February 22, 2013; Accepted June 26, 2013

Address correspondence to Yanle Li, School of Mechanical & Mining Engineering, The University of Queensland, St Lucia, Brisbane, QLD 4072, Australia; E-mail: yanle.li@uq.edu.au.

Color versions of one or more of the figures in the article can be found online at www.tandfonline.com/Immp.

size 2100 mm × 1450 mm × 550 mm with greater control and quality was used to conduct the forming process. In terms of the sliding conditions, three hemispherical head tools, 30 mm, 20 mm and 10 mm in diameter, have been used. From these experimental tests, the influence of tool sizes on the surface topography and on the value of the failure can be analyzed and revealed. In addition, some failure cases during the process are analyzed to provide experimental evidence on fracture forming limits. A FE model has also been created and utilized to analyze the strain behavior for better understanding the deformation mechanics.

EXPERIMENTATION AND SIMULATION METHODS

Experiment Setup

The groove forming tests have been performed on a state-of-the-art machine designed dedicated for the ISF process by Amino Corporation which can be numerical controlled by a controller provided by FANUC corporation. Fig. 1 shows a photograph of an experimental test.

Two types of tools; a ball tool and hemispherical head tool as pictured in Fig. 2, have been used in the experiment to produce four different contact interfaces between tool and workpiece. Among them, a ball, with a diameter of 25.4 mm, attached to the end of the ball tool can rotate freely. For the hemispherical tool, the tip is tungsten carbide and the body is made of K110 steel which was hardened and tempered to HRC60. The material used in the present study was aluminum 7075-O sheet of 300 mm × 300 mm in size and 1.016 mm in thickness. Alloy 7075 was one of the most successful Al–Zn–Mg–Cu alloys with high strength and good stress-corrosion cracking resistance and has been widely used for aerospace applications.

In the groove test, metal sheets were fixed along their edges in a special designed frame which mounted on the forming table of the machine; the tool moved back and forth

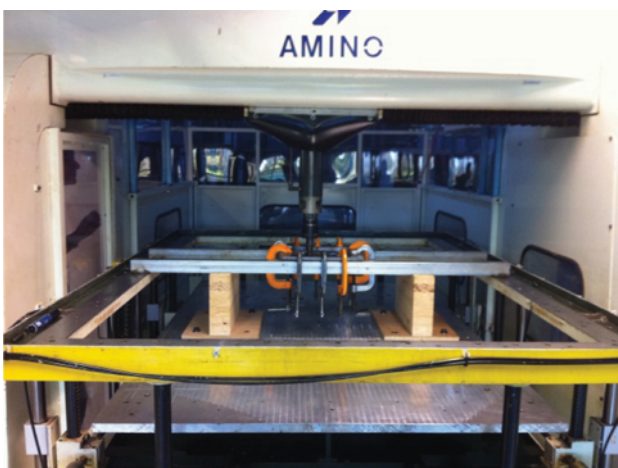


FIGURE 1.—Incremental sheet forming on Amino machine.

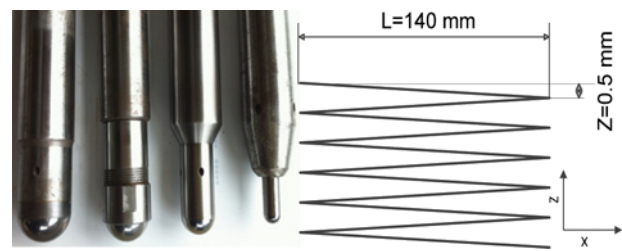


FIGURE 2.—Four different tools and tool path that were utilized in the experiments.

along a 140 mm long straight path (shown in Fig. 2) with a gradual step down of 0.5 mm in vertical position until a crack was observed. For every test, a feed rate of 1000 mm/min has been set out and a lubricant has been sprayed on the plate to reduce the friction coefficient between tool and sheet surfaces. More detailed configurations for the experimental parameters can be found in Table 1.

Finite Element (FE) Model

By comparing different simulation package and performance [17, 18], DYNA3D, a dynamic explicit FE code, is chosen to simulate the drawing process. It can accurately solve dynamic problems which have 3D elastic–plastic large deformation using explicit time integration. Due to the complexity of the ISF simulation, mass scaling and increasing working speed was essential to reduce computing time with insignificant influence on the simulation results.

The general geometry of the sheet is square with dimension 300 mm × 300 mm and it is meshed into 1.5 mm × 1.5 mm elements which are shown in Fig. 3 (only half of the sheet is presented). To simulate the boundary conditions in the forming process, nodes in all edges are constrained with both displacement and rotation in all degrees of freedom. In the FE model, forming tools are considered as rigid bodies and their boundary conditions that should be followed during the process are given by the path shown in Fig. 2. In the presented FE model, the sheet behavior is assumed to be isotropic and the plastic property is modeled by means of a power law expression. This expression considered the material hardening with an exponential dependence on strain but neglected the effect of both temperature and strain rate to simplify the model. Material parameters were obtained from the work by M. Durante [19] which are shown in Table 2. From our

TABLE 1.—Experimental parameters design for groove test.

Part No.	Tool size (mm)	Sheet thickness (mm)	Groove length (mm)	Speed (mm/min)
1	30	1.016	140	1000
2	20	1.016	140	1000
3	10	1.016	140	1000
4	25.4(ball)	1.016	140	1000

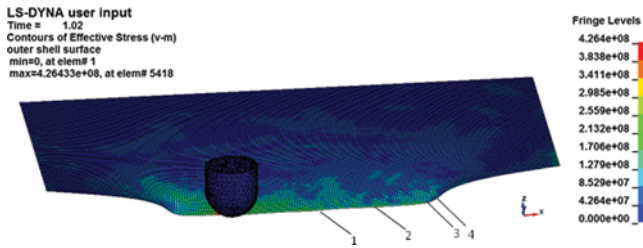


FIGURE 3.—FE model of the ISF process in LS-DYNA. Reference elements 1–4 marked.

experimental work, the friction at the contact surface between tool head and sheet has been assessed and analyzed with a value of 0.18. This value has been used in this FE model (see Fig. 4).

EXPERIMENTATION AND SIMULATION RESULTS

Force Measurement

To better understand the contact mechanics and predict the occurrence of failure, the forces between tool and workpiece have been measured continuously over time during the process. There are several ways to capture the forming force, such as the cantilever sensor designed by Jeswiet [20] and force dynamometer used by Duflou [21]. In the present work, three full Wheatstone bridges have been designed and mounted on the 30 mm hemispherical tool. Each bridge is configured by four strain gauges and designed to measure one of the three orthogonal forces: two bending directions, and one axial direction. Before taking any measurement, the strain gauges were calibrated twice in all three directions by applying a known force to get an accurate result. The calibrated system shows a rather linear relation between strain and output voltage.

The forces measured with this system shown in Fig. 4 are for a 1.016 mm thick 7075-O aluminum sheet. In this test, a groove was formed until it was 25 mm deep when fracture of the aluminum sheet occurred. It can be seen that both vertical and horizontal components experience a sharper increase at the end of each travel and the maximum forces encountered are around $F_v=2700\text{N}$ in the vertical direction and $F_h=1800\text{N}$ in the horizontal direction. These sharper increases are likely due to three main reasons; the increase of the contact area at the end of the groove, the dynamic

impact of the side wall and also the large acceleration of the forming tool caused by the sudden change of moving direction. For the steps (vertical depth from 15 mm to 25 mm where failure occurs) which were presented in Fig. 4, only a slight increase from 800 N to 1000 N for the vertical and from 150 N to 200 N for the horizontal component can be found for the nearly steady trend recorded in the middle of each travel. Evaluation of friction coefficients is conducted by calculating the absolute value of the ratios between horizontal and vertical components in the central area of the specimens, which has been widely used by Durante [19] and Hamilton [22]. According to Fig. 4, the absolute value of the ratios shows a slightly growing tendency in the middle area of the groove caused by the continual increase of the groove depth which requires more forces to stretch the sheet during each travel. An average value of 0.18 has been calculated as the average friction coefficient.

Failure Depth

Hemispherical head tools of three sizes were used: 10, 20 and 30 mm in diameter. We can obviously see from Fig. 5 that the failure depth is higher with an increase in tool diameter. More specifically, cracking occurs when the forming depth was 16, 21.5 and 25 mm for the tool diameters of 10, 20 and 30 mm with rolling direction (RD), respectively. It is worth noting that all the cracks first occurred near the end of each travelling path: this is due to the fact that these are the regions where the highest amount of deformation, straining and thinning will take place. It appears that there are linear relations between these failure depths and tool diameters in the test coverage. It can be clearly concluded from the

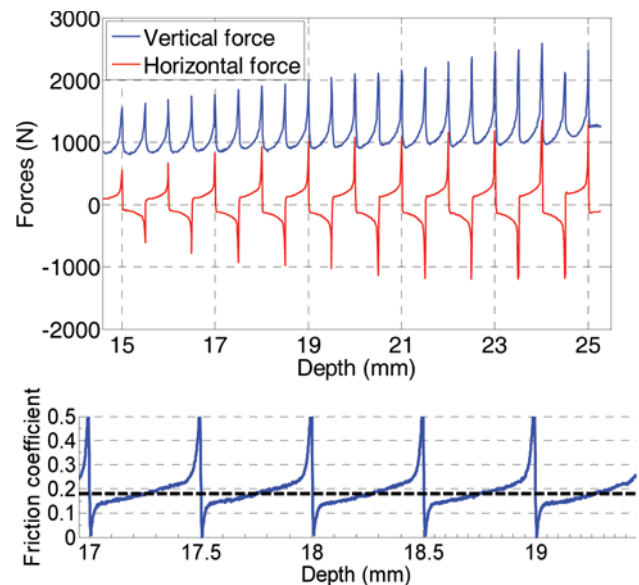


FIGURE 4.—Vertical and horizontal force with a tool of 30 mm in diameter and the absolute value of the ratios between two components.

TABLE 2.—Mechanical properties for 7075-O aluminum sheet.

Parameters	Value
Sheet thickness (mm)	1.016
Young's modulus (GPa)	75
Yield strength (MPa)	100
Ultimate tensile strength (MPa)	200
Poisson's ratio	0.33
Plastic property	$\sigma=330\epsilon^{0.19}$

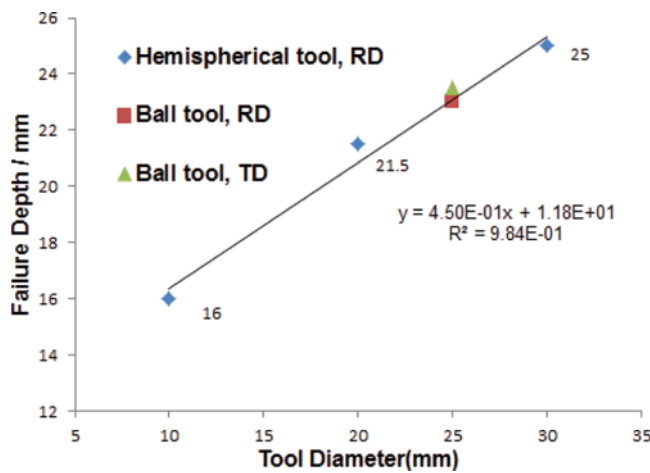


FIGURE 5.—Variations of failure depth of the groove test with tools different in diameter. (RD represents rolling direction and TD for transverse direction).

experimental results that the tool diameter should be chosen as large as possible to delay the fracture. These results are consistent with the technical literature [23] in that, with the decrease of the tool diameter, the plastic deformation area also descends but the strain level ascends. The higher level of stresses can explain the early failure with the smaller sized tools.

In terms of the ball tool with a diameter of 25.4 mm, two tests have been performed with the forming direction parallel to ball direction (RD) and transverse direction (TD). The failures of these grooves were recorded at 23 mm and 23.5 mm when the tool was moving along TD and RD, respectively. This phenomenon indicates that a small amount of plane-anisotropy results in the small difference of formability between two directions of the tool.

Figure 6 shows two different failure types at the end of the groove formed by 30 mm large ball tool (a) and hemispherical tool (b), respectively. By checking both macro (Fig. 6(a)) and micro (Fig. 6(c)) structure of the failure point, it is shown that plastic deformation develops by uniform thinning until fracture and in-plane stretching is the principal mode of deformation in this process.

Contact Forces, Strain Behavior and Thickness Distribution in FE Model

To validate the proposed FE model, the simulated contact forces were plotted and compared with experimental data which is shown in Fig. 7. In the FE model, both the tool and the sheet are modeled with the same parameters as in the experimental test (e.g. sheet thickness is 1.016 mm, tool diameter is 30 mm and groove length is 140 mm). From Fig. 7, the predicted forces both in vertical and horizontal components are in reasonable agreement with measured values, except that vertical forces are slightly overestimated and at the end points of the groove sharper force peaks were recorded in the experimental test. The deviation of the

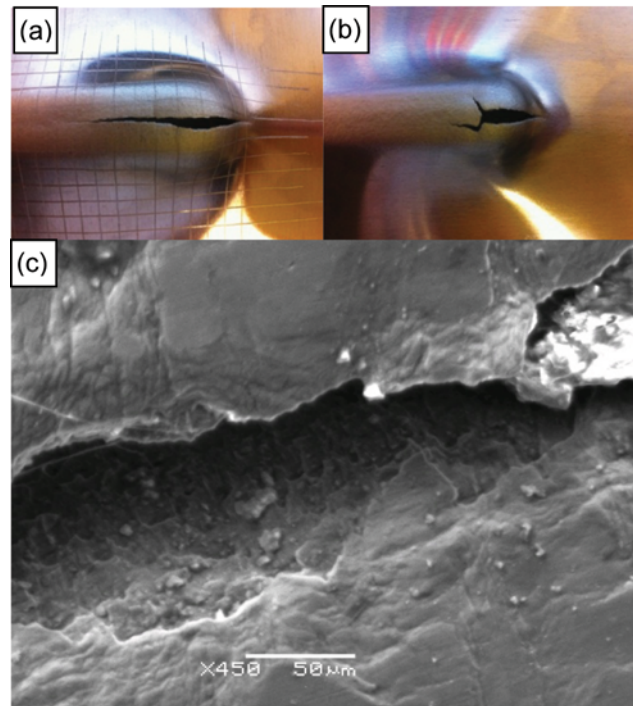


FIGURE 6.—Failure types of sheets formed with different tools. (a) Monodirectional; (b) bidirectional failure; (c) scanning electron micrograph of the onset of fracture and the cross section.

modeled and measured force results for the peak values may be due to two main aspects: (1) 7075-O aluminum alloy is strain-rate sensitive and in the case of strain-rate sensitive materials artificially increasing the working speed might adversely affect accuracy of predicted forming forces. In the current model, the forming speed is artificially increased by a time scaling factor of 16.8 to save computing time. (2) Model boundary conditions might not have corresponded to reality. Specifically, there may have been a small amount of sliding between metal sheets and the clamping frame that was not included in the model. It is also possible that dynamic impact of the side wall and acceleration of the forming tool have not been quite accurately modeled. These aspects should be further investigated for developing an accurate force prediction model. However, for the investigation of strain behavior and thickness distribution in this process, the predicted forming forces during the groove forming process are acceptable as conservative measures.

The strain behavior of the sheet was predicted by LS-DYNA. The results of the strain distribution can provide useful information to understand the trend of deformation. To compare the state of the strain for the tool diameter of 30 and 20 mm, the analysis were performed until the forming depth both reached 21 mm.

Figure 8 shows the major strain distribution in the middle of the groove along the longitude direction in which the value of the contacted surface and non-contacted are denoted by upper surface and lower surface, respectively. In this

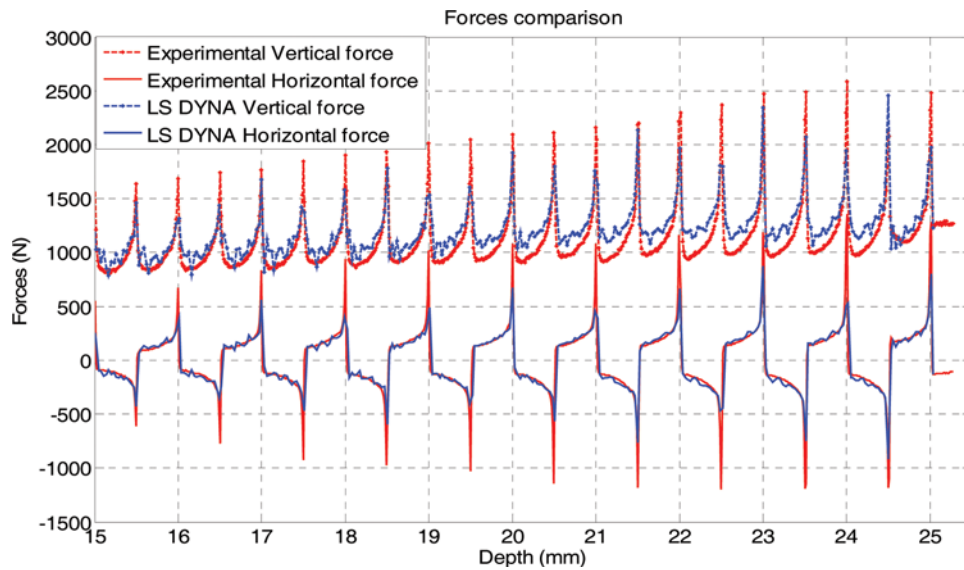


FIGURE 7.—Forces comparison between simulated and experimental results.

figure, the major strain is small in the middle and big at the end of the groove and the major strain on the lower surface is greater than that on the upper surface. It can also be noticed in Fig. 8 that the major strain with the 20 mm tool is greater than that with the tool diameter of 30 mm for both upper surface and lower surface. It suggests that the level of strain decreases as the tool size increases. This could be explained physically by the increase in the contact area and deformation zone. Since the forming limit of the sheet is restricted by the value of strain, earlier occurrence of failure using a smaller tool can be predicted.

To further study the strain behavior and the evolution of the groove, four elements at the bottom of the groove at different places have been selected to compare the strain

evolution history in the forming process as shown in Figs. 3, 9 and 10. In the current coordinate system, the origin is defined at the center of the sheet and the tool is travelling along the X-axis from -70 mm to 70 mm while keeping Y as 0. The X-coordinate values of the four selected elements 1, 2, 3 and 4 are 0 mm, 35 mm, 64 mm and 70 mm, respectively (see Figs. 3 and 10). Figure 9 illustrates the strain evolution history of the four elements during the whole forming process which uses a tool with a diameter of 30 mm. It can be clearly noticed that the strain values of the elements (1 and 2) in the middle of the groove keep the same level at each step and the lowest strain values always take place at the very end of the groove (element 4). However, by checking the strain values of each element, it was found that the maximum effective strain occurs before the corner of the groove (element 3) with a distance of 6 mm. The FE modeling results can be confirmed by Fig. 6 which shows that the crack first occurs just prior to the end of the groove.

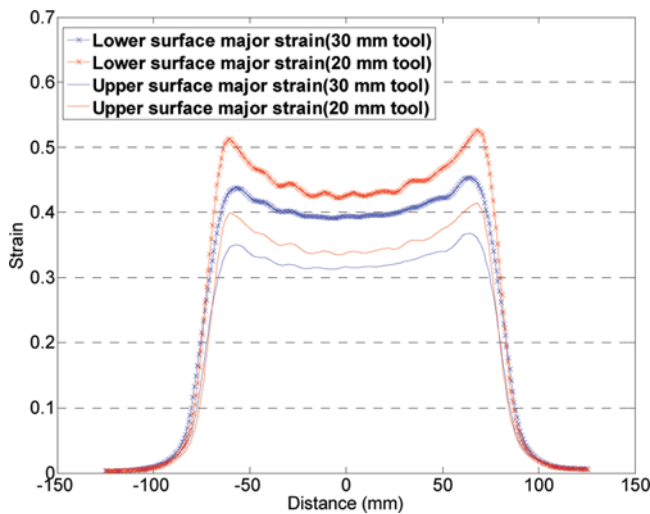


FIGURE 8.—Distributions of major strain predicted by LS-DYNA with different size tools at the depth of 21 mm.

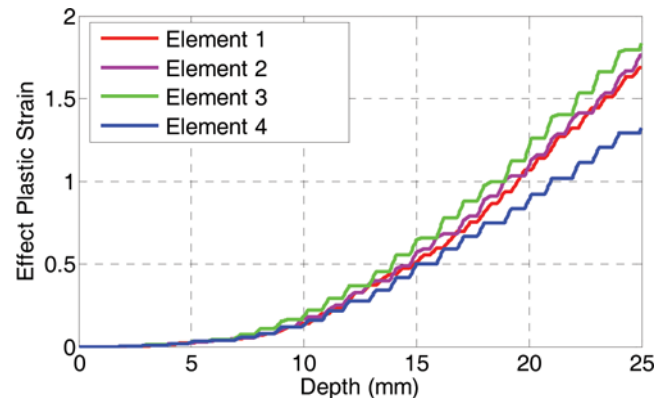


FIGURE 9.—Effective plastic strain evolution of four elements in a groove forming process with 30 mm tool.

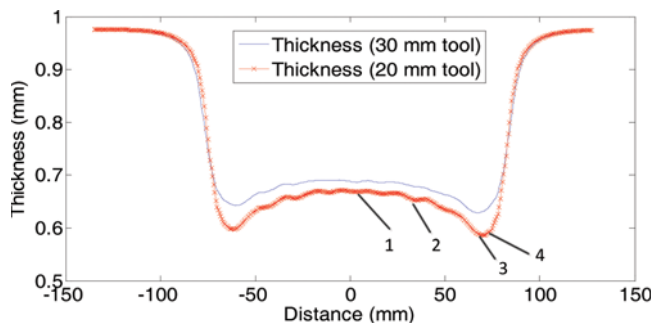


FIGURE 10.—Thickness distributions predicted by LS-DYNA with different size tools. Reference elements 1–4 marked.

Based on the assumption that the metal sheet is incompressible, the large deformation takes place by thinning the sheet. As a result, the thickness distribution is a critical factor to assess the formability and feasibility of a process. The thickness distribution with tools of 30 and 20 mm in diameter are simulated by LS-DYNA and shown in Figure 10. It can be obviously seen that the thickness is greater in the middle and smaller at the ends of the path which can explain why the failure always occurs at the end of the groove. At the same forming depth, the thickness of the groove formed by the 20 mm tool is thinner than that formed by the 30 mm tool, which suggests that failure should occur earlier for the smaller tool. These predicted FE strain and thickness analysis results are well corroborated by the experimental tests performed in the present work.

Surface Topography (SEM)

Figure 11 shows the aluminum sheet surface topography of the grooves produced by hemispherical (a) and ball tools (b) scanned by using JEOL6460 Scanning Electron Microscopy (SEM) with the supply power of 15 KV. The samples were cut into 2 cm squared for SEM observation and no other surface treatment was performed. Compared with sliding contact, the surface damage (striations) of the parts formed under rolling contact appears to be less. Fig. 11 also indicates that many small pits appear on the surface of the aluminum sheet formed with both hemispherical and ball tool. This appears to be due to the coating exfoliating [24] on the sheet.

The border zone between the touched and non-touched area formed by the ball tool are also captured by SEM (Fig. 12). Interesting differences between these two areas can be seen that the surface formed by the ball tool appears smoother than the initial unformed surface. To some extent, it appears that the rolling contact condition can improve the surface topography by flattening the rolling trace initially existing on the sheet surface. However, much more detailed examination should be taken to fully explain this phenomenon.

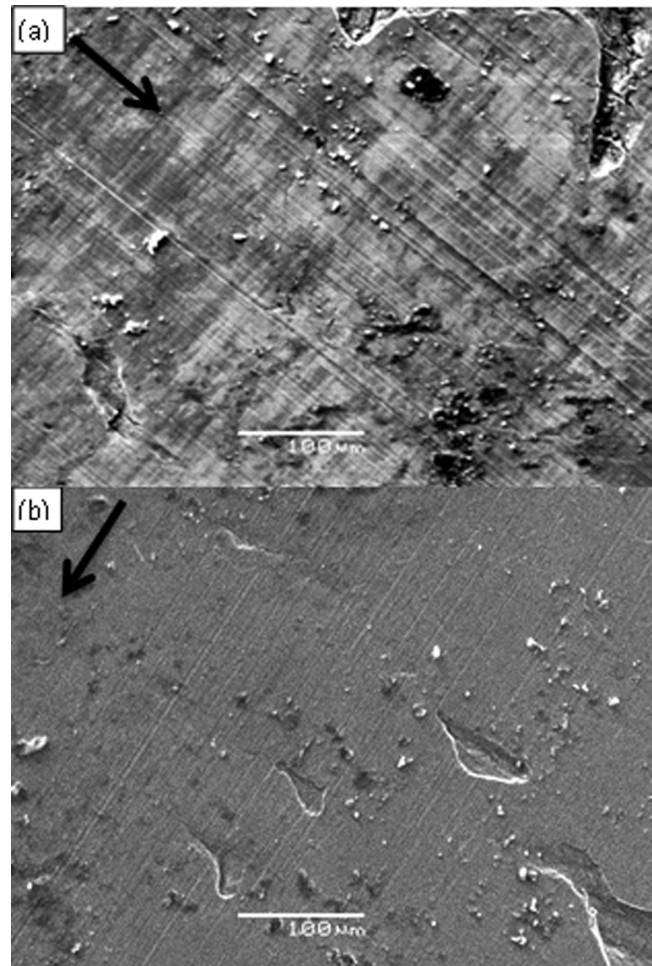


FIGURE 11.—Surface topography examined by SEM for sheets formed with different tools along the directions indicated by arrows: (a) hemispherical tool; (b) ball tool.

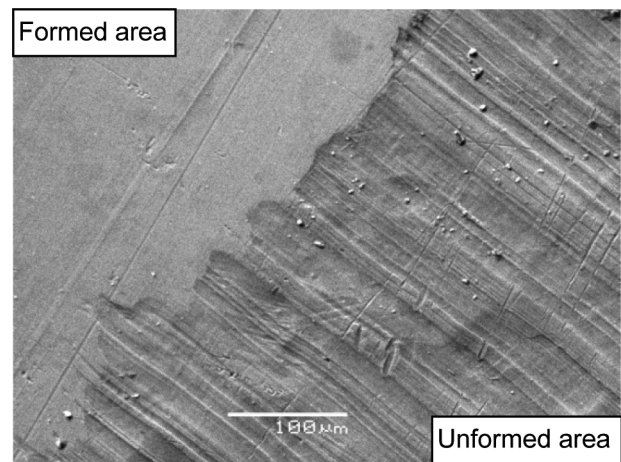


FIGURE 12.—Border zone of the contacted and non-contacted area with ball tool.

CONCLUSION

Forming forces have been measured by means of strain gauges and provide useful information to monitor and understand the forming process. Even though both vertical and horizontal forces present sharper increases at the end of each travel due to the increase of contact area and impact to the side wall, forces only show a slightly growing trend in the central area of the groove. This information proves that only localized deformation occurred in the process and thus it is possible to form large and complex shapes without higher forces required. By recording the forming depth using three different size tools, an obvious increasing trend in fracture depth was observed with the increase of tool diameter. Therefore, tool diameter should be selected as large as possible to improve formability with the constraints of geometrical complexity. Surface topography of parts formed by the hemispherical and ball tools has been scanned by SEM. The result shows that rolling contact condition causes much less local damage and scratching of the surface. FE analysis is an efficient way to determine the influence of different tool sizes on the strain behavior and thickness distribution, providing how different parameters affect the forming process.

To further compare the effect of contact types, the same size of hemispherical tool (25.4 mm) is being manufactured and would be utilized in future research. Surface roughness is another important parameter to evaluate the output quality of the process and should also be measured in the future.

ACKNOWLEDGMENTS

The authors are grateful to Paul Bellette and Peter Bleakley, for their assistance of the initial setup of the experiment test. Revision of the manuscript provided by Dr Prasad Gudimetla is also greatly acknowledged.

FUNDING

This work is financed by Australian Research Council (ARC) Linkage project which collaborates with QMI Solutions. China Scholarship Council (CSC) is acknowledged for the scholarship support.

REFERENCES

- Jeswiet, J., et al., Asymmetric single point incremental forming of sheet metal. *Annals of CIRP—Manufacturing Technology* **2005**, *54*(2), 623–649.
- Echrif, S.B.M.; Hrairi, M. Research and progress in incremental sheet forming processes. *Materials and Manufacturing Processes* **2011**, *26*(11), 1404–1414.
- Leacock, A.G.; The future of sheet metal forming research. *Materials and Manufacturing Processes* **2012**, *27*(4), 366–369.
- Iseki, H.; Kumon, H. Forming limit of incremental sheet metal stretch forming using spherical rollers. *The Japan Society for Technology of Plasticity* **1994**, *35*, 1336.
- Kim, T.J.; Yang, D.Y. Improvement of formability for the incremental sheet metal forming process. *International Journal of Mechanical Sciences* **2000**, *42*(7), 1271–1286.
- Sarraji, W.K.H.; Hussain, J.; Ren, W.-X. Experimental investigations on forming time in negative incremental sheet metal forming process. *Materials and Manufacturing Processes* **2011**, *27*(5), 499–506.
- Hussain, G.; Gao, L.; Hayat, N. Forming parameters and forming defects in incremental forming of an aluminum sheet: correlation, empirical modeling, and optimization: Part A. *Materials and Manufacturing Processes* **2011**, *26*(12), 1546–1553.
- Banabic, D.; Sester, M.; Influence of material models on the accuracy of the sheet forming simulation. *Materials and Manufacturing Processes* **2012**, *27*(3), 273–277.
- Silva, M.B.; Martinho, T.M.; Martins, P.A.F. Incremental forming of hole-flanges in polymer sheets. *Materials and Manufacturing Processes* **2013**, *28*(3), 330–335.
- Kim, Y.H.; Park, J.J. Effect of process parameters on formability in incremental forming of sheet metal. *Journal of Materials Processing Technology* **2002**, *130–131*, 42–46.
- Silva, M.B., et al. Single-point incremental forming and formability-failure diagrams. *Journal of Strain Analysis for Engineering Design* **2008**, *43*(1), 15–35.
- Allwood, J.; Shouler, D.; Tekkaya, A.E. The increased forming limits of incremental sheet forming processes. *Key Engineering Materials* **2007**, *344*, 621–628.
- Silva, M.B., et al. Failure mechanisms in single-point incremental forming of metals. *The International Journal of Advanced Manufacturing Technology* **2011**, *56*(9), 893–903.
- Minutolo, F.C., et al. Forces analysis in sheet incremental forming and comparison of experimental and simulation results. In *Intelligent Production Machines and Systems-2nd IPROMS Virtual International Conference*, Cardiff, England, July 3–14, 2006.
- Durante, M.; Formisano, A.; Langella, A. Observations on the influence of tool-sheet contact conditions on an incremental forming process. *Journal of Materials Engineering and Performance* **2011**, *20*(6), 941–946.
- Hussain, G., et al. Guidelines for tool-size selection for single-point incremental forming of an aerospace alloy. *Materials and Manufacturing Processes* **2012**, *28*(3), 324–329.
- Vafaesehat, A. Finite element simulation for blank shape optimization in sheet metal forming. *Materials and Manufacturing Processes* **2011**, *26*(1), 93–98.
- Cai, G.P.; Zhu, N.Y.; Wen, N. Stress analysis of sheet metal vibration incremental forming. In *Materials Processing Technologies, Pts 1 and 2*; Z.Y. Jiang, X.H. Liu, and J.L. Bu, Eds.; Trans Tech Publications Ltd: Stafa-Zurich, 2011; 166–170.
- Durante, M., et al. The influence of tool rotation on an incremental forming process. *Journal of Materials Processing Tech* **2009**, *209*(9), 4621–4626.
- Jeswiet, J.; Alexander Szekeres, J.R.D. Forces in single point and two point incremental forming. *Advanced Materials Research* **2005**, *6–8*, 449–456.
- Duflou, J.R. Force measurements for single point incremental forming: an experimental study. *Advanced Materials Research* **2005**, *6–8*, 441–448.

22. Hamilton, K.A.S. Friction and external surface roughness in single point incremental forming: a study of surface friction, contact area and the 'orange peel' effect, 2010.
23. Carrino, L.; Giuliano, G.; Strano, M. The effect of the punch radius in dieless incremental forming. In *Intelligent Production Machines and Systems–2nd IPROMS Virtual International Conference*, Cardiff, England, July 3–14, 2006; 204–209.
24. Hou, Y.K., et al. Surface topography evolvement of galvanized steels in sheet metal forming. *Transactions of Nonferrous Metals Society of China* **2009**, *19*(2), 305–310.

4.1.2 Geometric Accuracy

Paper D

Study on step depth for part accuracy improvement in incremental sheet forming process

Lu, H.B., Li, Y.L., **Liu, Z.B.**, Liu, S., Meehan, P.A.

Advanced Materials Research

2014, Volume: 939, Pages: 274-280.

Study on step depth for part accuracy improvement in incremental sheet forming process

Haibo Lu^{1,a}, Yanle Li^{1,b}, Zhaobing Liu^{1,c}, Sheng Liu^{1,d} and Paul A. Meehan^{1,e}

¹School of Mechanical & Mining Engineering, University of Queensland, St Lucia, Brisbane, QLD 4072, Australia

^ah.lu2@uq.edu.au, ^byanle.li@uq.edu.au, ^cz.liu7@uq.edu.au, ^ds.liu3@uq.edu.au, ^emeehan@uq.edu.au

Keywords: incremental sheet forming, step depth, part accuracy

Abstract. Incremental Sheet Forming (ISF) is a new-emerging sheet forming process well suited for small batch production or prototyping because it does not need any dedicated dies or punches. In this forming process, sheet metal parts are formed by a smooth-end tool in a stepwise way, during which plastic deformation is highly localized around the tool end. The part geometric accuracy obtained in the current ISF process, however, has not met the industry specification for precise part fabrication. This paper deals with a study on step depth, a critical parameter in ISF, for improving the geometric accuracy, surface quality and formability. Two sets of experiments were conducted to investigate the influence of step depth on part quality. Dimensional accuracy, surface morphology and material fracture of deformed parts were compared and analysed. An optimum value of step depth was suggested for forming a truncated cone. The present work provided significant fundamental information for the development of an advanced ISF control system on tool path control and optimization.

Introduction

Sheet metal forming is a widely used manufacturing process and plays a significant role in industry. There is a wide range of sheet metal forming processes, including stamping, pressing, etc. These require dedicated dies and punches to manufacture sheet-metal components with complex shapes. Due to the high cost in realizing such process and the lack of flexibility, conventional manufacturing methods are efficient for large scale production but less competitive for small scale fabrication of customised parts [1]. As market demand in the sheet forming area is becoming increasingly customer-oriented and sophisticated, more flexible manufacturing technologies for custom parts fabrication are demanded to be introduced and developed [2]. Incremental sheet forming (ISF) is a flexible process well suited for small batch production or prototyping because expensive dies and tools are not required, which makes it a promising alternative to meet the new market requests [3, 4].

In ISF, sheet metal parts are formed by a smooth-end tool, generally mounted on a three-axis CNC milling machine, in a stepwise way. Fig. 1 schematically illustrates the single point incremental forming (SPIF) process. The simple tool moves over the surface of the clamped metal sheet along a tool path directly generated from a 3D CAD file, during which plastic deformation is highly localized around the tool end. ISF is a dieless forming process and possesses a high degree of flexibility because specialised tooling is not required. The product design can be modified or changed easily and quickly. Additionally, the formability in ISF is higher than conventional processes due to the small plastic zone and incremental nature of the process, making it easier to deform sheet metal with low formability [5]. The small contact zone and incremental step size also contributes to small forces within the material. Therefore, the lead-time and cost of tooling in ISF can be greatly minimized. This forming technique makes rapid prototypes or small serial production of sheet metal parts relatively fast and economical [6].

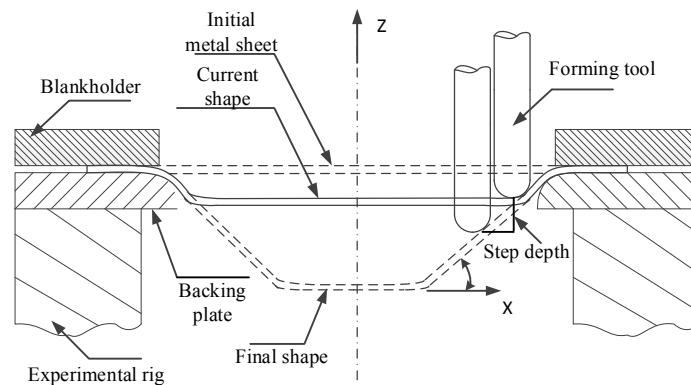


Fig.1 Process principle of SPIF: step depth (ΔZ) is the vertical distance between two neighbouring contours.

Nevertheless, the major limitation of ISF is that the geometric accuracy obtained currently is lower compared with conventional forming processes and cannot reliably reach suitable levels specified by industrial users. Hence, the ISF process is still in the embryonic stage with no widespread industrial applications although rapid advances have been achieved recently. Additionally, the forming process is slow due to its point-to-point forming nature.

Recently, the improvement of part accuracy and process optimization in ISF has been a key issue for researchers. During the ISF process, the tool path directly affects the forming accuracy since the shape is formed by a simple tool following a designed tool path. Regarding the generation of tool path, the most common method is a contour parallel method by which the tool path is generated in commercial CAM software and consists of a series of contours, with the step depth constant, parallel to the sheet plane. However, this method fails to fabricate complex parts with high precision. Many studies on the design, optimization and control of forming tool path have been carried out to overcome the limitations. Hirt et al. [7] proposed a tool path optimization method based on experiments and the modification of the tool path by a correction algorithm in the second run. Attanasio et al. [8] conducted a study on tool path optimization in TPIF and concluded that tool path with a small scallop height and variable step depth sizes contribute to better part quality. As reported in [9], a closed loop control scheme was used to modify the step depth during the forming process for tool trajectory control. Malhotra et al. [10] presented an automatic spiral tool path generation algorithm for SPIF, in which the incremental depth is controlled by the geometrical error between CAD model and formed parts.

According to the previous research, step depth has been considered as a critical parameter in the design, optimization and control of tool paths. At present, comprehensive research work on step depth is required to further study the relationship between step depth and part quality, especially for improving part accuracy via tool path control and optimization. This paper focuses on the investigation of step depth to fully understand its influence on the formability and part quality, including geometric accuracy and surface finish. This would be of great significance for ISF tool path control and optimization to address the limitation of low geometric accuracy.

Experiments

Experiments were carried out on an AMINO® DLNC-PC ISF machine (Fig. 2). The sheet blank is clamped between a blank holder and a steel backing plate to prevent any movement of the blank during forming process. The metal blank, with 1.6 mm in thickness and 300 mm × 300 mm in size, is made of aluminium (7075-O), commonly utilized for forming automotive and aviation components. A 30 mm diameter cylindrical steel tool with a hemispherical end was used to deform the blank; the tip of the tool is tungsten carbide and the body is made of K110 steel which was

hardened and tempered to HRC60. Lubricant (oil-Shell Tellus Oil 68) was used to reduce the wear of the tool and friction between the tool and the blank.



Fig. 2 AMINO® DLNC-PC ISF Machine

Two sets of tests were performed by varying the ΔZ values to study this parameter, focusing on geometric accuracy and surface quality and on material formability, respectively. CAD models of truncated cones with two different wall angles were designed in SOLIDWORKS. A laser scanner (Non-contact 3D Digitizer VIVID 9i) was used to measure the geometry of the deformed components. Surface morphology of machined faces on produced truncated cones was analysed as well. The parameter settings of experiments are shown in Tables 1, as follows.

Table 1 Parameter settings of experiments on step depth

Parameter	Geometric accuracy and surface quality test	Formability test
Shape design	Truncated cone	Truncated Cone
Wall angle (°)	50	60
Feed rate (mm/min)	4000	4000
Sheet thickness (mm)	1.6	1.6
Tool diameter (mm)	30	30
Step depth/ ΔZ (mm)	0.1, 0.6, 1.1	0.1, 0.2, 0.3, 0.4, 0.5, 0.7, 1.0

Results and Discussion

This section presents experimental results obtained in the tests to analyse the influence of step depth in ISF process in terms of geometric accuracy, surface morphology and material fracture.

Geometric accuracy. GEOMAGIC Qualify was used to produce 3D geometry data of the scanned shape and analyse the dimensional error between deformed test parts and designed CAD models. Specifically, both produced and designed profiles were given in large sets of points in the same Cartesian coordinate system. In this work, cross-sectional comparison along a defined section plane was used to evaluate the geometric accuracy since the truncated cone is symmetric. A system plane (plane XOZ) across the symmetry axis of the cone was set as the section plane. The deviation in Z direction between the designed and fabricated profiles was calculated as the geometric error in cross-sectional comparison.

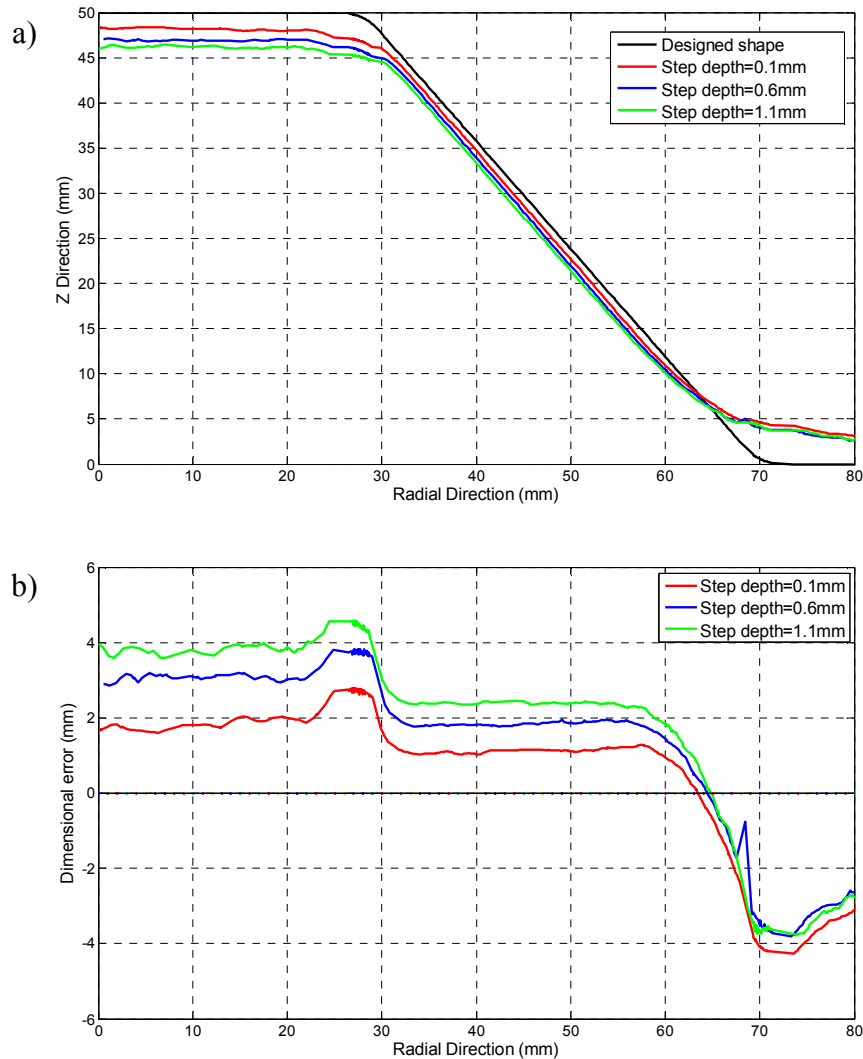


Fig.3: (a) Cross-sectional comparison among deformed profiles and the target profile; (b) Error distribution of deformed parts

The comparison among profiles of formed parts and the designed shape in geometric accuracy test is illustrated in the Fig. 3a), while detailed error distributions are correspondingly shown in Fig. 3b). According to the curves in Fig. 3, the profile with 0.1 mm step depth has the best dimensional accuracy in the test compared with the target profile. Therefore, step depth can significantly affect the geometric accuracy. Specifically, the geometric accuracy increases when decreasing the step depth size. This can be due to the fact that the generated forming contours are more intensive when setting step depth at a small value. Consequently, the movement of the forming tool would be smaller between two adjacent parallel contours, providing more homogeneous material distribution and deformation as well as the reduction of the spring-back effect.

Surface morphology. Surface morphology of inner faces, namely the machined faces, of deformed cones was shown in Fig. 5. Obviously, in the comparison of surface waviness among three produced parts, step depth has a great influence on the surface finish quality. As can be seen in Fig. 5a) and 5b), there are obvious tool marks left on the machined surfaces when using large step depth sizes (0.6mm and 1.1mm). The distance between two adjacent tool marks on the formed surface, d , illustrated in Fig. 4, increases with the increase of step depth value. The relationship between d and ΔZ coincides with the sine law, as shown in Equation 1.

$$d = \Delta Z / \sin \alpha . \quad (1)$$

Where α is the wall angle of the truncated cone.

Due to the geometric error, the measured d values (1.406mm and 0.751mm with ΔZ at 1.1mm and 0.6mm, respectively) are a little smaller than calculated ones (1.436mm and 0.783mm). On the contrary, as for small step depth (0.1mm), the formed surface shown in Fig. 5c) is much smoother than the two surfaces above, with no visible tool marks on the surface. Thus, it can be concluded that the surface quality can be improved by choosing small step depth in the ISF process.

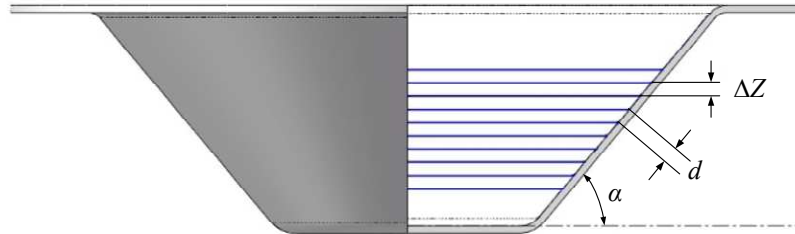


Fig. 4 Diagram of tool marks on the inner part face

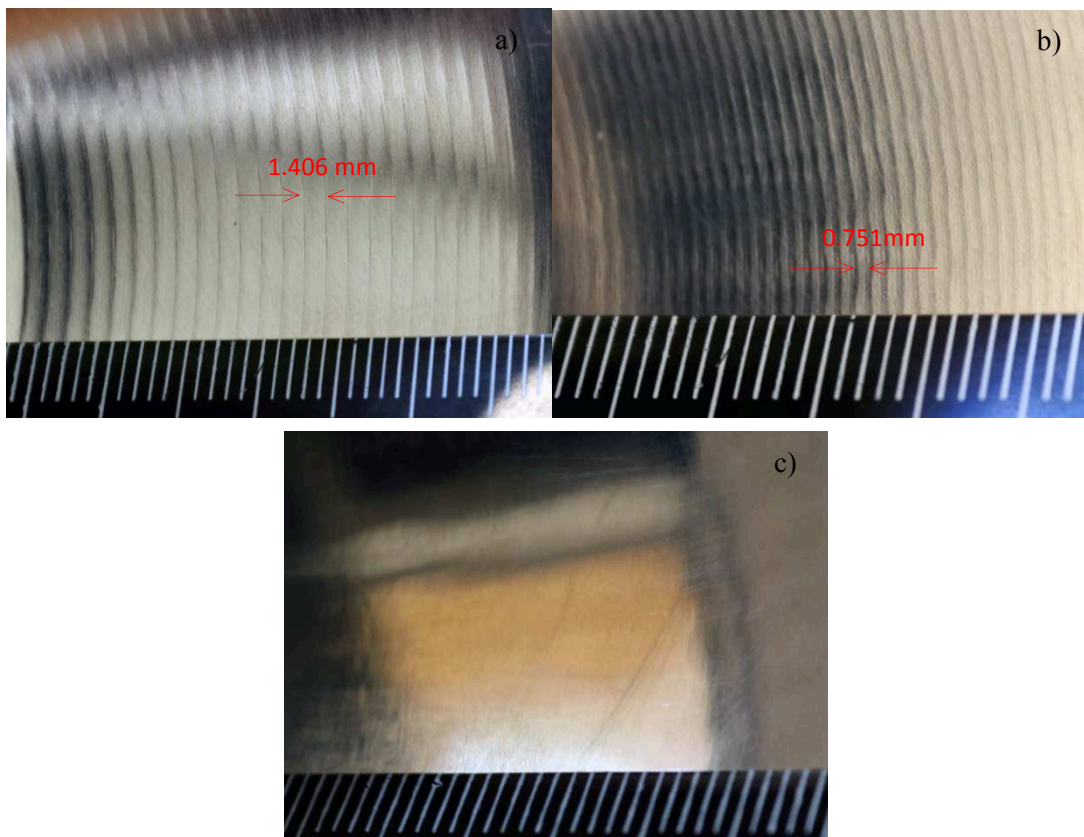


Fig. 5 Surface morphology of deformed parts in surface quality test: (a) $\Delta Z=1.1$ mm; (b) $\Delta Z=0.6$ mm; (c) $\Delta Z=0.1$ mm

Fracture analysis. Based on the analysis above, smaller step depth contributes to better geometric accuracy and part surface quality but lower efficiency due to the increase of forming time. More importantly, small step depth also adversely affects the forming process in terms of material formability, especially when the forming wall angle gets close to the forming wall angle limit. In the formability test, a truncated cone with a 60° wall angle (close to the wall angle limit) was used to evaluate the formability at different step depth sizes, with ΔZ ranging from 0.1 to 1.0 mm. The sheet fractured during the forming process with small step depth below 0.5 mm while only the parts with ΔZ over 0.7mm were successfully produced. Fig. 6a) shows the material fracture of a deformed cone with ΔZ being 0.1mm. Furthermore, the material failure occurs at smaller forming depth in Z direction when the step depth is smaller, which is illustrated in Fig. 6b). This can be due to the fact that a smaller step depth size means a smaller tool contour distance between two neighbouring contours. Thus, more intensive contact between sheet material and tool end will happen in the ISF

process, during which material in the contact zone of the metal sheet is pressed and hardened by the tool end in each forming contour. More already hardened material would be deformed again by the tool in the following several contours when using a tool path with smaller step depth. This leads to a great increase in the contact stress required to reach the target deformation. Consequently, sheet formability will be reduced due to higher stress state induced in the material. Therefore, too small step depth values should be avoided in consideration of material failure. In this case, 0.7 mm step depth was suggested to be the optimum value for the forming of the truncated cone with 60° wall angle.



(a)

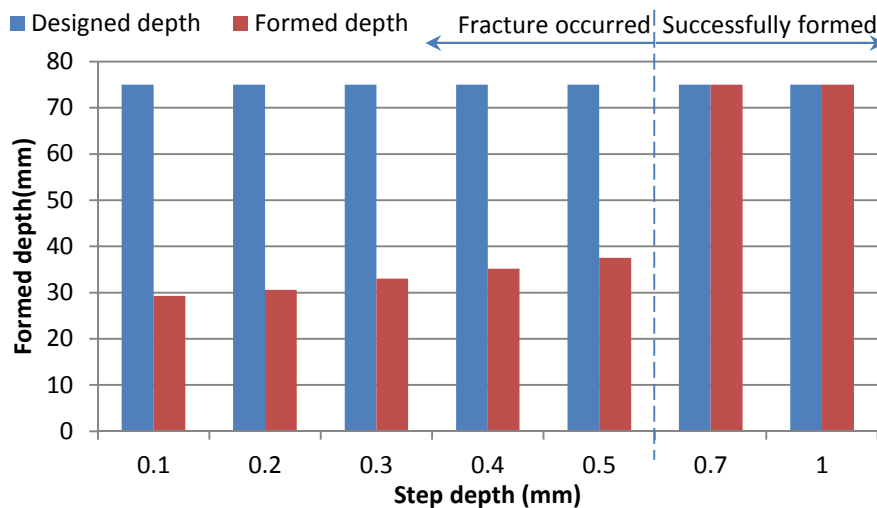


Fig. 6: (a) Part fracture in formability test ($\Delta Z=0.1$ mm); (b) Formed depth of parts in formability test

Conclusion and future work

This research aimed to provide a comprehensive investigation on step depth, as a critical process variable in ISF process, and to demonstrate that this variable is of great importance in design and control of tool path. Several experiments were conducted to investigate its influence on the part quality of the formed parts, including geometric accuracy, part surface quality and material formability. According to the results, smaller step depth leads to better geometric accuracy and part surface quality in ISF process. Parts deformed with large step depth cannot reach the required level both in geometric accuracy and surface quality but too small a step depth value should also be avoided with regard to the material fracture, especially when producing parts with large wall angles. Also, the forming time will increase as the step depth decreases. Even so, smaller step depth should be used within a reasonable range in tool path control and optimization. A trade-off among geometric accuracy, part surface quality, material failure and forming time should be made in the design and control of tool paths and the first two aspects should be considered as priorities. It is clearly suggested that there is an optimum value of step depth in the ISF path design; for instance

0.7mm in the case presented. Further research on the optimization of step depth should be included in the design of an advanced ISF control system. The presented work is a foundation, which offers significant information for tool path control and optimization, and needs to be developed to further determine the constraints in tool path control system. The inaccuracy of parts is still obvious in using contour tool paths with constant step depth. For the future, control of tool path will be developed for part accuracy improvement and to reduce design time for new parts in the ISF process.

Acknowledgements The present work was supported by China Scholarship Council (CSC) scholarship.

References

- [1] L. Filice, L. Fratini, F. Micari, Analysis of material formability in incremental forming, *CIRP Ann. Manuf. Technol.* 51 (2002) 199-202.
- [2] Y. H. Kim, J. J. Park, Effect of process parameters on formability in incremental forming of sheet metal, *J. Mater. Process. Technol.* 130 (2002) 42-46.
- [3] E. Hagan, J. Jeswiet, A review of conventional and modern single-point sheet metal forming methods, *Proc. Inst. Mech. Eng. Pt. B J. Eng. Manufact.* 217 (2003) 213-225.
- [4] S. B. M. Echrif, M. Hrairi, Research and Progress in Incremental Sheet Forming Processes, *Mater. Manuf. Processes* 26 (2011) 1404-1414.
- [5] J. Jeswiet, F. Micari, G. Hirt, A. Bramley, J. Duflou, J. Allwood, Asymmetric single point incremental forming of sheet metal, *CIRP Ann. Manuf. Technol.* 54 (2005) 88-114.
- [6] J.R. Duflou, J. Verbert, B. Belkassam, J. Gub, H. Sol, C.A.M Henrard, A.M. Habraken, Process window enhancement for single point incremental forming through multi-step toolpaths, *CIRP Ann. Manuf. Technol.* 57 (2008) 253-256.
- [7] G. Hirt, J. Ames, M. Bambach, R. Kopp, Forming strategies and process modelling for CNC incremental sheet forming, *CIRP Ann. Manuf. Technol.* 53 (2004) 203-206.
- [8] A. Attanasio, E. Ceretti, C. Giardini, L. Mazzone, Asymmetric two points incremental forming: improving surface quality and geometric accuracy by tool path optimization, *J. Mater. Process. Technol.* 197 (2008) 59-67.
- [9] W. Hao, S. Duncan, Optimization of tool trajectory for Incremental Sheet Forming using closed loop control, In *CASE, IEEE Int Conf.* (2011) 779-784.
- [10] R. Malhotra, N.V. Reddy, J. Cao, Automatic 3D spiral toolpath generation for single point incremental forming, *J. Manuf. Sci. Eng.* 132 (2010).

4.1.3 Forming Time

Paper E

Taguchi optimization of process parameters for forming time in incremental sheet forming process

Liu, Z.B., Li, Y.L., Daniel, W.J.T., Meehan, P.A.

Materials Science Forum

2014, Volume 773-774, Pages 137-143.

Taguchi Optimization of Process Parameters for Forming Time in Incremental Sheet Forming Process

Zhaobing Liu^{1,a}, Yanle Li^{1,b}, Bill Daniel^{1,b} and Paul Meehan^{1,c}

¹School of Mechanical and Mining Engineering, The University of Queensland, St Lucia, Brisbane, QLD 4072, Australia

^az.liu7@uq.edu.au, ^byanle.li@uq.edu.au, ^cBilld@uq.edu.au, ^dmeehan@uq.edu.au

Keywords: Incremental sheet forming, Optimization, Taguchi method, Orthogonal array

Abstract: Incremental sheet forming (ISF) is a new promising technology due to its flexibility and low-cost tooling properties compared with conventional forming processes. However, it is only suitable for small-batch production because of its incremental feature inducing relative long forming time. Presently, widespread usage of the process is restricted by a lack of predictive understanding of the process due to its complexity. In this paper, the aspect of forming time is studied by investigating the effects of four distinctive process parameters (step over, feed rate, sheet thickness and tool diameter). An effective analysis tool, Taguchi method together with design of experiment (DOE) and analysis of variance (ANVOA) is utilized to study the effects of the four process parameters on forming time and further to optimize parameter combinations in order to minimize forming time. Using these techniques, experimental results show that the step over of spiral tool path is the most important process parameter affecting forming time followed by feed rate. Sheet thickness and tool diameter have little effect on forming time. The comparison between the prediction of optimized parameter combination and the confirmation test result has further demonstrated the effectiveness of the proposed method. It is worth noting that the results of this study will indicate a further direction on how to optimize process parameters to find a balance between forming efficiency (forming time) and forming quality (forming accuracy and surface roughness).

Introduction

With the demands of niche markets and individual preferences on sheet metal products, incremental sheet forming (ISF), as a new promising technology, has received considerable attentions since its inception[1-3]. In the incremental forming process, a simple forming tool is controlled by a computer numerically controlled (CNC) machine following a prescribed tool path which plastically deforms the sheet metal into the desired shape. Basically, there are two variations of incremental sheet forming, single point incremental forming (SPIF) and two point incremental forming (TPIF). In single point incremental forming, the tool deforms the sheet metal into the concave shape without any dies while in two point incremental forming, the tool moves on the convex sheet surface with a positive die. The blank holder should be moved by the hydraulic actuator in order to firmly maintain the sheet metal in the proper working position. One of the advantages of this technology is the cost reduction compared with traditional forming processes such as stamping and deep drawing processes because punches or expensive dies are avoided. However, it is only suitable for small-batch production due to the slowness of the manufacturing process[4,5]. There is thus the challenge of improving forming time in ISF. Although numerous researches in ISF during the last decade has focused on deformation mechanism and the effects of different process parameters on forming process[6,7], proper combination and optimization of process parameters to improve forming efficiency and quality is still an active topic in ISF process and needs to be further investigated. In fact, the lack of forming process knowledge is the main reason behind difficulty of improvement of forming efficiency and quality. In this study, Taguchi-based optimization technique is utilized to investigate the effects of four process parameters, namely step over (S), feed rate (V), sheet thickness (T) and tool diameter (D), on forming

efficiency. It is noted that these four process parameters have the most relevant influence on SPIF process and have been mentioned in many ISF papers. Presently optimal values of these process parameters have been investigated experimentally

Experimental work

Equipment: The experiments were performed on an Amino ISF machine (Model DLNC-PC for industrial use) using steel tools with a tungsten carbide hemispherical head as shown in Fig.1. Shell Tellus Oil 68 was used in the tests as forming oil.



Fig.1. Amino ISF machine.

Material and testing geometry: The material used for the present investigation is AA7075-0 alloy. 7075 is the highest strength alloy of the commercially available aluminum, and is typically used as aircraft structures. The mechanical properties for AA7075-0 are shown in Table 1.

Table 1. Mechanical properties for AA7075-0.

Material Property	Value
Density (kg/m ³)	2,800
Young's modulus (MPa)	75,000
Poisson's ratio	0.33
Yield strength (MPa)	100
Ultimate tensile strength (MPa)	200
Strain hardening coefficient (MPa)	330
Power law coefficient	0.19

A truncated cone (frustum) with a slope angle of 45 degrees was selected as the shape to be optimized, beginning from a square sheet with a side of 300mm. The major base of the cone is 140mm and the height is 50mm. This slope angle for the truncated cone is safe in that fracture of the sheet has not occurred[8]. Fig.2 shows a truncated cone with a curvature generatrix and draw angle changing from 59° to 73°. This shape was successfully made and no fracture has been observed experimentally.

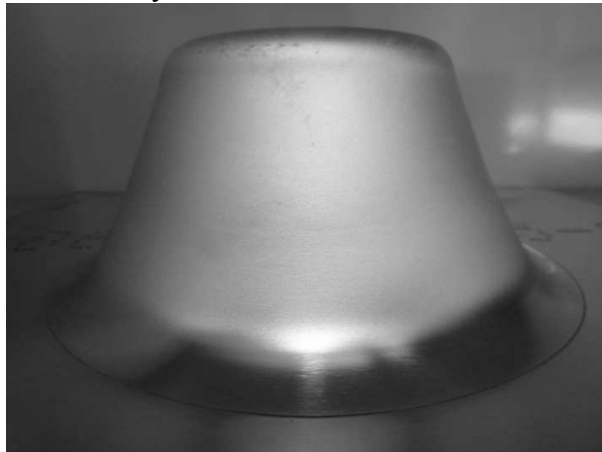


Fig.2. The formability test-a truncated cone with curvature generatrix.

Experimental design tool-Taguchi method

The present investigation utilizes the Taguchi method[7,9-10], which aims to optimize processes in order to minimize quality loss with one of the objective functions of “the-nominal-the-best”, “the-larger-the-better”, or “the-smaller-the-better” depending on the experimental objective. Taguchi method uses an orthogonal array to organize the parameters affecting the process and the levels at which they should be varies. Instead of having to test all possible combinations like the factorial design, the Taguchi method tests pairs of combinations. This allows for the efficient collection of the necessary data to determine which factors most affect product quality with a minimum amount of experimentation. The general design steps involved in Taguchi method are as follows:

1. Define the process objective, or more specifically, a target value for a performance measure of the process.
2. Determine the design parameters affecting the process. Parameters are variables within the process that affect the performance measure set above.
3. Create orthogonal arrays for the parameter design indicating the number of and conditions for each experiment.
4. Conduct the experiments and select the optimum level of process parameters through ANVOA analysis.
5. Perform a confirmation test to verify the optimal process parameters.

The Taguchi optimization procedure starts with selection of orthogonal array. The minimum number of runs in the array is

$$N_{\min} = (L-1)F + 1 \quad (1)$$

where L and F is number of levels and number of factors, respectively. In this study, four process parameters (step over, feed rate, sheet thickness, tool diameter) are chosen as factors to study the effect on forming time. Three levels are defined for each of the factors as summarized in Table 2. Calculated by Eq.(1), L_9 orthogonal array is selected as described in Table 3. The signal-to-noise ratio (S/N) is originally defined as the ratio of the signal to random noise. In Taguchi designs, the S/N ratio represents a measure of robustness used to identify controllable factors (step over, feed rate, sheet thickness and tool diameter) that reduce variability in a product or process by minimizing the effects of uncontrollable factors (loading and unloading time which refer to the time for movement of machine table with workpiece or deformed product to or away from the machine working zone). Higher values of the S/N ratio indicate controllable factor settings that minimize the effects of the uncontrollable factors. Therefore, the S/N ratio is a quality control indicator in which it reflects the influence of changing any process parameters on the performance of the process. Different S/N ratios can be chosen depending on the goal of the experiment. An S/N ratio of the-smaller-the-better as defined in [13] is chosen because the objective is to minimize the output value (forming time) and the target is zero. This is calculated as

$$\eta = -10 \log \left(\frac{1}{n} \sum_{i=1}^n y_i^2 \right) \quad (2)$$

where η is the S/N ratio, n is the number of experiments taken in one test run, y_i indicates the dimensionless output at the i th experiment with respect to one unit measure.

Table 2. Process parameters and their levels studied.

Factors	Description	Level 1	Level 2	Level 3
A	Step-over (Spiral path), S (mm)	0.5	1.0	2.0
B	Feed rate, V (mm/min)	1000	2000	3000
C	Sheet thickness, T (mm)	1.02	1.60	2.54
D	Tool diameter, D (mm)	10	12	15

Table 3. Orthogonal array L9 (3^4) of the experimental runs.

Factors/Run no.	A	B	C	D
	Step over(mm)	Feed rate(mm/min)	Sheet thickness(mm)	Tool diameter(mm)
1	1(0.5)	1(1000)	1(1.02)	1(10)
2	1(0.5)	2(2000)	2(1.60)	2(12)
3	1(0.5)	3(3000)	3(2.54)	3(15)
4	2(1.0)	1(1000)	2(1.60)	3(15)
5	2(1.0)	2(2000)	3(2.54)	1(10)
6	2(1.0)	3(3000)	1(1.02)	2(12)
7	3(2.0)	1(1000)	3(2.54)	2(12)
8	3(2.0)	2(2000)	1(1.02)	3(15)
9	3(2.0)	3(3000)	2(1.60)	1(10)

Experimental results and analysis

In this experiment, the forming time includes the loading and unloading time and can be measured accurately using the Fanuc controller in the Amino ISF machine. Fig.3 shows the formed truncated cones based on Taguchi design. The results of the nine experiments are listed in Table 4 and corresponding S/N ratio are calculated.



Fig.3. The nine formed truncated cones according to Taguchi design.

Table 4. Experimental results for forming time and S/N ratio.

Experimental run no.	Process parameter level				Measured forming time (s)	Calculated S/N ratio (dB)
	Step over (S)	Feed rate (V)	Sheet thickness (T)	Tool diameter (D)		
1	1(0.5)	1(1000)	1(1.02)	1(10)	1872	-65.446
2	1(0.5)	2(2000)	2(1.60)	2(12)	1008	-60.069
3	1(0.5)	3(3000)	3(2.54)	3(15)	717	-57.110
4	2(1.0)	1(1000)	2(1.60)	3(15)	967	-59.709
5	2(1.0)	2(2000)	3(2.54)	1(10)	525	-54.403
6	2(1.0)	3(3000)	1(1.02)	2(12)	380	-51.596
7	3(2.0)	1(1000)	3(2.54)	2(12)	512	-54.185
8	3(2.0)	2(2000)	1(1.02)	3(15)	292	-49.308
9	3(2.0)	3(3000)	2(1.60)	1(10)	217	-46.729

The process of estimating the main effects of each factor is called the analysis of means (ANOM) and the effect of a factor level is the deviation it causes from the overall mean response. The analysis of variance (ANOVA) establishes the relative significance of factors in terms of their percentage contribution to the response. ANOVA is also needed for estimating the error variance for the effects

and variance of the prediction error[11]. The results of the ANOM and ANOVA for four process parameters are presented in Tables 5 and 6 and Fig.4.

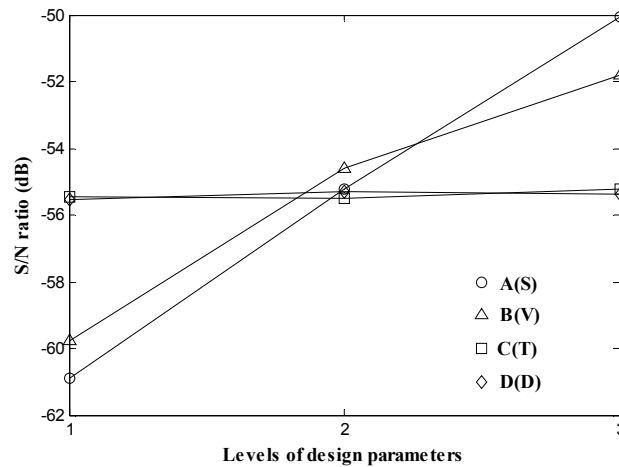


Fig. 4 Graph showing factor effects for S/N ratio.

Table 5. S/N response table for forming time.

Factors	Description	Mean S/N ratio (dB)			Max-min
		Level 1	Level 2	Level 3	
A	Step over, S	-60.875	-55.236	-50.074*	10.801
B	Feed rate, V	-59.780	-54.593	-51.812*	7.968
C	Sheet thickness, T	-55.450	-55.502	-55.233*	0.269
D	Tool diameter, D	-55.526	-55.283*	-55.376	0.243

The total mean S/N ratio=-55.395 dB and * indicates the optimum level.

Table 6. ANOVA table for effect of different forming time.

Factors	Description	Degrees of freedom	Sum of squares	Mean square	Contribution(%)
A	Step over, S	2	175.106	87.553	64.04
B	Feed rate, V	2	98.128	49.064	35.89
C	Sheet thickness, T	2	0.122	0.061	0.04
D	Tool diameter, D	2	0.090	0.045	0.03
Error		0	0	-	-
Total		8	273.446	136.723	100

Those results revealed that the step over (S), which reached 64.04%, made the major contribution to the forming time. While the contribution percentages of the feed rate (V), sheet thickness (T) and tool diameter (D) were at 35.89%, 0.04% and 0.03%, respectively. It can be concluded that the step over had the most significant effect on the forming time followed by feed rate, whereas the influence of sheet thickness and tool diameter can be ignored. Since the ANOVA has resulted in zero degree of freedom for error term, it is necessary to pool the factor having less influence on forming time.

According to the Taguchi method, the higher the η value is, the better the overall performance is. This means that the factor with the highest signal-to-noise ratio should be selected as the optimal level. The average value for each experimental level was calculated using the highest η value for each factor to establish Table 5 and Fig.4. As can be seen in Table 5 and Fig.4, the optimal condition is described as $A_3B_3C_3D_2$, which means step over $S = 2.0$ mm, feed rate $V = 3000$ mm/min, sheet thickness $T = 2.54$ mm and tool diameter $D = 12$ mm. This optimal condition provides minimum forming time to be calculated in the subsequent section.

Confirmation test

Once the optimal level of the design parameters has been selected, a confirmation experiment is needed to validate the results with the predicted optimal conditions in Table 5 and Fig.4. The estimated S/N ratio $\hat{\eta}$ using the optimal level of the design parameters can be calculated as:

$$\hat{\eta} = \eta_m + \sum_{i=1}^k (\bar{\eta}_i - \eta_m) \quad (3)$$

where η_m is the total mean S/N ratio, $\bar{\eta}_i$ is the mean S/N ratio at the optimal level, and k is the number of the main process parameters that affect the quality of the process. Table 7 shows the results of confirmatory tests at optimal level A₃B₃C₃D₂.

Table 7. Results of confirmatory tests at optimal level A₃B₃C₃D₂

	Predicted	Observed	Error
Forming time (s)	205	217	12
S/N ratio (dB)	-46.2	-46.7	0.5

As can be seen in Table 7, the optimal conditions provide a minimum forming time of 205s calculated by Eq.(3). The observed experimental forming time is higher than the predicted value (205s), but the error between them is only 5.9%. The deviation of S/N ratio is also only 1.1%, confirming a good agreement between predicted and observed S/N ratio values.

In order to verify the closeness of predicted S/N ratio with that of observed S/N ratio, confidence interval (CI) value of predicted S/N ratio for the optimum factor level combination at 95% CI is determined [12]. The prediction error, i.e., the difference between predicted S/N ratio and observed S/N ratio is within the CI value (± 0.80 dB), so the choice of optimal combination of process parameters for minimizing forming time is statistically confirmed.

Conclusions

In this paper, the process parameters influencing forming time in ISF process has been investigated. The Taguchi method, a powerful analysis tool, together with DOE and ANOVA is utilized to determine the best combination of process parameters in order to minimize forming time. Further, the best combination values were confirmed by the experimental verification. The conclusions drawn from the results are as follows:

1. The most significant process parameter influencing forming time is the step over followed by the feed rate. The sheet thickness and tool diameter have little effect on forming time, so in this study their influence can be ignored.
2. Using Taguchi method, the optimal combination of process parameters has been determined and minimum forming time has been predicted as 205 s based on optimal values of step over, feed rate, sheet thickness and tool diameter.
3. Additional confirmation experiments at these optimal conditions have been carried out. The experimental results have shown a very good agreement with the prediction results for forming time obtained by Taguchi analysis. Confidence interval was calculated as ± 0.80 dB to statistically confirm the good agreement between prediction and experimental results.

The contribution of this work is to clarify the most influential process factors influencing forming time and determine the best combination in order to improve forming efficiency. The next step is to investigate process parameter values to optimize the forming quality while simultaneously minimizing forming time.

Acknowledgments

This work was financially supported by the ARC Linkage Program, Boeing Research Technology and QMI Solutions. Many thanks to Michael Elford, Paul Bellette and Prasad Gudimetla for their support and useful comments.

References

- [1] J. Jeswiet, F. Micari, G. Hirt, A. Bramley, J. Duflou and J. Allwood, CIRP Ann. – Manuf. Techn. 54, 623(2005)
- [2] W.C. Emmens and A.H. van den Boogaard, J. Mater. Process. Technol. 209, 3688 (2009)
- [3] Z.B. Liu, P. Meehan and P. Bellette, Adv. Mater. Res. 337,452 (2011)
- [4] W.K.H. Sarraji, J. Hussain and W.X. Ren, Mater. Manuf. Process. 27, 499 (2012)
- [5] R. Malhotra, N.V.Reddy and J. Cao, J. Manuf. Sci. E.-T. ASME, 132, 061003-1 (2010)
- [6] K. Jackson and J. Allwood, J. Mater. Process. Technol., 209, 1158 (2009)
- [7] D.T. Nguyen, J.G. Park, H.J Lee and Y.S. Kim, P. I. Mech. Eng. B- J. Eng. 224, 913 (2009)
- [8] G. Hussain, L. Gao, N. Hayat and L. Qijian, Int. J. Mach. Tools Manuf. 47, 2177 (2007)
- [9] V.N. Gaitonde, S.R. Karnik, B.T. Achyutha and B. Siddeswarappa, J. Mater. Process. Technol. 202, 374 (2008)
- [10] C. Gologlu and N. Sakarya, J. Mater. Process. Technol. 206, 7 (2008)
- [11] M.S. Phadke, Editor, Quality Engineering using Robust Design, Prentice Hall, Englewood Cliffs, New Jersey (1989)
- [12] P.J. Ross, Editor, Taguchi Techniques for Quality Engineering, McGraw-Hill, New York (1996)
- [13] G. Taguchi, S. Chowdhury and Y.I. Wu, Editor, Taguchi's Quality Engineering Handbook, Wiley, Michigan (2005)

4.1.4 Surface Roughness

Paper F

Modelling and optimization of surface roughness in incremental sheet forming using a multi-objective function

Liu, Z.B., Liu, S., Li, Y.L., Meehan, P.A.

Materials and Manufacturing Processes

2014, Volume: 29(7), Pages: 808-818.

Modeling and Optimization of Surface Roughness in Incremental Sheet Forming using a Multi-objective Function

ZHAOBING LIU, SHENG LIU, YANLE LI, AND PAUL ANTHONY MEEHAN

*Department of Mechanical Engineering, School of Mechanical and Mining Engineering,
The University of Queensland, Brisbane, Australia*

As a critical product quality constraint, surface roughness is regarded as a weak point in incremental sheet forming (ISF). It is of great importance to identify the impact of forming parameters on the surface roughness and optimize the surface finish at the production stage. This paper proposes a systematic approach to modeling and optimizing surface roughness in ISF. The quantitative effects of four parameters (step down, feed rate, sheet thickness, and tool diameter) on surface roughness are analyzed using the response surface methodology with Box–Behnken design. The multi-objective function is used to evaluate the overall surface roughness in terms of the tool-sheet contact surface roughness, i.e., internal surface roughness and the noncontact surface roughness, i.e., external surface roughness. Additionally, the average surface roughness (R_a) on each surface is measured along the tool-path step-down direction taking the impact of sheet roll marks into account. The optimal conditions for the minimization of overall surface roughness are determined as step down (0.39 mm), feed rate (6000 mm/min), sheet thickness (1.60 mm), and tool diameter (25 mm). This study shows that Box–Behnken design with a multi-objective function can be efficiently applied for modeling and optimization of the overall surface roughness in ISF.

Keywords Aluminum; Box–Behnken; Deformation; Forming; Incremental; Objective; Optimization; Response; Roughness; Surface.

INTRODUCTION

New trends in sheet metal forming are rapidly developing to meet various demands in the niche market. Incremental sheet forming (ISF), as a promising technology, has demonstrated its high potential to shape complex three-dimensional parts without using specific tooling [1–6]. However, the forming accuracy, including the geometric accuracy at the macroscopic level and the surface finish at the microscopic level, is still one of the major concerns for industrial applications. Extensive research has been steered into the improvement of forming accuracy on a macro scale [3, 5, 6]. However, relatively high surface roughness is considered as a significant issue in ISF, which has gained research interest in the past few years [7–10]. Of particular interest, Hagan and Jeswiet [7] performed surface roughness tests and analyzed the influence of several forming variables, such as step-down size and spindle speed, on surface roughness. They concluded that the surface finish can be viewed as a resultant of large-scale waviness created by the tool path and small-scale roughness induced by large surface strains. With step-down sizes decreasing, the morphology of surfaces transforms from waviness to strict roughness without waviness.

In Ref. [8], analytical and experimental results were compared in terms of surface roughness in single point incremental forming (SPIF). Three process parameters – tool radius, step-down size, and slope angle were selected to establish the analytical model by means of considering geometrical relations. The roughness values R_a , R_z , and the mean spacing between profile peaks were evaluated as the output of the models. The prediction and experimental results showed that a good agreement can be achieved with an error below 10%. Hamilton et al. [9] investigated the influences of tool feed rates and spindle rotation at high speeds during forming on the noncontact side roughness (i.e., orange peel effect). A model for the orange peel prediction in SPIF was established, which provided some guidelines for the improvement of external surface quality by choosing desirable process parameters during forming. Powers et al. [10] investigated the surface metrology through a SPIF case analysis. The effect of sheet rolling mark direction and analysis direction on surface topology in SPIF considering two process variables (feed rate and forming direction) was first studied. The results showed that surface roughness R_z is greater with rolling marks perpendicular to forming orientation. Lasunon et al. [11] assessed the effects of three process parameters on the surface roughness in SPIF by a factorial design. The results showed that wall angle, depth increment, and its interaction play an important role on the surface roughness, while feed rate has little effect.

The previous studies have shown that focus was given to tool-sheet contact surface roughness, i.e., internal surface roughness and noncontact surface roughness, i.e., external surface roughness independently with

Received August 6, 2013; Accepted November 6, 2013

Address correspondence to Zhaobing Liu, Department of Mechanical Engineering, School of Mechanical and Mining Engineering, The University of Queensland, Brisbane, Australia; E-mail: zhaobing.liu@uqconnect.edu.au, z.liu7@uq.edu.au

Color versions of one or more of the figures in the article can be found online at www.tandfonline.com/lmmp.

respect to the influence of specific process parameters. However, in most applications, the surface quality of both internal and external surfaces of formed parts requires to be maximized with the aim of reaching a desired design level. An efficient forming process should be modeled and optimized to guarantee a steady manufacturing process with the aim of achieving the required surface roughness. Therefore, an efficient predictive modeling for surface roughness in ISF is needed to assist ISF designers to better understand and control the surface quality at the production stage. In this paper, a systematic approach to modeling and optimizing of the overall surface roughness in ISF has been developed considering the effect of four main process factors (step down, feed rate, sheet thickness, and tool diameter). The major work and contributions are briefly summarized as follows:

- The efficient surface roughness modeling is implemented using response surface methodology (RSM) with Box–Behnken design, which is widely employed to develop, improve, and optimize a production process and evaluate the corresponding importance of several process parameters considering complex interactions [12–15]. A similar research on modeling and optimization of thinning rate and forming force in SPIF can be found in Ref. [15]. However, as discussed above, little research has been focused on the evaluation of overall surface roughness.
- A multi-objective function [16], as a simple efficient approach to converting multiple responses to a single response, is used to evaluate the overall surface roughness associated with both the internal contact and the external noncontact surface roughness. Then, the overall surface roughness, as a single response, is minimized using a single-objective desirability function [13]. The predicted optimal forming conditions are determined and compared with the predicted values using a desirability function with multiple responses [14, 17].

- The impact of roll mark orientation of 7075-O aluminum sheets on surface roughness (R_a) is hypothesized and clarified when the surface roughness measurement is carried out along the step-down direction. Although this aspect has been considered in Ref. [10], the effect of only two process factors and the internal contact surface roughness was taken into account, which may limit the findings. This study has further investigated and clarified this aspect by taking more process factors and both internal and external surfaces into consideration.

METHODOLOGY

Surface Roughness Characterization in ISF

Throughout this study, surface roughness characterization is analyzed using SPIF. However, the analysis methodology can be easily applied to other types of ISF process, such as two point incremental forming. In SPIF, surface finish on the internal surface can be characterized as a resultant of large-scale waviness created by the forming path and small-scale roughness induced by large surface strains (Fig. 1(a)). As for the external surface, roughness is mainly caused by large surface strains, which usually leads to an orange peel phenomenon (Fig. 1(b)). In addition, as the step-down size decreases, the internal tool-sheet contact surface will change from a waviness look to a strict roughness look as seen in Fig. 2, which describes the evolution of internal tool-sheet contact surface look.

As discussed above, a typical internal surface in SPIF exhibits both roughness and waviness. A detailed illustration can be described in Fig. 3. It is noted that the measurement of surface irregularities due to roughness is carried out without considering the more widely spaced irregularities caused by waviness. In addition, in order to clarify the surface characterization created by SPIF, the roughness measurement on the internal and external surfaces is performed along the step-down direction perpendicular to tool-path direction.

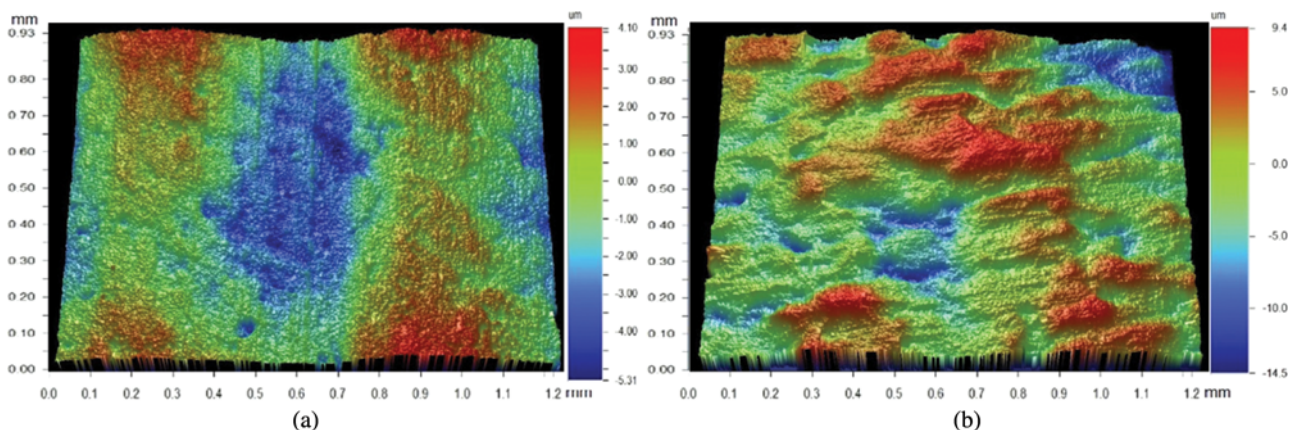


FIGURE 1.—Surface topography in SPIF: (a) internal tool-sheet contact surface; (b) external noncontact surface (shape: a 45° cone, step down: 0.5 mm, feed rate: 1000 mm/min, tool diameter: 10 mm, sheet thickness (AA7075-O): 1.02 mm).

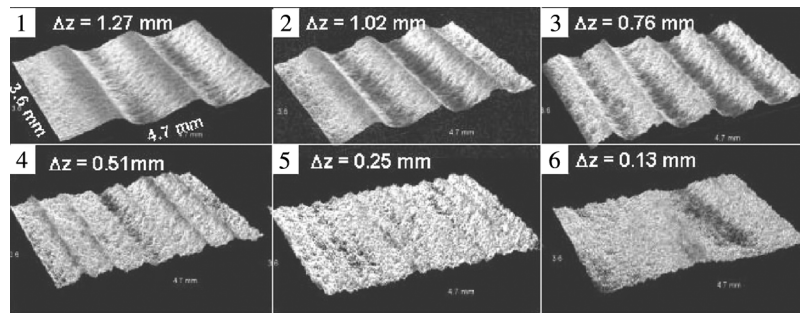


FIGURE 2.—Evolution of internal tool-sheet contact surface roughness with a tool diameter of 12.7 mm influenced by different step-down sizes [7].

Another focus of surface quality in ISF is to examine how much roll marks can influence the surface roughness. Roll marks on metal sheets are a kind of shallow marks created during the manufacture of the sheets (see the lines from top to bottom in Fig. 4). Roughness measurement direction relative to roll mark orientation is taken into account. In this research, a pyramidal shape with 55° draw angle is designed as a test benchmark, see Fig. 5. For this investigated pyramidal shape, the z-level tool path will travel parallel and perpendicular to the roll mark direction during forming. Figure 5 shows an example of tested pyramidal shapes, which illustrates that two squared samples with a size of 30 mm × 30 mm are taken from each side of the wall in regions A and B and used for the surface roughness measurement. The two samples in region A are measured parallel to the roll mark direction, and the other two samples in region B are measured perpendicular to the roll mark direction. Ten measurements are implemented on each sample, and then the arithmetic average is taken to represent the surface roughness values for each sample in regions A and B, respectively.

R_a is chosen as the studied quantity of surface roughness, which is the universally recognized, and most used, international parameter of roughness (ISO 4287:1997 standard). It is the arithmetic mean of the profile departures from the mean line within the measuring distance l (Fig. 6) [13].

Modeling Methodology – Response Surface Methodology with Box–Behnken Design

The surface roughness modeling employs the RSM based on design of experiments along with a statistical analysis. As an empirical modeling technique, RSM

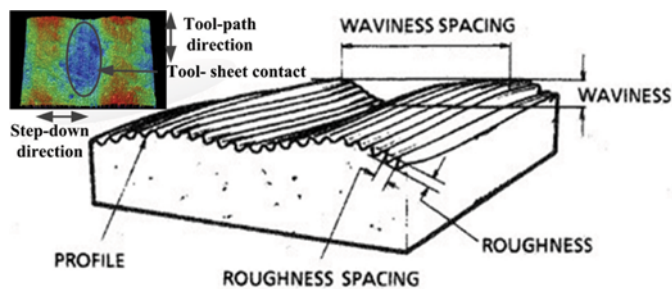


FIGURE 3.—Illustration of surface characteristics in detail.

can be used to evaluate the relationship between controllable process variables and experimental results. Three main procedures are involved in the optimization process: (i) performing a statistical experimental design;

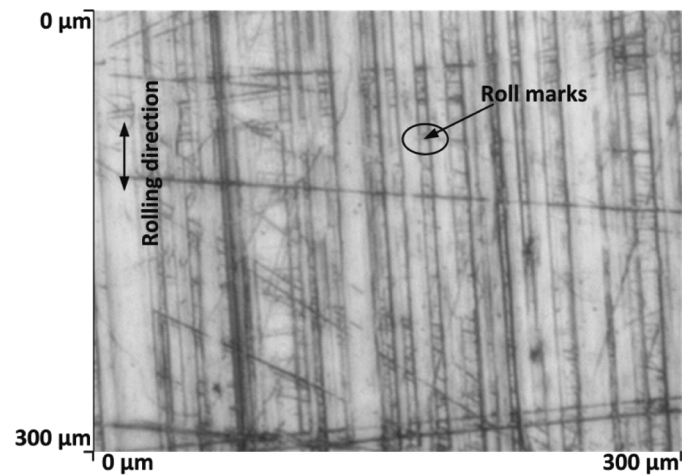


FIGURE 4.—Optical image for roll marks on AA7075-O sheets with a thickness of 1.02 mm.

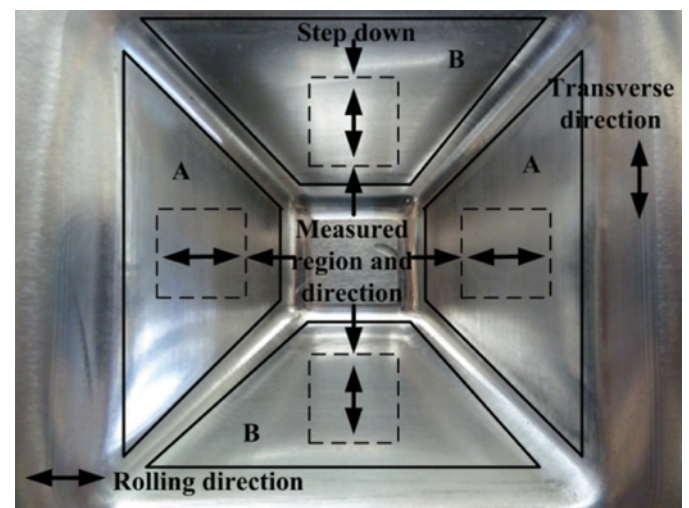


FIGURE 5.—An example of tested pyramidal shapes with 55° draw angle illustrating measured regions and directions parallel and perpendicular to roll mark direction.

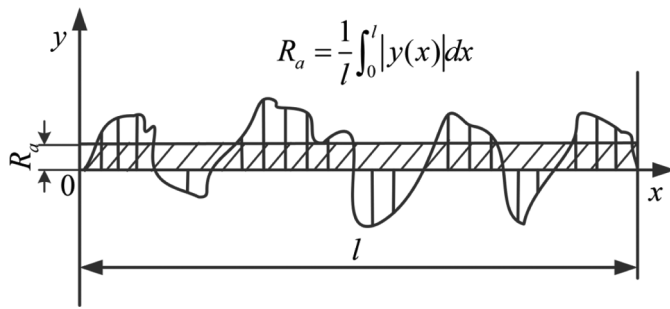


FIGURE 6.—Definition of R_a .

(ii) determining the coefficients in a mathematical model;
 (iii) predicting the response and checking the adequacy of the developed model [14]. Based on the developed model, surface roughness can be predicted under different process conditions over a wide range of forming process factors. In this study, a quadratic mathematical model with a four-factor, three-level design was constructed to explore quadratic response surfaces.

Twenty-seven experiments have been performed to evaluate the effects of four main independent factors on surface roughness. Using a nonlinear regression method, the quadratic mathematical model can be fit to the experimental results. The corresponding model terms can also be identified. Taking linear terms, square terms and linear by linear interaction terms into consideration, the quadratic response model can be established as

$$Y = \beta_0 + \sum_{i=1}^4 \beta_i X_i + \sum_{i=1}^4 \beta_{ii} X_i^2 + \sum_{i=1}^4 \sum_{j=2, i < j}^4 \beta_{ij} X_i X_j \quad (1)$$

where Y is the predicted response surface function, β_0 is the model constant, β_i is the slope or linear effect of the input factor X_i , β_{ii} is the quadratic effect of input factor X_i , and β_{ij} is the linear by linear interaction effect between the input factor X_i and factor X_j . In this work, the experimental design software Minitab 16 is used for data analysis and result plotting.

Multi-Objective Function

The original RSM is only limited to single response optimization. To minimize the internal surface roughness SR_i and the external surface roughness SR_e simultaneously, a simple modification to evaluate the overall surface response for multi-objective performance has been adopted [16]. As described in Fig. 7, this approach utilizes the membership functions μ_α and μ_β as weighting factors, which can be used to calculate the corresponding objective functions.

$$\mu_\alpha = 1 - \frac{SR_i}{SR_{i,max}} \quad (2)$$

$$\mu_\beta = 1 - \frac{SR_e}{SR_{e,max}} \quad (3)$$

where $SR_{i,max}$ and $SR_{e,max}$ are the maximum values of internal surface roughness SR_i and external surface roughness SR_e , respectively, assumed according to experimental measurements. The simultaneous optimization of SR_i and SR_e requires the minimization of the shaded area as depicted in Fig. 7. Therefore, the multi-objective function for the overall surface roughness $SR_{overall}$ is defined as

$$SR_{overall} = \frac{1}{2} SR_i (1 - \mu_\alpha) + \frac{1}{2} SR_e (1 - \mu_\beta) \quad (4)$$

EXPERIMENTAL WORK

Sheet Material

AA 7075 O-temper aluminum alloy sheets with thicknesses of 1.02, 1.60 and 2.54 mm are used, which have practical and wide industrial applications, such as aircraft structures due to their higher formability compared with the other temper conditions.

Experimental Equipment

Experimental investigations are performed on the AMINO[®] DLNC-PC incremental forming machine in

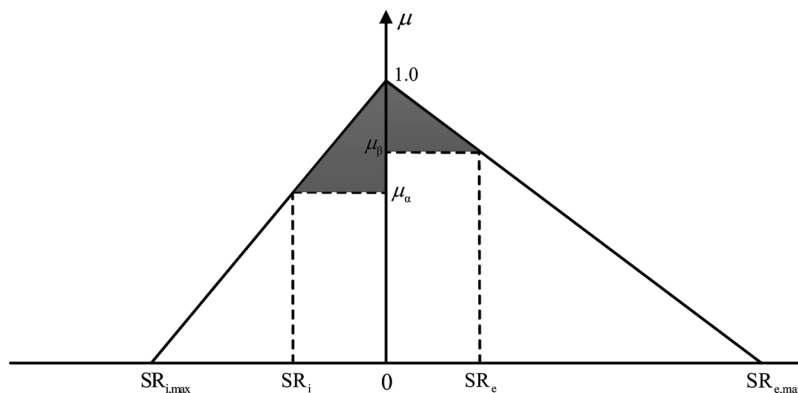


FIGURE 7.—Membership functions for internal tool-sheet contact surface roughness SR_i and external noncontact surface roughness SR_e [16].

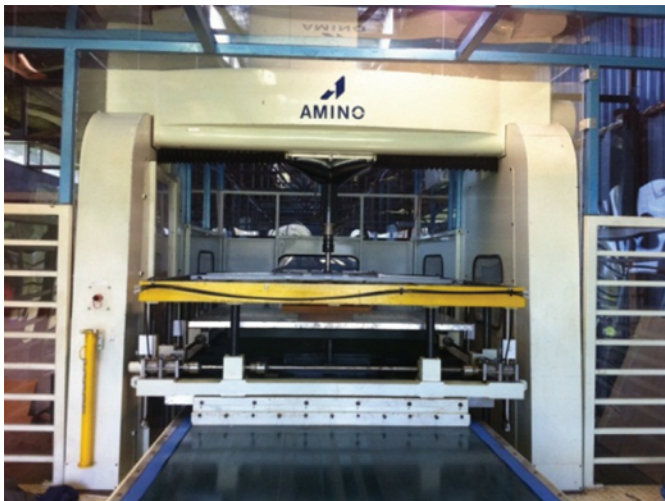


FIGURE 8.—The Amino ISF machine for experiments.

Fig. 8. The machine is a three-axis CNC machine with a maximum workspace of $2100 \times 1450 \times 500 \text{ mm}^3$ and can exert maximum forces of 3.0 kN in vertical axis and 1.5 kN in X - and Y -axis. The maximum feed rates in X - and Y -axes are 6000 mm/min and 1000 mm/min, respectively, in the Z -axis. In the experiments, the forming tools with diameters of 15, 20, and 25 mm are used. The applied forming feed rates are 4000, 5000, and 6000 mm/min. The step-down sizes of z -level tool path are set to be 0.2, 0.5 and 0.8 mm. Before forming, lubricant oil-Shell Tellus Oil 68 is sprayed on the blank.

Measuring Equipment for Surface Roughness

The surface roughness measurements are implemented using a portable, self-contained instrument (Taylor-Hobson Surtronic 3+ Profilometer [Leicester, United Kingdom] in Fig. 9). According to ISO standard, nonperiodic roughness profile evaluation has been



FIGURE 9.—Taylor-Hobson Surtronic 3+ Profilometer.

conducted with a high-pass Gaussian filter. In this work, the sampling length, evaluation length, and calculated resolution are set to be 0.8, 4, and 0.01 μm , respectively.

RESULTS AND DISCUSSION

Design of Experiments

The coded four main independent factors are described in Table 1. It is worth noting that the main purpose of this study is to provide a modeling and analysis methodology for surface roughness, therefore the selection of range of parameters is based on the feasibility and efficiency of actual forming (other choices could be chosen) and is not specifically optimized. The design matrix generated for Box–Behnken design is provided in Table 2.

As discussed in Section 2, surface roughness for the final part may be influenced by roll marks, which needs to be examined and clarified by measurements. Figure 10 shows the measured results, showing the influence of roll marks on surface roughness (internal surface and external surface) in regions A and B. For the internal tool-sheet contact surface, the surface roughness measured parallel (region A) and perpendicular (region B) to the roll mark direction is nearly the same in all cases, indicating that roll marks have little influence on the internal surface roughness for all experimental combinations in terms of R_a . As for the external noncontact surface, the biggest variation of the measured data is approximately 15.2%, which demonstrates the roughness of external noncontact surface is affected by the roll marks to some extent especially for experimental combinations (no. 5–8, 13–20) with sheet thicknesses of 1.02 and 2.54 mm. Furthermore, Fig. 10 shows that the trend of surface roughness can be compared in terms of different data group with only one factor changing.

In addition, the roughness (R_a) measured perpendicular to the roll mark direction is slightly greater than that measured parallel to the roll mark direction. In Fig. 11, optical images for experimental sample 17 are provided to further examine the hypothesis and analyze the impact of roll marks on surface measurements. From Fig. 11(a) and (b), it is noted that roll marks cannot be clearly observed after forming, which means the internal surface quality is mainly influenced by forming tool paths. The influence of roll marks can be neglected on internal tool-sheet contact surfaces. This conclusion consists with the roughness measurements depicted in Fig. 10. In contrast, the external noncontact surface

TABLE 1.—Independent factors and coded levels for response surface.

Independent factors	Coded symbols	Levels		
		−1	0	1
Step down – Sd (mm)	X_1	0.2	0.5	0.8
Feed rate – Fr (mm/min)	X_2	4000	5000	6000
Sheet thickness – St (mm)	X_3	1.02	1.60	2.54
Tool diameter – Td (mm)	X_4	15	20	25

TABLE 2.—Box–Behnken design for four factors and observed responses.

No.	X_1	X_2	X_3	X_4	SR_i (μm)	SR_e (μm)	SR_{overall} (μm)
1	-1(0.2)	-1(4000)	0(1.60)	0(20)	0.53	1.68	0.43
2	-1(0.2)	1(6000)	0(1.60)	0(20)	0.53	1.66	0.42
3	1(0.8)	-1(4000)	0(1.60)	0(20)	1.09	1.67	0.70
4	1(0.8)	1(6000)	0(1.60)	0(20)	1.03	1.69	0.67
5	0(0.5)	0(5000)	-1(1.02)	-1(15)	0.72	3.25	1.45
6	0(0.5)	0(5000)	-1(1.02)	1(25)	0.64	3.42	1.55
7	0(0.5)	0(5000)	1(2.54)	-1(15)	0.87	3.83	2.02
8	0(0.5)	0(5000)	1(2.54)	1(25)	0.68	3.77	1.87
9	-1(0.2)	0(5000)	0(1.60)	-1(15)	0.47	1.72	0.43
10	1(0.8)	0(5000)	0(1.60)	-1(15)	1.28	1.65	0.83
11	-1(0.2)	0(5000)	0(1.60)	1(25)	0.32	1.66	0.37
12	1(0.8)	0(5000)	0(1.60)	1(25)	0.71	1.76	0.53
13	0(0.5)	-1(4000)	-1(1.02)	0(20)	0.68	3.34	1.50
14	0(0.5)	-1(4000)	1(2.54)	0(20)	0.70	4.04	2.14
15	0(0.5)	1(6000)	-1(1.02)	0(20)	0.66	3.51	1.63
16	0(0.5)	1(6000)	1(2.54)	0(20)	0.73	3.75	1.88
17	-1(0.2)	0(5000)	-1(1.02)	0(20)	0.65	3.54	1.66
18	-1(0.2)	0(5000)	1(2.54)	0(20)	0.48	3.84	1.87
19	1(0.8)	0(5000)	-1(1.02)	0(20)	0.94	3.74	1.98
20	1(0.8)	0(5000)	1(2.54)	0(20)	1.61	3.86	2.61
21	0(0.5)	-1(4000)	0(1.60)	-1(15)	0.74	1.75	0.54
22	0(0.5)	-1(4000)	0(1.60)	1(25)	0.46	1.69	0.41
23	0(0.5)	1(6000)	0(1.60)	-1(15)	0.78	1.71	0.54
24	0(0.5)	1(6000)	0(1.60)	1(25)	0.42	1.72	0.42
25	0(0.5)	0(5000)	0(1.60)	0(20)	0.58	1.65	0.43
26	0(0.5)	0(5000)	0(1.60)	0(20)	0.57	1.69	0.45
27	0(0.5)	0(5000)	0(1.60)	0(20)	0.59	1.68	0.45

roughness is affected by roll marks to a small extent, which can be clearly distinguished in Fig. 11(c) and (d). The external surface quality in Fig. 11(c) along the roll mark orientation seems better than that in Fig. 11(d) perpendicular to the roll mark orientation. The possible reason is the external surface roughness perpendicular to the roll mark orientation is mainly

induced by large surface strains during forming together with initial roll marks compared with the roughness mainly caused by large surface strains along the roll mark direction. This finding is also verified by the roughness measurements as shown in Fig. 10, especially for the experimental combinations with sheet thicknesses of 1.02 and 2.54 mm.

In Table 2, the corresponding surface roughness results are also provided in the last three columns. To simplify the modeling process in terms of the observed experimental data, the average of the surface roughness values in regions A and B can be taken with the aim of representing the overall internal surface roughness and the overall external surface roughness, as seen in Table 2 (columns SR_i and SR_e). Furthermore, based on the roughness values (SR_i and SR_e), $SR_{i,\text{max}}$ and $SR_{e,\text{max}}$ in the membership functions (Eqs. (2) and (3)) can be assumed as 1.65 and 4.10 μm , respectively. The calculated overall surface roughness SR_{overall} in Eq. (4) is shown in Table 2 (see the last column). Therefore, the simultaneous minimization of SR_i and SR_e involves the minimization of multi-objective function SR_{overall} .

Estimated RSM Model

An empirical relationship described by a quadratic mathematical model (Eq. (1)) was fitted in terms of the experimental results derived from Box–Behnken design and multi-objective function. The empirical model with the coded factors is given as follows:

$$\begin{aligned}
 SR_{\text{overall}} = & 0.4425 + 0.1787X_1 - 0.0126X_2 + 0.2181X_3 \\
 & - 0.0547X_4 + 0.1539X_1^2 + 0.0036X_2^2 \\
 & + 1.3629X_3^2 - 0.0369X_4^2 - 0.0052X_1X_2 \\
 & + 0.1043X_1X_3 - 0.0605X_1X_4 - 0.0985X_2X_3 \\
 & + 0.0004X_2X_4 - 0.0616X_3X_4 \quad (5)
 \end{aligned}$$

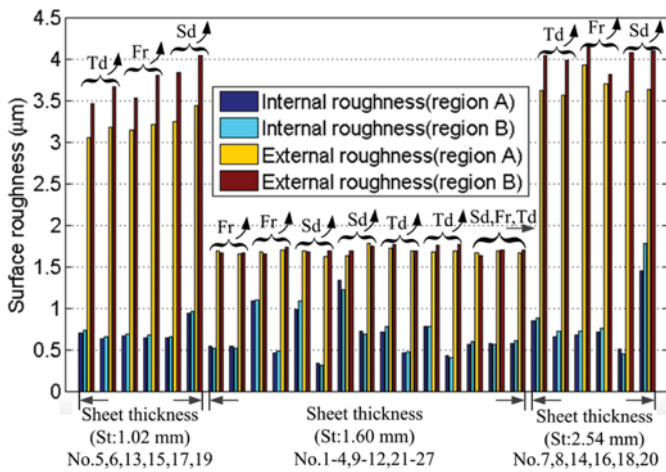


FIGURE 10.—Measured results of internal and external surface roughness. Note: Sd, Fr, St, and Td are defined as step down, feed rate, sheet thickness, and tool diameter, respectively.

Analysis of variance (ANOVA) is adopted in order to examine the test for the importance and fitness of the established model [12–14, 17]. The results of ANOVA for the overall surface roughness are given in Table 3. Usually, P -values less than 0.05 indicate that the model terms have an important impact on the response. As shown in Table 3, the model F -value of 94.80 with a probability P -value of less than 0.0001 implies the model is significant. In addition, it can be seen that sheet thickness (X_3) is the most influential factor on the overall surface roughness followed by step down (X_1) by examining the F -value and the P -value. The coefficients in Eq. (5) indicate the relative influence of each factor to the response, in which the positive sign means the ability to increase the response and vice versa. The value of predicted R^2 is used to measure the prediction ability of the established model. To achieve a reasonable agreement, the values of predicted R^2 and adjusted R^2 should be within approximately 0.20. Otherwise, a problem possibly exists in the experimental data or the fitted model. In this case, the predicted R^2 is 0.9484, which reasonably

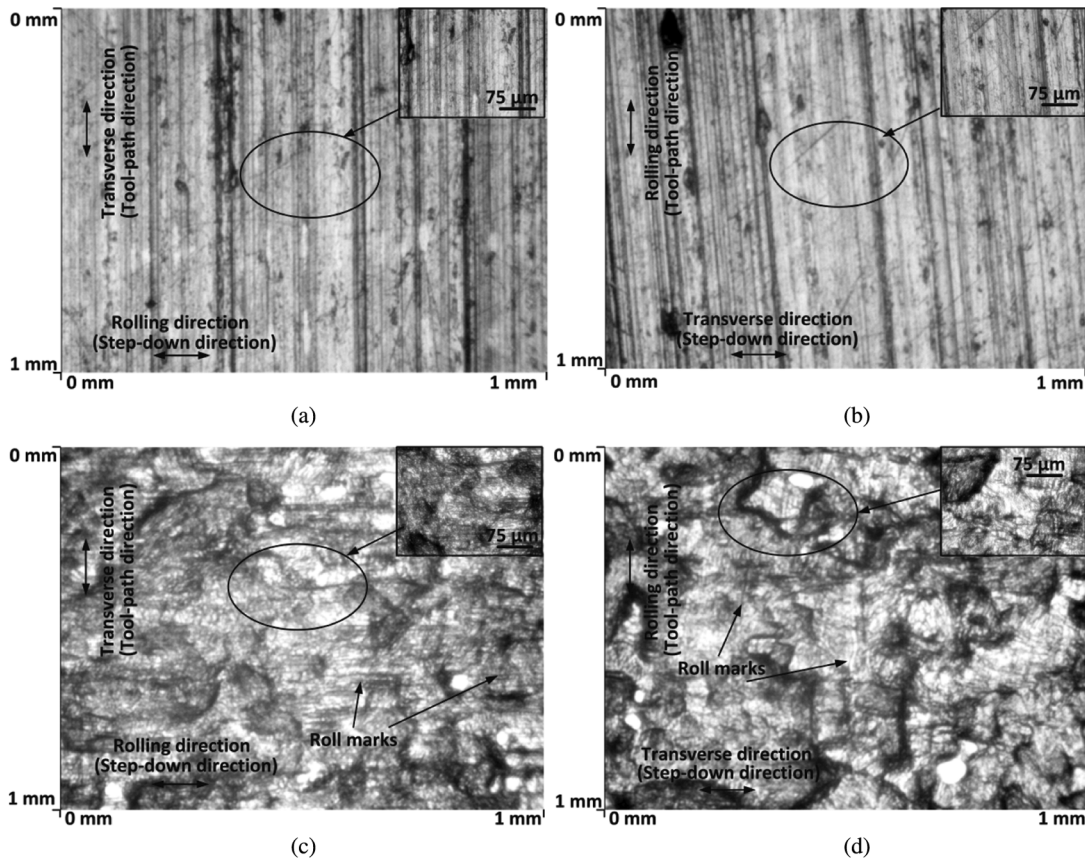


FIGURE 11.—Optical images for experimental sample 17: (a) internal roughness–region A; (b) internal roughness–region B; (c) external roughness–region A; (d) external roughness–region B.

consists with the adjusted R^2 of 0.9806. As some of the square and interaction terms presented little effect on the model (have a very high P -value), these less

significant sources can be excluded from the regression analysis. Therefore, the empirical model in Eq. (5) can be simplified as

TABLE 3.—Results of ANOVA for overall surface roughness (from Minitab).

Source	SS	DF	MS	F-value	P-value
Model	13.2306	14	0.9450	94.80	0.0000
X_1 (Step down)	0.3831	1	0.3831	38.43	0.0000
X_2 (Feed rate)	0.0019	1	0.0019	0.19	0.6690
X_3 (Sheet thickness)	0.5705	1	0.5705	57.23	0.0000
X_4 (Tool diameter)	0.0359	1	0.0359	3.60	0.0820
X_1^2 (Step down ²)	0.1262	1	0.1263	12.66	0.0040
X_2^2 (Feed rate ²)	0.0001	1	0.0001	0.01	0.9350
X_3^2 (Sheet thickness ²)	9.9072	1	9.9072	993.86	0.0000
X_4^2 (Tool diameter ²)	0.0073	1	0.0073	0.73	0.4100
X_1X_2 (Step down * Feed rate)	0.0001	1	0.0001	0.01	0.9180
X_1X_3 (Step down * Sheet thickness)	0.0435	1	0.0435	4.37	0.0590
X_1X_4 (Step down * Tool diameter)	0.0146	1	0.0146	1.47	0.2490
X_2X_3 (Feed rate * Sheet thickness)	0.0388	1	0.0388	3.89	0.0720
X_2X_4 (Feed rate * Tool diameter)	0.0000	1	0.0000	0.00	0.9940
X_3X_4 (Sheet thickness * Tool diameter)	0.0152	1	0.0152	1.52	0.2410
Residual	0.1196	12	0.0100		
Lack of Fit	0.1195	10	0.0120	147.99	0.0070
Cor total	13.3502	26			

Note: SS, DF, and MS denote sum of squares, degree of freedom, and mean square, respectively.

$$\begin{aligned}
 SR_{\text{overall}} = & 0.4425 + 0.1787X_1 - 0.0126X_2 + 0.2181X_3 \\
 & - 0.0547X_4 + 0.1539X_1^2 + 1.3629X_3^2 \\
 & - 0.0369X_4^2 + 0.1043X_1X_3 - 0.0605X_1X_4 \\
 & - 0.0985X_2X_3 - 0.0616X_3X_4 \quad (6)
 \end{aligned}$$

Analysis of Response Surface

The three-dimensional graphs are provided to illustrate the relationships between experimental factors and responses. In Fig. 12, the response surfaces are built by step down (X_1) and sheet thickness (X_3). To be more specific, Fig. 12(a) shows the changes of the overall surface roughness when feed rate (X_2) and tool diameter (X_4) are set as 4000 mm/min and 15 mm, respectively. The overall surface roughness slightly rises as step down (X_1) increases. However, as sheet thickness (X_3) becomes bigger, the overall surface roughness first decreases and then increases again. The big change shows that sheet thickness (X_3) is the most significant forming variable influencing the overall surface roughness, which is consistent with the analysis in the ANOVA table. The possible reason is the sheets with different thicknesses can lead to different surface strains during forming, which have a significant influence on surface finish. The evolution of the overall surface roughness in Fig. 12(b) and (c) represents a similar trend as that in Fig. 12(a),

which illustrates that the factors of feed rate (X_2) and tool diameter (X_4) have little influence on the overall surface roughness.

The response surfaces are constructed by feed rate (X_2) and tool diameter (X_4) in Fig. 13, in which step down (X_1) is kept as a constant 0.5 mm, and the factor sheet thickness (X_3) is changed from 1.02 to 2.54 mm. It is observed that as sheet thickness (X_3) increases, a large difference can be found in terms of the overall surface roughness between Fig. 13(a), (b), and (c). In Fig. 13(a), it can be noted that the trend of the overall surface roughness goes up as feed rate (X_2) and tool diameter (X_4) increase. On the contrary, in Fig. 13(b) and (c), the values of overall surface roughness go down as feed rate (X_2) and tool diameter (X_4) increases. This further illustrates that sheet thickness (X_3) has a significant impact on the overall surface roughness. The middle level with sheet thickness ($X_3 = 1.6$ mm) appears to be the turning point of the overall surface roughness, having the least range of overall surface roughness.

Figure 14 shows the response surfaces constructed by feed rate (X_2) and tool diameter (X_4) but with constant sheet thickness (X_3) of 1.60 mm and step down (X_1) changing from 0.2 to 0.8 mm. The trend of the overall surface roughness rises and then goes downwards as tool diameter (X_4) increases. As for the situations in Fig. 14(b) and (c), a descending trend of the overall

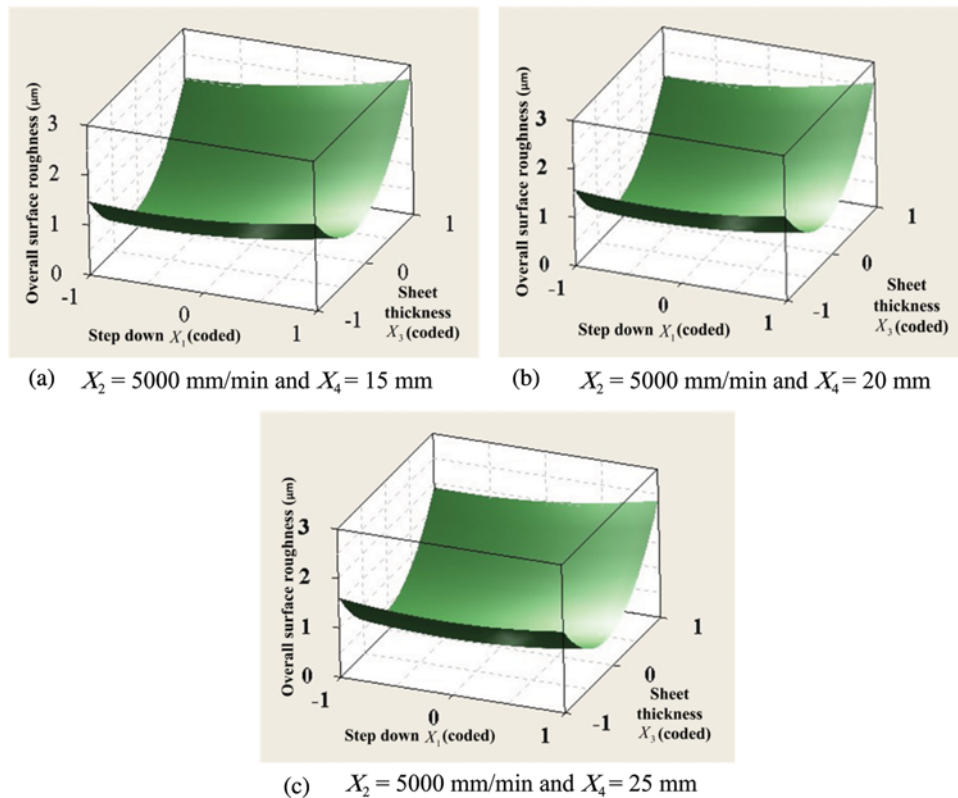


FIGURE 12.—Three-dimensional response surface showing the effect of factors step down (X_1) and sheet thickness (X_3) on the overall surface roughness with the constant feed rate (X_2) of 5000 mm/min: (a) tool diameter (X_4) = 15 mm; (b) tool diameter (X_4) = 20 mm; (c) tool diameter (X_4) = 25 mm.

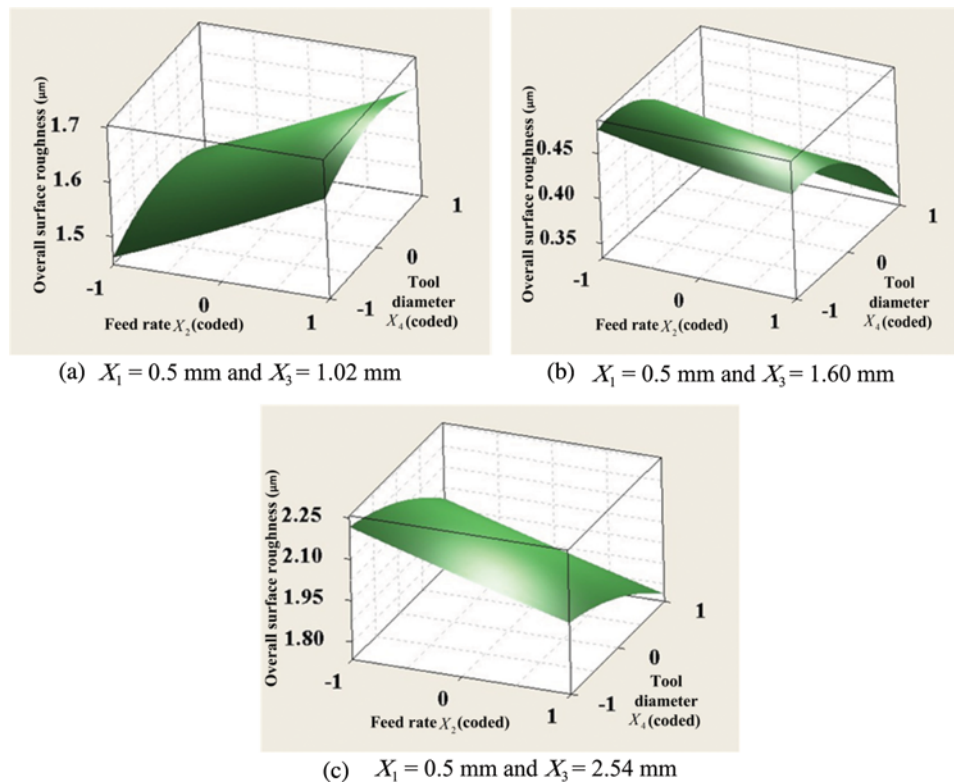


FIGURE 13.—Three-dimensional response surface showing the effect of factors feed rate (X_2) and tool diameter (X_4) on the overall surface roughness with the constant step down (X_1) of 0.5 mm: (a) sheet thickness (X_3) = 1.02 mm; (b) sheet thickness (X_3) = 1.60 mm; (c) sheet thickness (X_3) = 2.54 mm.

surface roughness can be observed. Feed rate (X_2) has little effect on the overall surface roughness in all these figures. As discussed in Ref. [4], the surface finish can be viewed as a resultant of large-scale waviness created by the tool path and small-scale roughness induced by large surface strains, which is less likely affected by feed rate (X_2). This is the possible reason why feed rate (X_2) represents little influence on the surface roughness. In addition, the magnitude of the overall surface roughness increases dramatically from Fig. 14(a) to (c), indicating that step down (X_1) is another important influential process factor on the overall surface roughness. The reason is step down (X_1) can cause waviness marks on the internal contact surface as shown in Figs. 1(a) and 2. This is also identified by the high F -value and low P -value in the ANOVA table.

Optimization

This section discusses the optimization method to minimize the overall surface roughness obtained from the multi-objective function with the aim of simultaneous minimization of both internal and external surface roughness. Two methods have been used. One is the proposed multi-objective function with single-response desirability function, which can simplify the optimization process. The other is the direct desirability function with multiple responses for a comparison purpose. The numerical optimization process in Minitab

has been performed with the aim of finding the specific optimal experimental conditions. The difference between the multi-objective function method and the direct desirability function method with multiple responses is that the multi-objective function method first converts the multiple observed values to a single observed value, and then the nonlinear programming approach (single-objective desirability function) is employed to find the optimal values [13]. In contrast, the direct desirability function method includes two stages: (i) determining levels of the independent factors in order to simultaneously produce the most desirable predicted responses on the dependent factors and (ii) maximizing the overall desirability in terms of the controllable factors [14].

Figure 15(a) shows the optimization results using the multi-objective function. As can be seen, the optimal conditions are determined as step down (0.39 mm), feed rate (6000 mm/min), sheet thickness (1.60 mm), and tool diameter (25 mm), obtaining a minimum overall surface roughness 0.32 μm . Figure 15(b) shows the optimization results using the desirability function with multiple responses. The calculated minimum overall surface roughness is 0.37 μm under the optimal conditions of step down (0.33 mm), feed rate (5333 mm/min), sheet thickness (1.60 mm), and tool diameter (25 mm). The predicted error between these two methods is 12.8%, showing that the proposed multi-objective function method is reliable.

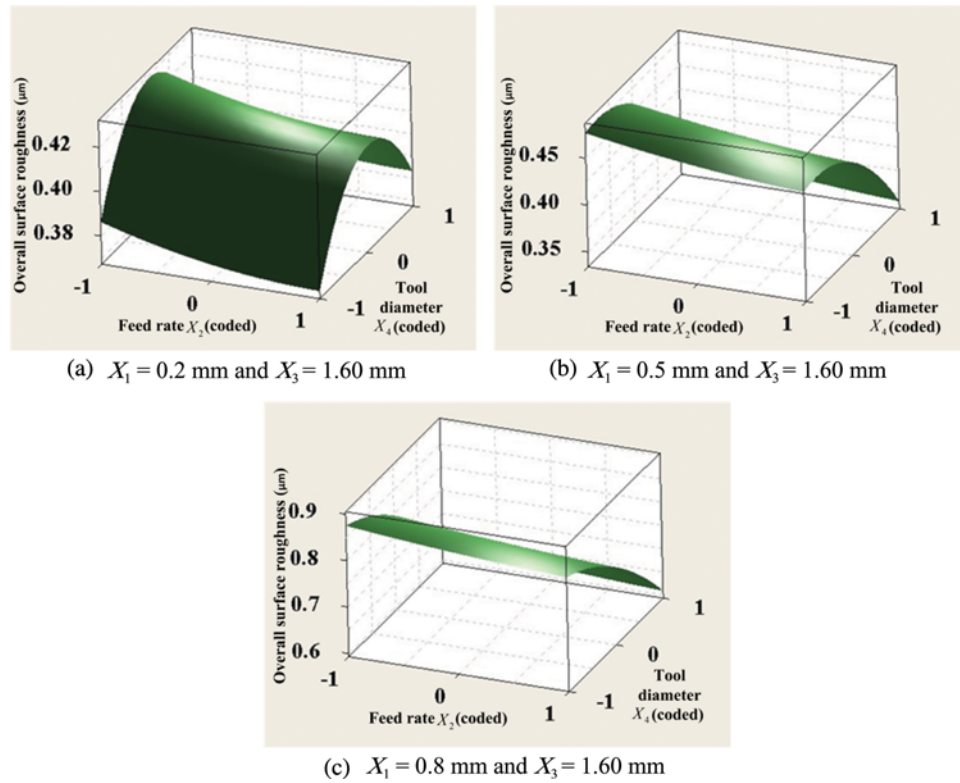


FIGURE 14.—Three-dimensional response surface showing the effect of factors feed rate (X_2) and tool diameter (X_4) on the overall surface roughness with the constant sheet thickness (X_3) of 1.60 mm: (a) step down (X_1) = 0.2 mm; (b) step down (X_1) = 0.5 mm; (c) step down (X_1) = 0.8 mm.

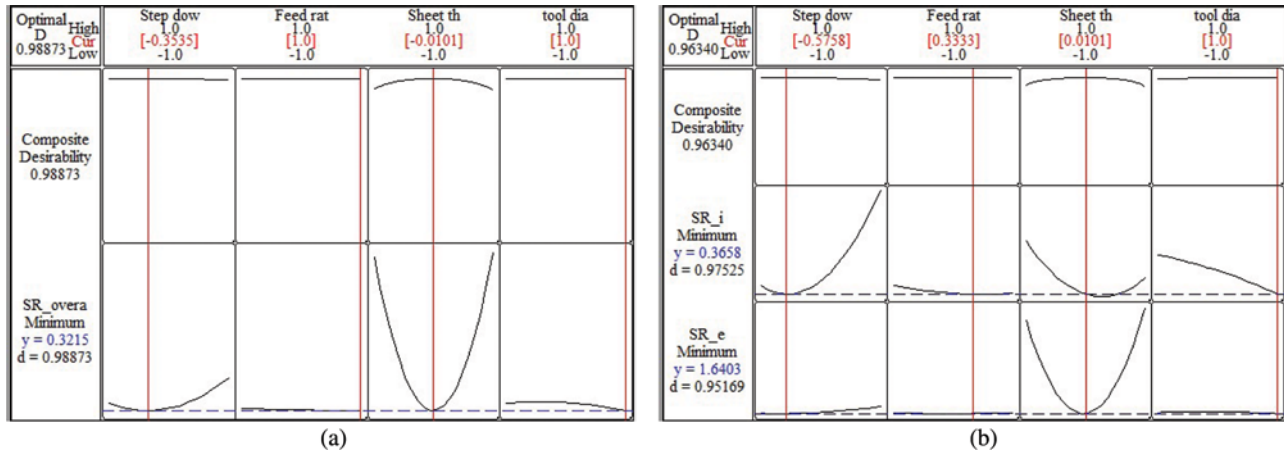


FIGURE 15.—Optimization results: (a) multi-objective function with single-objective desirability function; (b) desirability function with multiple responses.

Finally, for experimental validation, a duplicate confirmatory experiment on the ISF machine was conducted using the optimal parameters. The internal and external surface roughness was measured as 0.38 and 1.69 μm , respectively. This gives an overall surface roughness of 0.39 μm compared with 0.32 μm for the optimization analysis using the multi-objective function approach. It indicates that Box–Behnken design in conjunction with the multi-objective function can be used as a modeling

methodology to optimize the overall surface roughness in SPIF.

CONCLUSION

In this study, empirical modeling and optimization of the overall surface roughness in ISF have been investigated. RSM with Box–Behnken design and multi-objective function was employed to establish the

prediction model and examine the impact of four forming variables on the overall surface roughness. The conclusions can be drawn as follows:

- As an efficient and reliable approach, the proposed multi-objective method can be used to evaluate the overall surface roughness in SPIF compared with those of simultaneous optimization of multiple responses using a desirability function.
- Sheet thickness is the most influential forming variable on the overall surface finish, followed by step down. In contrast, feed rate and tool diameter have little influence on the overall surface roughness. Furthermore, the optimal experimental conditions were determined as step down (0.39 mm), feed rate (6000 mm/min), sheet thickness (1.60 mm), and tool diameter (25 mm) with a minimum overall surface roughness 0.32 μm , which is effectively confirmed by a validation experiment.
- Roll marks have small influences on the external surface roughness with respect to R_a for AA7075-O sheets with thicknesses of 1.02 and 2.54 mm. As for the internal surface, tool paths have dominant effects on the surface quality with little influence of roll marks. Surface roughness on the external noncontact surface is always higher than that of the internal tool-sheet contact surface in the range of investigated factor values.

This research provided a systematic insight into the impact of forming variables on the surface finish in ISF. This information could be extensively applied to a further design of process control system to predict and control the surface quality of final parts manufactured by ISF.

FUNDING

The authors would like to thank the ARC Linkage Program, Boeing Research and Technology Australia (BRTA) and QMI Solutions in Australia for the funding and assistance in undertaking this work.

REFERENCES

1. Jeswiet, J.; Micari, F.; Hirt, G.; Bramley, A.; Dufloy, J.; Allwood, J. Asymmetric single point incremental forming of sheet metal. *CIRP Annals – Manufacturing Technology* **2005**, *54* (2), 88–114.
2. Liu, Z.B.; Li, Y.L.; Meehan, P.A. Vertical wall formation and material flow control for incremental sheet forming by revisiting multistage deformation path strategies. *Materials and Manufacturing Processes* **2013**, *28* (5), 562–571.
3. Radu, C.; Tampu, C.; Cristea, I.; Chirita, B. The effect of residual stresses on the accuracy of parts processed by SPIF. *Materials and Manufacturing Processes* **2013**, *28* (5), 572–576.
4. Silva, M.B.; Martinho, T.M.; Martins, P.A.F. Incremental forming of hole-flanges in polymer sheets. *Materials and Manufacturing Processes* **2013**, *28* (3), 330–335.
5. Dejardin, S.; Thibaud, S.; Gelin, J.C.; Michel, G. Experimental investigations and numerical analysis for improving knowledge of incremental sheet forming process for sheet metal parts. *Journal of Materials Processing Technology* **2010**, *210* (2), 363–369.
6. Allwood, J.M.; Braun, D.; Music, O. The effect of partially cut-out blanks on geometric accuracy in incremental sheet forming. *Journal of Materials Processing Technology* **2010**, *210* (11), 1501–1510.
7. Hagan, E.; Jeswiet, J. Analysis of surface roughness for parts formed by computer numerical controlled incremental forming. *Proceedings of the Institution of Mechanical Engineers, Part B: Journal of Engineering Manufacture* **2004**, *218* (10), 1307–1312.
8. Durante, M.; Formisano, A.; Langella, A. Comparison between analytical and experimental roughness values of components created by incremental forming. *Journal of Materials Processing Technology* **2010**, *210* (14), 1934–1941.
9. Hamilton, K.; Jeswiet, J. Single point incremental forming at high feed rates and rotational speeds: Surface and structural consequences. *CIRP Annals – Manufacturing Technology* **2010**, *59* (1), 311–314.
10. Powers, B.M.; Ham, M.; Wilkinson, M.G. Small data set analysis in surface metrology: An investigation using a single point incremental forming case study. *Scanning* **2010**, *32* (4), 199–211.
11. Lasunon, O.U. Surface roughness in incremental sheet metal forming of AA5052. *Advanced Materials Research* **2013**, *753–755*, 203–206.
12. Wang, W.; Kweon, S.H.; Yang, S.H. A study on roughness of the micro-end milled surface produced by a miniature machine tool. *Journal of Materials Processing Technology* **2005**, *162–163*, 702–708.
13. Krajnik, P.; Kopac, J.; Sluga, A. Design of grinding factors based on response surface methodology. *Journal of Materials Processing Technology* **2005**, *162–163*, 629–636.
14. Mourabet, M.; El Rhilassi, A.; El Boujaady, H.; Bennani-Ziatni, M.; El Hamri, R.; Taitai, A. Removal of fluoride from aqueous solution by adsorption on apatitic tricalcium phosphate using Box–Behnken design and desirability function. *Applied Surface Science* **2012**, *258*, 4402–4410.
15. Bahloul, R.; Arfa, H.; Belhadjsalah, H. Application of response surface analysis and generic algorithm for the optimization of single point incremental forming process. *Key Engineering Materials* **2013**, *554–557*, 1265–1272.
16. Gaitionde, V.N.; Karnik, S.R.; Achyutha, B.T.; Siddeswarappa, B. Taguchi optimization in drilling of AISI 316L stainless steel to minimize burr size using multi-performance objective based on membership function. *Journal of Materials Processing Technology* **2008**, *202* (1–3), 374–379.
17. Li, M.; Feng, C.Q.; Zhang Z.Y.; Liu, X.; Ma, W.F.; Xue, Q.; Sugiura, N. Optimization of electrochemical ammonia removal using Box–Behnken design. *Journal of Electroanalytical Chemistry* **2011**, *657*, 66–73.

4.2 Multi-Pass Modeling and Its Validation

4.2.1 SPIF Multi-Pass Deformation Design

Paper G

**Vertical wall formation and material flow control for
incremental sheet forming by revisiting multi-stage
deformation path strategies**

Liu, Z.B., Li, Y.L., Meehan, P.A.

Materials and Manufacturing Processes

2013, Volume: 28(5), Pages: 562-571.

Vertical Wall Formation and Material Flow Control for Incremental Sheet Forming by Revisiting Multistage Deformation Path Strategies

ZHAOBING LIU, YANLE LI, AND PAUL ANTHONY MEEHAN

University of Queensland, School of Mechanical and Mining Engineering, Brisbane, Australia

In this article, multistage deformation path strategies for single point incremental forming (SPIF) are revisited with the purpose of controlling material flow (improving sheet thickness distribution) and forming a vertical wall surface for cylindrical cups. It is noted that stretching and thinning are two main deformation modes during SPIF. How to control material flow in an optimal way is a key point for successful forming. Multistage incremental forming shows more advantages than single-stage forming, especially dealing with shapes with steep walls. In this study, three basic multistage deformation path strategies have been proposed, that is: A. incremental part diameter; B. incremental draw angle; and C. incremental part height and draw angle. Those strategies and their combinations have been evaluated in terms of formability and compared in order to understand the material allocation mechanism and optimize the multistage forming process. In addition, approximate plane-strain analysis models have been given to provide formability predictions between single-stage and multistage strategies, and between strategies B and C, respectively. The prediction results show good agreement with the experimental results. It is demonstrated that the strategic combination A + B is the optimal way to achieve the forming target.

Keywords Aluminum; Deformation; Flow; Formability; Forming; Fracture; Material; Multistage; SPIF; Thickness.

INTRODUCTION

Nowadays, new trends of sheet metal forming are rapidly developing to meet various demands in the niche market. In order to achieve the aims of flexibility and cost reduction, several new metal forming processes have been proposed in recent years. An example is the incremental sheet forming (ISF) technology which has gained great attention due to its suitability for rapid prototyping and small volume production. In the ISF process, a forming tool is controlled by a computer numerically controlled (CNC) machine following a prescribed tool path which locally plastically deforms the sheet metal into the desired shape. Basically, there are two variations of incremental sheet forming; single point incremental forming (SPIF) and two point incremental forming (TPIF). The rudimentary illustrations are shown in Figs. 1 and 2, respectively. The characteristic feature of SPIF is that a part is shaped by the movement of a forming tool that has a single point contact with the sheet metal. The sheet is clamped with a sheet holder that remains at a constant height. In most cases, with the purpose of improving forming accuracy in the transition zone between the flange and the forming geometry, a backing plate is utilized underneath the sheet. For TPIF, a partial or full positive die is required to provide more control of the sheet deformation and enhance the accuracy to a part through the forming process. The sheet holder can be moved by the hydraulic

actuator with the aim of keeping the sheet metal in the exact working position.

Recently, articles [1] and [2] have provided a comprehensive review on the development of ISF technology and pointed out some research opportunities and challenges. Several active research directions have been focused to explain the deformation mechanism and develop the forming process, including formability [3–5]; process forces [6, 7]; process accuracy [8, 9]; surface finish [10, 11]; deformation path design [12, 13], forming process optimization [14, 15], and so on. In the following discussion, a detailed review of existing works is provided to clarify the motivation for this study.

One of the simplest geometrical models for ISF, which is widely utilized by ISF researchers to predict the sheet thickness in recent years, is the sine law [16]. It assumes the forming process is a pure projection of material points along the forming direction from the start to the end configuration. However, in view of the sine law, as draw angle tends to 90° , the final sheet thickness would be zero. So the sine law cannot predict acceptable thickness results when applied to this situation, but it reflects a decreasing trend on thickness distribution. Bambach [17] has developed a kinematic geometrical model to predict the sheet thickness which obtains more accurate results compared with the sine law. This is because the kinematic model reproduces the sine law on flat surfaces, and corrects it in curved areas. But it also has some limitations, i.e., bending effects are neglected and cannot be applied directly to multistage tool path strategies.

In order to overcome excessive thinning and avoid fracture, multistage deformation path strategies have

Received September 19, 2012; Accepted November 22, 2012

Address correspondence to Zhaobing Liu, University of Queensland, School of Mechanical and Mining Engineering, Brisbane, Australia; E-mail: z.liu7@uq.edu.au

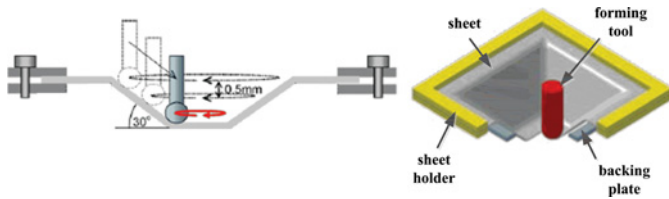


FIGURE 1.—Single point incremental forming (SPIF) [1,5] (color figure available online).

been proposed to address this problem and form metal parts with steep walls. The idea behind these strategies is to control material flow properly and relocate material as much as possible to the critical areas. In [16], a two-stage strategy was developed to improve the final thickness distribution for the geometries with steep walls. The results showed that the occurrence of a thinning band in the single-stage forming process can be delayed in the two-stage process. So it can be used to produce geometries with steep walls. Duflo et al. [18] explored a multistep tool path strategy to manufacture parts with vertical walls in order to avoid part failure. They observed that the final thinning in multistage forming process can exceed the maximum thickness reductions in the single-stage process, which means a formability shift. Manco et al. [12] studied the effect of tool trajectory on the final thickness distribution and formability. Four different multistage strategies have been implemented to manufacture the same shape and evaluate thickness distributions. Skjoedt et al. [13] investigated a multistage strategy to produce cylindrical cups with vertical walls. They pointed out that the movement of the forming tool in multistage SPIF has a great influence on thickness distribution. SPIF is limited by cracking rather than necking. The multistage forming idea is also applied to other ISF processes, such as hole-flanging, see [19], [20] for details.

Considering the above discussion, there is still no effective process model to predict the material thickness distribution in the multistage deformation path context, especially when forming vertical wall surfaces. Experimental measurement is still a reliable way to investigate the thickness distribution for the manufactured geometry. In this study, the methodology of forming vertical wall surfaces in SPIF is investigated with deformation path design by revisiting multistage strategies. Different strategies and their combinations with multistage ideas are evaluated and the optimal combination

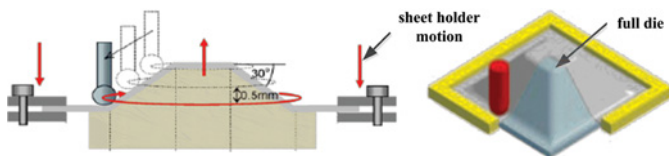


FIGURE 2.—Two point incremental forming (TPIF) [1,5] (color figure available online).

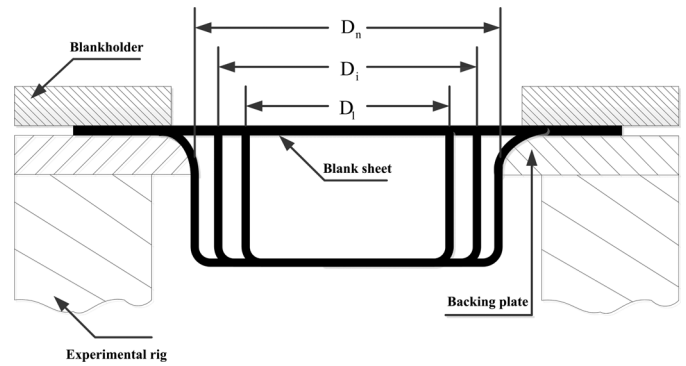


FIGURE 3.—Strategy A: incremental part diameter.

is determined based on formability. In addition, approximate plane-strain analysis models are proposed to provide formability predictions in comparison with experimental results. Corresponding thickness distributions are measured to analyze the material flow and to provide insight into the material relocation mechanism.

METHODOLOGY

In this section, three aspects are considered. First, three different multistage deformation path strategies have been proposed. Then, the experimental setup is introduced in detail. Finally, the approximate plane-strain analysis models have been given to provide formability predictions between single-stage and multistage strategies, and between strategies B and C, respectively.

Multistage Deformation Path Strategies

Three controllable parameters related to the formed geometry are considered, namely, part diameter, part draw angle, and part height, as variables in each strategy, see details in Figs. 3–5. For strategy A, the part diameter is increased from D_1 to D_n gradually. The reason of using this strategy is that material in the central area is expected to create more bending deformation rather than stretching deformation. For strategy B, draw angle can be increased gradually to reach the final wall

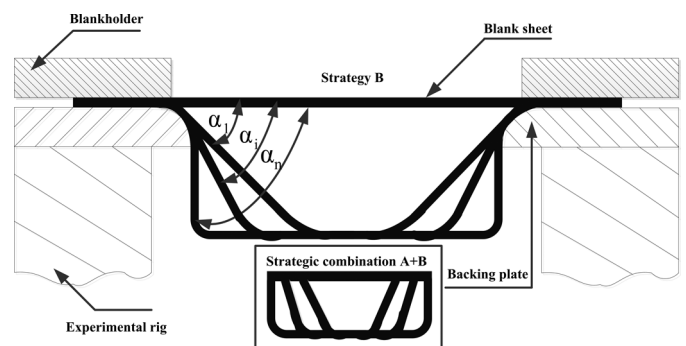


FIGURE 4.—Strategy B: incremental part draw angle.

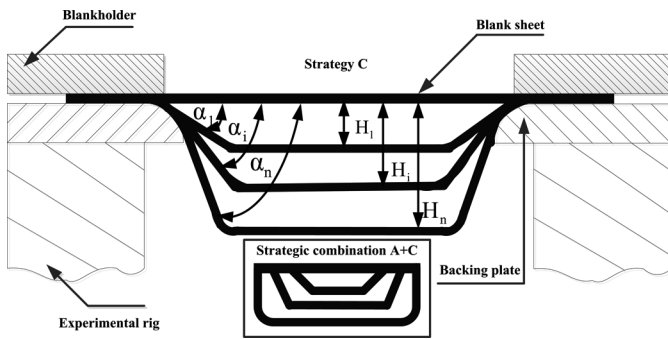


FIGURE 5.—Strategy C: incremental part height and draw angle.

angle (90°). The aim of using this strategy is to regulate as much material as possible to involve deformation. For strategy C, the formed part height and draw angle are increased simultaneously in steps to reach the final shape. It is noted that the individual use of strategy A is not practical and will be utilized in combination with strategy B and strategy C to evaluate the forming results.

In this study, five stages for each strategy or strategic combination are adopted to form the vertical wall surface for cylindrical cups, and corresponding parameter values are given in Table 1. It is worth noting that draw angle can be seen as a formability indicator, so two different initial draw angles for strategies B and C are chosen to estimate their influences on thickness distribution.

Experimental Setup

A series of multistage deformation path experiments were conducted to form the vertical wall surfaces for cylindrical cups on an Amino ISF machine (Model DLNC-PC for industrial use) shown in Fig. 6. The forming tool has a tungsten carbide hemispherical head with a radius of 10 mm. The material used for the present investigation is AA7075-O aluminum alloy. AA7075 aluminum alloy is the highest strength alloy of the commercially available aluminum and is typically used as aircraft structures. The mechanical properties for AA7075-O are shown in Table 2.

The size of blank sheet used in experiments is 300 mm \times 300 mm \times 1.6 mm. Before forming, lubricant oil-Shell Tellus Oil 68 was sprayed on the blank. A backing plate was utilized underneath the sheet in order to increase the rigidity between the forming area and sheet flange. Z-level tool path with vertical step-down size of 0.5 mm was utilized. The feed rate of forming



FIGURE 6.—Amino ISF machine at the University of Queensland (color figure available online).

tool was 2,000 mm/min. The corresponding movement of the forming tool can be illustrated from step 1 to step 4 in Fig. 7.

First, the tool moves in the vertical direction with the desired pitch. Then, it moves along circumferential path in counter clockwise direction. Once this circulation movement is finished, the tool moves and penetrates the sheet along the part surface and begins the next circulation movement in clockwise direction. As discussed in [21], this kind of tool path tends to cancel out the influence of shear during successive levels, and the twist phenomenon can be eliminated. The investigated geometry is a cylindrical cup with vertical wall surface shown in Fig. 8.

Simplified Qualitative Analysis of Multistage Deformation Path Design

In this section, an approximate analysis model has been proposed to qualitatively compare the formability between single-stage and multistage forming processes, and strategies B and C in multistage forming. The motivation is to provide an efficient simplified means of predicting the relative success of different forming strategies. The comparison of approximate prediction and experimental results will be provided in Section 3.1.

Recently, in article [22], authors gave a brief explanation why multistage deformation path strategy can

TABLE 1.—Parameter values for different stages.

Strategy	Stage 1	Stage 2	Stage 3	Stage 4	Stage 5
A	$D_1 = 120 \text{ mm}$	$D_2 = 125 \text{ mm}$	$D_3 = 130 \text{ mm}$	$D_4 = 135 \text{ mm}$	$D_5 = 140 \text{ mm}$
B	$\alpha_1 = 40^\circ$	$\alpha_2 = 52.5^\circ$	$\alpha_3 = 65^\circ$	$\alpha_4 = 77.5^\circ$	$\alpha_5 = 90^\circ$
	$\alpha_1 = 50^\circ$	$\alpha_2 = 60^\circ$	$\alpha_3 = 70^\circ$	$\alpha_4 = 80^\circ$	$\alpha_5 = 90^\circ$
C	$H_1 = 6 \text{ mm}$	$H_2 = 12 \text{ mm}$	$H_3 = 18 \text{ mm}$	$H_4 = 24 \text{ mm}$	$H_5 = 30 \text{ mm}$
	$\alpha_1 = 40^\circ$	$\alpha_2 = 52.5^\circ$	$\alpha_3 = 65^\circ$	$\alpha_4 = 77.5^\circ$	$\alpha_5 = 90^\circ$
	$\alpha_1 = 50^\circ$	$\alpha_2 = 60^\circ$	$\alpha_3 = 70^\circ$	$\alpha_4 = 80^\circ$	$\alpha_5 = 90^\circ$

TABLE 2.—Mechanical properties for AA7075-O sheets with 1.6 mm thickness.

Strategies and Strategic combinations	Initial draw angle	Stage 1	Stage 2	Stage 3	Stage 4	Stage 5	H _F
A + C	$\alpha_1 = 40^\circ$	Success	Success	Success	Failure		24 mm
	$\alpha_1 = 50^\circ$	Success	Success	Success	Failure		22.5 mm
	$\alpha_1 = 90^\circ$	Success	Success	Success	Failure		22 mm
A + B	$\alpha_1 = 40^\circ$	Success	Success	Success	Success	Success	
	$\alpha_1 = 50^\circ$	Success	Success	Success	Success	Success	
C	$\alpha_1 = 40^\circ$	Success	Success	Success	Failure		22.5 mm
	$\alpha_1 = 50^\circ$	Success	Success	Success	Failure		21 mm
B	$\alpha_1 = 40^\circ$	Success	Success	Success	Success	Failure	30 mm
	$\alpha_1 = 50^\circ$	Success	Success	Success	Success	Failure	29.5 mm

lead to less thickness thinning according to plain-strain deformation mechanism. Using a similar approach, the deformation mechanism has been approximately analysed in single-stage and multistage forming processes in Subsection 2.3.1, and strategies B, C adopted in this study in Subsection 2.3.2. Geometrical relations are expressed in Figs. 9a and 9b.

In this study, the analysis is simplified for qualitative purposes based on the following assumptions:

1. thickness strain deformation only occurs in shear (sloped) sections;
2. deformation is due to shear only;
3. incremental deformations in multistage forming may be superposed to provide a total strain measure for qualitative comparison of different forming strategies.

The purpose of the following analysis is to provide only a qualitative comparison of the forming strategies. More detailed quantitative analysis is recommended for future research.

Simplified deformation analysis for qualitative comparison of single-stage forming and multistage forming. For Fig. 9a, take the first two multi-stages (Stages 1 and 2) for instance, the forming target is the sloped wall section L_3 . It is noted that the sheared section lengthformed after stage 1 is $L_0 - L_2$ from an initial length L_1 and then

becomes $L_3 + L_4$ after stage 2. Therefore the principle strain due to shear only in multi-stage forming ϵ_M , can be expressed as,

$$\epsilon_M = \ln \frac{L_1}{L_0 - L_2} + \ln \frac{L_3 + L_4}{L_1} = \ln \frac{L_3 + L_4}{L_0 - L_2}. \quad (1)$$

In contrast, for the single-stage forming process, the final sheared wall section lengthformed is only L_3 from an initial section length $L_0 - L_2 - L_4$. Therefore the principal strain due to shear only, ϵ_S , can be expressed as,

$$\epsilon_S = \ln \frac{L_3}{L_0 - L_2 - L_4}. \quad (2)$$

Using Eqs. (1) and (2) and then,

$$\epsilon_M - \epsilon_S = \ln \frac{L^3 + L^4}{L^3 + L_3L_4}, \quad (3)$$

where $L' = L_0 - L_2 - L_4$.

From Fig. 9a, the geometrical relationship $L_3 > L'$ holds, and using Eq. (3) it is shown that

$$\epsilon_M < \epsilon_S. \quad (4)$$

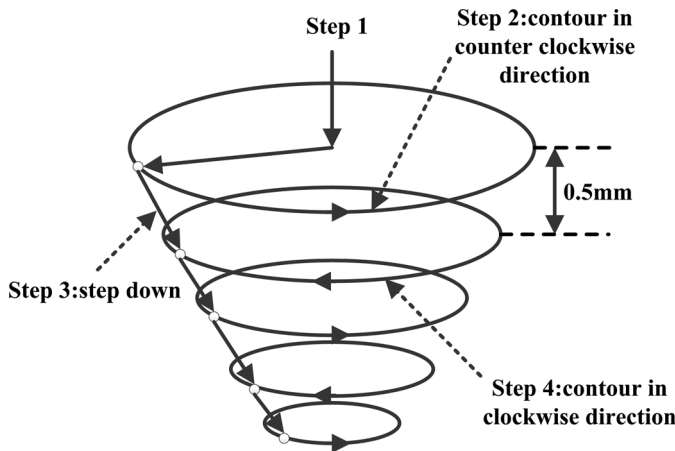


FIGURE 7.—Description of z-level tool path adopted in the experiments.

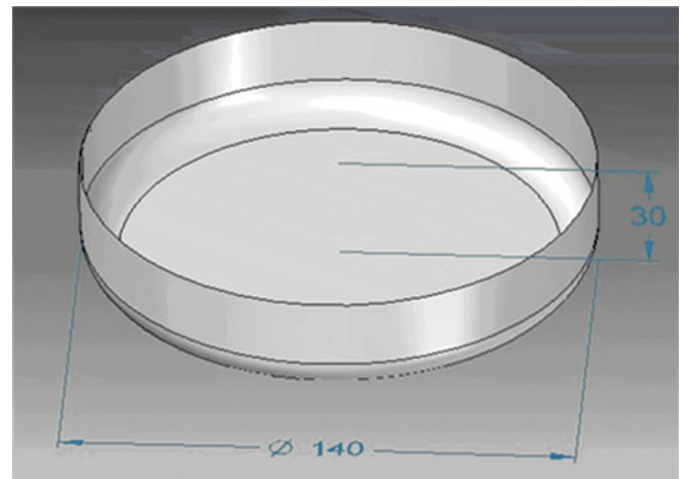


FIGURE 8.—Investigated geometry: a cylindrical cup with vertical wall (unit = mm) (color figure available online).

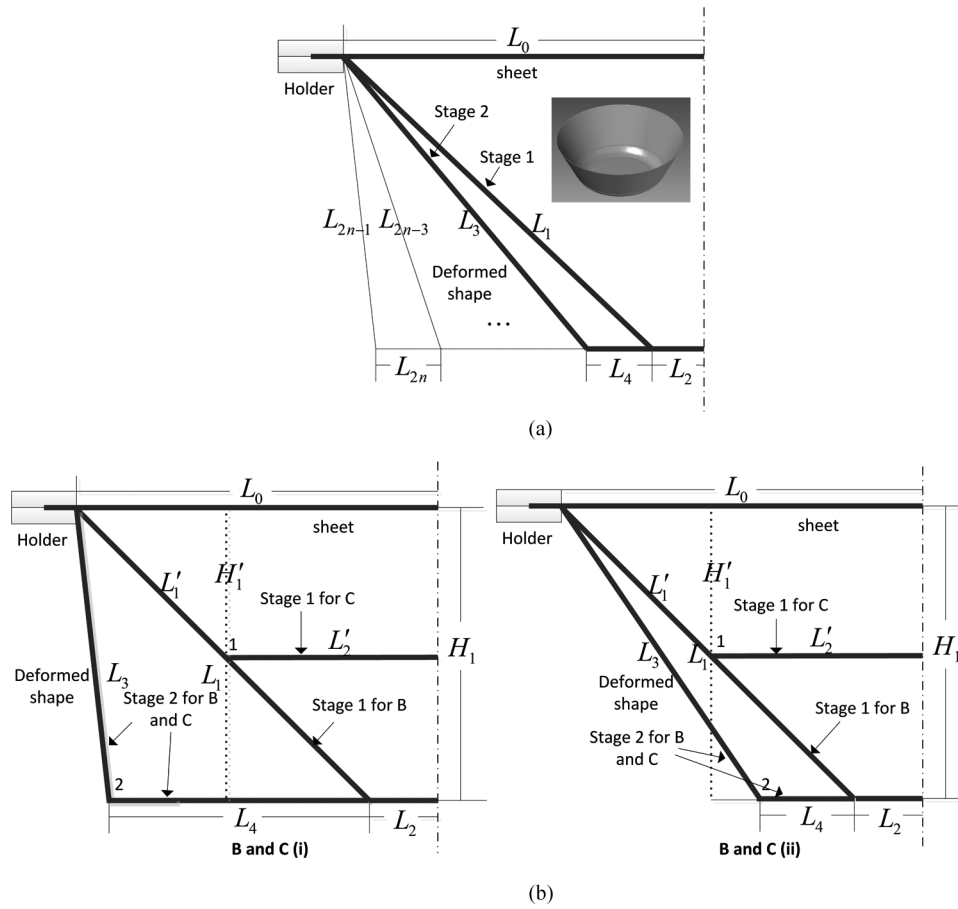


FIGURE 9.—Mechanism explanation: (a) strategy B and (b) comparison of strategy B and strategy C.

Equation (4) shows that the principal strain due to shear only in multistage deformation path strategies is smaller than that in single-stage forming process, which means less thinning is involved in multistage forming process. Therefore, its formability is higher than that of single-stage process.

Simplified deformation analysis for qualitative comparison of strategies B and C. The comparison of formability between strategies B and C is investigated in a similar manner to the previous subsection. Two possible incremental geometries need to be considered as shown in Fig. 9b where; (i), a larger final incremental draw angle is chosen with the corner 2 moving further away from the section centre than its previous stage position 1 such that $L_0 - L'_2 < L_4 < L_0 - L_2$ and (ii), a smaller final incremental draw angle is chosen with the corner 2 moving closer to the section centre than its previous stage position 1 such that $0 < L_4 \leq L_0 - L'_2$. Also, according to the design parameters in Table 1 and geometrical relationship in Fig. 9b, the following conditions hold:

$$H_1 = 2H'_1, \tag{5}$$

$$L_1 = 2L'_1. \tag{6}$$

For strategy B, in both cases (i) and (ii), the sheared section lengthformed after stage 1 is L_1 from an initial length $L_0 - L_2$ and then becomes $L_3 + L_4$ after stage 2. Hence the principal strain due to shear only can be derived as,

$$\varepsilon_B = \ln \frac{L_3 + L_4}{L_0 - L_2}. \tag{7}$$

For strategy C, we need to consider the two cases separately:

(i) The sheared section lengthformed after stage 1 is L'_1 from an initial length $L_0 - L'_2$ and then becomes $L_3 + L_4 - (L_0 - L'_2)$ after stage 2. Therefore, the principal strain due to shear only, ε_C , can be obtained as,

$$\varepsilon_C = \ln \frac{L_3 + L_4 - (L_0 - L'_2)}{L_0 - L'_2}. \tag{8}$$

Therefore, using Eqs. (7), (8) and the geometrical constraints of (i), it holds

$$\varepsilon_B - \varepsilon_C = \ln \frac{L_3 + L_4}{2[L_3 + L_4 - (L_0 - L'_2)]} \ln \frac{L_3 + L_4}{L_3 + L_3}. \tag{9}$$

In this case, the difference in strain is dependent on the shape and size of the final geometry. In particular, if $L_4 \leq L_3$, then $\varepsilon_B < \varepsilon_C$; otherwise the relative size of the geometrical parameters needs to be known.

(ii) The sheared section length formed after stage 1 is L'_1 from an initial length $L_0 - L'_2$ and then becomes L_3 after stage 2 from an intermediate length $L'_1 + L'_2 - (L_2 + L_4)$. Therefore, the principal strain due to shear only, ε_C , can be obtained as,

$$\varepsilon_C = \ln \frac{L'_1}{L_0 - L'_2} + \ln \frac{L_3}{L'_1 + L'_2 - (L_2 + L_4)}. \quad (10)$$

Therefore, using Eqs. (7), (10) and the geometrical constraints of (ii), it holds

$$\begin{aligned} \varepsilon_B - \varepsilon_C &= \ln \frac{L_3 + L_4}{L_0 - L_2} - \ln \frac{L'_1}{L_0 - L'_2} - \ln \frac{L_3}{L'_1 + L'_2 - (L_2 + L_4)} \\ &= \ln \frac{L_3 + L_4}{L_0 - L_2} - \ln \frac{L'_1 + L'}{L_0 - L_2 - L_4} \\ &\quad - \ln \frac{L'_1(L_0 - L'_2) + L'}{L'_1(L_0 - L'_2) + L'(L_0 - L'_2)} - \ln \frac{L_3}{L'_1 + L'} \\ &= \ln \frac{L_3(L_0 - L_2 - L_4) + L_4(L_0 - L_2 - L_4)}{L_3(L_0 - L_2 - L_4) + L_4 L_3} \\ &\quad - \ln \frac{L'_1(L_0 - L'_2) + L'}{L'_1(L_0 - L'_2) + L'(L_0 - L'_2)} 0, \end{aligned} \quad (11)$$

where $L' = L'_2 - (L_2 + L_4)$, and the following geometrical relationships from the sine law have been utilised; $L'_1 > L_0 - L'_2$ and $L_3 > L_0 - L_2 - L_4$.

Therefore,

$$\varepsilon_B < \varepsilon_C. \quad (12)$$

According to the design parameters, it is noted that case (ii) was used in the experiment. It is worth noting that strategy C can lead to more thickness reduction compared to strategy B considering the above approximate analysis. So, the introduction of strategy C in this study has a negative influence on the proper control for material flow. This will explain why strategic combinations including strategy C cause fracture earlier than the others in Section 3.1. These theoretical predictions will be compared with experimental results in the subsequent section.

RESULTS AND DISCUSSION

This section contains the results of the influence of different strategies and strategic combinations on the formation process of vertical wall surface and corresponding material flow and thickness distributions. First, experimental results will be provided, and then comparison will be made to verify the effectiveness of formability prediction results. Finally, thickness

distribution measurement is carried out to further explain the material flow and allocation mechanism between different strategies and strategic combinations.

Formability Results for Forming Strategies and Strategic Combinations for Vertical Wall Surface Formation

Different strategies and strategic combinations are evaluated to form vertical walls for cylindrical cups. The experimental results are given in Fig. 10 and Table 3.

The results in Table 3 show that for the same forming target, the adoption of different strategies and strategic combinations results in different experimental results. To be more specific, the cylindrical cup was manufactured successfully only using the strategic combination A + B regardless of initial draw angles, while the other strategies and strategic combinations failed in different stages. The forming process failed in stage 4 with the strategic combination A + C and the failure happened at the height of 24 mm, 22.5 mm, and 22 mm corresponding to initial draw angles 40°, 50°, and 90°, respectively. As for strategy C, the failure happened in stage 4 at the height of 22.5 mm and 21 mm with regard to initial draw angles of 40° and 50°, respectively. Besides, with only strategy B, fracture can be observed in the last forming stage with the height of 30 mm and 29.5 mm corresponding to initial draw angles 40° and 50°, respectively. This strategy has been widely adopted in literature [13, 18] and seems more advantageous than strategy C and strategic combination A + C. However, for the proposed forming target, it still exceeds its formability.

It is worth mentioning that the formability for producing cylindrical cups with vertical walls follows the same trend in the same strategy or strategic combination regardless of initial draw angles. However, the results have shown a significant difference between different strategies and strategic combinations, which illustrates that the adopted deformation path strategy has a great

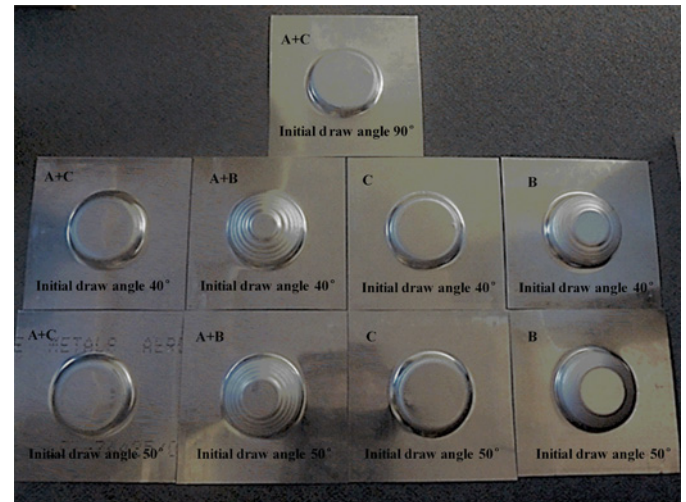


FIGURE 10.—Obtained experimental shapes for different strategies and strategic combinations (color figure available online).

TABLE 3.—Experimental results for strategies and strategic combinations for cylindrical cup formation (H_F means fracture happens at this height).

Strategies and strategic combinations	Initial draw angle	Stage 1st	Stage 2nd	Stage 3rd	Stage 4th	Stage 5th	H_F
A + C	$\alpha_1 = 40^\circ$	Success	Success	Success	Failure		24 mm
	$\alpha_1 = 50^\circ$	Success	Success	Success	Failure		22.5 mm
	$\alpha_1 = 90^\circ$	Success	Success	Success	Failure		22 mm
A + B	$\alpha_1 = 40^\circ$	Success	Success	Success	Success	Success	
	$\alpha_1 = 50^\circ$	Success	Success	Success	Success	Success	
C	$\alpha_1 = 40^\circ$	Success	Success	Success	Failure		22.5 mm
	$\alpha_1 = 50^\circ$	Success	Success	Success	Failure		21 mm
B	$\alpha_1 = 40^\circ$	Success	Success	Success	Success	Failure	30 mm
	$\alpha_1 = 50^\circ$	Success	Success	Success	Success	Failure	29.5 mm

effect on the final forming success. On the other side, observed from the experimental results, it seems that the occurrence of fracture has been delayed when using smaller initial draw angle in strategy B, strategy C, and strategic combination A + C. The most likely reason for this is that the smaller initial draw angle helps achieve better distribution of material involved in the deformation region. This can be further explained by thickness measurement.

It is noted that the addition of bending in strategy A will increase the overall formability. So considering the addition of bending into strategies B and C, the comparison results of formability prediction and experiments for initial draw angle 40° are represented in Table 4. The prediction analysis is similar for the case with initial draw angle 50° . The comparison between prediction and experimental results show the prediction analysis in this study is effective.

In [4], Silva et al. have pointed out that the fracture is the outcome of in-plane stretching caused by meridional tensile stresses σ_ϕ . It is also observed from the present experimental results, see the crack morphology in Fig. 11. On the other side, although the forming process was successful using strategic combination A + B, some forming defects can be observed as seen in Fig. 12. In SPIF configuration, there is no support underneath the metal forming area. When the forming tool travels in each stage, it will squeeze the material downwards. This explains why the formation of these defects happened.

TABLE 4.—Comparison of formability prediction and experimental results for initial draw angle 40° .

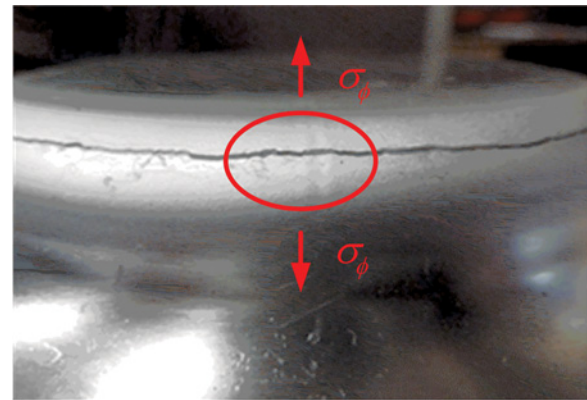
Strategies and strategic combinations	Likelihood of achieving forming target	
	Predicted results (Simplified strain analysis)	Experimental results
A + B***	success	
B**	failure in Stage 5 ($H_F = 30$ mm)	
A + C**	failure in Stage 4 ($H_F = 24$ mm)	
C*	failure in Stage 4 ($H_F = 22.5$ mm)	

Note: The number of * indicates the likelihood of achieving forming target for predicted results. Strategy B and strategic combination A + C cannot be compared directly based on current theoretical analysis, but the relations $A + B > B > C$ and $A + B > A + C > C$ can be predicted.

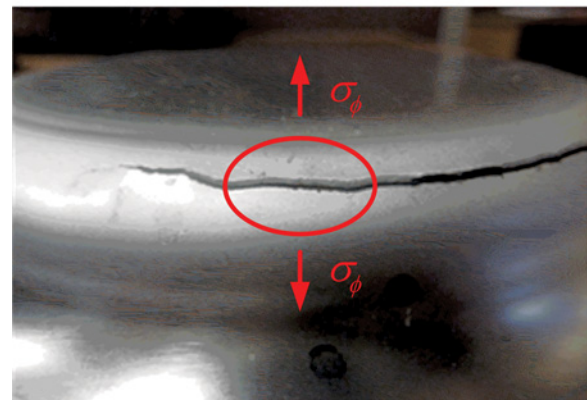
Vertical Wall Thickness Distribution for Different Forming Strategies and Strategic Combinations

In the previous section, formability comparison between approximate predictions and experimental results has been made. In view of cracks mainly caused by excessive thinning in multistage forming, it is reasonable to investigate the thickness distribution and give an insight into material flow mechanism.

In this section, the evolution of vertical wall thickness distribution will be evaluated for different strategies and

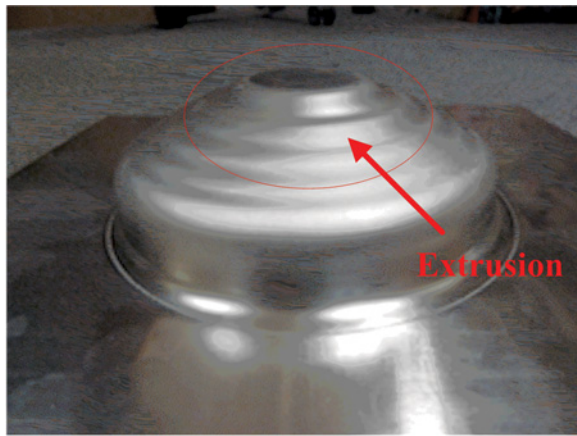


(a)

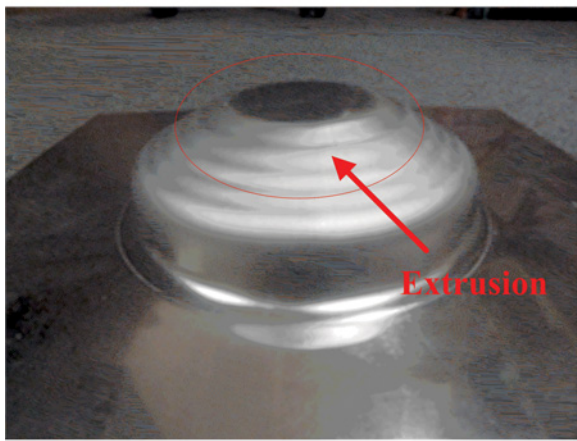


(b)

FIGURE 11.—Crack morphology caused by meridional tensile stress: (a) initial draw angle 40° and (b) initial draw angle 50° (color figure available online).



(a)

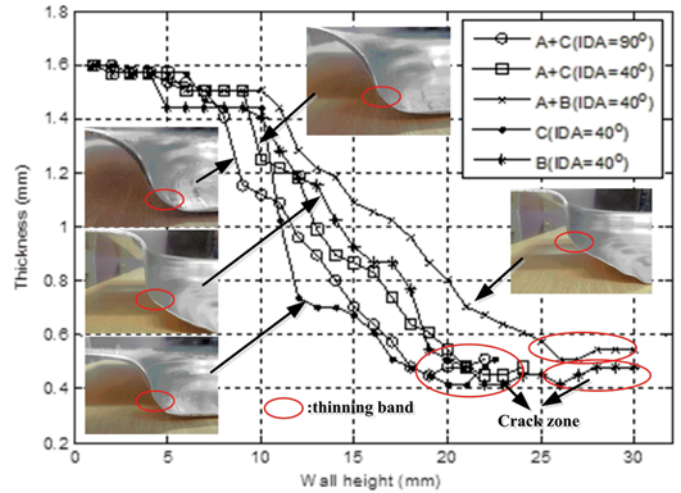


(b)

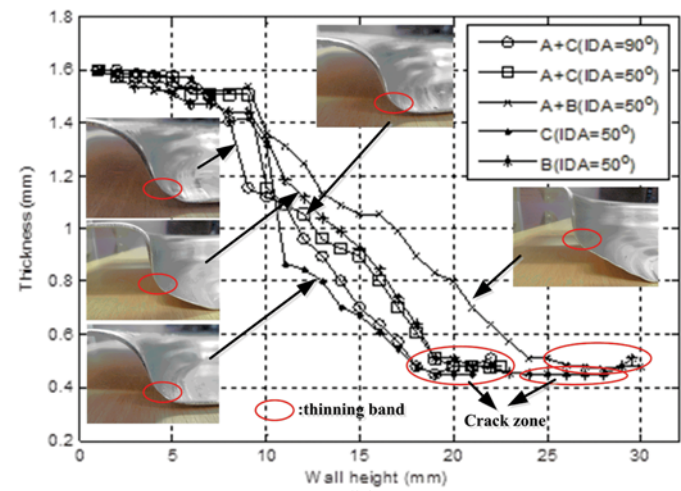
FIGURE 12.—Forming defects for strategic combination A + B: (a) initial draw angle 40° and (b) initial draw angle 50° (color figure available online).

strategic combinations. The thickness was measured along the wall height in the rolling direction. Figure 13 shows the thickness distribution for different strategies and strategic combinations with initial draw angles 40° and 50°, respectively.

Since the forming process is mainly limited by excessive thinning, how is the evolution of thickness distribution involved in the adopted strategies and strategic combinations? Overall, the measurements of thickness distribution show the same descent trends along the wall height in different strategies and strategic combinations. As seen in Fig. 13a, during the wall height 1–10 mm, bending effect prevails, and only a little stretching can be observed, which leads to less thinning in all strategies and strategic combinations. In the experiments, the diameter of backing plate is 156 mm, which is a little larger than the diameter of designed cylindrical cup (140 mm). Additional bending is introduced between the backing plate and the forming area due to the use of a little larger backing plate, which is applicable to all strategies and strategic combinations. This explains why thickness distribution looks quite similar in all



(a)



(b)

FIGURE 13.—Thickness distribution along wall height for different strategies and strategic combinations with two initial draw angles: (a) IDA = 40° and (b) IDA = 50° (IDA = Initial draw angle) (color figure available online).

strategies and strategic combinations in this area. For wall heights greater than approximately 10 mm, strategies and strategic combinations take effect, and the advantage of strategic combination A + B can be seen. It is noted that the least overall thinning can be observed when using strategic combination A + B compared with the other strategies and strategic combinations. In this case, the thinnest thickness is approximately 0.512 mm compared with that of 0.416 mm in strategies B and C, and 0.448 mm in strategic combination A + C. This measured results show good agreement with the observed experimental results discussed in the previous section, since forming target is successful only using this strategic combination. With proper deformation path design, the material flow is controlled and regulated in order to delay the occurrence of excessive thinning. The second least overall thinning can be found in strategy B followed by strategic combination A + C, A + C (initial draw angle 90°), and strategy C, where failure happens

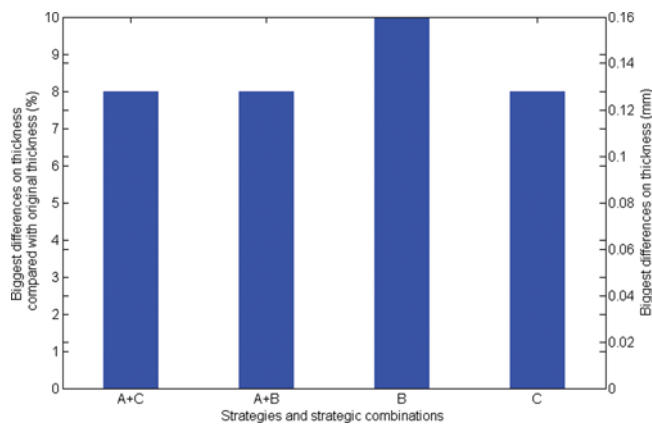


FIGURE 14.—Comparison of biggest differences on thickness measurement between the same strategic combinations A + C, A + B, strategies C and B with initial draw angles 40° and 50° (color figure available online).

at the height of 30 mm at stage 5th, 24 mm, 22 mm, and 22.5 mm in stage 4, respectively. It is worth noting that the introduction of a little bending in strategy A into strategy B and strategy C can help allocate the material and delay the occurrence of thinning band, while compared with strategy B, strategy C does not have any advantages of reducing material thinning. The analysis is quite similar in the case with initial draw angle 50° as shown in Fig. 13b.

In terms of the comparison of thickness distribution for the same strategies and strategic combinations with different initial draw angles, the overall thinning is slightly higher when using initial draw angle 50° compared with initial draw angle 40° based on the measured results. To make comparison clear, the biggest differences on thickness between the same strategic combinations A + C, A + B, and strategies B, C with two initial draw angles, were presented in Fig. 14. As shown in Fig. 14, the biggest thickness differences were measured as 0.128 mm, 0.128 mm, 0.16 mm, and 0.128 mm at the same height, which account for 8%, 8%, 10%, and 8% compared with original sheet thickness 1.6 mm. This illustrates the selection of a smaller initial draw angle can also delay the occurrence of thinning and increase the likelihood of successful forming.

CONCLUSION

Fracture happens during ISF process when excessive thinning occurs in the critical areas of a part. In this study, by revisiting multistage methodology, cylindrical cups with vertical wall surface have been formed with proper strategies and strategic combinations by material flow control. The findings of experiments are summarized as follows:

1. For the investigated cylindrical cup, in the present study, it could not be formed only using strategy B, although this strategy has been adopted to form a cylindrical cup successfully in article [18]. In this study, strategic combination A + B has shown the

advantage of forming vertical walls without failure. The reason is most likely that a small amount of bending in strategy A is introduced to control material flow and regulate the thickness distribution, thus delaying the occurrence of thinning band and increasing the likelihood of successful forming.

2. It was revealed that the wall thickness distribution can be also controlled by changing the initial draw angle. The smaller the initial draw angle is, the less thinning of wall thickness occurs. However, in reality, the choice of the initial draw angle should be within a reasonable range considering the effects of other process parameters, such as tool radius, the number of adopted stages in one strategy, on the likelihood of successful forming.
3. The introduction of strategy C shows no advantage of controlling material flow to reduce thinning. The reason is that less material is involved in each forming stage and more thinning happens as analyzed in Section 2.3.

Additionally, the results in this study can also provide insights into forming complex geometries with steep wall surfaces by controlling material flow to avoid excessive thinning.

The simplified predictive analysis performed in this paper is used qualitatively only to efficiently predict the relative success of forming. However, it is limited to shear only deformation according to the sine law [16] and is theoretically simplified. It is planned to perform more accurate quantitative analysis to predict the absolute size of the principle strain associated with each forming strategy using more complex FE analysis in the future.

ACKNOWLEDGMENTS

This research was supported by the ARC Linkage Program, Boeing Research, and Technology Australia and QMI Solutions in Australia.

REFERENCES

1. Jeswiet, J.; Micari, F.; Hirt, G.; Bramley, A.; Duflou, J.; Allwood, J. Asymmetric single point incremental forming of sheet metal. *CIRP Annals—Manufacturing Technology* **2005**, *54*, 88–114.
2. Emmens, W.C.; Sebastiani, G.; van den Boogaard, A.H. The technology of incremental sheet forming—A brief review of the history. *Journal of Materials Processing Technology* **2010**, *210*, 981–997.
3. Filice, L.; Fratini, L.; Micari, F. Analysis of material formability in incremental forming. *CIRP Annals—Manufacturing Technology* **2002**, *51*, 199–202.
4. Silva, M.B.; Skjoedt, M.; Martins, P.A.F.; Bay, N. Revisiting the fundamentals of single point incremental forming by means of membrane analysis. *International Journal of Machine Tools and Manufacture* **2008**, *48*, 73–83.
5. Jackson, K.; Allwood, J. The mechanics of incremental sheet forming. *Journal of Materials Processing Technology* **2009**, *209*, 1158–1174.
6. Filice, L.; Ambrogio, G.; Micari, F. On-line control of single point incremental forming operations through punch force

- monitoring. *CIRP Annals–Manufacturing Technology* **2006**, 55, 245–248.
7. Duflou, J.; Tunçkol, Y.; Szekeres, A.; Vanherck, P. Experimental study on force measurements for single point incremental forming. *Journal of Materials Processing Technology* **2007**, 189, 65–72.
 8. Allwood, J.M.; Braun, D.; Music, O. The effect of partially cut-out blanks on geometric accuracy in incremental sheet forming. *Journal of Materials Processing Technology* **2010**, 210, 1501–1510.
 9. Bambach, M.; Taleb Araghi, B.; Hirt, G. Strategies to improve the geometric accuracy in asymmetric single point incremental forming. *Production Engineering* **2009**, 3, 145–156.
 10. Attanasio, A.; Ceretti, E.; Giardini, C.; Mazzoni, L. Asymmetric two points incremental forming: Improving surface quality and geometric accuracy by tool path optimization. *Journal of Materials Processing Technology* **2008**, 197, 59–67.
 11. Hamilton, K.; Jeswiet, J. Single point incremental forming at high feed rates and rotational speeds: Surface and structural consequences. *CIRP Annals–Manufacturing Technology* **2010**, 59, 311–314.
 12. Manco, L.; Filice, L.; Ambrogio, G. Analysis of the thickness distribution varying tool trajectory in single-point incremental forming. *Proceedings of the Institution of Mechanical Engineers Part B–Journal of Engineering Manufacture* **2011**, 225, 348–356.
 13. Skjoedt, M.; Silva, M.B.; Martins, P.A. F.; Bay, N. Strategies and limits in multi-stage single-point incremental forming. *Journal of Strain Analysis for Engineering Design* **2010**, 45, 33–44.
 14. Hussain, G.; Gao, L.; Hayat, N. Forming parameters and forming defects in incremental forming of an aluminum sheet: correlation, empirical modelling, and optimization: Part A. *Materials and Manufacturing Processes* **2011**, 26, 1546–1553.
 15. Sarraji Wisam, K.H.; Hussain, J.; Ren, W.X. Experimental investigation on forming time in negative incremental sheet metal forming process. *Materials and Manufacturing Processes* **2012**, 27, 499–506.
 16. Young, D.; Jeswiet, J. Wall thickness variations in single-point incremental forming. *Proceedings of the Institution of Mechanical Engineers Part B–Journal of Engineering Manufacture* **2004**, 218, 1453–1459.
 17. Bambach, M. A geometrical model of the kinematics of incremental sheet forming for the prediction of membrane strains and sheet thickness. *Journal of Materials Processing Technology* **2010**, 210, 1562–1573.
 18. Duflou, J.R.; Verbert, J.; Belkassam, B.; Gu, J.; Sol, H.; Henrard, C.; Habraken, A.M. Process window enhancement for single point incremental forming through multi-step toolpaths. *CIRP Annals–Manufacturing Technology* **2008**, 57, 253–256.
 19. Cui, Z.; Gao, L. Studies on hole-flanging process using multi-stage incremental forming. *CIRP Journal of Manufacturing Science and Technology* **2010**, 2, 124–128.
 20. Centeno, G.; Silva, M.B.; Cristino, V.A.M.; Vallellano, C.; Martins, P.A.F. Hole-flanging by incremental sheet forming. *International Journal of Machine Tools and Manufacture* **2012**, 59, 46–54.
 21. Dejardin, S.; Thibaud, S.; Gelin, J.C.; Michel, G. Experimental investigations and numerical analysis for improving knowledge of incremental sheet forming process for sheet metal parts. *Journal of Materials Processing Technology* **2010**, 210, 363–369.
 22. Li, J.; Hu, J.; Pan, J.; Geng, P. Thickness distribution and design of a multi-stage process for sheet metal incremental forming. *The International Journal of Advanced Manufacturing Technology* **2012**, 62, 981–988.

Erratum

Article title: Vertical Wall Formation and Material Flow Control for Incremental Sheet Forming by Revisiting Multistage Deformation Path Strategies

Authors: Zhaobing Liu, Yanle Li, and Paul Anthony Meehan

Journal: *Materials and Manufacturing Processes*

Bibliometrics: Volume 28, Issue 5, pages 562–571

DOI: 10.1080/10426914.2013.763964

Several equations and Table 4 appeared incorrectly in the online and print versions of this article. The correct equations and table are below.

$$\varepsilon_M - \varepsilon_S = \ln \frac{L'L_3 + L'L_4}{L'L_3 + L_3L_4}, \quad (3)$$

$$\varepsilon_B - \varepsilon_C = \ln \frac{L_3 + L_4}{2[L_3 + L_4 - (L_0 - L'_2)]} < \ln \frac{L_3 + L_4}{L_3 + L_3}. \quad (9)$$

$$\begin{aligned} \varepsilon_B - \varepsilon_C &= \ln \frac{L_3 + L_4}{L_0 - L_2} \\ &\quad - \ln \frac{L'_1}{L_0 - L'_2} - \ln \frac{L_3}{L'_1 + L'_2 - (L_2 + L_4)} \\ &= \ln \frac{L_3 + L_4}{L_0 - L_2} - \ln \frac{L'_1 + L'}{L_0 - L_2 - L_4} \end{aligned}$$

$$\begin{aligned} & - \ln \frac{L'_1(L_0 - L'_2) + L'L'_1}{L'_1(L_0 - L'_2) + L'(L_0 - L'_2)} - \ln \frac{L_3}{L'_1 + L'} \\ &= \ln \frac{L_3(L_0 - L_2 - L_4) + L_4(L_0 - L_2 - L_4)}{L_3(L_0 - L_2 - L_4) + L_4L_3} \\ & - \ln \frac{L'_1(L_0 - L'_2) + L'L'_1}{L'_1(L_0 - L'_2) + L'(L_0 - L'_2)} < 0, \quad (11) \end{aligned}$$

TABLE 4.— Comparison of formability prediction and experimental results for initial draw angle 40°.

Strategies and strategic combinations	Likelihood of achieving forming target	
	Predicted results (simplified strain analysis)	Experimental results
A + B	***	success
B	**	failure in Stage 5 ($H_F = 30$ mm)
A + C	**	failure in Stage 4 ($H_F = 24$ mm)
C	*	failure in Stage 4 ($H_F = 22.5$ mm)

Note: The number of * indicates the likelihood of achieving forming target for predicted results. Strategy B and strategic combination A + C cannot be compared directly based on current theoretical analysis, but the relations $A + B > B > C$ and $A + B > A + C > C$ can be predicted.

The publisher apologizes for this error.

4.2.2 AMINO TPIF Multi-Pass Deformation Design

Paper H

Thickness distribution and forming strategy analysis for two point incremental forming with a male die

Liu, Z.B., Meehan, P.A., Bellette, P.A.

Advanced Materials Research

2011, Volume: 337, Pages: 452-455.

Thickness distribution and forming strategy analysis for two point incremental forming with a male die

Zhaobing Liu^{1, a}, Paul Meehan^{2, b} and Paul Bellette^{3, c}

^{1,2,3}School of Mechanical and Mining Engineering, The University of Queensland, 4072, Australia

^az.liu7@uq.edu.au, ^bmeehan@uq.edu.au, ^cp.bellette@uq.edu.au

Keywords: Incremental forming, Formability, Sine's law, Thickness distribution, Male die

Abstract. Incremental Sheet Forming (ISF) is a promising sheet-metal-forming technology which is drawing more and more researchers' attention due to its flexibility of manufacturing three-dimensional products at a relatively low cost for rapid prototyping and small-batch production. This paper is focused on the thickness distribution and the forming strategy analysis for two point incremental forming with a male die. The analyzed benchmark is half a torus which is generated by revolving a semi-circle. Such a part is hardly able to be formed by single point incremental forming because its slope varies from 0 degree to 90 degrees. In terms of the varying slope, the variant of sine's law is derived to give an approximate prediction of the thickness distribution from an analytical perspective. In addition, a multi-stage forming strategy is proposed in order to form the part successfully. In particular, a keying operation is implemented carefully in order to avoid twist phenomenon and achieve good dimensional accuracy.

Introduction

Incremental sheet forming (ISF) is an innovative and flexible sheet metal-forming process that is economically promising for small-series production manufacturing. In this process, a simple forming tool (usually with a semi-spherical head or a ball head) moves along a defined CNC (Computer Numerical Control) tool path which plastically deforms the blank according to the desired shape in an incremental fashion. There are mainly two variants of this process: (1) Single Point Incremental Forming (SPIF), and Two Point Incremental Forming (TPIF). In single point incremental forming the forming tool moves on the concave surface on the part, whereas in two point incremental forming the forming tool works on the convex surface. When the die has a positive geometry (male die), the blank holder should be moved in a vertical direction by air cylinders, which allows the forming down pressure on the sheet to be adjusted appropriately. While in the case of negative geometry (female die), the blank can be fixed. During the ISF process, the deformation imposed by the forming tool is extremely localized, so the formability of metal sheets is greatly enhanced compared with those conventional forming processes. Reviewing the previous work on formability done by researchers, Kim et al. [1] carried out a straight groove test to investigate the effect of some process parameters on the formability. Park et al. [2] assessed the formability of an aluminum sheet under various forming conditions and difficult-to-form shapes were produced. They pointed out that with the single point forming method, it is difficult to form sharp corners or edges because cracks easily occur due to the biaxial mode of deformation. While with the two point forming method, it is possible to form complicated shapes with sharp corners or edges because the plane-strain mode of deformation becomes quite dominant. For given materials and process parameters, Hussein and his coworkers [3-5] gave a novel method by using the parts with varying slopes to test the thinning limits of sheet metals in single point incremental forming. On the other hand, authors in [6] regarded the tool trajectory as an optimization variable in the process design and compared four strategies' merits and demerits.

In this paper, the thickness distribution and the forming strategy have been investigated for two point incremental forming with a male die. Multi-stage forming strategy is proposed to guarantee the successful forming of the final part. In order to avoid twist phenomenon and improve accuracy, a keying operation has been carefully implemented. It is noted that the analytical method to estimate the thickness distribution and the optimization forming strategy are highlighted throughout this paper.

Formability and Thickness Distribution

There are mainly two configurations for incremental sheet forming process. Here, two point incremental forming with a male die is adopted, see Fig.1 for details. The forming die provides greater control and accuracy to a part through the ISF forming process. All but the simplest of shapes require a forming die. The design and machining of the forming die applies an understanding of the forming process, including the compensation for material thickness and spring-back by machining the die undersize generally over the whole die and in specific regions. In the experiment, the male die is produced from MDF (Medium Density Fiberboard) composite timber, which is quick, economical and performs well during the forming process.

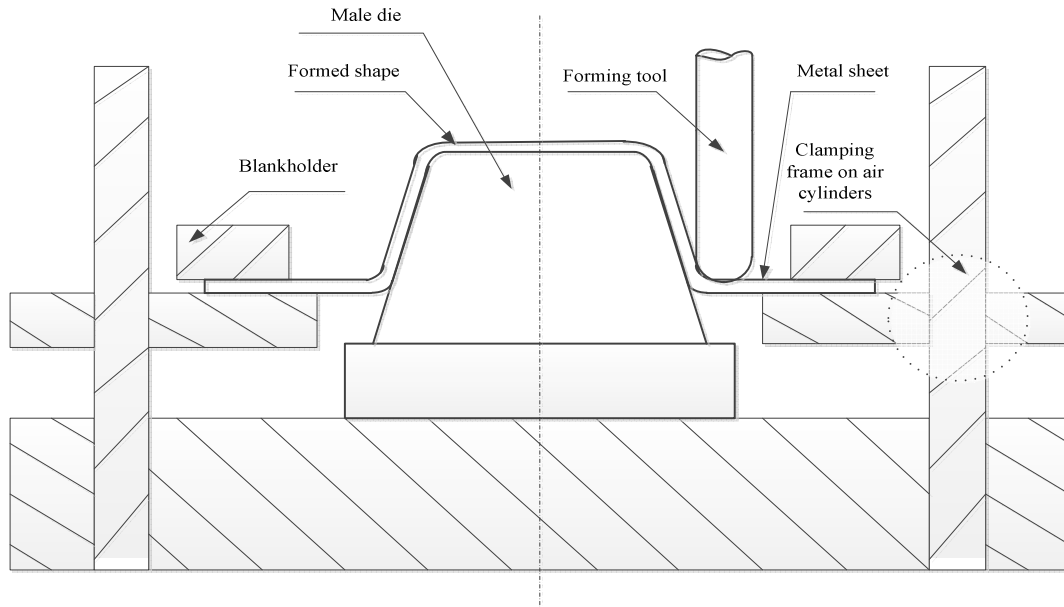


Fig. 1. Configuration of two point incremental forming with a male die

From the analytical perspective, sine law is widely used to predict the final sheet thickness distribution,

$$t = t_0 \sin\left(\frac{\pi}{2} - \alpha\right) = t_0 \cos \alpha, \quad (1)$$

where t is the current sheet thickness, t_0 is the initial thickness, and α is the inclination angle of the formed part. For the part with constant slope, the value of sine law is a constant, while for the part with varying slope, a variant of sine law can be derived. Here, the calculation process is still the same as that in [3-5],

$$t_p = t_0 \cos \alpha_p = t_0 \frac{y_p}{R} = ky_p, \quad (2)$$

where t_p is the thickness of the part at arbitrary point $P(x, y)$, k is a constant. The slope angle α_p at point $P(x, y)$ can be calculated by the relation,

$$\alpha_p = \cos^{-1}\left(\frac{y_p}{R}\right). \quad (3)$$

As pointed out in [3], no part can be formed up to 90° slope angle with single point incremental forming because the thickness of the part at 90° will become zero which is practically not possible. However, 90° slope angle is the target to be achieved in this study.

Multi-Stage Optimization Forming

In [6], the authors mentioned that it is possible to change the strain path in order to improve the thickness distribution. So, four manufacturing strategies (named as Single slope, Incremental slope, Wall slope, Decremental slope) were tested to form the same shape with single point incremental forming. In view of their experimental results, decremental slope strategy showed a higher variability and flexibility in thickness distribution. The minimum thickness is 40 per cent higher than the single slope. In view of these, in this paper, a multi-stage forming strategy is proposed to form half a torus based on two point incremental forming with a male die. In the experiment, the forming methodology can fall into the following four concrete procedures.

1. Keying the perform shape against the die

The purpose of this step is to avoid the twist phenomenon and improve the dimensional accuracy. A good key between the formed part and the die can give good location and stability for the remainder of the pre-form and subsequent finishing operations.

2. Restraining and Compressing during the TPIF process

When forming the part, there are two major restraints. The first one is the crude clamping restraints around the metal sheet boundary. The clamps do not need to be excessively tight because a small amount of lateral movement is advantages to allow metal to be drawn in from the outer areas. The second restraint is the transition line where the material changes from the unformed horizontal sheet to the part which is being formed. As the forming tool moves down below the current level in the forming process, the flat sheet has little control over the preceding level of forming. This forming transition line is at tool position, which progresses down with every step down, until it is somewhere around the lowest level of the part. The sheet supporting frame follows it by applying air cylinder pressure that exerts a downward pressure force of the sheet against the forming die. As observed, material flow in the ISF process, is achieved and controlled through the induced restraint occurring at this transition line. This is a significant control mechanism of ISF.

For forming sharp angle walls, it requires considerable compression to wrap aggressively, causing the material to flow against the die with minimal thinning. This process involves moving material via the controlled transition line by bending rather than stretching. Compression without the aid of the transition forming line is extremely difficult. Therefore, compressing the excess material should be taken good care of, otherwise buckling may occur.

3. Moving material

The trick of this procedure is to involve flowing sufficient material into areas that needs material to be stretched. The creation of 'pseudo transition forming line' allows compression as the material is flowing rather than compressing. For the vertical wall to be formed against the die, it offers the resistance to the sideways pressure of the tool and allows the tool to push a wave of material into the die.

4. Regulating and Wrapping material

When forming a very steep wall, the splitting occurs easily. The reason is that no new material is flowing or repositioned into the wall during this process. It is all being drawn from the preceding wall behind the forming tool. The material must elongate resulting in eventual splitting when the downward tool pressure overcomes the tensile strength of the thinning wall material. The solution is the use of pre-form and tool path optimization. The pre-form has moved the material into place aggressively to minimize elongation, at the same time allowing an excess for wrapping into the outer walls.

Preform Path Simulation and Experimental Setup

The preform path strategy is described in Fig.2. It is shown that the keying operation is delicately performed in the first three pictures in order to avoid the twist phenomenon.

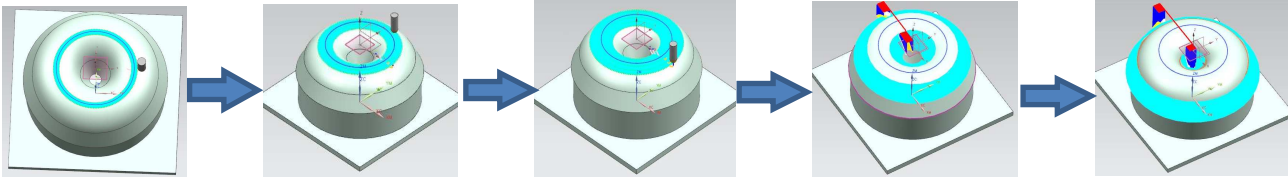


Fig. 2. The method to obtain preform shape and path generation simulation

The pictures in Fig.3 give a general view of the ISF machine used in the experiment.



Fig.3. ISF machine

An AA5005 blank sheet, with 3mm thick, is taken into account. Mineral oil is used as a lubricant. Following the four procedures mentioned in the previous section, the shape has been made successfully.

Conclusions

In this paper, the thickness distribution and the forming strategy analysis have been considered for two point incremental forming with a male die. Under the frame of the proposed forming strategy, the formability has been greatly enhanced compared with single point incremental forming. At the same time, the usage of delicate keying operation helps avoid twist phenomenon and improve the final accuracy.

It is worth noting that the forming strategy analysis is the main focus of this study. The further investigation of the analytical, simulation, and experimental results is ongoing in another paper.

Acknowledgements

This work is financially supported by the ARC Linkage Program and Boeing Research Technology. Thanks also to QMI Solutions, especially Geoff Wakeley for providing the training and the Operations Manual for Incremental Sheet Forming on an AMINO machine.

References

- [1] Y. H. Kim, J. J. Park, *J. Mater. Process Tech.* 130-131 (2002) 42-46.
- [2] J. J. Park, Y. H. Kim, *J. Mater. Process Tech.* 140 (2003) 447-453.
- [3] G. Hussain and L. Gao, *Int. J. Mach. Tool Manu.* 47 (2007), 419-435.
- [4] G. Hussain, N. U. Dar, L. Gao and M. H. Chen, *J. Mater. Process Tech.* 187-188 (2007), 94-98.
- [5] G. Hussain, N. Hayat and L. Gao, *Int. J. Mach. Tool Manu.* 48 (2008), 1170-1178.
- [6] L. Manco, L. Filice and G. Ambrogio, *Proc. IMechE Part B: J. Engineering Manufacture*, 225 (2010), 348-356.

4.2.2 AMINO TPIF Multi-Pass Deformation Design

Paper I

An analytical model for deformation path design in multistage incremental sheet forming process

Liu, Z.B., Li, Y.L., Daniel, W.J.T., Meehan, P.A.

Advanced Materials Research

2014, Volume: 939, Pages: 245-252.

An analytical model for deformation path design in multistage incremental sheet forming process

Zhaobing Liu^{1,a}, Yanle Li^{1,b}, Bill Daniel^{1,c} and Paul Meehan^{1,d}

¹ School of Mechanical and Mining Engineering, The University of Queensland, St Lucia, Brisbane, QLD 4072, Australia

^az.liu7@uq.edu.au, ^byanle.li@uq.edu.au, ^cbilld@uq.edu.au, ^dmeehan@uq.edu.au

Keywords: Incremental sheet forming, Deformation path, Intermediate shape, Formability, Thickness distribution, Thickness strain, Finite element analysis

Abstract. Incremental sheet forming (ISF) is a new promising technology due to its flexibility and low-cost tooling properties compared with conventional forming processes. However, a common technical problem encountered in ISF is non-uniform thickness variation of formed parts, particularly excessive thinning on severely sloped regions, which may lead to the part fracture and limit the process formability. Design of multistage deformation paths (intermediate shapes or preforms) before the final part is a desirable and practical way to control the material flow in order to obtain more uniform thickness distribution and avoid forming failure. Based on the shear deformation and the strain compensation idea, an analytical model for designing multistage deformation paths and predicting the thickness strain distribution is proposed. The feasibility of the proposed model is validated by the finite element analysis (FEA) and experimental tests in terms of the comparison of prediction, simulation and experimental results on the thickness strain distribution and the process formability.

1. Introduction

Incremental sheet forming (ISF), as a new promising technology, has gained great attention in the sheet metal forming community in the past decade [1-9]. In ISF process, a simple forming tool is controlled by a computer numerically controlled (CNC) machine following a prescribed tool path which plastically deforms the sheet metal into the desired shape. There are mainly two variations of the ISF process: single point incremental forming (SPIF) without a forming die and two point incremental forming (TPIF) with a partial or full forming die. More details of the development of ISF technology are summarized in the review paper by Jeswiet et al. [3].

Much research in ISF has been performed to investigate the forming limits and increase the formability by adopting multistage deformation path design [1,4-5,8-9]. In particular, Filice et al. [4] investigated the material formability in ISF performing several tests with different strain conditions. The results indicate that local stretching is the dominant deformation mode in ISF. However, Jackson et al. [5] further investigated the mechanics of ISF through an experimental campaign. It was revealed that shear in the tool direction is the most significant strain component and increasing stretching and shear also exist perpendicular to the tool direction. Hence although there is uncertainty as to the deformation mode (shear and/or stretching) involved, failure in ISF is most likely to be caused by the non-uniform thickness distribution and typically the excessive localized thinning of steep walls, which decreases the forming limits of materials. This makes it difficult to manufacture complex parts with steep walls. Therefore, the proper allocation of deformation during forming is important to aim to uniformly distribute the material thickness on the final parts in order to avoid the occurrence of forming failure.

Numerical simulation of sheet metal forming processes is a useful and effective way to design and optimize the process parameters and to evaluate the forming defects such as fracture, springback, wrinkling, geometric deviations and residual stresses. In the past decade, a few researches have used the finite element method (FEM) to model the ISF process. In Thibaud et al. [6], a fully parametric toolbox has been developed to simulate the SPIF process with the finite element software. The prediction results of geometric deviations, thickness distribution and forming forces showed good agreement with the experimental results. Shanmuganatan et al. [7] presented an explicit numerical simulation using the finite element code, Abaqus. The stress and thickness distribution have been derived and validated by experimental tests. Although FEM is an effective way to model and simulate the multistage ISF process and can obtain accurate results, it usually takes long time (several days or even more than a week), which leads to inefficiency on the design of multistage ISF process.

The above review of recent studies shows that most of previous work on multistage deformation path design is still based on the trial and error method in ISF. Although there was an analytical model developed in Kim et al. [8], it is only suitable for two-stage forming. For the manufacture of more complex parts, more forming stages are needed [1,9]. This paper proposes an analytical model for multistage deformation path design with the prediction of the thickness strain distribution on the deformation paths based on the shear deformation and strain compensation mechanism, which considers the global average thickness strain and only material in the final part region involved in the forming. This model extends the work of Kim et al.[8]. The purpose is to develop an appropriate efficient model to be validated by more accurate FEA and experimental results in terms of the thickness strain distribution and the process formability. The rest of this paper is as follows. Section 2 introduces the modeling methodology including FEM and experimental conditions. Section 3 provides the model validation by comparing the analytical results with FE and experimental results. Then, some discussions are provided. Finally, conclusions are drawn.

2. Methodology

2.1 Analytical model-shear deformation

For simplicity, the efficient model assumes the dominant mode of the deformation is via shear. For an arbitrary part, it can be discretized by triangular meshes. Based on shear deformation, x and y coordinates are the same for both initial and final configurations. Fig.1 shows the mechanism of 3D shear deformation for one triangular mesh. Due to the assumption of volume constancy, the thickness strain can be calculated in the following equation [8],

$$\varepsilon_f = \ln \frac{t_f}{t_0} = \ln \frac{A_0}{A_f} \quad (1)$$

where ε_f is the thickness strain in one mesh in the final configuration. t_0 and t_f are the initial and final thickness in one mesh. A_0 and A_f are the initial and final area in one mesh, which can be calculated by x, y, z coordinates.

The following method is a modification of the application [8] for multistage deformation path design. In order to control the material deformation flow and obtain the uniform thickness distribution, the localized region of a part requiring severe shear deformation to achieve its final form should be compensated by less shear deformation in the multistage deformation paths. While the part region with less shear deformation should be kept close to the final shape in the deformation paths in order to reduce the occurrence of forming defects. On this basis the analytical model is developed to design multistage deformation paths by calculating the thickness strain distribution given a design part and compensating the strain in each multistage deformation path. Some modeling assumptions are made as follows:

- a. The deformation mode is only based on shear deformation;
- b. The intermediate thickness strains for each deformation path are calculated based on the thickness strains of the designed shape;
- c. Material properties are not considered here.

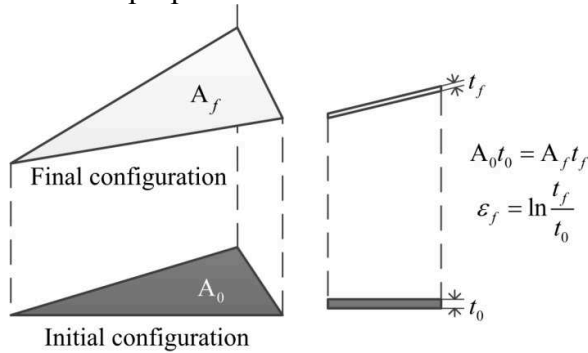


Fig.1. Mechanism of shear deformation.

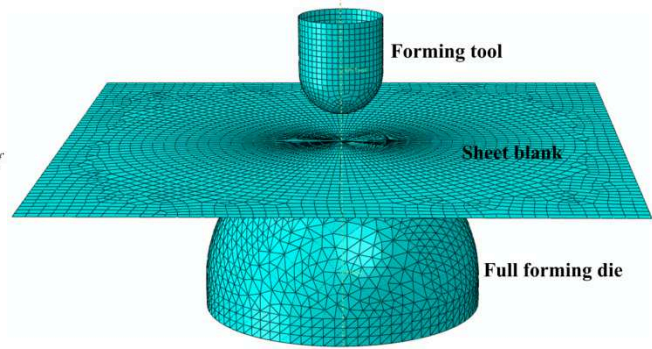


Fig.2. Simplified FE modeling for TPIF.

During modeling, only material in the deformed region of the design part is used in the forming. The global average thickness strain in the design part is used as a basis to compensate the strain in severely sloped regions. The local thickness strain in the design part is used to estimate the non-severely sloped region.

Based on this design approach, the intermediate thickness strain for each triangular mesh i (from 1 to N) of the design part in the corresponding deformation path can be determined as follows:

For $i=1:N$

If $\epsilon_f(i) \leq \epsilon_{Gavg}$

$$\epsilon_{int}(i) = a_1 * \epsilon_{Gavg} - b_1 (\epsilon_f(i) - \epsilon_{min}) / (\epsilon_{max} - \epsilon_{min}) * \epsilon_{Gavg} \tag{2}$$

Else

$$\epsilon_{int}(i) = a_2 * \epsilon_f(i) - b_2 (\epsilon_f(i) - \epsilon_{min}) / (\epsilon_{max} - \epsilon_{min}) * \epsilon_f(i) \tag{3}$$

End If

End For

where $\epsilon_f(i)$ is the thickness strain in mesh i in the final state, and $\epsilon_{int}(i)$ is the thickness strain in mesh i in the intermediate state. $a_1, a_2, b_1,$ and b_2 are parameters which need to be tuned to determine the intermediate strain.

$$\epsilon_{min} = \min[\epsilon_f(1), \epsilon_f(2), \dots, \epsilon_f(n)], \epsilon_{max} = \max[\epsilon_f(1), \epsilon_f(2), \dots, \epsilon_f(n)], \epsilon_{Gavg} = \sum_{j=1}^n \epsilon_f(j) / n.$$

It is worth mentioning that all these thickness strains in the above model are negative, i.e. ϵ_{min} and ϵ_{max} corresponding to the maximum and minimum magnitudes, respectively. The first term of Eq.(2) scales the **global average** thickness strain ϵ_{Gavg} in the final shape to estimate an intermediate shape. This would have uniform thickness strain. However, this is corrected by the second term, which gives the most deformed triangle in the final state (with ϵ_{min}) this average strain, but reduces the magnitude of strain induced in triangular elements with a higher magnitude of thickness strain. This delays the forming of the regions to be stretched the most. If $b_1 = a_1$, then the least deformed triangular elements in the final state (with ϵ_{max}) has $\epsilon_{int} = 0$. In Eq.(3), the first term scales the **local** thickness strain ϵ_f in the final shape to estimate an intermediate shape, more closely reflecting the final shape. The second term corrects this so that if $b_2 = a_2$, then again no reduction in strain occurs at a triangle with the minimum thickness change in the final shape, but the strain is reduced to zero (delaying forming),

where the final shape has the maximum thickness strain. $b_1 = a_1$ and $b_2 = a_2$ gives consistent results where $\varepsilon_f = \varepsilon_{Gavg}$.

Once all the thickness strains are derived in one deformation path, the z coordinates of each triangular mesh can be achieved recursively. The intermediate shape for this deformation path can be determined. More details can refer to Kim et al. [8] (Section 4).

2.2 FE model

The FEA simulation is used to investigate the influence of different deformation paths obtained from the previous design on the possibilities of improving the process formability. The simplified FE process modeling was performed for two-point incremental forming (TPIF) using ABAQUS[®]/Explicit software 6.11, see Fig.2. AA 7075-O aluminum sheets with 1.016 mm thickness are used in this study. The mechanical properties can be summarized in Table 1. In order to reduce the FE model size, a smaller sheet blank with the size of 200 mm × 200 mm is used in the simulation. The blank is considered as a deformable body and is discretized with shell elements S4R, which are reduced integration elements with an integration point in the plane and five integration points along the thickness. The size of each shell element is 4mm. The forming tool and die are modeled using rigid surface elements R3D4 with sizes of 2mm and 4mm, respectively. The friction behavior is modeled using the Coulomb friction law with a friction coefficient of 0.1 between the blank and the forming tool and a friction coefficient of 0.8 between the blank and the forming die.

Table 1. Mechanical properties of AA 7075-O aluminum alloy sheets with 1.016 mm thickness.



Fig.3. The Amino ISF machine used for experiments.

Material	AA7075-O
Density(t/mm ³)	2.81×10^{-9}
Young's modulus(MPa)	70000
Poisson's ratio	0.33
Tensile Yield Strength (MPa)	89
Ultimate Tensile Strength (MPa)	191
Plastic coefficient K	352.9
Hardening exponent n	0.23

2.3 Experimental conditions

Siemens NX CAM 7.5 is utilized to obtain cutter location (CL) data. In this software, a Z-level milling operation is selected with 4 mm step-down size in deformation path one and two and 2 mm step-down size in the final shape. Experimental investigations were performed on the AMINO[®] DLNC-PC incremental forming machine (Fig.3). The machine is a 3-axis CNC machine with a maximum workspace of 2100×1450×500 mm³ and can exert maximum forces of 3.0 kN in vertical axis and 1.5 kN in the X and Y axis. The maximum feed rate in X and Y axis is 6000 mm/min and 1000 mm/min in Z axis. The forming tool is 15mm radius. The applied forming feed rate is equal to 4000 mm/min and the forming down pressure is set to be 0.015 MPa.

3. Results

3.1 Analytical results-a case study

In this section, a design example (hemisphere with 50 mm radius with thickness strain distribution obtained from shear deformation, see Fig.4) is defined to further illustrate the modeling method for multistage deformation path design. This shape has been tested by experiments and cannot be successfully formed in the single pass because the region with steep slope causes severe thinning. Therefore, it can be considered to evaluate the capability of multistage deformation path design on improving the overall formability.

The above established model was realized using Matlab software. The parameters in the model can be tuned to obtain the derived intermediate shape for each forming stage. In this case, three forming stages are adopted, of which two deformation paths need to be designed. The design parameters for each deformation paths are shown in Table 2. The deformation paths for the first two stages can be determined as shown in Fig.5(a). The predicted thickness strain distribution for these deformation paths are shown in Fig.5(b). In this case, the minimum thickness strain for each deformation path is defined based on Table 2 to be -0.288 and -0.644, respectively.

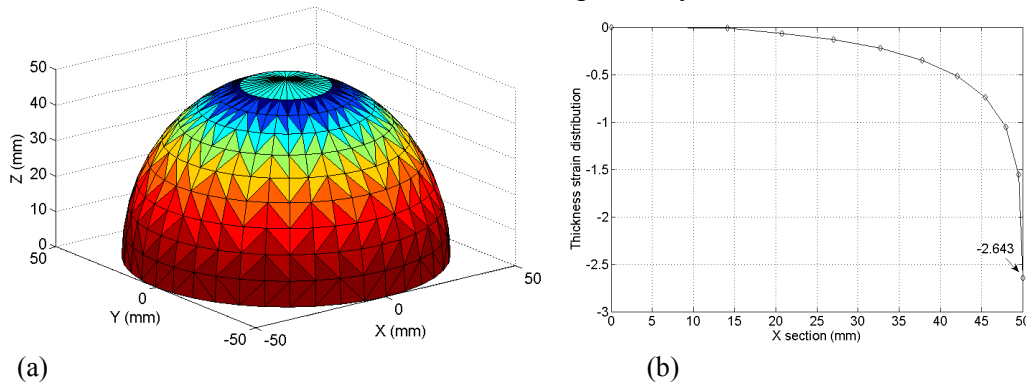


Fig.4. (a) Hemisphere with 50 mm radius; (b) thickness strain distribution.

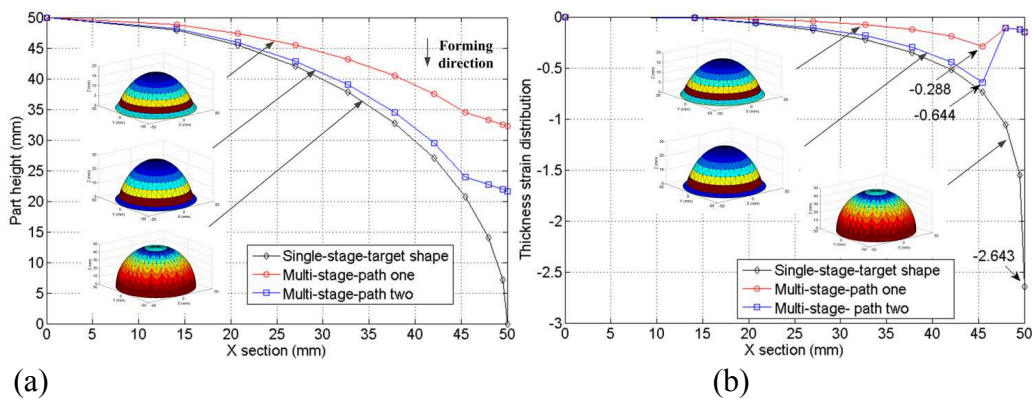


Fig.5. (a) Deformation paths; (b) predicted thickness strain distribution for deformation path one and two obtained from the model (a quarter section of the part).

Table 2. Designed parameters for deformation paths in the model.

Deformation paths	Tunable parameters			
	a_1	b_1	a_2	b_2
One	0.2	0.1	0.535	0.2
Two	0.2	0.1	1.018	0.2

3.2. FE simulation and experimental results

The validation of the proposed model is made for the hemispherical shape by comparing the analytical results with the FE simulation and experimental results. The comparison is made in terms of two aspects: process formability and thickness strain distributions for different deformation paths. The verification and validation of the process formability is determined based on the possibilities of successful forming of the final part considering the comparison of experimental results between the single-stage and the multi-stage forming. The results are shown in Table 3. It is noted that the crack occurred a little earlier in the designed multistage forming than the case of single-stage forming. In addition, FE results give a good prediction of the concentrated strain zone where the cracks occur.

Table 3. Comparison of formability between single-stage and designed multi-stage forming

Forming method	Forming result	Comparison of formability		
		Forming fracture position (mm)	Final part morphology	FE simulation (thickness strain)
Single-stage	Failure	Radius=49.96		
Multi-stage	Failure	Radius=48.99		

In order to understand the mechanism of material flow in the designed deformation paths and the final shape, the thickness strain distribution is considered in each deformation path and the final shape along the rolling and transverse directions by comparing the prediction, simulative and experimental results. Table 4 shows the comparison of the minimum thickness strain between the model prediction, FE simulation and experiments. Figs.6 and 7 show the thickness strain distribution of the deformation path one and two in terms of the comparison between the model prediction, FE simulation and experimental results. Fig.8 shows the thickness strain distribution of the final shape considering the comparison of FE simulation and experimental results in the single-stage and designed multistage forming, respectively. It is seen that the thickness strain from the model prediction overestimates the FE simulative and experimental results in deformation path one and two. The FE simulation results are in agreement with the experimental results in deformation path one and two and the final shape.

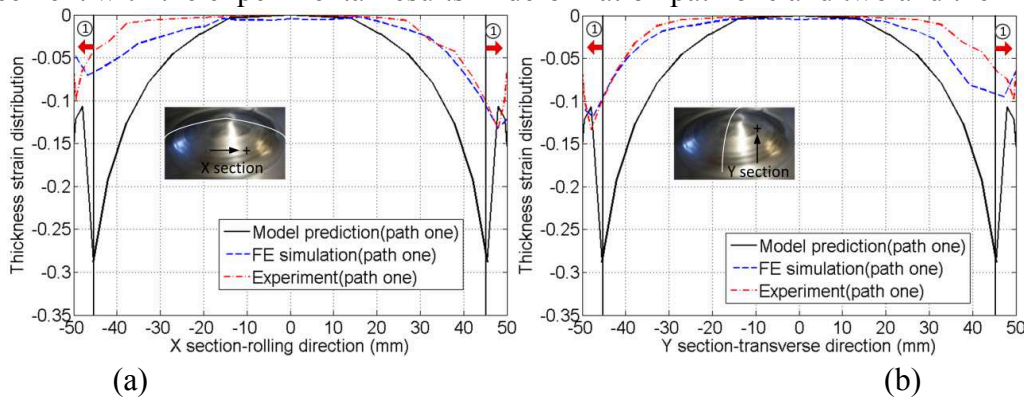
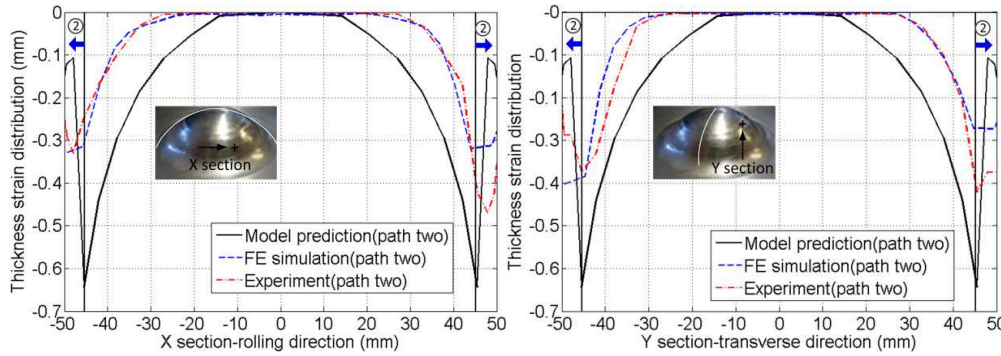


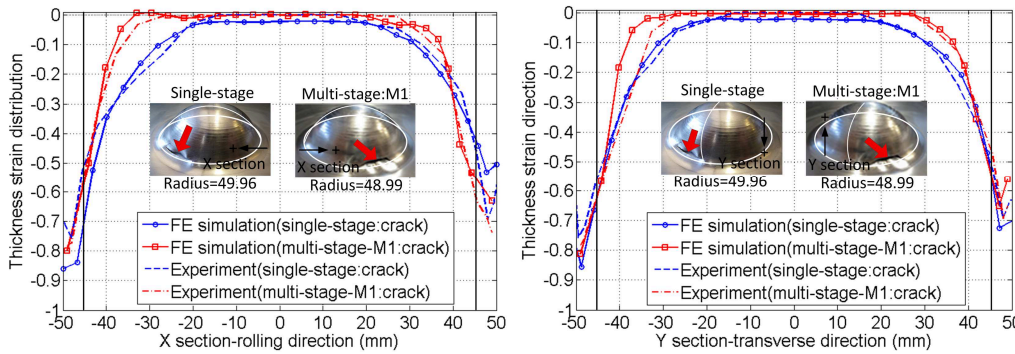
Fig.6. Thickness strain distribution with X and Y sections of deformation path one: X section (rolling direction); (b) Y section (transverse direction).

Table 4. Comparison of minimum thickness strain between model prediction, FE simulation and experiments.

Deformation paths	Comparison of minimum thickness strain		
	Prediction	FE simulation	Experiment
One	-0.2880	-0.1388	-0.1335
Two	-0.6440	-0.4167	-0.4700



(a) (b)
Fig.7. Thickness strain distribution with X and Y sections of deformation path two: (a) X section (rolling direction); (b) Y section (transverse direction).



(a) (b)
Fig.8. Thickness strain distribution with X and Y sections of the final shape formed by single-stage and designed multi-stage forming: (a) X section (rolling direction); (b) Y section (transverse direction).

3.3. Discussion

It is worth mentioning that from the above results, the formability of the proposed multistage deformation path design is no better than that of only single-stage forming. The predicted thickness strains from the model show that the minimum thickness strains are located at the part radius 45.5mm for the first two deformation paths, which means the small concentrated strain zone is likely to occur around the radius 45.5mm during the forming of the final part compared with the minimum strain location (radius 50mm) in the single-stage forming. In addition, in Bambach et al. [2], the author concluded that the movement of material flow in TPIF was experimentally observed from ‘outside’ to ‘inside’ (Fig.9), in other words, which needs more material (outside the final part region) involved in the forming to make sure the enough material allocated. If only the material in the final part region is involved in the multistage forming, the already thinned material in the current stage will be more locally stretched in the subsequent stage and failure may occur earlier by accumulating the risk of excessive thinning as the forming stages increase. Therefore, although the strain compensation idea is introduced, no more material can be allocated to the severely sloped region. Another possible reason is the influence of process parameters in ISF process, especially the asymmetric tool path. It will

cause the asymmetric thickness strain distribution. However, the experiments show that the multistage deformation path is still the most significant factor on the influence of the process formability.

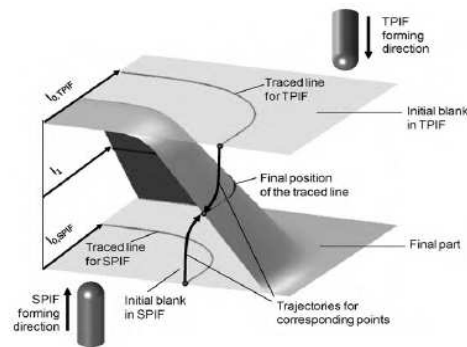


Fig.9. Traces of material points in SPIF and TPIF [2].

4. Conclusions

Based on the shear deformation and strain compensation idea, an analytical model for multistage deformation path design has been developed with the aim of improving the process formability and achieving more uniform thickness distribution. However, the results show the process formability has not been enhanced compared with the single-stage forming. The possible reason has been discussed. Additionally, the developed FE model can successfully predict the area with high magnitude of thickness strains, which can lead to cracks. In view of the drawback of this model, a modified analytical model using more material involved in the forming is being investigated and some new results will be reported in the future.

Acknowledgement

This research was supported by the ARC Linkage Program and QMI Solutions in Australia.

References

- [1] M.Skjoedt, M.B.Silva, P.A.F.Martins, N. Bay, Strategies and limits in multi-stage single-point incremental forming, *J. Strain Anal. Eng.* 45 (2010) 33-44.
- [2] M.Bambach, A geometrical model of the kinematics of incremental sheet forming for the prediction of membrane strains and sheet thickness, *J. Mater. Process. Tech.* 210 (2010) 1562-1573.
- [3] J.Jeswiet, F.Micari, G.Hirt, A.Bramley, J.Duflou, J.Allwood, Asymmetric single point incremental forming of sheet metal, *CIRP Ann.-Manuf. Techn* 54 (2005) 88-114.
- [4] L.Filice, L.Fantini, F.Micari, Analysis of material formability in incremental forming, *CIRP Ann.-Manuf. Techn.* 51 (2002) 199-202.
- [5] K.Jackson, J.Allwood, The mechanics of incremental sheet forming, *J. Mater. Process. Tech.* 209 (2009) 1158-1174.
- [6] S.Thibaud, R.Ben Hmida, F.Richard, P.Malécot, A fully parametric toolbox for the simulation of single point incremental sheet forming process: Numerical feasibility and experimental validation, *Simul. Model. Pract. Th.* 29 (2012) 32-43.
- [7] S.P.Shanmuganatan, V.S.Senthil Kumar, Experimental investigation and finite element modeling on profile forming of conical component using Al 3003(O) alloy, *Mater. Design* 36 (2012) 564-569.
- [8] T.J.Kim, D.Y.Yang, Improvement of formability for the incremental sheet metal forming process, *Int. J. Mech. Sci.* 42 (2000) 1271-1286.
- [9] Z.B.Liu, Y.L.Li, P.A.Meehan, Vertical Wall Formation and Material Flow Control for Incremental Sheet Forming by Revisiting Multistage Deformation Path Strategies, *Mater. Manuf. Process.* 28 (2013) 562-571.

4.2.2 AMINO TPIF Multi-Pass Deformation Design

Paper J

Multi-pass deformation design for incremental sheet forming: Analytical modeling, finite element analysis and experimental validation

Liu, Z.B., Daniel, W.J.T., Li, Y.L., Liu, S., Meehan, P.A.

Journal of Materials Processing Technology

2014, Volume: 214(3), Pages: 620-634.



Multi-pass deformation design for incremental sheet forming: Analytical modeling, finite element analysis and experimental validation

Zhaobing Liu*, William J.T. Daniel, Yanle Li, Sheng Liu, Paul A. Meehan

School of Mechanical and Mining Engineering, The University of Queensland, St Lucia, Brisbane, QLD 4072, Australia

ARTICLE INFO

Article history:

Received 8 July 2013

Received in revised form 22 October 2013

Accepted 8 November 2013

Available online 19 November 2013

Keywords:

Incremental sheet forming

Deformation pass

Intermediate shape

Formability

Thickness distribution

Thickness strain

Finite element analysis

ABSTRACT

Incremental sheet forming (ISF) is a promising rapid prototyping technology with high potential to shape complex three-dimensional parts. However, a common technical problem encountered in ISF is the non-uniform thickness distribution of formed parts; particularly excessive thinning on severely sloped regions. This may lead to fracture and limit the process formability. Design of multi-stage deformation passes (intermediate shapes or preforms) before the final part, is a desirable and practical way to control the material flow in order to obtain a more uniform thickness distribution and avoid forming failure. In the present paper, a systematic methodology for designing multi-stage deformation passes considering the predicted thickness strains given the design shape is proposed based on the shear deformation and the strain compensation mechanism. In this methodology, two analytical models ($M1$ and $M2$) are developed by taking into account; the global average thickness strain and only the material in the final part region used in the forming ($M1$), and the local weighted average thickness strain and the additional material around the final part region used in the forming ($M2$), respectively. The feasibility of the proposed design methodology is validated by finite element analysis (FEA) and experimental tests using an Amino ISF machine. The results show that a more uniform thickness strain distribution can be derived using $M2$. The incurrence of the highest strains can be delayed in the intermediate stages and the flow of material is allowed into the deformed region, thereby allowing a compressive stress state to develop and enabling steeper shapes to be formed. Therefore, the process formability can be enhanced via the optimized design of deformation passes.

© 2013 Elsevier B.V. All rights reserved.

1. Introduction

As a promising technology for rapid prototyping and small-batch production, incremental sheet forming (ISF) has gained great attention in the sheet metal forming community in the past decade. In the ISF process, a forming tool is controlled by a computer numerically controlled (CNC) machine following a prescribed tool path which locally plastically deforms the sheet metal into the desired shape. Thus an infinite variety of 3D shapes can be produced using one tool. This forming process can be categorized into two main types: single point incremental forming (SPIF) without a forming die and two point incremental forming (TPIF) with a partial or a full forming die. The technology of ISF is promising and advantageous by providing higher formability compared with deep drawing or stamping. However, it is still limited by the significant thinning

of the deformed sheet metal, forming defects and long forming time induced by the long travel path of the forming tool. A comprehensive review of ISF research is provided by Jeswiet et al. (2005).

Much research in ISF has been performed to investigate the forming limits and increase the formability by adopting multi-stage deformation pass design in the past decade. In particular, Filice et al. (2002) investigated the material formability in ISF under different strain conditions. The results indicated that local stretching is the dominant deformation mode in ISF. On the other hand, Jackson and Allwood (2009) further investigated the mechanics of ISF through an experimental campaign. It was revealed that shear in the tool direction is the most significant strain component and increasing stretching and shear also exist perpendicular to the tool direction. The above discussions show the shear and/or stretching deformation modes lead to material thinning in the ISF process. Failure in ISF is most likely to be caused by the non-uniform thickness distribution and typically the excessive localized thinning of steep walls in a part, which decreases the maximum wall angle that can be achieved in materials formed by ISF in comparison to some other processes.

* Corresponding author. Tel.: +61 7 33653885.

E-mail addresses: zhaobing.liu@uqconnect.edu.au, zhaobingliu@hotmail.com, z.liu7@uq.edu.au (Z. Liu).

This makes it difficult to manufacture complex parts with steep walls. Therefore, the proper allocation of materials during forming is important to uniformly distribute the material thickness on the final parts in order to avoid the occurrence of forming failure. Kim and Yang (2000) proposed a double-pass forming method to improve the formability for the ISF process. This method is based on shear deformation using the predicted thickness strain distribution to design intermediate shapes in order to get a uniform thickness distribution of a final part. Young and Jeswiet (2004) also developed a two-stage strategy to improve the final thickness distribution for the parts with steep areas. The results showed that the occurrence of a thinning band in the single-stage forming process can be delayed in the two-stage process so that complex parts with steep walls can be successfully made. Duflou et al. (2008) explored a multi-step tool path strategy to manufacture parts with vertical walls in order to avoid part failure. The final thinning in the multi-stage forming process can exceed the maximum thickness reductions in the single-stage process, which means a formability increase. In Manco et al. (2011), the effect of the tool trajectory has been studied in terms of the final thickness distribution and the formability. The advantages and disadvantages of single-stage forming and three different multi-stage forming strategies have been compared and analyzed by manufacturing the same shape and evaluating the thickness distributions. It was concluded that formability can be conveniently enhanced with proper multi-stage deformation design by involving as much material as possible from a theoretical point of view. Skjoedt et al. (2010) investigated a multi-stage strategy to produce cylindrical cups with vertical walls. They pointed out that the movement of the forming tool in the multi-stage SPIF has a great influence on the thickness distribution and SPIF is limited by cracking rather than necking. Zhang et al. (2013) proposed an FEM-based multi-stage SPIF method, which treats the SPIF process as hydro-bulging forming. The intermediate surfaces obtained from the FEM results can be used for the tool path generation. Li et al. (2013) used a part regional division idea in the multi-pass deformation design to manufacture a car taillight bracket with nearly straight-wall region and the groove region. They found that an intermediate surface which is geometrically closer to the final part can obtain better forming quality. Liu et al. (2013) proposed three multi-stage deformation pass strategies for forming cups with vertical walls. Those strategies and their combinations have been evaluated in terms of the process formability. The results showed that the forming strategy using more material in the forming as well as the addition of a small amount of bending can greatly improve the formability. However, in most of existing multi-stage forming design in ISF, material flow and thickness strain distribution can still not be quantitatively controlled.

Numerical simulation of sheet metal forming processes is an effective way to design and optimize the process parameters and to evaluate the forming defects such as fracture, springback, wrinkling, geometric deviations and residual stresses. In the past decade, researchers have used the finite element method (FEM) to model the ISF process. In Thibaud et al. (2012), a fully parametric toolbox has been developed to simulate the SPIF process using FEM. The prediction results of geometric deviations, thickness distribution and forming forces showed good agreement with the experimental results. Shanmuganatan and Senthil Kumar (2012) presented an explicit numerical simulation using Abaqus. The stress and thickness distribution have been derived and validated by experimental tests. Dejardin et al. (2010) used a FE model with shell elements to perform the simulation of the SPIF process in order to analyze the shape distortions and spring-back effects. The comparison between experimental and simulated results showed that the developed FE model can predict accurate results. Although FEM is an effective way to model and simulate the multi-stage ISF process, it usually takes long computational hours (several days or even

more than a week), and therefore cannot be used effectively for the design of the full multi-stage ISF process.

The above review of recent studies shows that most of the previous work on the multi-stage deformation pass design in ISF is still based on the trial and error method so that material flow cannot be quantitatively controlled. Although there was an analytical model developed by Kim and Yang (2000), it is only suitable for two-stage forming. For the manufacture of more complex parts, more forming stages are needed. This paper proposes a systematic methodology to design multi-stage deformation passes in terms of the predicted thickness strains given a final part based on the shear deformation and the strain compensation mechanism. In this methodology, two analytical models ($M1$ and $M2$) are developed considering: the *global average thickness strain* and only the material in the final part region used in the forming ($M1$), and the *local weighted average thickness strain* and the additional material around the final part region used in the forming ($M2$), respectively. The proposed design methodology is compared with finite element analysis (FEA) and experimental tests using an Amino ISF machine with reference to the process formability and the thickness strain distribution.

2. Methodology

The shear-based modeling for deformation pass design in ISF was first proposed in Kim and Yang (2000). However, this model is only suitable for double-pass deformation design. In some cases, multi-stage deformation pass design is necessary for making complex parts, such as examples in Duflou et al. (2008), Skjoedt et al. (2010), Zhang et al. (2013), Li et al. (2013) and Liu et al. (2013). A systematic design methodology for multi-stage deformation pass design is provided in this section. First, the shear-based modeling for single-pass deformation design is briefly reviewed. Then, two analytical models are developed. In addition, a systematic design methodology incorporating the two models is proposed. Finally, the methodology for the FEA and experimental tests is introduced.

It is worth mentioning that the aim of the development of the two models is to improve the process forming limits. The underlying hypothesis of these models can be summarized as follows:

- (i) The use of intermediate stages in the forming process will delay the incurrence of the highest strains, and therefore allow steeper shapes to be formed than would be possible by using single-pass forming.
- (ii) By forming a wider area than the perimeter of the shape, it is possible to:
 - Avoid discontinuities in the intermediate thickness strains, and therefore allow steeper shapes to be formed than would be possible by using single-pass forming;
 - Allow the flow of material into the deformed region, thereby allowing a compressive stress state to develop and enabling steeper shapes to be formed than would be possible in single-pass forming.

The first model ($M1$) has been developed to test the first of the above points, whilst the second model ($M2$) has been developed to test all three of the above points.

2.1. Single-pass deformation model – shear deformation

An arbitrarily designed part can be discretized by triangular elements. Based on the shear deformation, x and y coordinates are the same for both initial and final configurations. Fig. 1 illustrates the 3D shear deformation for one sheared triangular element in a part.

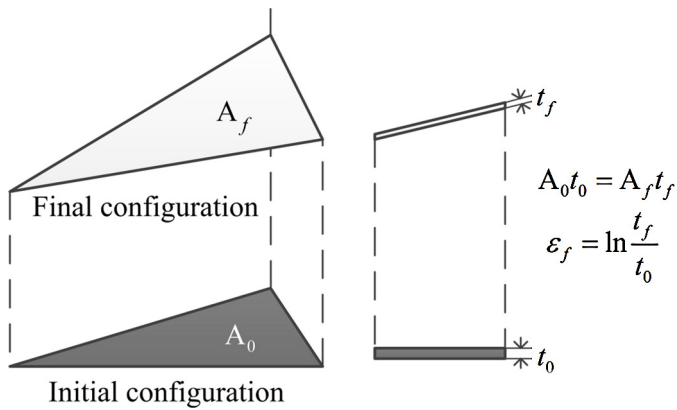


Fig. 1. Mechanism of shear deformation.

Based on the assumption of volume constancy, the thickness strain can be calculated in the following equation,

$$\epsilon_f = \ln \frac{t_f}{t_0} = \ln \frac{A_0}{A_f} \quad (1)$$

where ϵ_f is the thickness strain in one element in the final configuration. t_0 and t_f are the initial and final thickness in one element. A_0 and A_f are the initial and final areas in one element, which can be calculated by x, y, z coordinates.

In this way, the thickness strains of all elements on the designed part can be approximately estimated, which are the input of the multi-stage deformation pass models developed in the following sections. It is worth mentioning that the shear deformation assumption in this single-pass model can be relaxed. In fact, the deformation mechanism can be shear and/or stretching, or a combination of any of these as long as the centroidal plane of a sheet does not displace horizontally, which would result in the same thickness relationship compared to the pure shear assumption. However, in order to develop a simple and efficient model for multi-pass design, the shear deformation is still used to calculate the intermediate thickness strains in the following multi-pass modeling process.

2.2. Open-loop multi-stage deformation pass models

Within the modeling process, it is assumed that the deformation mode is only based on shear deformation and the material properties need not be considered in this case. The following modeling process involves two aspects: (i) devise intermediate thickness strains in the corresponding intermediate passes given the thickness strains of the designed part predicted by the single-pass model; (ii) determine the intermediate passes (intermediate shapes) based on the intermediate thickness strains.

In order to control the material flow and obtain the uniform thickness distribution, the forming in the localised region of a part requiring severe shear deformation (with higher magnitude of thickness strains) to achieve the final form should be delayed by compensating with less shear deformation (with lower magnitude of thickness strains) in the multi-stage passes. In other words, the incurrance of the highest thickness strains will be delayed using intermediate stages in the forming, and therefore steeper shapes are allowed to be formed than would be possible by using single-pass forming. The part regions with less shear deformation (with lower magnitude of thickness strains) should be kept close to the final shape in the deformation passes in order to reduce the occurrence of forming defects. On this basis, two analytical models are developed to design multi-stage deformation passes by calculating and compensating the intermediate thickness strains in each multi-stage deformation pass given a final part.

2.2.1. Open-loop multi-pass design-Model one (M1)

In this model, it is assumed that only the material in the final part region is used in the forming. The global average thickness strain of the final part is used to compensate the strain in the severely sloped region of the final part in the intermediate stages. The local thickness strain of the final part is used to estimate the intermediate shape in the non-severely sloped region of the final part.

The intermediate thickness strain for each triangular element i (from 1 to N) of the final part in the corresponding deformation pass can be determined as follows:

A loop calculation applies to the following two equations until all the intermediate thickness strains of triangular elements ($i=1:N$) are calculated.

For the severely deformed region of the final part, i.e. $\epsilon_f(i) < \epsilon_{Gavg}$, the intermediate thickness strains can be calculated as,

$$\epsilon_{int}(i) = a_1(m) \times \epsilon_{Gavg} - b_1(m) \times \frac{\epsilon_f(i) - \epsilon_{min}}{\epsilon_{max} - \epsilon_{min}} \times \epsilon_{Gavg}. \quad (2)$$

For the non-severely deformed region of the final part, i.e. $\epsilon_f(i) > \epsilon_{Gavg}$, the intermediate thickness strains can be calculated as,

$$\epsilon_{int}(i) = a_2(m) \times \epsilon_f(i) - b_2(m) \times \frac{\epsilon_f(i) - \epsilon_{min}}{\epsilon_{max} - \epsilon_{min}} \times \epsilon_f(i), \quad (3)$$

where $\epsilon_{min} = \min[\epsilon_f(1), \epsilon_f(2), \dots, \epsilon_f(n)]$, $\epsilon_{max} = \max[\epsilon_f(1), \epsilon_f(2), \dots, \epsilon_f(n)]$,

$$\epsilon_{Gavg} = \frac{\sum_{j=1}^n \epsilon_f(j)}{n}. \quad (4)$$

$\epsilon_f(i)$ is the thickness strain in element i of the final part, and $\epsilon_{int}(i)$ is the intermediate thickness strain in element i of the deformation pass. $a_1(m)$, $a_2(m)$, $b_1(m)$, and $b_2(m)$, are parameters which need to be tuned to determine the intermediate thickness strain and (m) is the index of the intermediate stage ($m=1:M$). M denotes the number of intermediate passes.

It is worth mentioning that all these thickness strains in the above model are negative, i.e. ϵ_{min} and ϵ_{max} corresponding to the maximum and minimum magnitudes, respectively. Eq. (2) applies when the local thickness strain $\epsilon_f(i)$ in the final shape has a higher magnitude than that of the global average thickness strain ϵ_{Gavg} . The first term of the right side in this equation scales the global average thickness strain ϵ_{Gavg} in the final shape to estimate an intermediate shape (deformation pass). This would have uniform thickness strain. However, this is corrected by the second term, which gives the least deformed triangular element in the final shape (with ϵ_{max}) this average thickness strain, but reduces the magnitude of thickness strain induced in triangular elements which have a higher magnitude of the thickness strain. This delays the forming of the regions to be stretched the most. If $b_1(m) = a_1(m)$, then the most deformed triangular element in the final shape (with ϵ_{min}) has $\epsilon_{int} = 0$. Similarly, when the local thickness strain $\epsilon_f(i)$ in the final shape has a lower magnitude than that of the global average thickness strain ϵ_{Gavg} , then Eq. (3) applies. In this case, in the right side of Eq. (3), the first term scales the local thickness strain ϵ_f in the final shape to estimate an intermediate shape, more closely reflecting the final shape. The second term corrects this so that if $b_2(m) = a_2(m)$, then again no reduction in the thickness strain occurs at a triangular element with the minimum thickness change in the final shape. However, the magnitude of thickness strain at the intermediate stage is reduced to zero (delaying forming), where the final shape has the maximum thickness strain (minimum thickness strain magnitude). $b_1(m) = a_1(m)$ and $b_2(m) = a_2(m)$ gives consistent results where $\epsilon_f = \epsilon_{Gavg}$.

Once all the intermediate thickness strains are derived in the deformation passes by the model developed, the second aspect as discussed above is to determine the positions of all triangular

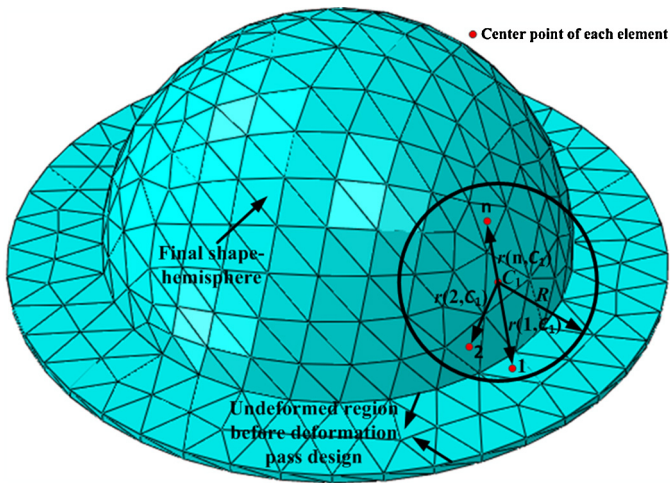


Fig. 2. Illustration of model two in detail.

elements given these intermediate thickness strains in order to construct the deformation passes (intermediate shapes). Due to the shear assumption, the z coordinate of the unknown node in each triangular element can be achieved recursively. For more details, the readers can refer to Kim and Yang (2000) (Section 4). The positions of corresponding elements (three nodes in one element) can be imported to a CAD software to build the deformation passes (intermediate shapes). Then, the tool path generation can be implemented based on the determined deformation passes (intermediate shapes) using Siemens NX CAM 7.5 software (details can be found in Section 2.4).

2.2.2. Open-loop multi-pass design-Model two (M2)

Bambach (2010) discussed the deformation mechanism of ISF (SPIF and TPIF) by tracing the material points during forming (see Fig. 14(a) in Section 3.1). It is found that the movement of material points is from outside to inside (“pull material in” deformation) in TPIF, which results in a “compression” mode in TPIF compared with a stretching mode in SPIF. In the multi-stage forming process, deformation passes (intermediate shapes) can be devised to encompass the final shape and provide the additional material, thereby allowing for manufacturing more complex parts than that in SPIF.

Taking into account the discussion above, model two (M2) is developed, which is a modified model based on M1. In this model, the additional material around the final part is incorporated in the multi-stage forming. It is noted that, by forming a wider area than the perimeter of the design shape, it is possible to

- Avoid discontinuities in the intermediate thickness strains, and therefore allow steeper shapes to be formed than would be possible by using single-pass forming.
- Allow the flow of material into the deformed region, thereby allowing a compressive stress state to develop and enabling steeper shapes to be formed than would be possible in single-pass forming.

The *local weighted average thickness strain* is proposed to compensate the thickness strain in the severely sloped region instead of the *global average thickness strain* in Eq. (2) in the intermediate passes. The *local thickness strain* in the final part is used to estimate the intermediate shape in the non-severely sloped region. An illustration of M2 is shown in Fig. 2 and the details are presented as follows:

Consider the center point j (from C_1 to C_N) of each triangular element and its neighbour i (from 1 to n) with $r(i, j) \leq R$

The first loop calculation applies to Eqs. (5)–(7) to determine $\varepsilon_{Wavg}(i, j)$ until all the neighbours ($i = 1:n$) of center point j of the triangular element are calculated.

$$r(i, j) = \sqrt{(\bar{x}_{i,j} - \bar{x}_j)^2 + (\bar{y}_{i,j} - \bar{y}_j)^2 + (\bar{z}_{i,j} - \bar{z}_j)^2}. \quad (5)$$

$$d_{disfac}(i, j) = 1.0 - \alpha \times \frac{r(i, j)}{R}. \quad (6)$$

$$\varepsilon_{Wavg}(i, j) = \varepsilon_f(i, j) \times d_{disfac}(i, j). \quad (7)$$

Then, $\varepsilon_{Lavg}(j)$ can be derived from Eq. (8)

$$\varepsilon_{Lavg}(j) = \frac{\sum_{i=1}^n \varepsilon_{Wavg}(i, j)}{\sum_{i=1}^n d_{disfac}(i, j)}. \quad (8)$$

Next, for the severely deformed region of the final part, i.e. $\varepsilon_f(j) \leq \varepsilon_{Gavg}$ (region in the final part) or $\varepsilon_f(j) = 0$ (additional material region outside the final part), the intermediate thickness strain can be calculated as,

$$\varepsilon_{int}(j) = a_1(m) \times \varepsilon_{Lavg}(j) - b_1(m) \times \frac{\varepsilon_f(j) - \varepsilon_{min}}{\varepsilon_{max} - \varepsilon_{min}} \times \varepsilon_{Lavg}(j). \quad (9)$$

For the non-severely deformed region of the final part, i.e. $\varepsilon_f(j) > \varepsilon_{Gavg}$, the intermediate thickness strain can be calculated as,

$$\varepsilon_{int}(j) = a_2(m) \times \varepsilon_f(j) - b_2(m) \times \frac{\varepsilon_f(j) - \varepsilon_{min}}{\varepsilon_{max} - \varepsilon_{min}} \times \varepsilon_f(j). \quad (10)$$

The second loop calculation applies to all Eqs. (5)–(10) until all the triangular elements ($j = C_1:C_N$) are calculated. where $r(i, j)$ is the radius between the center point j and its neighbour i . R is the radius, which defines the size of the region over which the thickness strains of neighbour elements are averaged. \bar{x} , \bar{y} and \bar{z} represent the arithmetic average of corresponding coordinates in an element. $d_{disfac}(i, j)$ is the distance factor for the i th neighbor element, which linearly decreases with the distance to the center point j . α is an adjustable slope parameter, which changes the influence of the distance on the weighted average thickness strain. $\varepsilon_{Wavg}(i, j)$ is the weighted average thickness strain for the i th neighbor element. $\varepsilon_{Lavg}(j)$ is the local weighted average thickness strain for local element j . Other expressions are defined in M1.

Because M2 allocates more undeformed material involved in the multi-stage deformation pass design (allow the flow of material into the deformed region, thereby allowing a compressive stress state to develop and enabling steeper shapes to be formed), it improves the process formability and achieves a more uniform thickness strain distribution compared to M1, in which only the material in the final part region is used. In addition, M2 substitutes the global average thickness strain ε_{Gavg} in Eq. (2) for the local weighted average thickness strain $\varepsilon_{Lavg}(i)$ in Eq. (9), which can provide a more smooth estimate of the deformation transition period from the initial state to the final shape to compensate the severely sloped regions (avoid discontinuities in the intermediate thickness strains, and therefore allow steeper shapes to be formed). In M2, the other settings are the same as in M1.

2.3. Methodology for closed-loop multi-stage deformation pass design

In this subsection, a systematic methodology for multi-stage deformation pass design is proposed based on the deformation pass models developed previously. In this methodology, the thinning rate is set as a forming target to optimize the design of multi-stage deformation passes in order to increase the possibilities of successful forming and control the material flow to achieve more uniform thickness strain distributions on the final part.

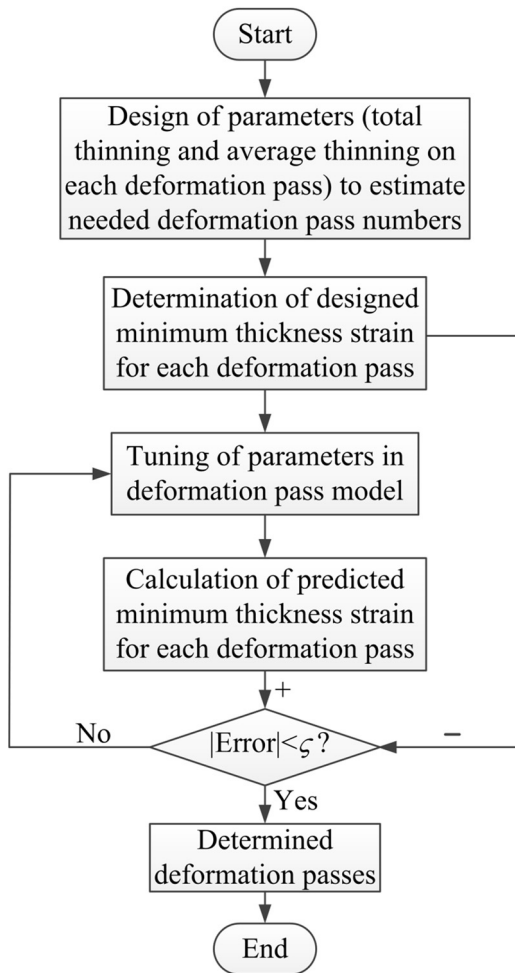


Fig. 3. Systematic methodology for closed-loop multi-stage deformation pass design (ζ is a very small number).

Due to volume conservation during forming, the relationship between thickness strains of multi-stage deformation passes and the final part can be expressed as,

$$\varepsilon_1 + \varepsilon_2 + \dots + \varepsilon_n = \varepsilon_f \quad (11)$$

where ε_i is the thickness strain of the i th forming stage ($i=1, 2, \dots, n$) and ε_f is the final thickness strain of the formed part. The deformation defects are not considered here. Taking the thickness thinning rate into consideration, Eq. (11) can be expressed as follows, see Li et al. (2012):

$$\ln(1 - T_1) + \ln(1 - T_2) + \dots + \ln(1 - T_n) = \ln(1 - T_0) \quad (12)$$

where T_i is the thickness thinning rate of the i th deformation pass ($i=1, 2, \dots, n$) and T_0 is the total thickness thinning rate. By assuming $T_1 = T_2 = \dots = T_n = \bar{T}$, the total number of forming stages needed can be approximately estimated as follows:

$$n_e = \frac{\ln(1 - T_0)}{\ln(1 - \bar{T})} \quad (13)$$

The systematic methodology for multi-stage deformation pass design is proposed as described in Fig. 3. The desired minimum total thinning rate and the minimum average thinning rate for all forming stages are set to estimate the number of needed forming stages. Then, the minimum thinning rate for each forming stage is designed given the average thinning rate and the corresponding thickness strain is calculated. The predicted minimum thickness strain for each deformation pass is calculated by tuning the parameters in

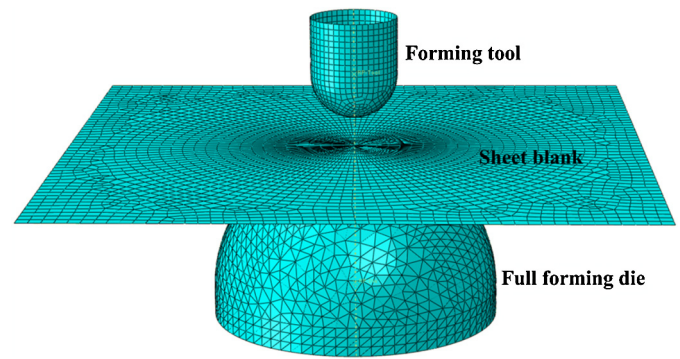


Fig. 4. Simplified FE modeling for TPIF.

the deformation models until the error between the predicted value and the designed value is smaller than a predefined value. Finally, the deformation passes (intermediate shapes) can be determined.

2.4. FEA and experimental methodology

In this subsection, validation methodology using FE simulation and experimental tests with an Amino ISF machine is introduced.

The FEA is performed to validate the proposed analytical models. A simplified FE model is developed to simulate the forming process for TPIF using ABAQUS®/Explicit software 6.11, as seen in Fig. 4. In this FE model, it is assumed that the material is isotropic and elastic strains are neglected. Additionally, the process deformation is homogeneous. The periphery of the sheet blank is rigidly clamped and endures a constant pressure to mimic the movement of the hydraulic actuator in the real Amino ISF machine. For simplicity, to reduce the FE model size, a smaller sheet blank with the size of 200 mm × 200 mm is used in the simulation, which is proved to not influence the simulation results. The blank is considered as a deformable body and is discretized with shell elements S4R, which are reduced integration elements with one integration point in the plane and five integration points through the thickness. The size of each shell element is 4 mm. The forming tool and die are modeled using rigid surface elements R3D4 with sizes of 2 mm and 4 mm, respectively. The friction behavior is modeled using the Coulomb friction law with a friction coefficient of 0.1 between the blank and the forming tool and a friction coefficient of 0.8 between the blank and the forming die.

In this study, AA 7075-O aluminum sheets with the size of 300 mm × 300 mm and 1.016 mm thickness are used in the experiments. The mechanical properties derived from the tensile test for three directions (rolling, diagonal and transverse) are presented in Fig. 5.

From the results, the material can be assumed to be isotropic. The true stress values for three directions can be averaged, similar to r -value averaging, as:

$$\bar{\sigma} = \frac{\sigma_0 + 2\sigma_{45} + \sigma_{90}}{4} \quad (14)$$

The true stress–true strain curves can be fit by the Hollomon power law,

$$\bar{\sigma} = K\bar{\varepsilon}^n \quad (15)$$

where K is the strength coefficient and n is the strain-hardening exponent. $\bar{\sigma}$ and $\bar{\varepsilon}$ are the flow stress and the plastic strain, respectively.

On this basis, mechanical properties of AA 7075-O aluminum sheets with 1.016 mm thickness can be summarized in Table 1.

Siemens NX CAM 7.5 is utilized to obtain the cutter location (CL) data. The designed CAD shape is imported to NX CAM 7.5, which

Table 1
Mechanical properties of AA 7075-O aluminum alloy sheets with 1.016 mm thickness.

Material	AA7075-O
Density (t/mm^3)	2.81×10^{-9}
Young's modulus (MPa)	70,000
Poisson's ratio	0.33
Tensile yield strength (MPa)	89
Ultimate tensile strength (MPa)	191
Plastic coefficient K	352.9
Hardening exponent n	0.23

is used to generate the CL data and define the tool motion during the forming process. In this software, a Z-level milling operation is selected with 4 mm step-down size in deformation passes one and two and 2 mm step-down size in the final shape. The in-out downward movement of the tool is defined and the connection between two levels can be adjusted by the ramp angle, which guarantees that the tool path is continuous and leaves no obvious marks on the part surface. Then, the CL file is generated and utilized to the FE simulation and experiments. Fig. 6 shows the Z-level milling tool path for hemisphere with ramp angle 10° used in the FE simulation and experiments.

A method to import the tool path into Abaqus is also developed in order to fulfill the whole simulation process. It is noted that the forming tool movements are defined through the step module, which means the movements are correlated with the steps in the step module. Even for a simple part, there are thousands of incremental steps needed to simulate this forming process. Fig. 7 shows an approach to importing the tool path into the FE model.

Experimental investigations are performed on the AMINO® DLNC-PC incremental forming machine (Fig. 8) to validate the proposed models. The machine is a 3-axis CNC machine with a maximum workspace of 2100 mm × 1450 mm × 500 mm and can exert maximum forces of 3.0 kN in vertical axis and 1.5 kN in the X and Y axis. The maximum feed rate in X and Y axis is 6000 mm/min and 1000 mm/min in Z axis. In the experiments, the forming tool with 15 mm radius is used. The applied forming feed rate is equal to 4000 mm/min and the forming down pressure is set to be 0.015 MPa. The deformation passes one, two and the final shape

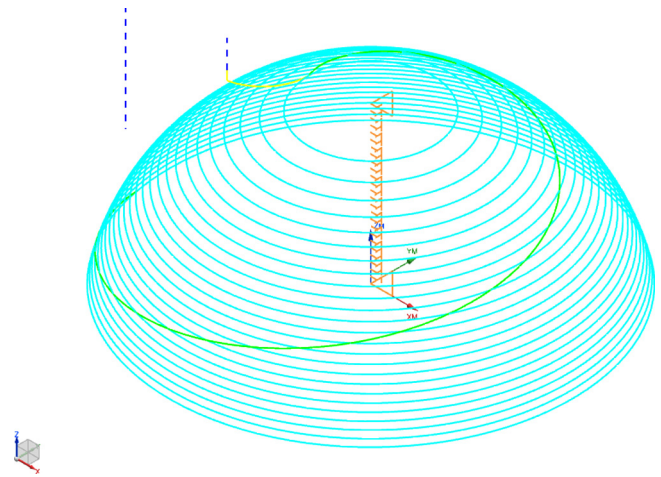


Fig. 6. Z-level milling tool path for hemisphere: ramp angle = 10° .



Fig. 8. The Amino ISF machine used for experiments.

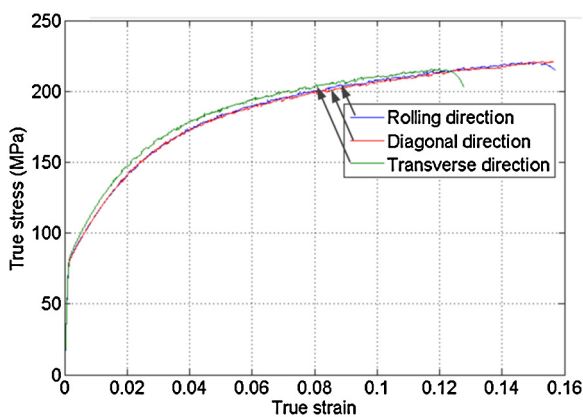


Fig. 5. True stress-true strain curves for AA7075-O aluminum alloy sheets with 1.016 mm thickness.

are all formed against the full forming die (it is made of Australian blackbutt hardwoods in this case).

3. Results

This section includes two aspects. Firstly, the analytical model results for the case study are provided in Section 3.1. Then, the results of the FEA and Amino TPIF forming tests are provided in terms of the material flow analysis, the process formability and thickness strain distributions in Section 3.2.

A design benchmark example (hemisphere with 50 mm radius, see Fig. 9) is provided to further illustrate the systematic methodology for multi-stage deformation pass design. This shape has been tested by experiments and cannot be successfully formed in only single-stage forming because severe thinning occurs in the steep slopes. This benchmark is used to determine the capability of multi-stage deformation pass design of improving the formability.

In the following, the analytical model results for closed-loop multi-stage deformation pass design are provided.

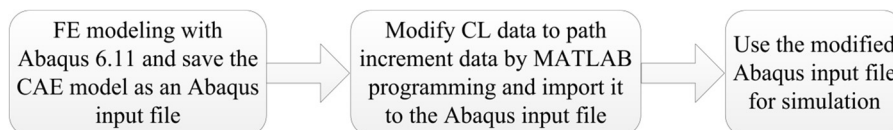


Fig. 7. An approach to importing the tool path into the FE model.

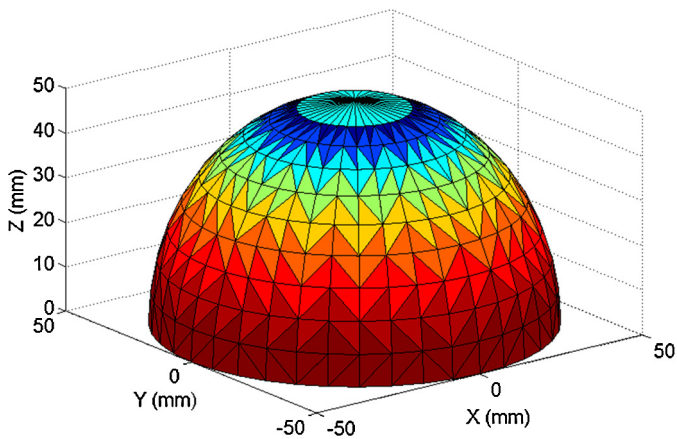


Fig. 9. Hemisphere with 50 mm radius.

3.1. Analytical model results for multi-stage deformation pass design

According to the systematic methodology in Section 2.3, the overall thinning rate T_0 is set to be less than 0.65 in this case. The average thinning rate \bar{T} is assumed to be less than 0.3. Then, the number n_e of forming stages needed can be estimated to be 3 using Eq. (13). As described in Li et al. (2012), the thinning rate of each forming stage can be adjusted. Therefore, the thinning rate for the forming stage (T_1, T_2, T_3) can be set to be 0.25, 0.30 and 0.35 (other choices could be used), respectively. The corresponding minimum thickness strains in different forming stages are $-0.29, -0.64$ and -1.08 . The parameters in the developed deformation models can be tuned until the error between the predicted minimum strain and the designed minimum thickness strain is satisfied. The whole design described is realized using MATLAB® software. The determined parameters are shown in Table 2. The deformation passes (intermediate shapes) for the corresponding forming stages were determined as shown in Figs. 10 and 11.

The predicted thickness strain distributions for multi-stage deformation passes are shown in Fig. 12. As can be seen in both Fig. 12(a) and (b), the trends of thickness strain distributions in deformation passes are first decreasing in the non-severe slope region and then ascending in the severe slope region based on M1 and M2, in which the algorithms incorporating a piecewise function are devised to estimate and compensate the corresponding thickness strains in deformation passes. The positions of the occurrence of the minimum negative intermediate thickness strains (maximum absolute value) in deformation passes characterize the weakest forming positions of the part, which are critical for fracture during the multi-stage forming. The arrows in red and blue color (marked as (1) and (2)) in Fig. 12(a) and (b) show the material flow direction in each deformation pass. It further illustrates that, by forming a wider area than the perimeter of the shape in M2, the incurrance of the highest thickness strains has been delayed in the intermediate passes (see the position of vertical solid line: 50 mm in M2 vs 45.5 mm in M1). Therefore, it will allow the flow

of material into the deformed region and enable steeper shapes to be formed. In addition, discontinuities in the intermediate thickness strains can be avoided so that steeper shapes are allowed to be formed compared to M1 in Fig. 12(a). Hence these results show that M2 is expected to have better formability than M1.

3.2. FE and experimental results

In this subsection, the results for two analytical models are compared with FE simulation and experimental tests. The comparison is made in terms of three aspects: the material flow analysis, process formability for the forming of the final part and thickness strain distributions for different deformation passes and the final part.

3.2.1. Material flow analysis

First, in order to verify the discussed conclusion about the kinematics of material points in Bambach (2010) (Section 2.2.2), we performed a test with a hemispherical shape of 50 mm radius in TPIF using the coordinate measurement technique similar to the method in Werner et al. (1998). Measurements were taken using the Amino ISF machine with a suitable small probe. Coordinate data can be read from the screen on the control panel. The positions of three representative material points were recorded. Although the method adopted here cannot obtain the trace of material points in the intermediate state, the initial and final positions of the material points show there is a compression mode occurring in TPIF, which is in agreement with the findings in Bambach (2010), see Fig. 13. In addition, the movement of material points is also evidenced by the FEM as seen in Fig. 14. A “pull material in” movement can be found in the final forming in M2 from the initial position $(-60, 0)$ in Fig. 14(a) through pass one $(-58.69, 0.8)$ in Fig. 14(b) and pass two $(-55.55, 1.23)$ in Fig. 14(c) to the final position $(-47.19, 3.05)$ within the perimeter of the hemisphere in Fig. 14(d).

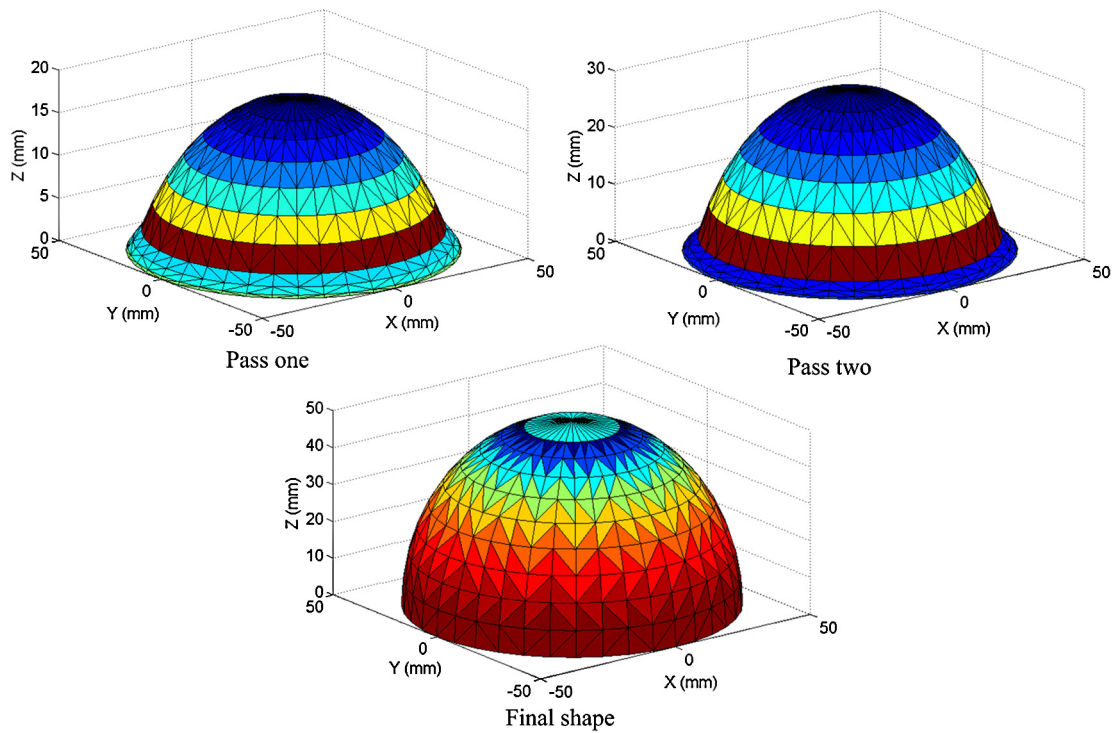
It is believed that in-plane movement causes a compressive state in TPIF which suppresses the failure. The greatest component of the compressive state in TPIF is in the direction normal to the sheet at the point of contact caused by the reaction between the tool and the positive die, whilst the component in the plane of the sheet both parallel and perpendicular to the tool direction is generally stretching. In the case of this paper, the material is shown to displace inwards causing a compressive stress state close to the center of the hemisphere in the plane of the sheet, which can be clearly seen in the final forming of all methods in Fig. 14(d), (e) and (f). However, this increases the tensile stress state around the perimeter of the hemisphere, and hence is likely to actually increase the propensity for failure. This is apparent on the dark blue region in Fig. 14(d), (e) and (f), and is particularly acute in this case because the region of greatest stretching in the x - y plane is also the region with greatest stretching in the z direction. However, it should be mentioned that, by forming a wider area than the perimeter of the shape, the greatest stretching region (with highest thickness strains) in M2 in Fig. 14(d) is actually shifted to the outside of the hemispherical perimeter compared to on the perimeter in single-pass forming (Fig. 14(e)) and the inside of the perimeter in M1 (Fig. 14(f)). Therefore, the formability in M2 is expected to be higher than that in the single-pass forming and M1. These findings can be further confirmed by the formability results in the following section.

3.2.2. Formability

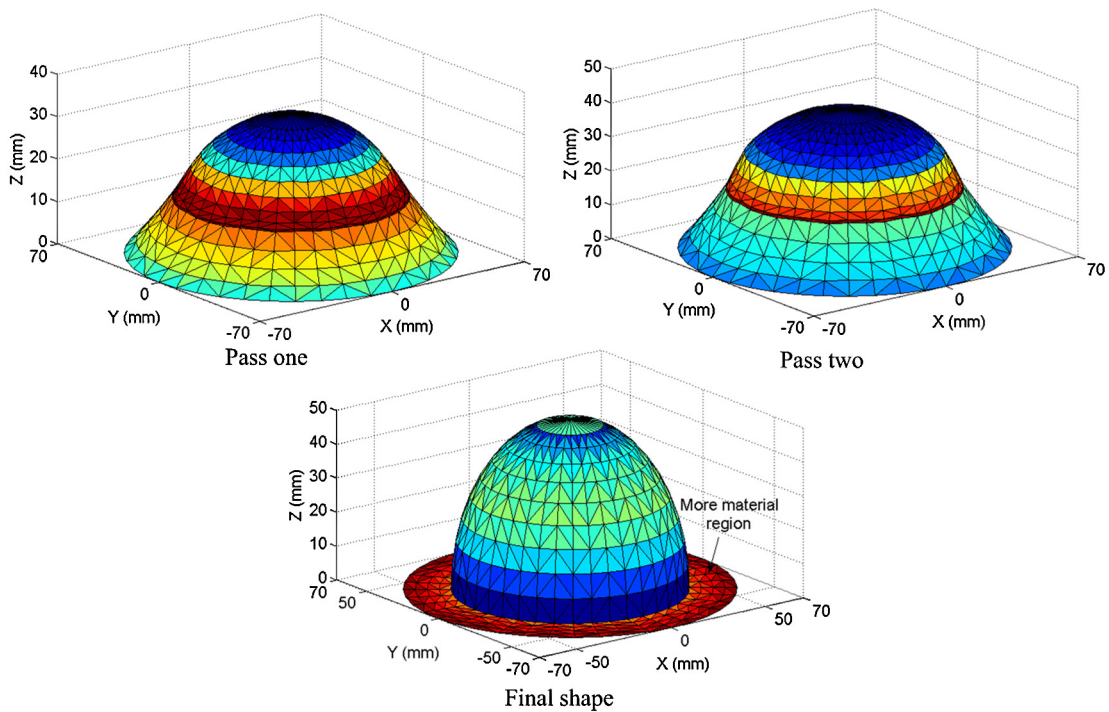
The process formability is analyzed based on the forming outcome (failure or success) of the final part formed by single-stage forming and the proposed multi-stage forming methodology considering the comparison of experimental and FE prediction results as summarized in Table 3. It is worth noting that the position of failure can be determined from the Amino ISF machine controller panel. It can be further calculated and expressed as a part radius.

Table 2
Determined parameters for multi-stage deformation passes in M1 and M2.

Model	Deformation passes	Tunable parameters					
		a_1	b_1	a_2	b_2	α	R
M1	Pass one	0.20	0.10	0.54	0.20	×	×
	Pass two	0.20	0.10	1.02	0.20	×	×
M2	Pass one	0.33	0.05	0.80	0.70	0.50	25
	Pass two	0.73	0.30	0.90	0.60	0.50	25



(a)



(b)

Fig. 10. Designed deformation passes (intermediate shapes) and final shape: (a) M1; (b) M2.

For each case (single-pass, M1 and M2), three experiments were performed to measure the position at which failure occurred in order to confirm the results. For the single-pass case, the measured results were 49.98 mm, 49.95 mm and 49.96 mm. For M1, the measured results were 49.04 mm, 49.01 mm and 48.93 mm. For M2, all forming shapes were completed successfully. The averaged data are provided in Table 3.

From Table 3, it is seen that the successful forming of the final part can be only achieved by adopting the design of multi-stage forming (M2) compared with the unsuccessful forming of the part with cracks occurring in single-stage forming (Radius = 49.96 mm) and multi-stage forming (M1) (Radius = 48.99 mm). The FE results, compared with the morphology of final parts in experiments, show the exact predicted positions of the likely occurrence of cracks

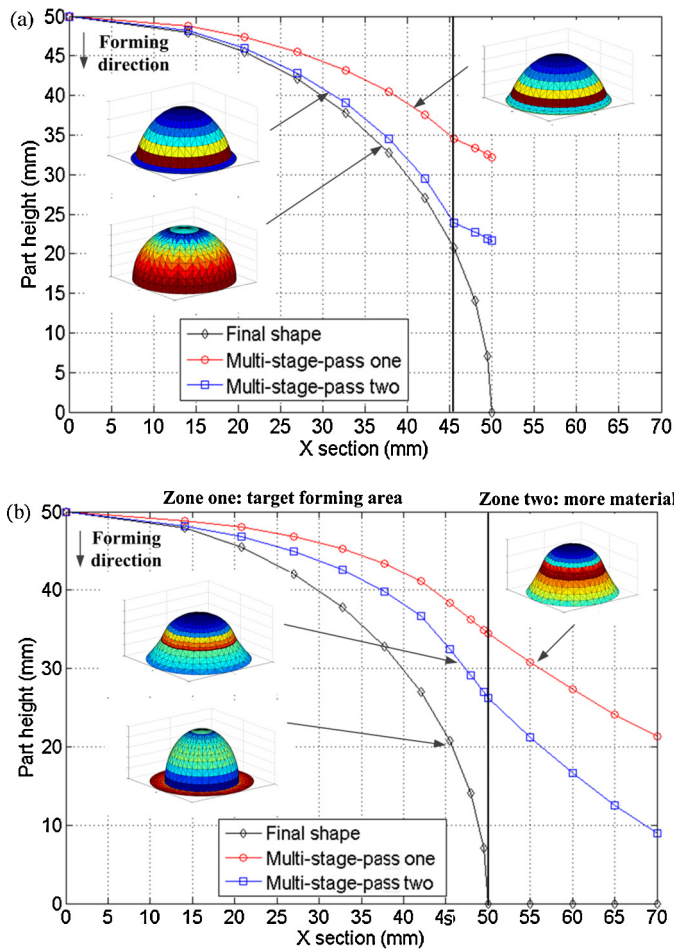


Fig. 11. Multi-stage deformation passes obtained from the developed models (a quarter section of the part): (a) M1; (2) M2. (Vertical solid line indicates the position of minimum intermediate thickness strains.)

caused by the concentrated small thickness strains (high magnitude strains) in single-stage forming and multi-stage forming (M1). The zones with a high magnitude of thickness strains (marked by white ovals) in FE results is most likely caused by the adopted symmetric tool path but with a ramped asymmetric transition line between consecutive path contours (Fig. 6), which leads to uneven material flow. In addition, with multi-stage forming (M2), the minimum (maximum magnitude) thickness strain in the concentrated small strain zone is predicted using FEA to be only around -0.66 , far

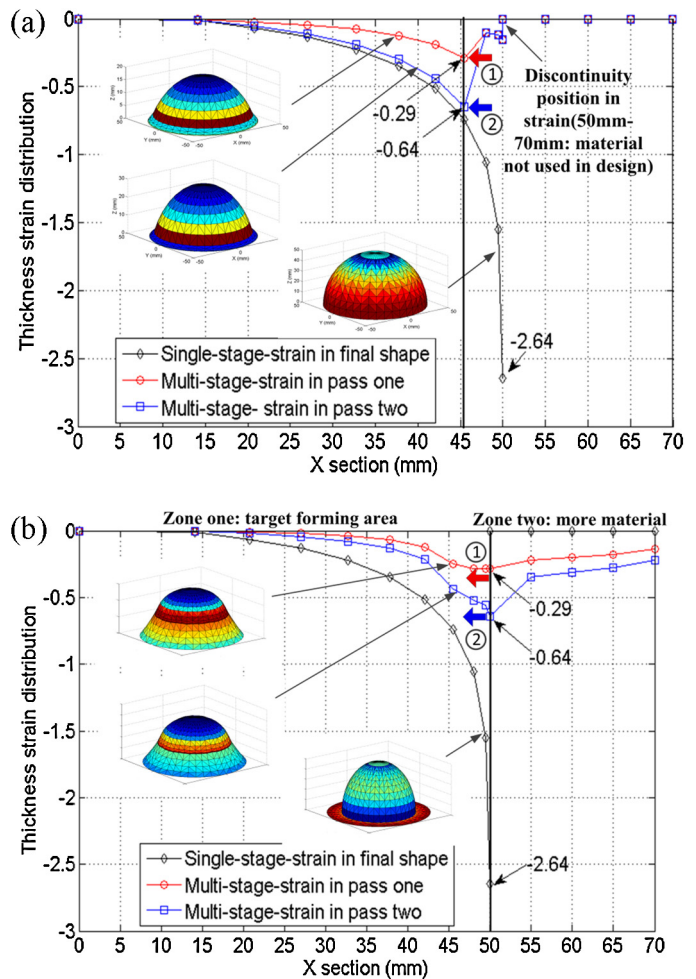


Fig. 12. The predicted thickness strain distribution obtained from the developed models (a quarter section of the part): (a) M1; (2) M2. (Vertical solid line indicates the position of minimum intermediate thickness strains.)

smaller in magnitude than around -0.91 and -0.85 in single-stage forming and multi-stage forming (M1), respectively. It is noted that from the previous analytical prediction of thickness strain distributions in deformation passes, the designed minimum intermediate thickness strain is located at the radius 45.5 mm in M1 and the radius 50 mm in M2, which means the concentrated small thickness strain zone is likely to occur around the radius 45.5 mm and the radius 50 mm during the forming of the final part using M1 and

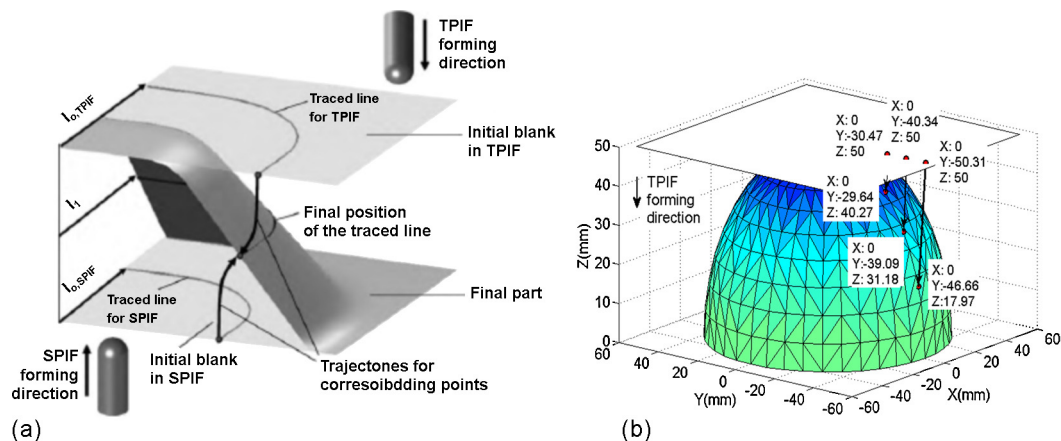

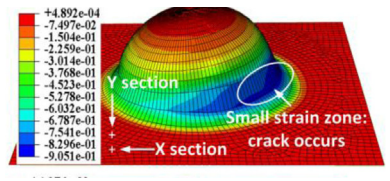
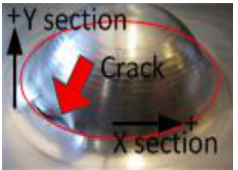
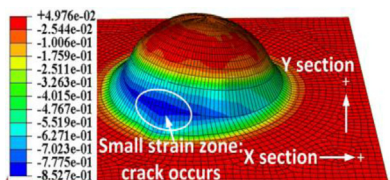

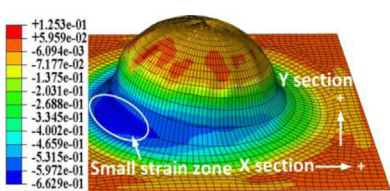


Fig. 13. Kinematics of material points in ISF: (a) results in Bambach (2010); (b) results in this study.

Table 3

Comparison of the formability between the single-stage forming and the proposed multi-stage forming.

Forming method	Forming result	Comparison of formability		
		Position at which failure occurred (mm)	Final part morphology	FE prediction (thickness strain)
Single-stage	Failure	Radius = 49.96		
Multi-stage (M1)	Failure	Radius = 48.99		
Multi-stage (M2)	Success	N/A		

M2. Additionally, in single-stage forming, the predicted minimum thickness strain is located at the radius 50 mm. Hence, the analytical prediction results show that the formability of multi-stage forming (M1) is likely to be no better than that of single-stage forming and multi-stage forming (M2). This is confirmed by the experimental and FE results. It is also worth mentioning that the minimum thickness strains of two deformation passes and the final part are -0.26 , -0.43 and -0.66 from the FE results (as shown in Table 4) for multi-stage forming (M2), which are nearly consistent with the designed value in the first deformation pass and larger (smaller magnitude) than the designed values in the second deformation pass and the final part. The designed minimum thickness strains (-0.29 , -0.64 and -1.08) in M2 overestimate the corresponding FE results, which illustrates that the designed overall thinning rate is satisfied (the final shape with the magnitude of minimum thickness strain is much less than 1.08). The minimum thickness strain predicted by the single-pass forming (-2.64 as shown in Fig. 12) is also provided for the comparative purposes to show the improvement of the closed-loop multi-pass design on the forming limits. A detailed comparison of the minimum thickness strains between

the single-stage forming and the proposed closed-loop multi-stage forming (M1 and M2) is shown in Table 4.

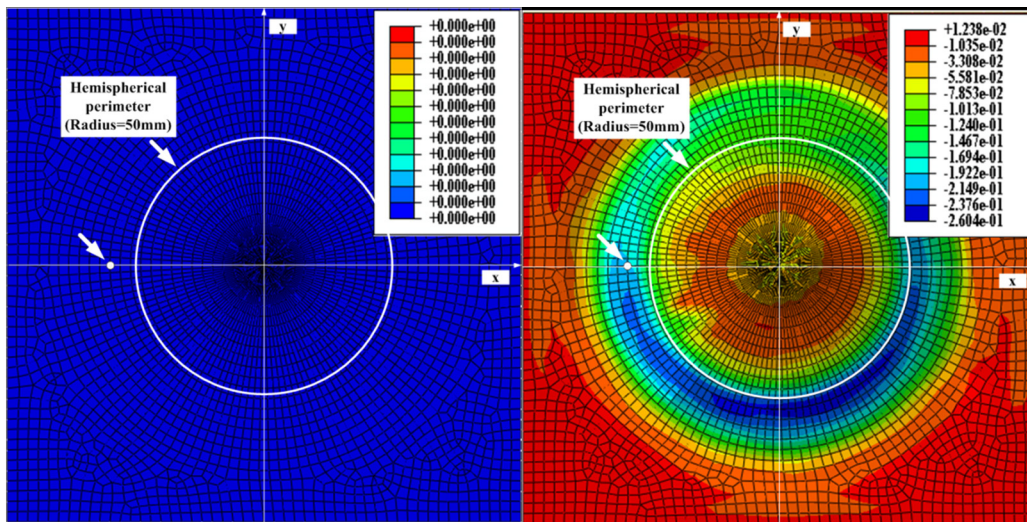
3.2.3. Thickness strain distribution

In order to understand the material flow in the designed deformation passes and the final shape, the thickness strain distribution is analyzed in each deformation pass and the final shape along X (rolling) and Y (transverse) sections by comparing the analytical prediction, FE simulation and experimental results. Figs. 15 and 16 show the thickness strain distributions in the case of deformation passes one and two for M1 and M2, respectively. On the one hand, the differences in thickness behavior from Fig. 15 to Fig. 16 can be observed, i.e. more overall thinning can be found as deformation passes increase for both M1 and M2. To be more specific, the thickness reduction is not so obvious in the part areas with shallow angles. However, the magnitude of thickness strains becomes higher in the part areas with steep angles. On the other hand, as can be seen, the analytical prediction results from M1 and M2 overestimate the FE simulation and experimental results in deformation passes one and two in both X and Y sections. This is possibly due to

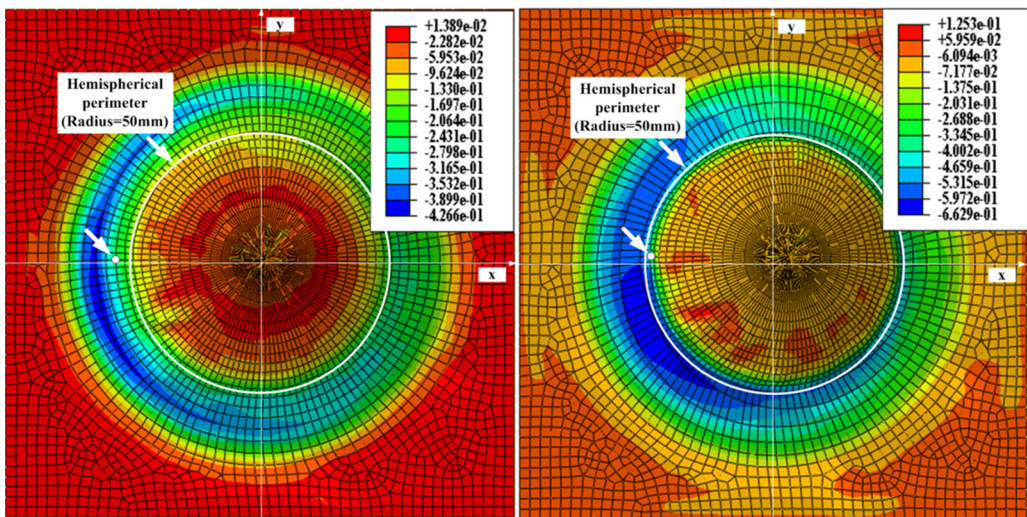
Table 4

Comparison of the minimum thickness strains between the single-stage forming and the proposed closed-loop multi-stage forming.

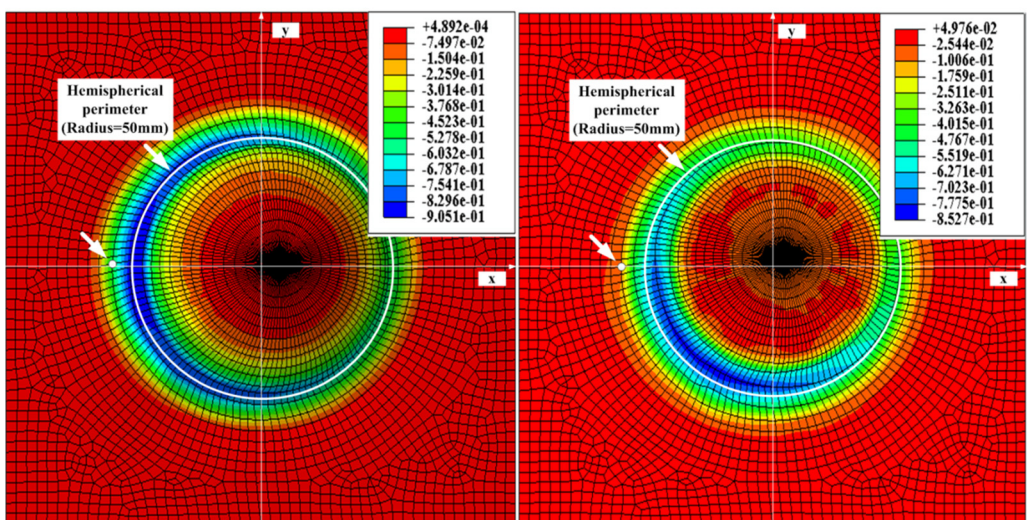
Forming method	Forming stage	Minimum thickness strain		
		Single-stage prediction/ multi-stage design	FE prediction	Experimental measurement
Single-stage	Final (Failure)	-2.64	-0.91	-0.95
Multi-stage (M1)	Pass one	-0.29	-0.14	-0.13
	Pass two	-0.64	-0.42	-0.47
	Final (Failure)	-1.08(design)	-0.85	-0.88
Multi-stage (M2)	Pass one	-0.29	-0.26	-0.17
	Pass two	-0.64	-0.43	-0.33
	Final (Success)	-1.08(design)	-0.66	-0.83



(a) Initial sheet for all forming methods (b) Pass one in *M2*



(c) Pass two in *M2* (d) Final shape in *M2*



(e) Final shape in single-pass forming (f) Final shape in *M1*

Fig. 14. The movement of material point evidenced by FEM results (thickness strain distribution).

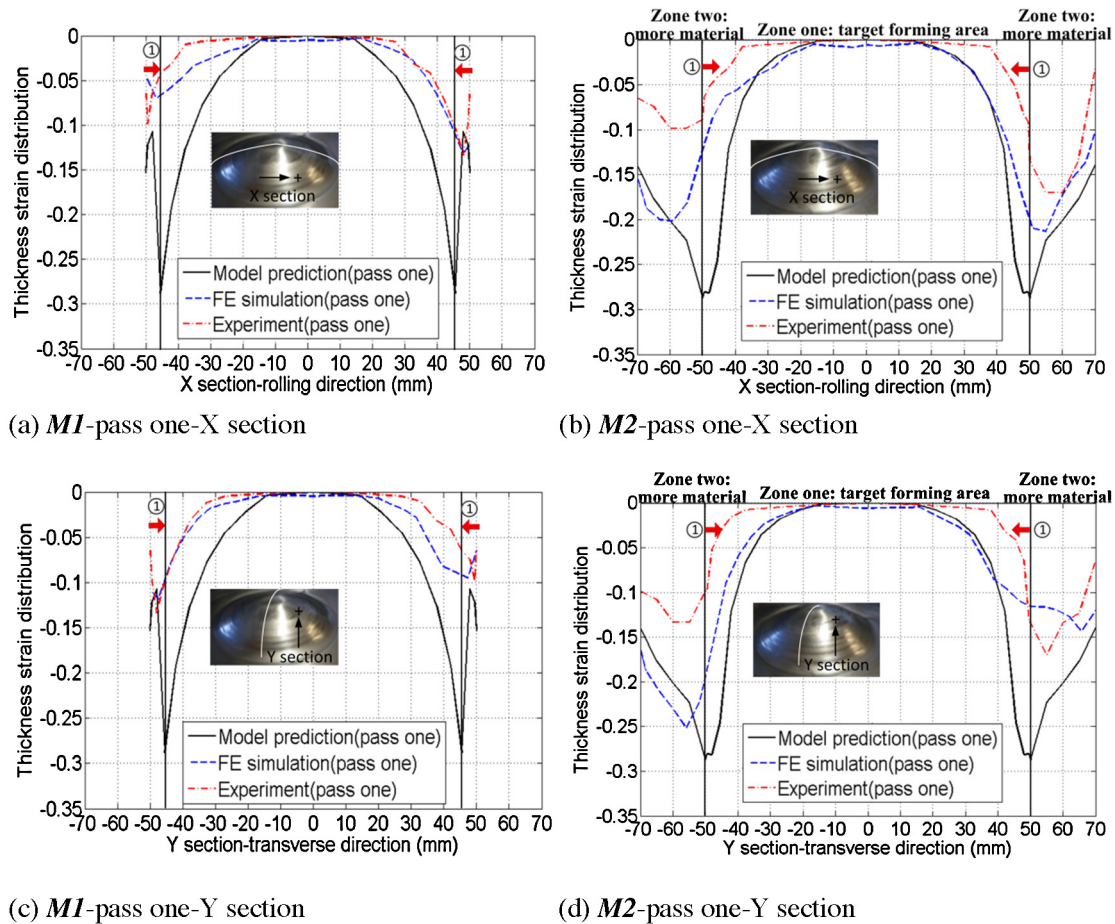


Fig. 15. Thickness strain distribution in the case of deformation pass one for M1 and M2: (a) M1-X section; (b) M2-X section; (c) M1-Y section; (d) M2-Y section.

the assumption of shear deformation, which is a pure geometrical model, independent of the material properties. In reality, there are other modes of deformation (i.e. stretching and/or bending) existing in the ISF process, which may lead to a lower magnitude of thickness strains compared with the shear only assumption. The simulation and experimental results show the similar trend of the thickness strain distribution and approximately coincide with each other. In addition, it is worth mentioning that the arrows in red and blue color (marked as (1) and (2)) in Figs. 15 and 16 show the movement of the material flow in the corresponding deformation passes designed by M1 and M2. It also illustrates that by forming a wider area than the perimeter of the shape, the incurrence of the highest thickness strains can be delayed to the larger radius area in M2 in the intermediate passes compared to M1 (see the predicted positions of the minimum intermediate thickness strains in Fig. 12(a) and (b)). Therefore, it will allow the flow of material into the deformed region and enable steeper shapes to be formed, which are also confirmed by the FE and experimental results.

Fig. 17 shows the thickness strain distribution of the final part obtained from FE and experimental results for single-stage forming and the proposed multi-stage forming (M1 and M2). In Fig. 17(a) and (c), the thickness strain comparison in experiments between single-stage forming and multi-stage forming (M1) shows that in the region (about -43.5 mm to 38 mm in X section and -36.5 mm to 47 mm in Y section), the thickness strain in single-stage forming is smaller (higher in magnitude) than that of multi-stage forming (M1). On the contrary, in the region about -50 mm to -43.5 mm, 38 mm to 50 mm in X section and -50 mm to -36.5 mm, 47 mm to 50 mm in Y section, the thickness strain decreases faster in

multi-stage forming (M1) than that of single-stage forming, reaching the critical small thickness strain zone first. However, as the difference in the failure position between single-stage forming and multi-stage forming (M1) is very small (Table 3) and only results observed from two sections (X and Y) are provided, the above discussion can only provide a possible illustration why cracking observed occurs earlier in multi-stage forming (M1) than that of single-stage forming. In Fig. 17(b) and (d), the thickness strain comparison between single-stage forming and multi-stage forming (M2) shows that in the whole target forming area, the magnitude of overall thickness strain in multi-stage forming (M2) is smaller than that of single-stage forming. In the region around -40 mm to $+40$ mm in both X and Y sections, the thickness strain is more evenly distributed. In the region around -50 mm to -40 mm and 40 mm to 50 mm in both X and Y sections, the thickness strain begins to decrease dramatically. However, the magnitude of overall thickness strain in these sections in multi-stage forming (M2) is still smaller than that of single-stage forming. The thickness strain in multi-stage forming (M2) can reach a much smaller value at the radius 50 mm (-50 mm in X section) compared with the thickness strains in the crack positions in single-stage forming and multi-stage forming (M1). This observed result is in agreement with the findings in Duflou et al. (2008), in which the author concluded that the resulting thinning of the sheet during multi-stage forming can exceed the maximum thickness reductions in single-stage forming, i.e. a formability shift. Furthermore, it is noted that the FE results derived from the simplified FE model in this study agree with the experimental results quite well. The adoption of symmetric tool paths with a ramped

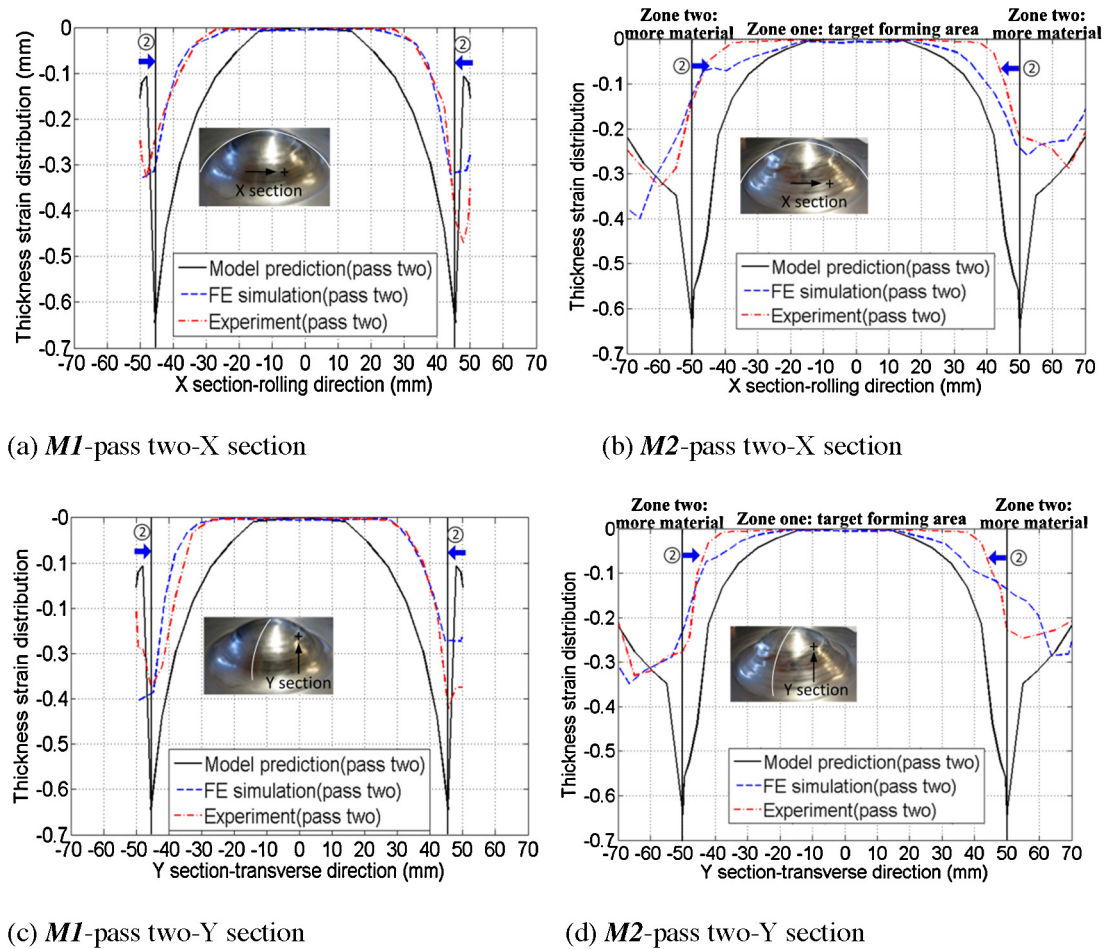


Fig. 16. Thickness strain distribution in the case of deformation pass two for M1 and M2: (a) M1-X section; (b) M2-X section; (c) M1-Y section; (d) M2-Y section.

asymmetric transition line between consecutive path contours (Fig. 6) leads to different thickness strain distributions in X and Y sections in all deformation passes and the final shape (Figs. 15–17). However, the overall evolution trends of these thickness strain distributions are quite similar.

4. Discussion

Some limitations of the proposed models and experimental findings during the multi-pass forming process were noticed and are discussed in the following.

- An inherent restriction of the developed models is that the modeling is only based on shear deformation. As the wall angle tends to 90° , the thickness will tend to zero. This may cause the predicted thickness strains (especially the steeper angle region) to be an overestimation of the magnitude of the actual thickness strains in each deformation pass (as shown in Table 4). However, based on these results, the present model provides an efficient and conservative means of designing multi-pass intermediate shapes. Another aspect that needs to be mentioned is the material behavior of the sheet metal has not been taken into account. This means that all materials will have the same multi-pass intermediate shapes. However, in reality, a different multi-stage strategy can be devised for different materials.
- It should be emphasized that the modeling is based on the fact (especially in M2) that the “pull material in” deformation leads to the compression in the middle region of a part but tension around the perimeter of the part in the TPIF process, which is

clearly evidenced by FEA in Fig. 14. The shear-based models cannot reflect the horizontal material flow. However, taking the “pull material in” deformation into account, additional material around the final part has been involved in the deformation in M2 to improve the process formability. Compared to M1, the fundamental differences in M2 are that by forming a wider area than the perimeter of the shape, it can: (i) avoid discontinuities in the intermediate thickness strains, and therefore allow steeper shapes to be formed; (ii) allow the flow of material into the deformed region, thereby allowing a compressive stress state to develop and enabling steeper shapes to be formed. This has been further confirmed by the detailed FEM results in Fig. 14(d), (e), and (f). In addition, although M1 offers no benefit to the forming process (actually it advances the failure risk), the reason we put it in the paper is for the comparison purposes and it is the basis of the development of M2. Furthermore, it provides insight into the modeling and deformation analysis.

- Our developed shear-based models are mainly defining intermediate shapes to achieve different wall angles of a part. These intermediate shapes designed in the two models give rise to different final thickness strain states that are not captured in the models. However, the models provide a means of delaying the highest strains using intermediate stages so that steeper shapes are allowed to be formed. In other words, the assumed outputs of our models (with the horizontal material flow) have a conflict with one of the assumptions in setting our models up (shear only assumption without considering the horizontal material flow in the x - y plane) although it still provides a means of optimal intermediate pass design. Hence there is a missing ‘link’ which is not

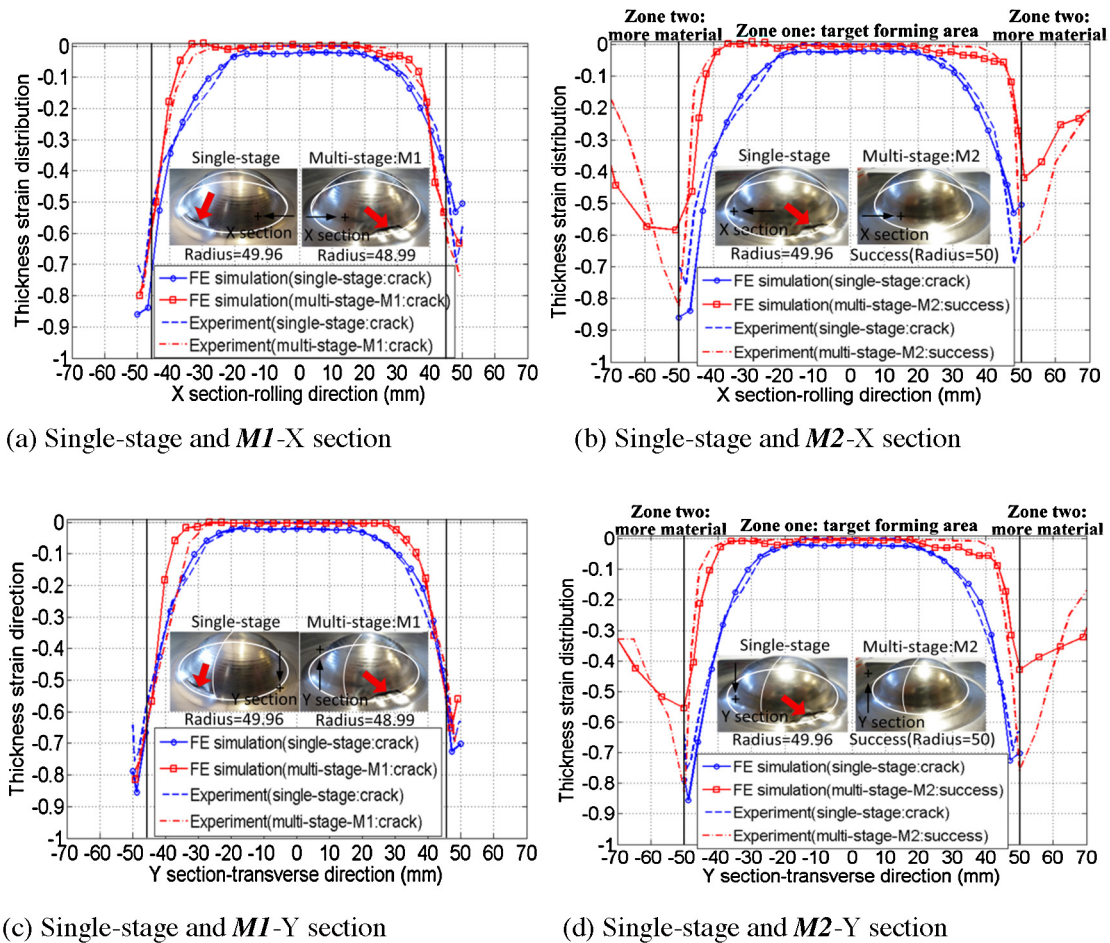


Fig. 17. Thickness strain distribution in the case of final shape for single-stage forming and multi-stage ($M1$ and $M2$) forming: (a) Single-stage and $M1$ -X section; (b) Single-stage and $M2$ -X section; (c) Single-stage and $M1$ -Y section; (d) Single-stage and $M2$ -Y section.

modeled in this study. Our future work will focus on the development of the modified models to bridge this missing gap.

- The developed models were not originally intended to predict the final thickness strains after the multi-pass forming, but do predict the final strains assuming single-pass forming. This is because, as discussed above, our shear-based models (without considering the horizontal material flow in the x - y plane) cannot capture the actual final thickness strain states after the multi-pass forming. Therefore, only the final thickness strains in the single-pass forming (as seen in Fig. 12) are provided for comparative purposes to show the improvement of the forming limits compared to the thickness strains (FE and experimental results) after multi-pass forming.
- The scope of this study is mainly focused on multi-stage deformation pass design. Some process parameters are deliberately set constant for comparative purposes and were not optimized. Given that the geometric accuracy is a concern for the practical application, a comparison of geometric accuracy between the designed shape and the manufactured shape is made in Fig. 18. The largest difference on the section profile can be found in the part regions with steep angles. This is possibly caused by the usage of a larger forming tool (30 mm diameter), which cannot achieve the geometric details in the steep regions. Springback is another source of geometric inaccuracy. However, the geometric accuracy can be further improved by using a smaller forming tool in the finishing process of the final shape and an undersize forming die to compensate the springback. The FE and experimental results in Section 3.2 show that the ramp angle and the

monotonous movement of the tool path generation cause an asymmetric thickness strain distribution as well as geometric distortion in the deformation passes and the final shape, thereby influencing the forming quality. Further investigations will be implemented in the future to improve the forming quality by optimizing the process parameters considered in the multi-stage deformation pass design.

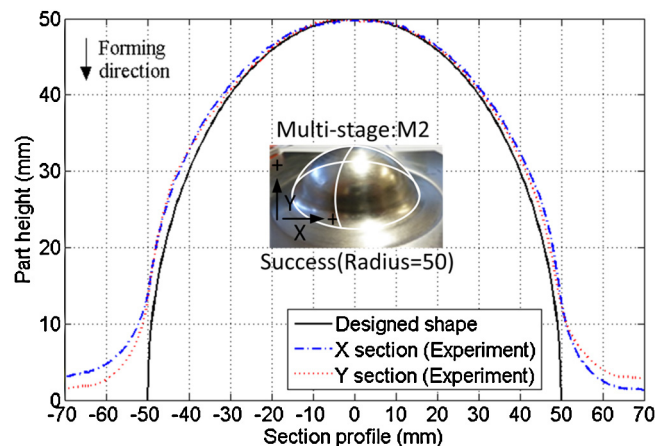


Fig. 18. Geometric accuracy comparison between designed shape and manufactured shape by multi-stage forming ($M2$).

- Due to the choice of the challenging benchmark shape with a vertical wall, wrinkling phenomenon can be observed in the final part, which is a forming defect that may cause failure during multi-stage forming. One possible solution to eliminating the wrinkling may be to increase the number of forming stages. This will be performed in future research.

5. Conclusions

In this study, a comprehensive methodology with two developed analytical models for multi-stage deformation pass design has been proposed. The models are compared with FEA and experimental tests on evaluating the process formability of the final part and thickness strain distributions. The following conclusions can be drawn from this study:

- Two open-loop analytical models have been developed and tested given the predicted thickness strain of the final part as a main parameter using the assumption of shear deformation. In *M1*, only the material in the final part region is involved in the forming. The global thickness strain is used to compensate the strain in the severely sloped region of the final part to determine the deformation passes. By doing so, it is expected to delay the incurrence of the highest thickness strains and therefore allow steeper shapes to be formed. However, in *M2*, the additional material around the final part region is used in the forming process. Additionally, a concept ‘*local weighted average thickness strain*’ is proposed in this model to compensate the strain in the severely sloped region of the final part and the additional material region to determine the multi-stage deformation passes. By doing so, it is expected to avoid discontinuities in the intermediate strains and allow the flow of material into the deformed region, thereby allowing a compressive stress state to develop and enabling steeper shapes to be formed.
- A comprehensive methodology for closed-loop multi-stage deformation pass design incorporating two models is proposed. Using the similar procedure in Li et al. (2012), the designed forming stages can be estimated first based on the design parameters (total thinning and average thinning rate). Then, the minimum thickness strains in the intermediate forming stages can be devised to calculate the predicted thickness strains in each forming stage to determine the corresponding deformation pass.
- A case study is provided to illustrate the design methodology. Given the same design parameters (the devised minimum thickness strain in each forming stage), the predicted thickness strain distribution obtained from *M2* is more uniform than the result from *M1* (discontinuities in the intermediate strains can be avoided). In addition, the predicted position of the minimum (maximum magnitude) intermediate thickness strain in each deformation pass is shifted from the part radius 45.5 mm (*M1*) to the part radius 50 mm (*M2*), which allows the flow of sufficient material into the deformed region, thereby allowing a compressive stress state to develop and enabling steeper shapes to be formed. It further illustrates that *M2* has higher formability than *M1*. These predicted results were confirmed by the FEA and experimental results in Section 3.2.

Further investigation is still needed in terms of generalizing *M2* to manufacture more complex parts and the influence of process parameters (step down, ramp angle, tool radius, feed rate, forming

down pressure, etc.) during the multi-stage forming on the quality of the final parts in order to avoid forming defects such as wrinkling and distortion.

Acknowledgements

This research was supported by the ARC Linkage Program, Boeing Research & Technology-Australia and QMI Solutions in Australia.

Appendix A. Supplementary data

Supplementary material related to this article can be found, in the online version, at <http://dx.doi.org/10.1016/j.jmatprotec.2013.11.010>.

References

- Bambach, M., 2010. A geometrical model of the kinematics of incremental sheet forming for the prediction of membrane strains and sheet thickness. *Journal of Materials Processing Technology* 210, 1562–1573.
- Dejardin, S., Thibaud, S., Gelin, J.C., Michel, G., 2010. Experimental investigations and numerical analysis for improving knowledge of incremental sheet forming process for sheet metal parts. *Journal of Materials Processing Technology* 210, 363–369.
- Dufloy, J.R., Verbert, J., Belkassam, B., Gu, J., Sol, H., Henrard, C., Habraken, A.M., 2008. Process window enhancement for single point incremental forming through multi-step toolpaths. *CIRP Annals - Manufacturing Technology* 57, 253–256.
- Filice, L., Fantini, L., Micari, F., 2002. Analysis of material formability in incremental forming. *CIRP Annals - Manufacturing Technology* 51, 199–202.
- Jackson, K., Allwood, J., 2009. The mechanics of incremental sheet forming. *Journal of Materials Processing Technology* 209, 1158–1174.
- Jeswiet, J., Micari, F., Hirt, G., Bramley, A., Dufloy, J., Allwood, J., 2005. Asymmetric single point incremental forming of sheet metal. *CIRP Annals - Manufacturing Technology* 54, 88–114.
- Kim, T.J., Yang, D.Y., 2000. Improvement of formability for the incremental sheet metal forming process. *International Journal of Mechanical Sciences* 42, 1271–1286.
- Li, J.C., Hu, J.B., Pan, J.J., Geng, P., 2012. Thickness distribution and design of a multi-stage process for sheet metal incremental forming. *International Journal of Advanced Manufacturing Technology* 62, 981–988.
- Li, J.C., Shen, J.J., Wang, B., 2013. A multipass incremental sheet forming strategy of a car taillight bracket. *International Journal of Advanced Manufacturing Technology*, <http://dx.doi.org/10.1007/s00170-013-5179-3>.
- Liu, Z.B., Li, Y.L., Meehan, P.A., 2013. Vertical wall formation and material flow control for incremental sheet forming by revisiting multistage deformation path strategies. *Materials and Manufacturing Processes* 28, 562–571.
- Manco, L., Filice, L., Ambrogio, G., 2011. Analysis of the thickness distribution varying tool trajectory in single-point incremental forming. *Proceedings of the Institution of Mechanical Engineers Part B-Journal of Engineering Manufacture* 225, 348–356.
- Shanmuganatan, S.P., Senthil Kumar, V.S., 2012. Experimental investigation and finite element modeling on profile forming of conical component using Al 3003(O) alloy. *Materials & Design* 36, 564–569.
- Skjoedt, M., Silva, M.B., Martins, P.A.F., Bay, N., 2010. Strategies and limits in multi-stage single-point incremental forming. *Journal of Strain Analysis for Engineering Design* 45, 33–44.
- Thibaud, S., Ben Hmida, R., Richard, F., Malécot, P., 2012. A fully parametric toolbox for the simulation of single point incremental sheet forming process: numerical feasibility and experimental validation. *Simulation Modelling Practice and Theory* 29, 32–43.
- Werner, A., Skalski, K., Piszczatowski, S., Świeszkowski, W., Lechniak, Z., 1998. Reverse engineering of free-form surfaces. *Journal of Material Processing Technology* 76, 128–132.
- Young, D., Jeswiet, J., 2004. Wall thickness variations in single-point incremental forming. *Proceedings of the Institution of Mechanical Engineers Part B-Journal of Engineering Manufacture* 218, 1453–1459.
- Zhang, C., Xiao, H.F., Yu, D.H., 2013. Incremental forming path-generated method based on the intermediate models of bulging simulation. *International Journal of Advanced Manufacturing Technology* 67, 2837–2844.

4.2.2 AMINO TPIF Multi-Pass Deformation Design

Paper K

Tool path strategies and deformation analysis in multi-pass incremental sheet forming process

Liu, Z.B., Li, Y.L., Meehan, P.A.

International Journal of Advanced Manufacturing Technology

2014, Volume: 75(1-4), Pages: 395-409.

Tool path strategies and deformation analysis in multi-pass incremental sheet forming process

Zhaobing Liu · Yanle Li · Paul A. Meehan

Received: 4 March 2014 / Accepted: 3 July 2014 / Published online: 23 July 2014
© Springer-Verlag London 2014

Abstract Incremental sheet forming (ISF) is a new promising manufacturing technology with high potential to shape complex three-dimensional parts by using a relative small tool. However, ISF is presently limited due to non-uniform thickness distribution of formed parts, especially excessive thinning on severely sloped regions. This typically leads to fracture and hence limits process formability. This paper aims to tackle this issue by developing appropriate tool path strategies for multi-pass deformation design in ISF. More specifically, two more complex shapes are designed to validate the proposed multi-pass deformation design methodology by finite element simulations and experiments. The interactions of different tool path strategies on material thinning of the final part are evaluated in terms of process formability and thickness strain distribution given the same multi-pass design. Furthermore, the movement of material points is traced to explain the material flow mechanism in multi-pass forming compared to single-pass forming. It is concluded that both deformation passes (intermediate shapes) and tool path generation strategies would influence the thickness strain distribution as well as process formability. Appropriate tool paths should be devised to further reduce material thinning and improve the process formability by taking the geometrical features of the designed part into account. Additionally, the proposed multi-pass deformation design enables sufficient material to flow into the deformed region from the outside region so as to allow

a compressive deformation state to develop and steeper shapes to be formed.

Keywords Incremental sheet forming · Intermediate shape · Formability · Thickness strain · Finite element analysis · Tool path

1 Introduction

The last decade has witnessed an increasing interest in the development of incremental sheet-forming (ISF) technology as it is suitable for rapid prototyping and small-batch production of complex shapes. In the ISF process, plastic deformation occurs in a small contact zone on the interface of sheet metal induced by the movement of a forming tool. The ISF process can be categorized into two main types: single-point incremental forming (SPIF) without a forming die and two-point incremental forming (TPIF) with a partial or a full-forming die. A comprehensive review of ISF developments through the years can be found in [1] and [2].

The ISF process is promising and advantageous by providing higher formability compared to other forming processes like deep drawing and stamping. Moreover, the tool path which defines the formed shape can be easily controlled by a CAD/CAM software which increases the design flexibility. However, the ISF process is still limited by the significant thinning and therefore fracture of the deformed sheet metal when forming a part with geometrical features such as steep angles. Multi-pass forming is an effective way to tackle this issue. In the past decade, much work has been performed in this area with attempts to regulate the material flow so as to overcome the excessive thinning and increase the formability. Kim and Yang [3] developed a double-pass forming method to improve the process formability in ISF. This method is

Z. Liu (✉) · Y. Li · P. A. Meehan
School of Mechanical and Mining Engineering, The University of Queensland, St Lucia, Brisbane, QLD 4072, Australia
e-mail: zhaobing.liu@uqconnect.edu.au

Z. Liu
e-mail: z.liu7@uq.edu.au

based on the shear deformation theory using the predicted thickness strain distribution to design intermediate shapes in order to uniformize the thickness distribution of a final part. Young and Jeswiet [4] also proposed a double-pass SPIF strategy to form a cone with a steep draw angle. This strategy introduces bending in the first pass forming with the aim to encourage the undeformed material in the flange area to bend downwards over the backing plate and into the part. The results showed that the occurrence of a thinning band in the single-pass forming would be delayed in the two-pass forming process so that complex parts with steep angles can be made. Duflou et al. [5] developed a multi-pass ISF strategy to redistribute the material from the previously unformed base of the part to the side wall and manufactured parts with vertical walls without failure. The final thinning in multi-pass forming can exceed the maximum thickness reductions in single-pass forming, which means a formability increase. A multi-stage forming strategy was investigated in [6] to manufacture cylindrical cups with vertical walls. The authors pointed out that the movement of the forming tool in the multi-stage SPIF has a great influence on the thickness distribution. SPIF is limited by cracking rather than necking. Cui and Gao [7] proposed three multi-pass strategies to produce hole-flanging parts. It was shown that increasing the part diameter in small steps, named as strategy (a), to achieve the final part is proved to be an effective way to improve the formability of flanges and avoid the occurrence of the thinning band. In [8], the effect of tool paths in single-stage forming and three different multi-stage forming strategies has been compared and analyzed by manufacturing the same shape and evaluating the formability as well as thickness distributions. It was concluded that formability could be conveniently improved with proper multi-stage deformation design by involving as much material as possible. Malhotra et al. [9] proposed a new methodology for multi-pass SPIF with mixed tool paths to eliminate the material extrusion phenomenon (also called stepped features) in SPIF. They developed analytical formulations to predict the rigid body translation and then generated a new mixed tool path to achieve a smoother component base by using a combination of in-to-out and out-to-in tool paths for each intermediate shape. However, finite element simulations are needed to perform every time to calibrate the model constants when the material type or sheet thickness of the blank is changed. Xu et al. [10] extended the work in [9] by relating the material constants in analytical formulations to the yield stress and the sheet thickness of the blank. Therefore, the required number of prior finite element analysis (FEA) simulations is reduced to only six for arbitrary material types and thicknesses, which is a significant addition to the prior work. Although a multi-pass

forming strategy benefits the increase of formability, it is still uncertain how material flows between intermediate and final forming stages. A finite element (FE) model for a double-pass forming was developed in [11] to simulate the actual forming process. Compared to single-pass forming, the results indicated that more uniform thickness distribution in double-pass forming can be achieved, which benefits from the increase of the total plastic deformation zone. Additionally, Li et al. [12] made an attempt to produce a complex part—a car taillight bracket with a nearly straight wall region and a groove region. In order to avoid cracks and wrinkles in the two aforementioned critical regions, a multi-pass forming strategy based on a regional division idea was proposed. It was found that an intermediate surface which is geometrically closer to the final part can obtain better forming quality. Liu et al. [13] proposed three multi-stage deformation pass strategies for forming cups with vertical walls. Those strategies and their combinations have been evaluated in terms of the process formability. The results showed that the forming strategy using more material in the forming as well as the addition of a small amount of bending can greatly improve the formability. As opposed to trial-and-error methods, a closed-loop analytical methodology for multi-pass deformation design has been proposed recently in [14] which focuses on the determination of deformation passes (intermediate shapes). The methodology was developed based on shear deformation and the strain compensation mechanism. The results revealed that a more uniform thickness strain distribution can be derived when involving more material in the multi-pass forming.

The above literature review shows that multi-pass deformation design in ISF involves two aspects: (i) determination of deformation passes and (ii) generation of corresponding tool paths based on the deformation passes. In the ISF process, the shape is determined only by the tool movement, which means that there are infinite possible paths to realize the same shape [15]. Therefore, there is scope to control material flow during forming by designing different tool paths. Unfortunately, the interaction of tool paths generated in multi-pass forming on material thinning has not been fully investigated yet. Additionally, the flow of material during multi-pass forming needs to be further clarified so as to facilitate ISF development. The work in this paper is an extension of the previous work in [14], which aims to clarify three points by using finite element simulations and experiments: (i) the generalization of simple shapes to complex shapes using the developed multi-pass design methodology, (ii) the interaction of different tool paths on material thinning of the final part given the same multi-pass design, and (iii) the material flow mechanism during multi-pass forming. The remainder of this paper is organized as follows. The methodology is introduced in Section 2, which includes a tool path generation strategy in multi-pass forming, finite element method (FEM) modeling,

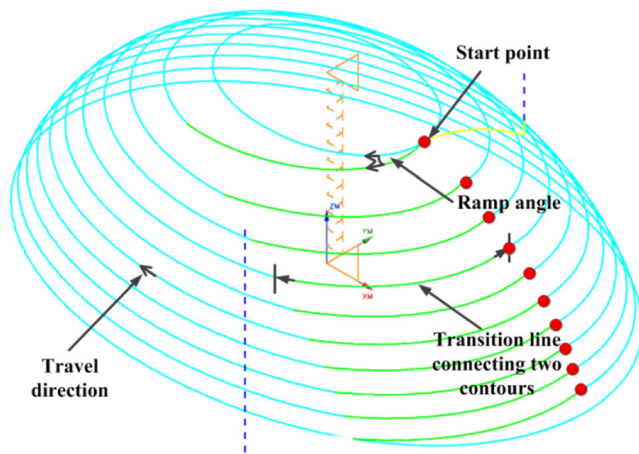


Fig. 1 The designed tool path with three adjustable parameters—ramp angle, start point, and travel direction

experimental setup, and forming benchmarks. Section 3 presents and discusses the results, analyzing the material thinning as well as material flow mechanism. Section 4 provides the conclusions.

2 Methodology

In this section, the strategy for tool path generation in multi-pass forming is first proposed. Then, details of the finite element (FE) modeling are presented followed by a summary of the experimental setup. Finally, the designed forming benchmarks are detailed.

2.1 Strategy for tool path generation in multi-pass forming

Tool path generation is one of the key topics in ISF development. The research in multi-pass forming can be directed towards two aspects: (i) deformation pass design (intermediate shapes or preforms), and (ii) corresponding tool path

generation. The first aspect looks for the appropriate intermediate deformation shapes to enhance the forming quality by reallocating material concerning the characteristics of the designed shape. The second aspect is to realize the deformation passes and the final shape by determining suitable tool paths so as to further improve the forming quality. Our previous results have revealed that deformation passes (intermediate shapes or preforms) have an overall influence on material flow during an ISF process. The appropriate preform design can greatly improve the process formability and enhance the final product quality. In addition, tool path generation representing different deformation passes and the final part in multi-pass forming also plays a role on the final product quality (such as thickness distribution, formability, etc.). On this point, the interaction of different tool paths in intermediate forming passes and the final part on material thinning has not been widely investigated yet. A guideline for tool path generation given the same multi-pass design is needed to further improve the forming quality of the final product. This section presents a strategy for tool path generation in a multi-pass deformation design which aims to clarify the interaction between the intermediate and the final tool paths on material thinning.

In this study, Siemens NX CAM 7.5 software is utilized to define the tool paths given the CAD models for designed intermediate passes and the final part. A z-level tool path with a ramp angle is adopted in the multi-pass forming process, see Fig. 1.

The in-out downward movement of the tool is defined and the connection between two levels can be adjusted by the ramp angle, which guarantees that the tool path is continuous and leaves no obvious marks on the part surface. It is worth mentioning that the tool path devised in this study is quite similar to the tool path used in strategy 2 in [15]. In fact, this kind of tool path is a generalized tool path and more like a combination of tool

Fig. 2 Simplified FE modeling for TPIF

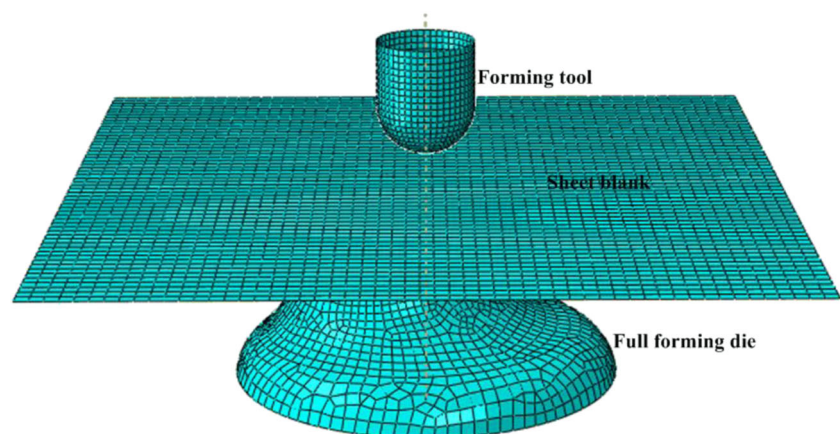


Table 1 Tensile test results of AA7075-O aluminum alloy sheets with 1.016- and 1.6-mm thicknesses for three directions

Material (AA7075-O)	Orientation	Yield strength (MPa)	Ultimate yield strength (MPa)	Elongation (%)	Young's modulus (GPa)
1.016 mm	Rolling (0°)	88	190	17	69
	Diagonal (45°)	88	191	18	71
	Transverse (90°)	91	192	14	70
1.60 mm	Rolling (0°)	91	199	20	70
	Diagonal (45°)	91	196	22	69
	Transverse (90°)	94	202	19	70

paths in strategies 1, 2, and 3. Specifically, when the ramp angle is set to be 90°, a tool path similar to that in strategy 1 can be obtained. Otherwise, when the ramp angle tends to 0°, a spiral-shape tool path more similar to that in strategy 3 can be derived. It is noted that several process parameters involved in the forming process can influence the final product quality. Since these have been investigated in the previous work, this paper focuses on the most relevant tool path parameters in the multi-pass forming process and the other parameters (such as feed rate, tool diameter, etc.) are deliberately set as constants. In particular, the step-down size has been fully investigated in [16], where it was shown that a larger step-down size can increase the process formability while a smaller one can be used to detail local characteristics of the manufactured shape and improve the forming quality. Hence, this parameter will be set as a constant in multi-pass forming of this study.

Conversely, three parameters, that have not been widely investigated yet, ramp angle, start point, and travel direction in a tool path, are studied in terms of their influence on material thinning, as they are relevant to the control of multi-pass tool path generation. All three parameters are assumed to influence the material allocation in multi-pass forming. More specifically, start point refers to the beginning position of each path contour. In this case, all start points can be determined by the first

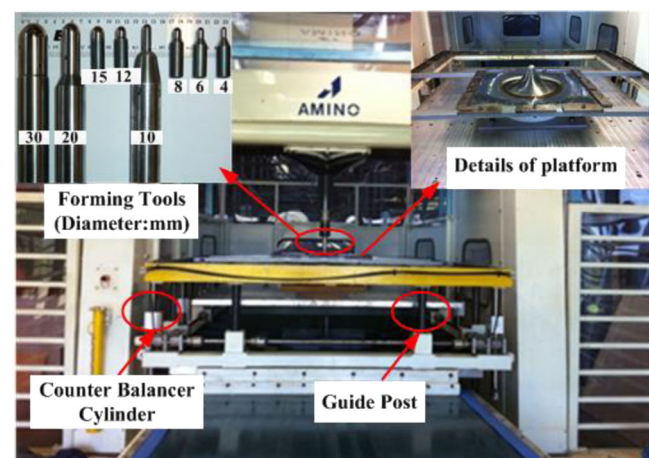
start point as shown in Fig. 1 and for simplicity, in the following discussion, the start point refers to the first start point of a tool path. Its position is designed in forming passes, and the final shape relative to the geometric feature of the final part and is expected to influence material thickness distribution. Ramp angle can change the length of transition line between two consecutive path contours, which is also expected to have an effect on material thinning. The change of travel direction tends to cancel out the unbalanced material flow during forming and so is expected to obtain more symmetric thickness strain distribution in the final part. In the following, the effects of these parameters are investigated, based on the evaluation of process formability and thickness strain distributions using FEM simulations as well as experimental tests.

2.2 FEM simulations

A simplified FE model is developed to simulate the forming process for TPIF using ABAQUS®/Explicit software 6.11, as seen in Fig. 2. In this model, several assumptions are made as follows:

Table 2 Mechanical properties of AA7075-O aluminum alloy sheets with 1.016- and 1.6-mm thicknesses

Material (AA7075-O)	1.016 mm	1.60 mm
Density (t/mm^3)	2.81×10^{-9}	2.81×10^{-9}
Young's modulus (MPa)	70000	69500
Poisson's ratio	0.33	0.33
Tensile yield strength (MPa)	88.75	91.75
Ultimate tensile strength (Mpa)	191	198.25
Plastic coefficient K	352.9	352.6
Hardening exponent n	0.23	0.22

**Fig. 3** The AMINO ISF machine used for experiments

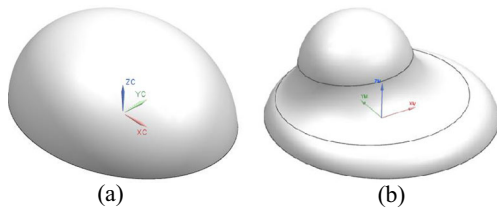


Fig. 4 Designed shapes: **a** ellipsoidal cup (symmetric shape) and **b** free-form shape (asymmetric shape)

- The material is isotropic and elasto-plastic. Elastic recovery after forming is neglected.
- The process deformation is homogeneous. Strain hardening is assumed to be constant in the whole multi-pass forming process.
- The periphery of the sheet blank is rigidly clamped and endures a constant pressure to mimic the movement of the hydraulic actuator in the real AMINO ISF machine.

It is noted that there are two ways to clamp the sheet metal: (i) constrain the translational and rotational degrees of freedom of sheet elements or (ii) build a full model of the blank holder. The first method is adopted here to reduce the computational time. To reduce the size of the FE model, smaller sheets with sizes of 200 mm×200 mm and 220 mm×220 mm are used in the simulations, which are determined based on the sizes of forming benchmarks. These appear to not influence the simulation results. The blank is considered as a deformable body and is discretized with shell elements S4R, which are reduced integration elements with one integration point in the plane and five integration points through the thickness. The size of each shell element is 4 mm. The forming tool and die are modeled using rigid surface elements R3D4 with sizes of 2 and 4 mm, respectively. The friction behavior is modeled using the Coulomb friction law with a friction coefficient of 0.1 between the blank and the forming tool and a friction coefficient of 0.8 between the blank and the forming die. The mass scaling factor is set to be 500.

In this study, AA7075-O aluminum sheets with the size of 300 mm×300 mm and 1.016- and 1.60-mm thicknesses are used in the experiments. The tensile tests for three

directions (rolling, diagonal, and transverse) were performed twice, and the data were averaged to reduce the measurement error. The tensile test results are presented in Table 1. Additionally, the corresponding true stress-true strain curves can be found in Figs. 3 and 4 in [16], in which the curves look smooth and no obvious scattering can be observed in the data. The tensile test results show that there is no substantial anisotropy for the investigated sheet metal. Therefore, the material can be assumed to be isotropic in the simulation. The true stress and strain values for three directions can be averaged using the following equation,

$$\bar{\sigma} = \frac{\sigma_0 + 2\sigma_{45} + \sigma_{90}}{4}, \tag{1}$$

where σ_0 , σ_{45} , and σ_{90} are stress or strain values for rolling, diagonal, and transverse directions.

The true stress-true strain curves are fitted using the Hollomon power law,

$$\bar{\sigma} = K \bar{\epsilon}^n, \tag{2}$$

where K is the strength coefficient and n is the strain-hardening exponent. $\bar{\sigma}$ and $\bar{\epsilon}$ are the flow stress and the plastic strain, respectively.

On this basis, mechanical properties of AA7075-O aluminum sheets with 1.016- and 1.60-mm thicknesses can be summarized in Table 2.

It is noted that the possible limitation of the developed FE model would be

- Simplified material model that cannot capture the relevant cyclic strain hardening during the multi-pass forming simulation.

Despite the possible limitation as discussed above, the developed simplified FE model would provide an efficient means of analyzing the complex multi-pass ISF process. The detailed validation and discussion are given in Section 3.

Table 3 Determined parameters in multi-pass deformation design for designed shapes

Geometry	Deformation passes	Model parameters					
		a_1	b_1	a_2	b_2	α	R
Ellipsoidal cup	Pass 1	0.28	0.05	0.80	0.70	0.50	35
	Pass 2	0.62	0.25	0.90	0.50	0.50	35
Free-form shape	Pass 1	0.39	0.05	1.00	0.70	0.50	35
	Pass 2	0.86	0.30	1.05	0.80	0.50	35

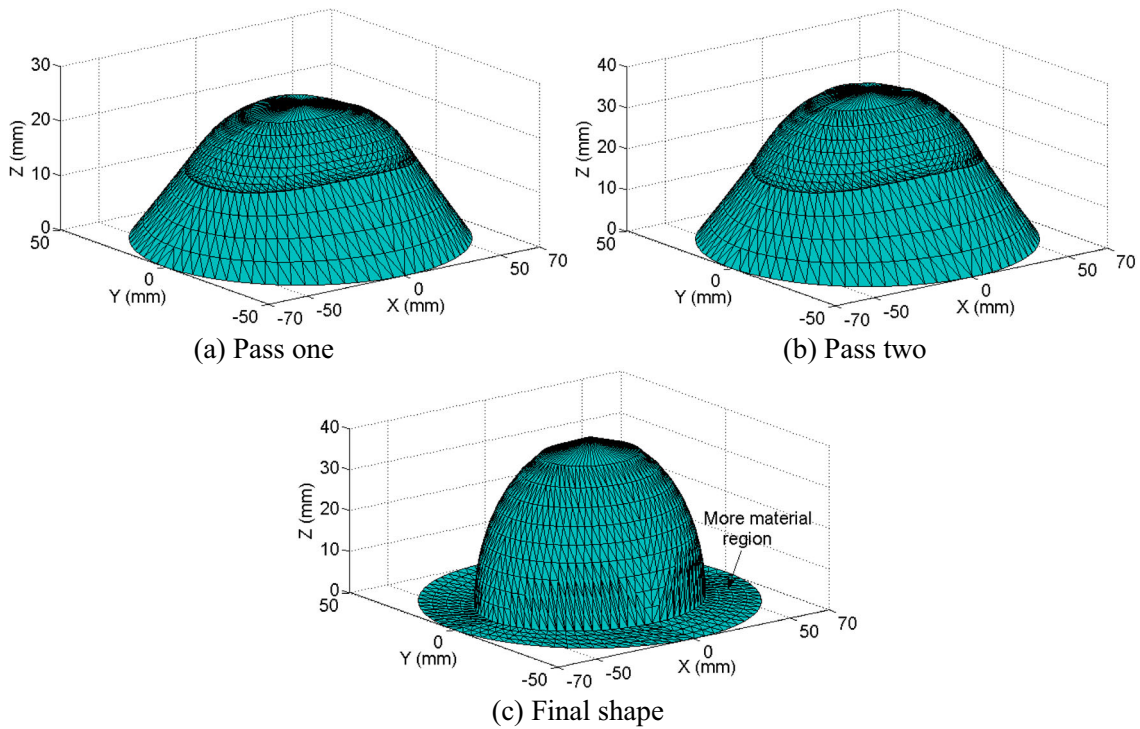


Fig. 5 Deformation pass design for ellipsoidal cup (MATLAB meshes). **a** Pass 1. **b** Pass 2. **c** Final shape

2.3 Experimental setup

Experimental investigations are carried out on the AMINO® DLNC-PC incremental forming machine (see

details in Fig. 3) to validate the analytical multi-pass design and FEM simulations. The machine is a three-axis CNC machine with a maximum workspace of $2,100 \times 1,450 \times 500 \text{ mm}^3$ and can exert maximum forces

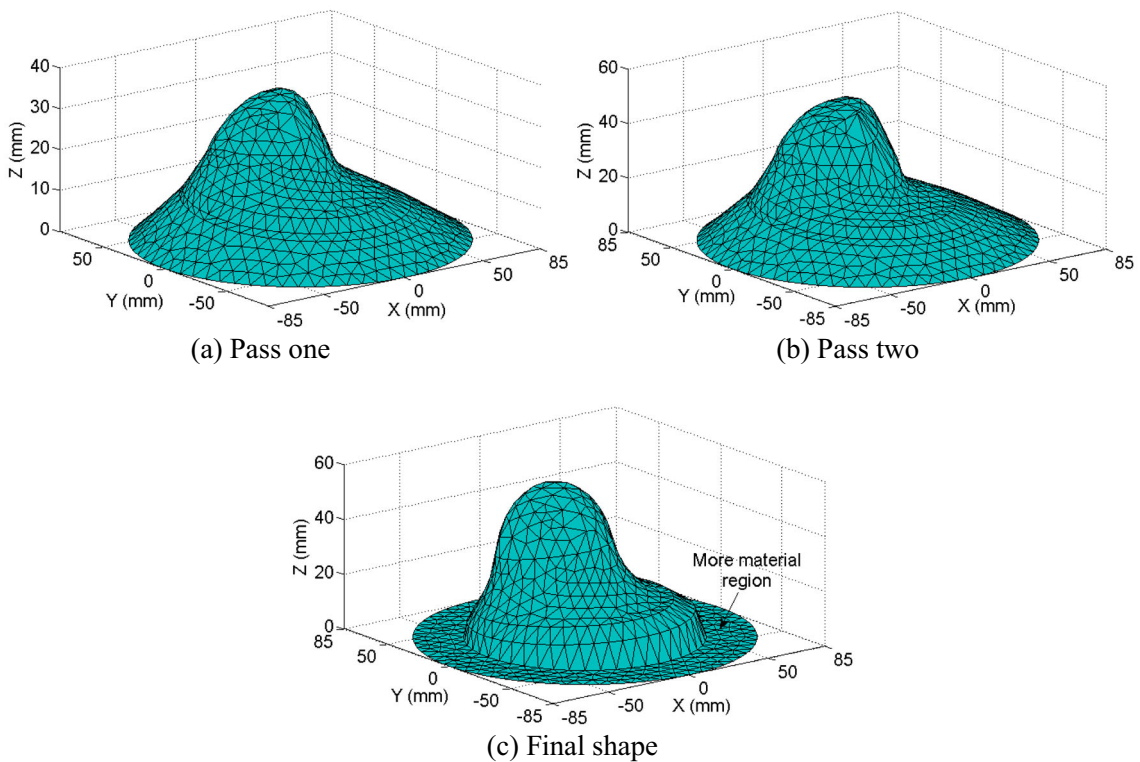


Fig. 6 Deformation pass design for asymmetric free-form shape (MATLAB meshes). **a** Pass 1. **b** Pass 2. **c** Final shape

Table 4 Tool path parameters designed in multi-pass forming for ellipsoidal cup

Geometry	Test	Pass 1				Pass 2				Final part			
		RA (°)	SP	TD	SD (mm)	RA (°)	SP	TD	SD (mm)	RA (°)	SP	TD	SD (mm)
Ellipsoidal cup	No. 1	5	P1	CW	4	5	P2	CW	4	5	P3	CW	2
	No. 2	20	P1	CW	4	20	P2	ACW	4	20	P3	CW	2
	No. 3	60	P1	CW	4	60	P2	CW	4	60	P3	CW	2
	No. 4	20	P4	CW	4	20	P5	CW	4	20	P6	CW	2
	No. 5	20	P4	CW	4	20	P5	CW	4	20	P6	CW	2

P1=(-17.156,-23.611,36.424); P2=(-30.794,4.885,36.322); P3=(-12.107,-11.026,38.095); P4=(0.052,-26.632,36.424); P5=(0,22.983,36.322); P6=(-20.192,-0.205,38.095)

RA ramp angle, SP start point of a tool path, TD travel direction of a tool path, CW clockwise, ACW anti-clockwise, SD step-down size of a tool path

of 3.0 kN in Z axis and 1.5 kN in X axis and Y axis. The maximum feed rate in X axis and Y axis is 6,000 and 1,000 mm/min in Z axis. In the experiments, the forming tool with 15-mm radius is used. The applied forming feed rate is equal to 4,000 mm/min and the forming down pressure is set to be 0.015 MPa. The designed intermediate shapes and the final shape are all formed against the final-shaped wooden die. After forming, experimental samples are cut and the thickness distribution along the section profile was measured manually using a micrometer.

2.4 Forming benchmarks


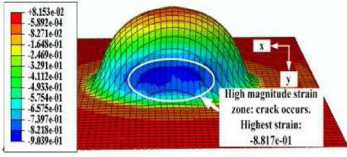

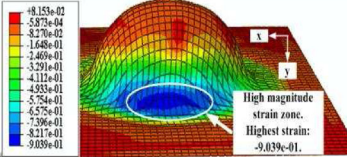
Two general shapes (ellipsoidal cup and free-form shape as shown in Fig. 4) are designed to evaluate the interaction of multi-pass tool paths on material thinning and material flow. The studied ellipsoidal cup can be described as an analytical equation in [3]:

$$\begin{aligned}
 x &= A \cos\theta \cdot \sqrt{1 - \frac{z^2}{C^2}} \\
 y &= B \sin\theta \cdot \sqrt{1 - \frac{z^2}{C^2}}
 \end{aligned}
 \tag{3}$$

where A=50 mm, B=30 mm, C=40 mm.

For the ellipsoidal cup, the height is 40 mm. The major radius and minor radius are 50 and 30 mm, respectively. For the free shape, its height is 55.74 mm and the base diameter is around 120.12 mm (more details are provided in Appendix). Its shape is based on a symmetric combination of a chamfered disk base and hemisphere; the latter position of which has been skewed from the central disk axis. Both shapes include a steep wall region which are difficult to be formed using single-pass forming only.

Table 5 Comparison of the formability for ellipsoidal cup between single-pass forming and multi-pass forming

Forming method	Forming results	Comparison of formability		
		Position at which Failure occurred(mm)	Final part morphology	FE prediction (thickness strain)
Single-pass	Failure	Height=40 		High magnitude strain zone: crack occurs. Highest strain: -8.817e-01
Multi-pass	Success (all tests)	N/A 		High magnitude strain zone. Highest strain: -9.039e-01

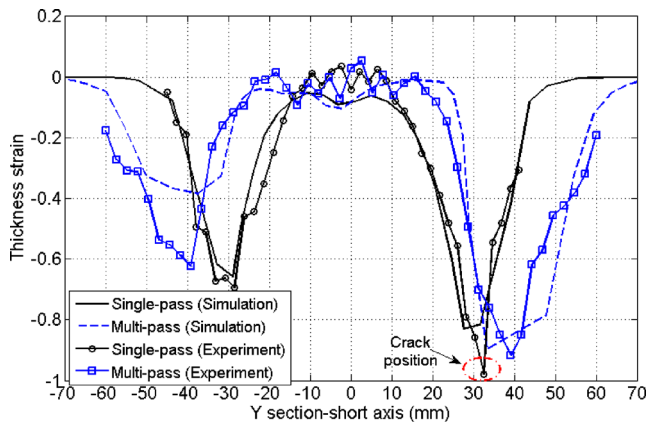


Fig. 7 Comparison of thickness strain distributions for ellipsoidal cup (single-pass forming vs. test no. 2 in multi-pass forming)

3 Results and discussions

In this section, multi-stage deformation passes are designed for both investigated shapes. For the ellipsoidal cup, FEA and

AMINO TPIF experimental results are provided to evaluate the interaction of tool paths in deformation passes and the final part on the process formability. Then, thickness strain distributions are compared given the same multi-pass forming design and different tool path strategies. Additionally, the material flow mechanism in multi-pass forming is analyzed and compared with the single-pass forming via FEA. Further FEA and experimental results in terms of forming of the asymmetric free-form shape are performed to validate the analysis for multi-pass tool path strategies.

3.1 Multi-pass deformation design

The multi-pass deformation design follows the systematic methodology proposed in [14], which can be adapted to the generalized shapes. The overall thinning rate T_0 is set to be less than 0.65 in this case. The average thinning rate \bar{T} is assumed to be less than 0.3. Then, the

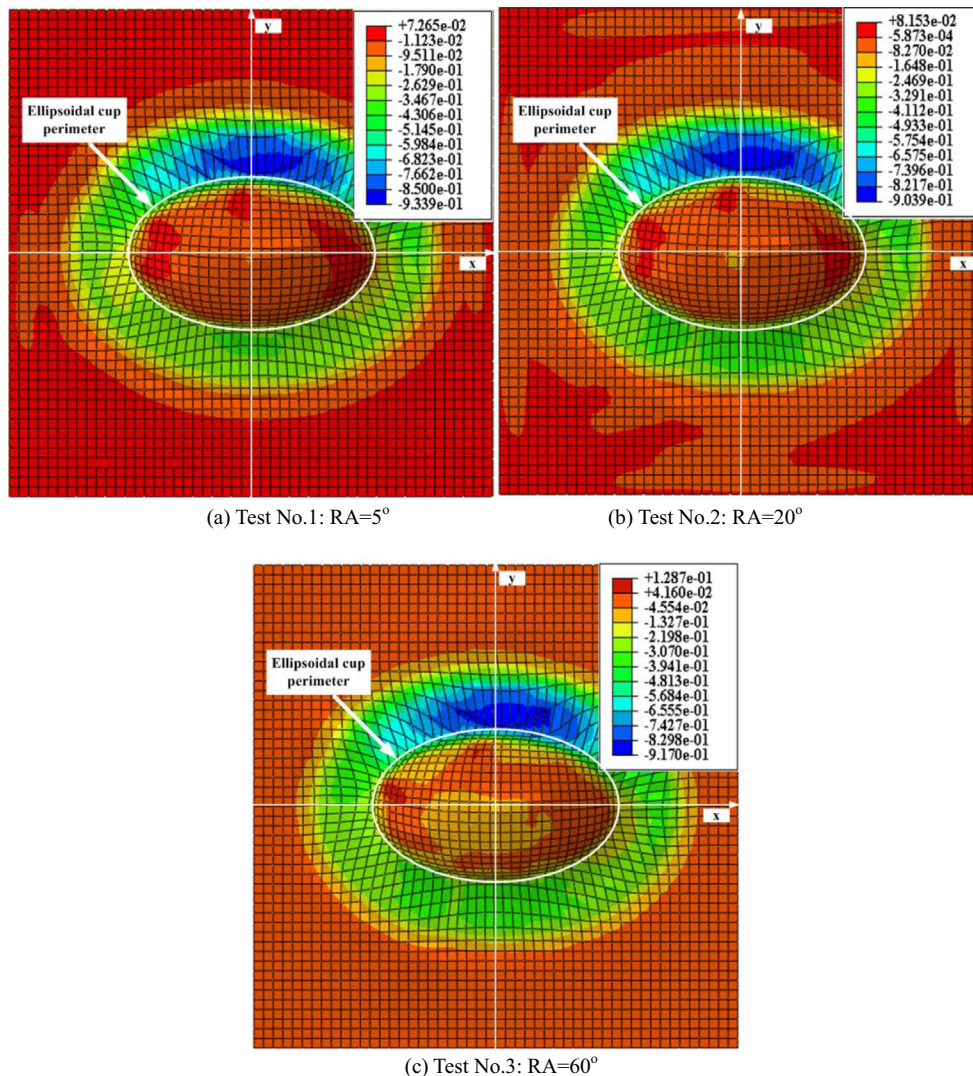
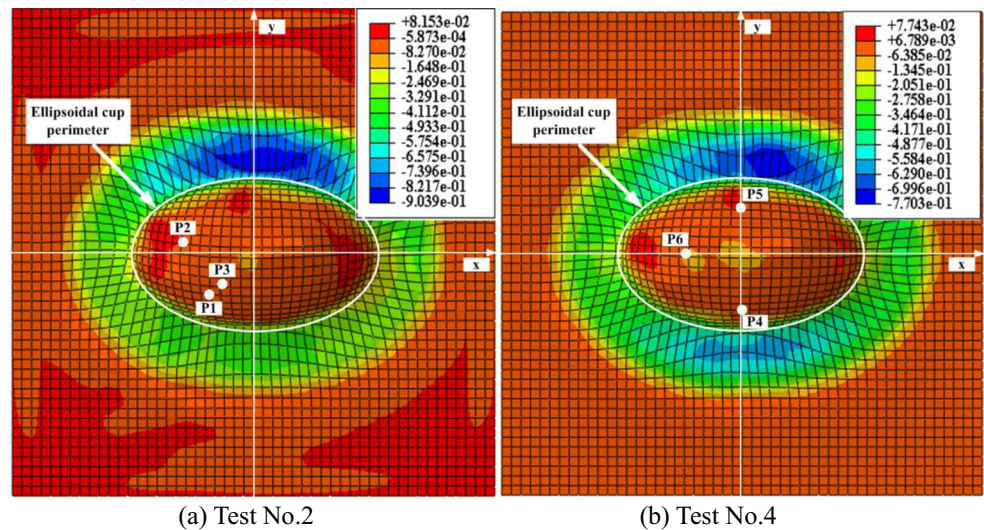


Fig. 8 Influence of ramp angle (RA) on thickness strain distribution of the final shape. **a** Test no. 1: $RA=5^\circ$. **b** Test no. 2: $RA=20^\circ$. **c** Test no. 3: $RA=60^\circ$

Fig. 9 Influence of start point (SP) on thickness strain distribution of the final shape (RA=20°). **a** Test no. 2. **b** Test no. 4

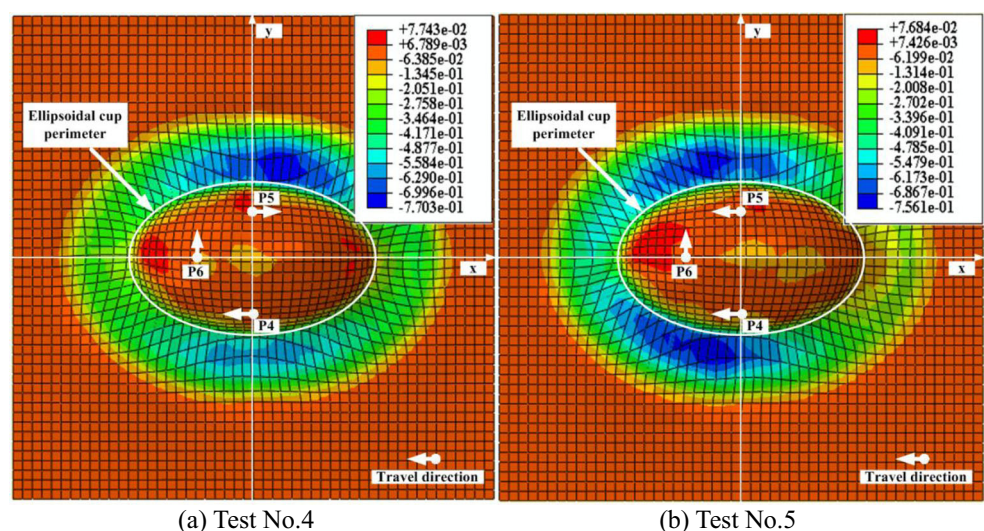


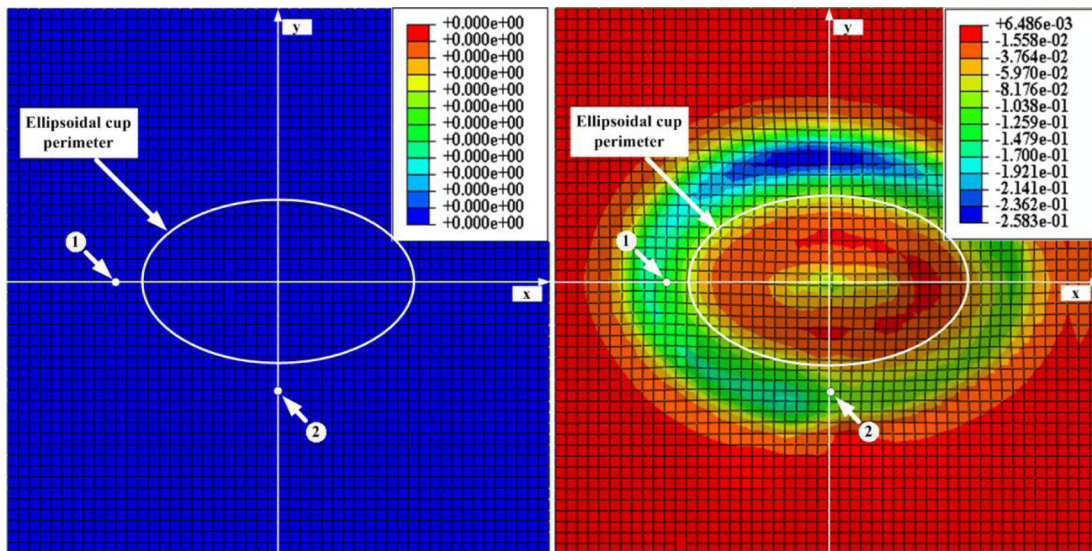
required number n_e of forming stages can be estimated to be 3. The thinning rate for the forming stage (T_1, T_2, T_3) can be set to be 0.25, 0.30, and 0.35, respectively. The corresponding highest thickness strains in different forming stages are $-0.29, -0.64,$ and -1.08 . The determined parameters are shown in Table 3. $a_1, a_2, b_1,$ and b_2 are model parameters which can be tuned to calculate the intermediate thickness strain and therefore determine the intermediate shapes. α is an adjustable slope parameter, which changes the influence of the distance on the weighted average thickness strain. R is the radius, which defines the size of the region over which the thickness strains of neighboring elements are averaged. More details are provided in the description of Eqs. 2, 3, and 6 in [14]. The deformation passes (intermediate shapes) for the corresponding forming stages are determined as shown in Figs. 5 and 6.

3.2 Results for ellipsoidal cup

Five experimental tests were devised to evaluate the tool path effects on material thinning during the multi-pass forming process for the ellipsoidal cup. AA7075-O aluminum sheets with 1.016-mm thickness are used in these tests. FEA and experimental results are provided to compare the process formability and thickness strain distributions for different deformation passes and the final part considering different parametric settings for tool path generation. Table 4 presents the tool path parameters associated with each test in the multi-pass forming. Tests no. 1 to no. 3 only consider the influence of RA (ramp angle) on the multi-pass forming process. The influence of parameters start point (SP) and travel direction (TD) on the final shape are tested in tests no. 4 and no. 5, respectively. This work does not intend to provide the optimal values for each tool path parameter but identify the effects of

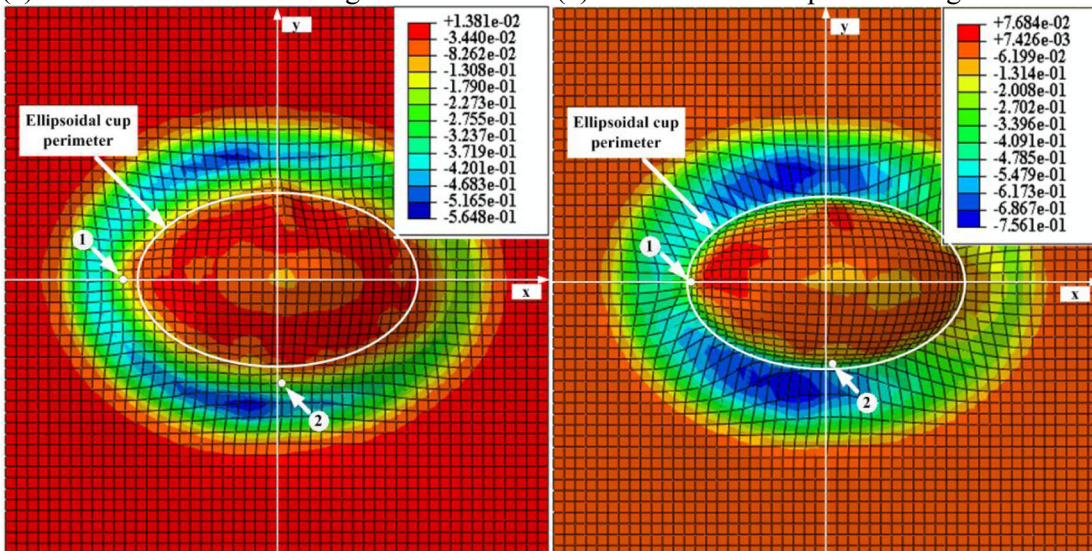
Fig. 10 Influence of travel direction (TD) on thickness strain distribution of the final shape. **a** Test no. 4. **b** Test no. 5





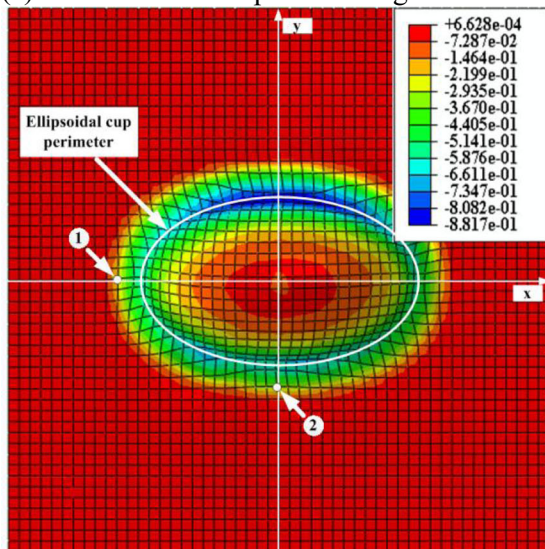
(a) Initial sheet for all forming methods

(b) Pass one in multi-pass forming



(c) Pass two in multi-pass forming

(d) Final shape in multi-pass forming



(e) Final shape in single-pass forming

◀ **Fig. 11** Material flow analysis by FEA (thickness strain distribution). **a** Initial sheet for all forming methods. **b** Pass 1 in multi-pass forming. **c** Pass 2 in multi-pass forming. **d** Final shape in multi-pass forming. **e** Final shape in single-pass forming. Note: Initial sheet for all forming methods (single-pass and multi-pass). Horizontal position of two material points (*white nodes* N1 and N2): **a** N1(−60,0), N2(0,−40); **b** N1(−58.62,0.12), N2(0.71,−39.95); **c** N1(−55.08,0.09), N2(1.786,−36.70); **d** N1(−48.75,0.39), N2(1.96,−29.1453); and **e** N1(−59.28,0.56), N2(−0.65,−39.10)

strategic combinations of studied tool path parameters on the multi-pass forming process. This provides a guideline for the manufacturing of a high-quality part.

3.2.1 Formability

The process formability is analyzed based on the forming outcome (failure or success) of the final part formed by single-pass forming and the designed multi-pass forming considering the comparison of experimental and FE prediction results as summarized in Table 5.

Referring to Table 5, failure occurred at the part height of 40 mm in the single-pass forming, while all multi-pass tests were performed successfully. The high-magnitude strain zone in FEA results indicates the likely failure position, which is confirmed by the experimental result in the single-pass forming. As discussed in [14], the proposed multi-pass deformation design can delay the occurrence of the highest thickness strains in intermediate stages and therefore allow steeper shapes to be formed than that by using single-pass forming. Although the multi-pass forming is successful, it is of interest to investigate whether material thinning can be further reduced by considering the interaction of tool path generations in deformation passes and the final part. This motivates the investigation in the next section.

3.2.2 Thickness strain distribution

In order to validate the established FE model, a comparison between FE simulation and experimental thickness measurements has been made given the final formed part. Measurements were performed along the short axis of the ellipsoidal cup in terms of single-pass forming and multi-pass forming (test no. 2). The results are provided in Fig. 7. Overall, the FE results are in agreement with the experimental measurements although the FE simulation underestimates the actual situation in some regions of the part. The highest thickness strain in single-pass forming can be found around 30 mm (part height 40 mm) in the positive Y direction, where the fracture occurred. While the thickness strains in multi-pass forming in the same position are much lower, at the same time, the highest thickness strain has been shifted to a larger radius region, thereby reducing the failure risk. These findings further confirm the formability results in Table 5. Additionally, a

more uniform thickness strain distribution has been achieved, which improves the quality of the final parts.

(i) Influence of ramp angle on thickness strain distribution

Figure 8 shows the influence of ramp angle on the thickness strain distribution of the final part. As can be seen, the thickness strain distribution is quite similar in all these three cases. The dark blue region represents the concentrated thickness strain zone with the highest magnitude strains, where the fracture is most likely to occur. In addition, the highest thickness strains are -0.93 , -0.90 , and -0.92 , respectively. These FEA results indicate there is little influence of ramp angle on the final thickness strain distribution.

(ii) Influence of start point on thickness strain distribution

Figure 9 shows the influence of start point on the thickness strain distribution of the final shape. It is noted that the highest magnitude thickness strain in the dark blue region in Fig. 9b can be greatly reduced compared to that in Fig. 9a (-0.77 vs. -0.90) by deliberately changing the start point of the tool path generation in each intermediate deformation pass and the final part. The possible reason to explain this result is the positions of start points in different deformation passes and the final part are more symmetric relative to the final part so as to balance the stretching deformation. This means that less stretching deformation is induced in the critical region with the excessive concentrated high-magnitude strains as shown in Fig. 9a. In the meantime, other regions with relative low-magnitude strains are stretched more. Additionally, the multi-pass tool path in pass 1 starts around the part region with steep angles, which would possibly shift the most stretched deformation to the region away from the steep region. This can be observed in Fig. 9b, in which the first tool path with start point (P4) creates a concentrated strain zone in the positive y axis, while the second tool path with start point (P5) creates another in the negative y axis. The risk of failure would be reduced and therefore, the formability is increased.

(iii) Influence of travel direction on thickness strain distribution

It is expected that the tool travel direction also plays a role on material thinning control during a multi-pass forming process. As shown in Fig. 10b, two obvious concentrated strain regions (with relatively high-magnitude strains) in dark blue, which can be found with symmetry about the x axis, are obtained compared to only one dark blue region in Fig. 10a. It illustrates that the change of tool travel direction does not show obvious advantages on eliminating the concentrated high-thickness strains although the highest thickness strain is slightly reduced compared to the case in Fig. 10a (-0.76 vs. -0.77). However,

Table 6 Tool path parameters designed in multi-pass forming for the asymmetric free-form shape

Geometry	Tests	Pass 1				Pass 2				Final part			
		RA (°)	SP	TD	SD (mm)	RA (°)	SP	TD	SD	RA (°)	SP	TD	SD (mm)
Free-form shape	No. 1	20	Pa	CW	4	20	Pb	CW	4	20	Pc	CW	2
	No. 2	20	Pc	CW	4	20	Pd	CW	4	20	Pa	CW	2

No. 1: Pa=(-35.418,2.936); Pb=(-7.485,-14.276); Pc=(7.967,8.147). No. 2: Pc=(16.969,4.925); Pd=(-1.681,34.334); Pa=(-26.914,6.617)

symmetric thickness strain distributions may be more desirable in terms of obtaining the balanced material flow and eliminating the material twisting phenomenon.

3.2.3 Analysis of material flow via FEA

The successful forming of all five multi-pass tests further demonstrates that material flow induced by the deformation passes has a major influence on the process formability and thickness strain distributions of the final part. However, it is quite difficult to predict the material flow analytically during the multi-pass forming process. This section provides a means of the material flow analysis via FEA. This gives more insight into the material flow behavior in the multi-pass forming process.

The material flow behavior is analyzed based on the FEA results in test 5 for the ellipsoidal cup as the analysis is quite similar for the other four cases. The analysis consists of three stages corresponding to each deformation pass. In addition, the result for single-pass forming is also provided for comparative purposes. Figure 11 shows the material flow. An in-plane inward movement can be found in the final shape forming in the multi-pass process from the initial position N1(-60,0) and N2(0,-40) in Fig. 11a through pass 1 (N1(-58.62,0.12), N2(0.71,-39.95)) in Fig. 11b and pass 2 (N1(-55.08,0.09), N2(1.786,-36.70)) in Fig. 11c to the final position (N1(-48.75,0.39), N2(1.96,-29.1453)) within the perimeter of the ellipsoidal cup in Fig. 11d. On the contrary, there is no obvious in-plane inward movement found in single-pass forming in Fig. 11e.

It is believed that in-plane movement causes a compressive deformation state in TPIF which suppresses the failure. The greatest component of the compressive state in TPIF is in the direction normal to the sheet at the point of contact caused by the reaction between the tool and the positive die, while the component in the plane of the sheet both parallel and perpendicular to the tool direction is generally stretching. In the case of this paper, the material is shown to displace inwards causing a compressive deformation state close to the center of the ellipsoidal cup in the plane of the sheet, which can be clearly seen in the final forming of multi-pass and single-pass methods in Fig. 11d, e. However, this increases the tensile deformation

state around the perimeter of the ellipsoidal cup and hence is likely to actually increase the propensity for failure.

This is apparent on the dark blue region in Fig. 11d, e and is particularly acute in this case because the region of greatest stretching in the x - y plane is also the region with greatest stretching in the z direction. However, it should be mentioned that, by forming a wider area than the perimeter of the shape in the multi-pass design, the greatest stretching region (with highest magnitude thickness strains) in Fig. 11d is actually shifted to the outside of the ellipsoidal cup perimeter compared to on the perimeter in single-pass forming (Fig. 11d). Therefore, the formability in multi-pass forming is expected to be higher than that in single-pass forming. These findings were confirmed by the formability results in Section 3.2.1. This material movement has been measured experimentally in [14].

3.3 Results for free-form shape

From a geometrical point of view, the part region with a steep angle will lead to higher magnitude deformation strains during forming. The multi-pass deformation design in [14] aims to provide more material in the intermediate passes so as to delay the occurrence of the highest thickness strains than would be possible in single-pass forming. The flow of sufficient material is allowed into the deformed region, thereby enabling steeper shapes to be formed. Apart from the deformation pass design, the previous results for the ellipsoidal cup confirm that the final thickness strain distribution is also affected by the

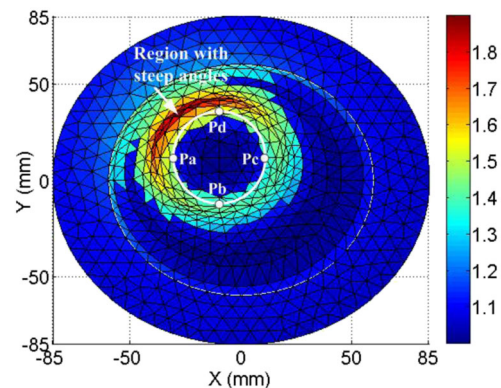


Fig. 12 Illustration of tool path start points relative to final part region (top view) with steep angles (angle increases as the color changes from blue to red)

Table 7 FEM results (Avg 75 %) for maximum thinning points in single-pass forming and multi-pass forming

Forming method	Tests	Pass 1		Pass 2		Final part	
		Thickness strain	Point position	Thickness strain	Point position	Thickness strain	Point position
Single-pass		N/A	N/A	N/A	N/A	-0.866	(-40.45,27.48)
Multi-pass	No. 1	-0.187	(-0.96,49.49)	-0.442	(21.52,-0.7)	-0.553	(20.73,-3.82)
	No. 2	-0.194	(12.85,-15.53)	-0.442	(-0.80,-20.47)	-0.555	(24.81,12.89)

tool path start point and travel direction. As for the start point, the design for different start points in deformation passes can reduce the stretching deformation in the region with the concentrated high-magnitude thickness strains (excessive thinning region). The changes in the tool path travel direction of multi-pass forming can obtain more symmetric thickness strain distribution but generate more concentrated high-magnitude strain zones. As start point is the most influential parameter on material thinning, a further study is provided to clarify its influence on the material deformation behavior in terms of forming of an arbitrary asymmetric free-form shape and possibly provide a guideline for multi-pass tool path design for an arbitrary shape.

Two tests in terms of multi-pass forming for the asymmetric free-form shape are devised as presented in Table 6.

The first test assumes that the multi-pass tool path starts around the region of the free-form shape with a steep draw angle in deformation pass 1. This is expected to shift the most stretched deformation to the region away from the steep region, which has a dominant influence on the subsequent forming. For comparison, the second test assumes that the multi-pass tool path starts away from the region of the free-form shape with a steep draw angle in deformation pass 1. In addition, the tool path start points in the subsequent multi-pass forming are designed in an order opposite to the travel direction with the aim to further control material flow to reduce thinning. It is noted that the positions of tool path start points would not be symmetric relative to the geometrical features of an arbitrary shape. However, in this case, the positions of start points are determined to evenly distribute in a half circle to reduce the influence of geometrical asymmetry as shown in Fig. 12. AA7075-O aluminum sheets with 1.60-mm thickness are used in these tests. To verify the above assumptions, FEM simulations are performed. As all multi-pass forming and single-pass forming were successful, only thickness strains are provided and compared to validate the design assumptions.

3.3.1 Thickness strains

The thickness strains and positions for the maximum thinning points in each deformation pass and the final part are compared

as presented in Table 7. It is concluded that the highest magnitude thickness strain can be reduced in multi-pass forming compared to that in single-pass forming. The position of the highest magnitude thickness strain can be shifted to the part region with a small draw angle in multi-pass forming by deliberately changing the tool path start points in the deformation passes. Furthermore, it is shown that the final highest magnitude thickness strain can be slightly reduced in test no. 1 compared to test no. 2, which confirms the test design assumptions through FEM results although these differences are negligible.

Figure 13 shows the changes of thickness strains for the maximum thinning point in the final part of multi-pass forming (no. 1) during the FEM simulation. It is seen that the material thinning occurs several times (small steps) in pass 1, pass 2, and final forming. More specifically, the material thinning occurs in each small step due to the localized deformation in the tool-sheet contact zone as the tool passes nearby. As the tool passes away from the contact zone, a small elastic recovery can be observed. It is further noted that the material thinning dissipates as the tool travels away from the contact zone level along the forming direction.

In order to validate the FEM simulations, a comparison of thickness strain distributions for a section profile with experimental measurements is provided for single-pass forming and test no. 1 in multi-pass forming as seen in Fig. 14. The overall material thinning in multi-pass forming is lower than that in single-pass forming, which

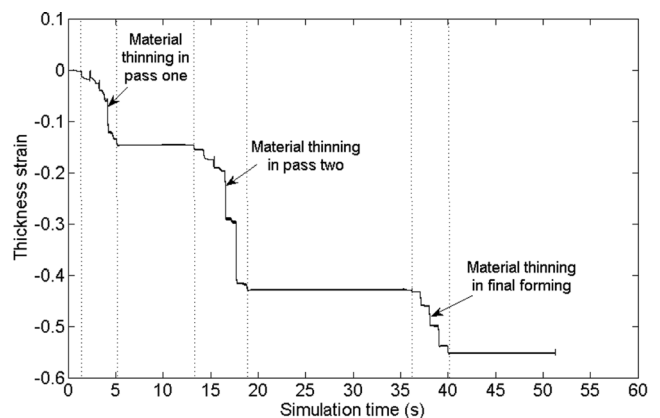
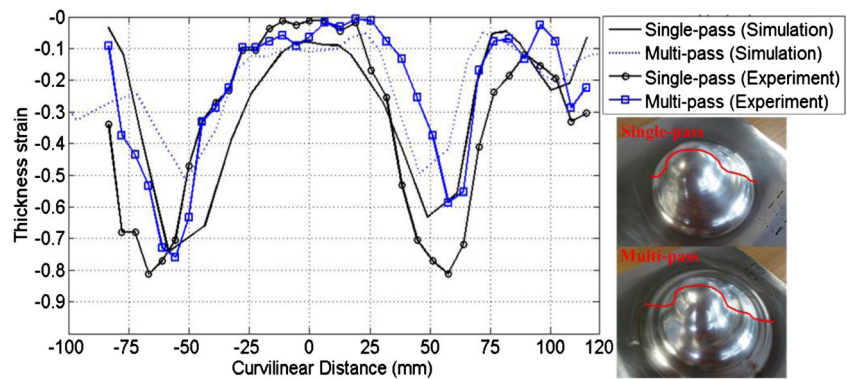


Fig. 13 Evolution of thickness strains for the maximum thinning point in the final part of multipass forming (no. 1) during the FEM simulation

Fig. 14 Comparison of thickness strain distributions for free-form shape (single-pass forming vs. test no. 1 in multi-pass forming)



is evidenced by both FEM simulations and experimental measurements. Additionally, the free-form shape formed by multi-pass forming has more uniform thickness distribution along the chosen section profile. It is noted that the FEM simulations underestimate the experimental results in this case, which is consistent with the findings in Fig. 7. The most possible explanation for this deviation is material strain hardening in multi-pass forming experiments increases as deformation pass increases. This would possibly entail a large amount of plastic strain. However, as mentioned in Section 2.2, only a power-law curve was used to characterize the material behavior, which means the relevant effects of kinematic strain hardening are not taken into account in FEM simulations so that the simulations would possibly underestimate the actual experimental results. However, the deviation would be reduced by introducing more advanced material model into the FE modeling in the future. Although an underestimation is observed between FEM and experimental results, it importantly shows similar material thinning trends, which can be used for the qualitative analysis of material thinning behavior during multi-pass forming. This further demonstrates that the proposed multi-pass design and tool path generation strategies are more effective in forming the complex shapes.

4 Conclusions

This paper investigates the tool path generation strategies for multi-pass ISF design by FEM simulations and experiments. Two complex shapes are designed to validate the generalization ability of the developed multi-pass design methodology. Process formability and thickness strain distribution are analyzed and compared in terms of different tool path generation strategies. Three parameters, which are relevant to the control of multi-pass tool path generation, have been evaluated in terms of their influence on material thinning. Additionally, the material flow mechanism in multi-pass forming has been

explained by FEA. The major conclusions are summarized as follows:

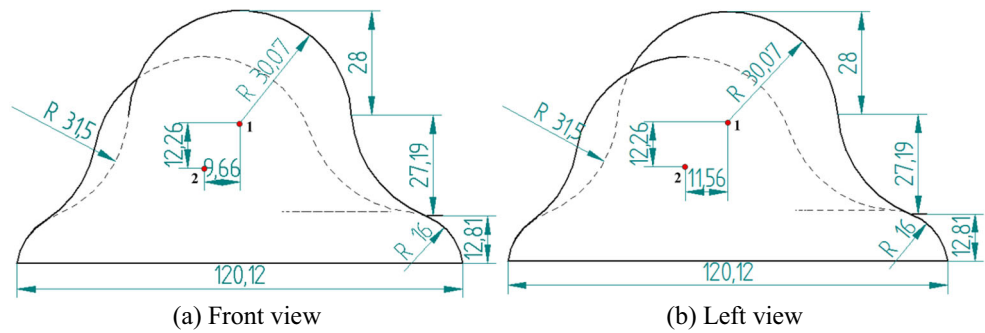
- Complex shapes can be formed using the proposed multi-pass design methodology with higher formability and uniform thickness distribution compared to single-pass forming.
- Ramp angle shows little influence on material thinning. Changes in travel direction can balance the thickness strain distribution so that material twisting phenomenon can be eliminated to some extent.
- Tool path start point in multi-pass forming is the most important controllable parameter to reduce material thinning of the final part compared to ramp angle and travel direction. The multi-pass tool path start points are suggested to be distributed as evenly as possible relative to the geometrical features of a designed part. Additionally, the tool path in pass 1 is suggested to start around the final part region with steep angles. However, the reasons behind these findings still need to be further clarified in the future work so as to facilitate the multi-pass design.
- The inward in-plane material flow mechanism has been evidenced by FEA given the proposed multi-pass design. It appears to cause a compressive deformation state and therefore allows steeper shapes to be formed. This clarifies the reason why multi-pass forming can achieve higher formability compared to single-pass forming.

Acknowledgments This research was supported by the ARC Linkage Program, Boeing Research and Technology, Australia, and QMI Solutions in Australia.

Appendix (drawings for asymmetric free-form shape)

It is noted that the asymmetric free-form shape is obtained by shifting the center point 1 of the hemispherical shape in a symmetric part to the center point 2 of the hemispherical shape in the asymmetric free-form shape (for detailed dimensions, refer to Fig. 15 below).

Fig. 15 Drawings for asymmetric free-form shape (unit: mm). **a** Front view. **b** Left view



References

- Jeswiet J, Micari F, Hirt G, Bramley A, Duflou JR, Allwood JM (2005) Asymmetric single point incremental forming of sheet metal. *CIRP Ann Manuf Technol* 54(2):623–650
- Emmens WC, Sebastiani G, van den Boogaard AH (2010) The technology of incremental sheet forming—a brief review of the history. *J Mater Process Technol* 210(8):981–997
- Kim TJ, Yang DY (2000) Improvement of formability for the incremental sheet metal forming process. *Int J Mech Sci* 42(7):1271–1286
- Young D, Jeswiet J (2004) Wall thickness variations in single-point incremental forming. *Proc IMechE Part B: J Eng Manuf* 218(11):1453–1459
- Duflou JR, Verbert J, Belkassam B, Gu J, Sol H, Henrard C, Habraken AM (2008) Process window enhancement for single point incremental forming through multi-step toolpaths. *CIRP Ann Manuf Technol* 57(1):253–256
- Skjoedt M, Silva MB, Martins PAF, Bay N (2010) Strategies and limits in multi-stage single-point incremental forming. *J Strain Anal Eng* 45(1):33–44
- Cui Z, Gao L (2010) Studies on hole-flanging process using multistage incremental forming. *CIRP J Manufact Sci Tech* 2(2):124–128
- Manco L, Filice L, Ambrogio G (2011) Analysis of the thickness distribution varying tool trajectory in single-point incremental forming. *Proc IMechE Part B: J Eng Manuf* 225(3):348–356
- Malhotra R, Bhattacharya A, Kumar A, Reddy NV, Cao J (2011) A new methodology for multi-pass single point incremental forming with mixed toolpaths. *CIRP Ann Manuf Technol* 60(1):323–326
- Xu DK, Malhotra R, Reddy NV, Chen J, Cao J (2012) Analytical prediction of stepped feature generation in multi-pass single point incremental forming. *J Manuf Process* 14(4):487–494
- Li JC, Hu JB, Pan JJ, Geng P (2012) Thickness distribution and design of a multi-stage process for sheet metal incremental forming. *Int J Adv Manuf Technol* 62(9–12):981–988
- Li JC, Shen JJ, Wang B (2013) A multipass incremental sheet forming strategy of a car taillight bracket. *Int J Adv Manuf Technol* 69(9–12):2229–2236
- Liu ZB, Li YL, Meehan PA (2013) Vertical wall formation and material flow control for incremental sheet forming by revisiting multistage deformation path strategies. *Mater Manuf Processes* 28(5):562–571
- Liu ZB, Daniel WJT, Li YL, Liu S, Meehan PA (2014) Multi-pass deformation design for incremental sheet forming: analytical modeling, finite element analysis and experimental validation. *J Mater Process Technol* 214(3):620–634
- Rauch M, Hascoet JY, Hamann JC, Plenel Y (2009) Tool path programming optimization for incremental sheet forming applications. *Compu Aided Design* 41(12):877–885
- Liu ZB, Li YL, Meehan PA (2013) Experimental investigation of mechanical properties, formability and force measurement for AA7075-O aluminum alloy sheets formed by incremental forming. *Int J Precis Eng Manuf* 14(11):1891–1899

Chapter 5 Conclusions and Future Work

This chapter provides a summary of the conducted work in this thesis followed by a discussion of possible pathways in future work to further explore ISF technology.

The work in the first part of this thesis is the process investigation including process formability, forming forces, geometric accuracy, forming time and surface quality. In particular, tensile tests were carried out to characterize the mechanical properties of AA7075-O aluminium alloy sheets with three different thicknesses, showing that anisotropy increases as the sheet thickness increases and the strain-hardening exponent in diagonal direction is smaller than that in rolling direction and transverse direction for all three thicknesses. **(i) Process formability.** First, the effect of tool type and size on formability was studied by forming a straight groove. An obvious increasing trend in fracture depth was observed with the increase of tool diameters. Therefore, the tool diameter should be selected as large as possible to improve the formability with the constraints of geometrical complexity. Then, the effects of tool path types with different incremental steps on the maximum forming angle as well as the successful forming height were evaluated to clarify the formability. It was concluded that spiral and z-level tool paths have no significant difference in terms of formability. Formability can increase as step-down size increases and geometrical features such as part height also play a role on formability. Additionally, a fracture forming limit diagram was developed to give the design limits for strain, showing a fracture band with maximum major true strain (0.92) and minimum major true strain (0.68). **(ii) Forming forces.** First, forming forces have been measured by means of strain gauges during a groove test. Vertical and horizontal forces presented sharper increases at the end of each travel due to the increase of contact area and the impact of the side wall. Forces only showed a slightly growing trend in the central area of the groove. This proves that only localized deformation occurred in the process and thus it is possible to form large and complex shapes without higher forming forces required. Then,

the trends in forming forces were analysed considering the influence of different draw angles, sheet thicknesses, step-down sizes and sheet orientation. For different tool path types (spiral and z-level), the overall trend of resultant force is similar. However, the evolution force curve for the spiral tool path is smoother than that for the z-level tool path. In addition, the slope of force curve after the peak value can be seen as a forming failure predictor. The slope decreases as the draw angle increases. This provides an approach to on-line control and failure detection of incremental forming. Furthermore, the maximum vertical force increases as the step-down size increases. The maximum vertical force increases in an approximately linear way with the increase in the sheet thickness. The measured largest vertical force is 6792 N with 2.54 mm sheet thickness and 1.5 mm step-down size. The influence of sheet orientations on the forming force was first considered in incremental forming. Results have shown that the vertical force is found to be smaller in the sheet orientation 45° compared with that in the sheet orientation 0° due to the smaller strain-hardening exponents in diagonal directions. **(iii) Geometric accuracy.** A study on the effect of step-down size on geometric accuracy was implemented. It was shown that step-down size can significantly affect the geometric accuracy. Specifically, the geometric accuracy increases when the step-down size is decreased. However, too small step-down size should also be avoided with regard to the formability as well as forming time. It was clearly suggested that there is an optimum value of step depth in the ISF tool path design; for instance 0.7mm presented in the case. A trade-off among geometric accuracy, surface quality, formability and forming time should be made in the design and control of tool paths, which motivates the further research on the design of an advanced ISF control system. **(iv) Forming time.** Design of experiments (DOE) together with Taguchi method was used to investigate the effects of process parameters (step over, feed rate, sheet thickness and tool diameter) on forming time. It was concluded that the most significant process parameter influencing forming time is the step over (spiral tool path) followed by the feed rate. The sheet thickness and tool diameter have little effect on forming time. Using Taguchi method, the optimal combination of process parameters has been determined and the minimum forming time has been predicted as 205s for a cone-forming process.

(v) Surface roughness. The effect of tool type and size on surface integrity was studied by forming a straight groove. Surface topography of parts formed by the sliding and rolling tools has been scanned by SEM. The result showed that the rolling contact condition causes less local damage and scratching of the surface. Furthermore, design of experiments (DOE) together with response surface methodology (RSM) was used to investigate the effects of process parameters (step-down size, feed rate, sheet thickness and tool diameter) on surface roughness. An empirical model has been established for the overall surface roughness (tool-sheet contact surface roughness and non-contact surface roughness) prediction of a part formed by ISF. Sheet thickness was found to be the most influential forming variable on the overall surface roughness followed by the step down. The optimal experimental conditions were determined as step down (0.39 mm), feed rate (6000 mm/min), sheet thickness (1.60 mm) and tool diameter (25 mm) with a minimum overall surface roughness 0.32 μm . Furthermore, roll marks have small influences on the external surface roughness with respect to R_a for AA7075-O sheets with thicknesses of 1.02 mm and 2.54 mm. As for the internal surface, tool paths have dominant effects on the surface quality with little influence of roll marks. Surface roughness on the external non-contact surface is always higher than that of the internal tool-sheet contact surface in the range of investigated factor values.

The work performed in the second part of this thesis is the multi-pass ISF modelling and its validation. **(i) SPIF multi-pass deformation design.** An empirical trial-and-error method has been proposed for SPIF multi-pass deformation design in which three forming strategies and their combinations have been evaluated in terms of the process formability. The results showed that the forming strategy using more material in the forming as well as the addition of a small amount of bending can greatly improve the formability. **(ii) AMINO TPIF multi-pass deformation design.** A closed-loop systematic methodology incorporating two open-loop analytical models (**M1** and **M2**) for AMINO TPIF multi-pass deformation design considering the predicted thickness strains given the design geometry has been developed based on shear

deformation and the strain compensation mechanism. The feasibility of the proposed design methodology was validated by finite element analysis (FEA) and experimental tests. The results revealed that a more uniform thickness strain distribution can be derived using *M2*. The occurrence of the highest strains can be delayed in the intermediate stages to larger perimeter area and the flow of material is allowed into the deformed region in the actual TPIF process, thereby allowing a compressive deformation state to develop and enabling steeper shapes to be formed. Therefore, the process formability can be enhanced via the proper design of deformation passes. Additionally, the generalization of simple shapes to complex shapes using the developed multi-pass design methodology has also been performed. The interaction of different tool paths on material thinning of the final part given the same multi-pass design was evaluated and analysed. It was concluded that ramp angle shows little influence on material thinning. Changes in travel direction can balance the thickness strain distribution so that material twisting phenomenon can be eliminated to some extent. It was found that the tool path start point in multi-pass forming is the most important controllable parameter to reduce material thinning of the final part compared to the other two parameters (ramp angle and travel direction). The maximum material thinning and the thickness strain distribution can be controlled by deliberately changing the tool path start points in multi-pass forming. It was suggested that the multi-pass tool path start points should be distributed as evenly as possible relative to the geometrical features of a designed part.

5.1 Thesis Contributions

The following results from this thesis are believed to be the novel contributions to the existing literature:

- A detailed experimental study for the effects of process parameters on process formability, forming forces, surface integrity and geometric accuracy.

- One of experimental design methods-Taguchi's method used for forming time prediction and optimization of process parameters to minimise forming time.
- A detailed study on surface roughness and the development of an empirical model for surface roughness prediction based on response surface methodology and a novel multi-objective function.
- Development of three SPIF multi-stage forming strategies and their combinations for cylindrical cup forming based on an empirical trial-and-error method. The novelty is that more material and bending deformation are considered in the design of SPIF multi-stage forming to further improve the process formability.
- Simplified plane-strain analytical models to predict the formability between single-stage and multi-stage forming strategies, and between the different multi-stage strategies.
- Development of two open-loop analytical models for AMINO TPIF multi-pass deformation design with the aim to improve the process formability as well as obtain more uniform thickness strain distributions of final parts. The pros and cons of two models are compared and analysed in terms of process formability and thickness strain distribution.
- A closed-loop AMINO TPIF multi-pass design methodology incorporating two open-loop analytical models.
- FE modeling for AMINO TPIF multi-pass deformation design. The developed FE model can simulate the actual AMINO TPIF process and derive reliable predicted results in terms of process formability and thickness strains.
- AMINO TPIF experimental validation for the analytical closed-loop multi-pass design and FE predictions.
- Investigation of multi-pass tool path generation strategies and their effects on material thinning during forming.

5.2 Suggestions for Future Work

The work presented in this thesis highlights many possible pathways in future work to further explore ISF technology, which are listed in the following:

- Development of a simplified analytical model taking into account the bending deformation to predict the process formability. This current study is limited to the shear only assumption in SPIF multi-pass deformation analysis.
- Extension of the trial-and-error SPIF multi-stage deformation design method to more complex shapes with vertical walls. The current case study is only limited to cylindrical cup forming.
- Material behaviour of the sheet metal in AMINO TPIF multi-pass deformation design has not been taken into account. Future work needs to be performed to test more materials so as to understand the influence of material behaviour on the multi-stage deformation during forming which will help determine proper multi-pass strategies.
- The influences of process parameters (step down, tool radius, feed rate, forming down pressure, etc.) during the multi-pass forming on the quality of the final parts should be further investigated so as to improve the forming accuracy and avoid forming defects such as wrinkling and distortion. The current closed-loop multi-pass ISF design methodology did not consider these influences.
- The force prediction model can be further developed to predict the tangential, radial and vertical components of the forming force at the same time. The current study is mainly limited to the forming force investigation via experimental measurements although a tangential force prediction model has been developed in collaborative work (**Paper L**).
- An intelligent neural network/fuzzy logic model can be developed incorporating the knowledge of the effects of process parameters on the forming process, which will serve to correct the forming tool path in order to improve the forming quality (both surface roughness and geometric accuracy). The current study is limited to the investigation of effects of

process parameters on surface roughness and geometric accuracy, separately.

References

Aerens, R., Eyckens, P., Van Bael, A., Duflou, J.R., 2010. Force prediction for single point incremental forming deduced from experimental and FEM observations. *International Journal of Advanced Manufacturing Technology* 46, 969-982.

Ambrogio, G., Costantino, I., De Napoli, L., Filice, L., Frantini, L., Muzzupappa, M., 2004a. Influence of some relevant process parameters on the dimensional accuracy in incremental forming: a numerical and experimental investigation. *Journal of Materials Processing Technology* 153-154, 501–507.

Ambrogio, G., Filice, L., Fratini, L., Micari, F., 2004b. Process mechanics analysis in single point incremental forming. In Ghosh, S., Castro, J.C., and Lee, J.K. editors, *Proc. of the 8th Numiform conference*, vol.712 of AIP Conf. Proc., pp. 922-927, Columbus, OH, USA. The Ohio State University. doi:10.1063/1.1766645.

Ambrogio, G., De Napoli, L., Filice, L., Gagliardi, F., Muzzupappa, M., 2005. Application of incremental forming process for high customized medical product manufacturing. *Journal of Materials Processing Technology* 162-163, 156-162.

Ambrogio, G., Filice, L., Micari, F., 2006. A force measuring based strategy for failure prevention in incremental forming. *Journal of Materials Processing Technology* 177, 413-416.

Ambrogio, G., Cozza, V., Filice, L., Micari, F., 2007. An analytical model for improving precision in single point incremental forming. *Journal of Materials Processing Technology* 191(1-3), 92–95.

Ambrogio, G., Filice, L., Manco, G.L., 2008. Warm incremental forming of magnesium alloy AZ31. *CIRP Annals - Manufacturing Technology* 57, 257–260.

Ambrogio, G., Filice, L., Guerriero, F., Guido, R., Umbrello, D., 2011. Prediction of incremental sheet forming process performance by using a neural network approach. *International Journal of Advanced Manufacturing Technology* 54, 921-930.

Ambrogio, G., Filice, L., Gagliardi, F., 2012. Formability of lightweight alloys by hot incremental sheet forming. *Materials & Design* 34, 501-508.

Ambrogio, G., Gagliardi, F., Filice, L., 2013. Robust design of incremental sheet forming by Taguchi's method. *Procedia CIRP* 12, 270-275.

Amino North America Corporation: http://www.aminonac.ca/product_e_dieless_models.asp.

Allwood, J.M., Shouler, D.R., Tekkaya, A.E., 2007. The increased forming limits of incremental sheet forming processes. *Key Engineering Materials* 344, 621-628.

Allwood, J.M., Music, O., Raithathna, A., Duncan, S.R., 2009. Closed-loop feedback control of product properties in flexible metal forming processes with mobile tools. *CIRP Annals - Manufacturing Technology* 58, 287–290.

Allwood, J.M., Braun, D., Music, O., 2010. The effect of partially cut-out blanks on geometric accuracy in incremental sheet forming. *Journal of Materials Processing Technology* 210(14), 1934-1941.

Attanasio, A., Ceretti, E., Giardini, C., 2006. Optimization of tool path in two points incremental forming. *Journal of Materials Processing Technology* 117, 409-412.

Attanasio, A., Ceretti, E., Giardini, C., Mazzoni, L., 2008. Asymmetric two point incremental forming: improving surface quality and geometric accuracy by tool path optimization. *Journal of Materials Processing Technology* 197(1–3), 59–67.

Azaouzi, M., Lebaal, N., 2012. Tool path optimization for single point incremental sheet forming using response surface method. *Simulation Modelling Practice and Theory* 24(5), 49-58.

Bahloul, R., Arfa, H., Belhadjsalah, H., 2013. Application of response surface analysis and generic algorithm for the optimization of single point incremental forming process. *Key Engineering Materials* 554-557, 1265-1272.

Bambach, M., Taleb Araghi, B., Hirt, G., 2009. Strategies to improve the geometric accuracy in asymmetric single point incremental forming. *Production Engineering* 3, 145-156.

Bambach, M., 2010. A geometrical model of the kinematics of incremental sheet forming for the prediction of membrane strains and sheet thickness. *Journal of Materials Processing Technology* 210(12), 1562-1573.

Behera, A.K., Verbert, J., Lauwers, B., Duflou, J.R., 2013. Tool path compensation strategies for single point incremental sheet forming using multivariate adaptive regression splines. *Computer-Aided Design* 45(3), 575-590.

Belchior, J., Guillo, M., Courteille, E., Maurine P., Leotoing L., Guines, D., 2013. Off-line compensation of the tool path deviations on robotic machining: Application to incremental sheet forming. *Robotics and Computer-Integrated Manufacturing* 29, 58-69.

Bezerra, M.A., Santelli, R.E., Oliveira, E.P., Villar, L.S., Escalera, L.A., 2008. Response surface methodology (RSM) as a tool for optimization in analytical chemistry. *Talanta* 76, 965-977.

Buffa, G., Campanella, D., Fratini, L., 2013. On the improvement of material formability in SPIF operation through tool stirring action. *International Journal of Advanced Manufacturing Technology* 66, 1343-1351.

Capece Minutolo, F., Durante, M., Formisano, A., Langella, A., 2007. Evaluation of the maximum slope angle of simple geometries carried out by incremental forming process. *Journal of Materials Processing Technology* 194, 145-150.

Cui, Z., Gao, L., 2010. Studies on hole-flanging process using multistage incremental forming. *CIRP Journal of Manufacturing Science and Technology* 2(2), 124-128.

Duflou, J.R., Callebaut, B., Verbert, J., De Baerdemaeker, H., 2007a. Laser assisted incremental forming: formability and accuracy improvement. *CIRP Annals -Manufacturing Technology* 56, 273–276.

Duflou, J.R., Tunckol, Y., Szekeres, A., Vanherck, P., 2007b. Experimental study on force measurements for single point incremental forming. *Journal of Materials Processing Technology* 189, 65-72.

Duflou, J.R., Callebaut, B., Verbert, J., De Baerdemaeker, H., 2008a. Improved SPIF performance through dynamic local heating. *International Journal of Machine Tools & Manufacture* 48, 543-549.

Duflou, J.R., Verbert, J., Belkassam, B., Gu, J., Sol, H., Henrard, C., Habraken, A.M., 2008b. Process window enhancement for single point incremental forming through multi-step toolpaths. *CIRP Annals - Manufacturing Technology* 57, 253-256.

Durante, M., Formisano, A., Langella, A., 2010. Comparison between analytical and experimental roughness values of components created by incremental forming. *Journal of Materials Processing Technology* 210(14), 1934–1941.

Emmens, W.C., van den Boogaard, A.H., 2009a. An overview of stabilizing deformation mechanisms in incremental sheet forming. *Journal of Materials Processing Technology* 209(8), 3688-3695.

Emmens, W.C., van den Boogaard, A.H., 2009b. Incremental forming by continuous bending under tension - An experimental investigation. *Journal of Materials Processing Technology* 209(14), 5456-5463.

Essa, K., Hartley, P., 2011. An assessment of various process strategies for improving precision in single point incremental forming. *International Journal of Material Forming* 5, 1-12.

Eyckens, P., 2010. Formability in incremental sheet forming: generalization of the Marciniak-Kuczynski model. Doctoral Thesis, Leuven: Katholieke Universiteit Leuven.

Fan, G.Q., Gao, L., Hussain, G., Wu, Z.L., 2008. Electric hot incremental forming: A novel technique. *International Journal of Machine Tools & Manufacture* 48, 1688-1692.

Fan, G.Q., Sun, F.T., Meng, X.G., Gao, L., Tong, G.Q., 2010. Electric hot incremental forming of Ti-6Al-4V titanium sheet. *International Journal of Advanced Manufacturing Technology* 49, 941-947.

Filice, L., Fantini, L., Micari, F., 2002. Analysis of Material Formability in Incremental Forming. *CIRP Annals - Manufacturing Technology* 51, 199-202.

Filice, L., 2006a. A phenomenology-based approach for modelling material thinning and formability in incremental forming of cylindrical parts. *Proceedings of the Institution of Mechanical Engineers, Part B: Journal of Engineering Manufacture* 220, 1449-1455.

Filice, L., Ambrogio, G., Micari, F., 2006b. On-line control of single point incremental forming operation through punch monitoring. *CIRP Annals - Manufacturing Technology* 55(1), 245-248.

Fiorentino, A., 2013. Force-based failure criterion in incremental sheet forming. *International Journal of Advanced Manufacturing Technology* 68, 557-563.

Fratini, L., Ambrogio, G., Di Lorenzo, R., Filice, L., Micari, F., 2004. Influence of mechanical properties of the sheet material on formability in single point incremental forming. *CIRP Annals - Manufacturing Technology* 53, 207-210.

Göttmann, A., Diettrich, J., Bergweiler, G., Bambach, M., Hirt, G., Loosen, P., Poprawe, R., 2011. Laser-assisted asymmetric incremental sheet forming of titanium sheet metal parts. *Production Engineering* 5, 263-271.

Guzmán, C.F., Gu, J., Duflou, J., Vanhove, H., Flores, P., Habraken, A.M., 2012. Study of the geometrical inaccuracy on a SPIF two-slope pyramid by finite element simulations. *International Journal of Solids and Structures* 49, 3594-3604.

Hagan, E., Jeswiet, J., 2004. Analysis of surface roughness for parts formed by computer numerical controlled incremental forming. *Proceedings of the Institution of Mechanical Engineers, Part B: Journal of Engineering Manufacture* 218(10), 1307-1312.

Ham, M., Jeswiet, J., 2006. Single point incremental forming and the forming criteria for AA3003. *CIRP Annals - Manufacturing Technology* 55(2) 241-244.

Ham, M., Jeswiet, J., 2007. Forming limit curves in single point incremental forming. *CIRP Annals - Manufacturing Technology* 56(1), 277-280.

Hamilton, K., Jeswiet, J., 2010. Single point incremental forming at high feed rates and rotational speeds: Surface and structural consequences. *CIRP Annals -Manufacturing Technology* 59(1), 311-314.

Han, F., Mo, J.H., Qi, H.W., Long, R.F., Cui, X.H., Li, Z.W., 2013. Springback prediction for incremental sheet forming based on FEM-PSO NN technology. *Transactions of Nonferrous Metals Society of China* 23, 1061-1071.

Henrard, C., Bouffioux, C., Eyckens, P., Sol, H., Duflou, J.R., Van Houtte, P., Van Bael, A., Duchêne, L., Habraken, A.M., 2011. Forming forces in single point incremental forming: prediction by finite element simulations, validation and sensitivity. *Computational Mechanics* 47(5), 573-590.

Hirt, G., Ames, J., Bambach, M., Kopp, R., 2004. Forming strategies and process modelling for CNC incremental sheet forming. *CIRP Annals - Manufacturing Technology* 53(1), 203-206.

Hussain, G., Gao, L., 2007a. A novel method to test the thinning limits of sheet metals in negative incremental forming. *International Journal of Machine Tools & Manufacturing* 47, 419-435.

Hussain, G., Gao, L., Hayat, N., Qijian, L., 2007b. The effect of variation in the curvature of part on the formability in incremental forming: An experimental investigation. *International Journal of Machine Tools & Manufacture* 47, 2177-2181.

Hussain, G., Gao, L., Dar, N.U., 2007c. An experimental study on some formability evaluation methods in negative incremental forming. *Journal of Materials Processing Technology* 186, 45-53.

Hussain, G., Dar, N.U., Gao, L., Chen, M.H., 2007d. A comparative study on the forming limits of an aluminium sheet metal in negative incremental forming. *Journal of Materials Processing Technology* 187-188, 94-98.

Hussain, G., Gao, L., Zhang, Z.Y., 2008a. Formability evaluation of a pure titanium sheet in the cold incremental forming process. *International Journal of Advanced Manufacturing Technology* 37, 920-926.

Hussain, G., Hayat, N., Gao, L., 2008b. An experimental study on the effect of thinning band on the sheet formability in negative incremental forming. *International Journal of Machine Tools & Manufacture* 48, 1170-1178.

Hussain, G., Gao, L., Hayat, N., Xu, Z.R., 2009. A new formability indicator in single point incremental forming. *Journal of Materials Processing Technology* 209, 4237-4242.

Iseki, H., Naganawa, T., 2002. Vertical wall surface forming of rectangular shell using multistage incremental forming with spherical and cylindrical rollers. *Journal of Materials Processing Technology* 130-131, 675-679.

Jackson, K., Allwood, J.M., 2009. The mechanics of incremental sheet forming. *Journal of Materials Processing Technology* 209, 1158-1174.

Jeswiet, J., Duflou, J., Szekeres, A., Levebre, P., 2005a. Custom manufacture of a solar cooker - a case study. *Advanced Materials Research* 6-8, 487-492.

Jeswiet, J., Micari, F., Hirt, G., Bramley, A., Duflou, A., Allwood, J., 2005b. Asymmetric single point incremental forming of sheet metal. *CIRP Annals - Manufacturing Technology* 54(2), 623-649.

Jeswiet, J., Young, D., 2005c. Forming limit diagrams for single-point incremental forming of aluminium sheet. *Proceedings of the Institution of Mechanical Engineers, Part B: Journal of Engineering Manufacture* 219(4), 359-364.

Jeswiet, J., Young, D., Ham, M., 2005d. Non-traditional forming limit diagrams for incremental forming. *Advanced Materials Research* 6-8, 409-416.

Junk, S., 2003. Inkrementelle Blechumformung mit CNC Werkzeugmaschinen: Verfahrensgrenzen und Umformstrategien. Doctoral Thesis, Universität des Saarlandes, Germany.

Kim, T.J., Yang, D.Y., 2000. Improvement of formability for the incremental sheet metal forming process. *International Journal of Mechanical Sciences* 42, 1271-1286.

Kim, Y.H., Park, J.J., 2002. Effect of process parameters on formability in incremental forming of sheet metal. *Journal of Materials Processing Technology* 130-131, 42-46.

Lasunon, O.U., 2013. Surface roughness in incremental sheet metal forming of AA5052. *Advanced Materials Research* 753-755, 203-206.

Li, J.C., Hu, J.B, Pan, J.J., Geng, P., 2012a. Thickness distribution and design of a multi-stage process for sheet metal incremental forming. *International Journal of Advanced Manufacturing Technology* 62, 981-988.

Li, M., Zhang, L.C., Mo, J.H., Lu, Y., 2012b. Tool-path generation for sheet metal incremental forming based on STL model with defects. *International Journal of Advanced Manufacturing Technology* 63(5-8), 535-547.

Li, J.C., Shen, J.J., Wang, B., 2013. A multipass incremental sheet forming strategy of a car taillight bracket. *International Journal of Advanced Manufacturing Technology* DOI 10.1007/s00170-013-5179-3.

Liu, J., Mo, J.H., Huang, S.H., 2004. Sheet metal dieless forming and its tool path generation based on STL files. *International Journal of Advanced Manufacturing Technology* 23(9-10), 696-699.

Lu, B., Chen, J., Ou, H., Cao, J., 2013. Feature-based tool path generation approach for incremental sheet forming. *Journal of Materials Processing Technology* 213(7), 1221–1233.

Malhotra, R., Reddy, N.V., Cao, J., 2010. Automatic 3D spiral toolpath generation for single point incremental forming. *ASME Journal of Manufacturing Science and Engineering* 132(6), 061003(1)-061003(10).

Malhotra, R., Bhattacharya, A., Kumar, A., Reddy, N.V., Cao, J., 2011a. A new methodology for multi-pass single point incremental forming with mixed tool paths. *CIRP Annals - Manufacturing Technology* 60(1), 323-326.

Malhotra, R., Cao, J., Ren, F., Kiridena, V., Xia, Z.C., Reddy, N.V., 2011b. Improvement of geometric accuracy in incremental forming by using a squeezing toolpath with two forming tools. *ASME Journal of Manufacturing Science and Engineering* 133(6), 061019(1)-061019(10).

Malhotra, R., Cao, J., Beltran, M., Xu, D.K., Magargee, J., Kiridena, V., Xia, Z.C., 2012a. Accumulative-DSIF strategy for enhancing process capabilities in incremental forming. *CIRP Annals - Manufacturing Technology* 61, 251-254.

Malhotra, R., Xue, L., Belytschko, T., Cao, J., 2012b. Mechanics of fracture in single point incremental forming. *Journal of Materials Processing Technology* 212, 1573-1590.

Manco, L., Filice, L., Ambrogio, G., 2011. Analysis of the thickness distribution varying tool trajectory in single-point incremental forming. *Proceedings of the Institution of Mechanical Engineers Part B - Journal of Engineering Manufacture* 225, 348-356.

Martins, P.A.F., Bay, N., Skjoedt, M., Silva, M.B., 2008. Theory of single point incremental forming. *CIRP Annals - Manufacturing Technology* 57, 247–252.

Meier, H., Buff, B., Laurischkat, R., Smukala, V., 2009. Increasing the part accuracy in dieless robot-based incremental sheet metal forming. *CIRP Annals - Manufacturing Technology* 58, 233–238.

Micari, F., Ambrogio, G., Filice, L., 2007. Shape and dimensional accuracy in Single Point Incremental Forming: State of the art and future trends. *Journal of Materials Processing Technology* 191, 390–395.

Mirnia, M.J., Dariani, B.M., 2012. Analysis of incremental sheet forming using the upper-bound approach. *Proceedings of the Institution of Mechanical Engineers, Part B: Journal of Engineering Manufacture* 226, 1309-1320.

Palumbo, G., Brandizzi, M., 2012. Experimental investigations on the single point incremental forming of a titanium alloy component combining static heating with high tool rotation speed. *Materials & Design* 40, 43-51.

Park, J.J., Kim, Y.H., 2003. Fundamental studies on the incremental sheet metal forming technique. *Journal of Materials Processing Technology* 140, 447-453.

Park, J., Kim, J., Park, N., Kim, Y., 2010. Study of forming limit for rotational incremental sheet forming of magnesium alloy sheet. *Metallurgical and Materials Transactions A* 41(1), 97-105.

Petek, A., Kuzman, K., Suhač, B., 2009. Autonomous on-line system for fracture identification at incremental sheet forming. *CIRP Annals - Manufacturing Technology* 58, 283–286.

Powers, B.M., Ham, M., Wilkinson, M.G., 2010. Small data set analysis in surface metrology: An investigation using a single point incremental forming case study. *Scanning* 32(4), 199-211.

Rauch, M., Hascoet, J.Y., Hamann, J.C., Plenel, Y., 2009. Tool path programming optimization for incremental sheet forming application. *Computer-Aided Design* 41, 877-885.

Sarraji, W.K.H., Hussain, J., Ren, W.X., 2012. Experimental investigation on forming time in negative incremental sheet metal forming process. *Materials and Manufacturing Processes* 27, 499-506.

Schafer, T., Schraft, R.D., 2005. Incremental sheet metal forming by industrial robots. *Rapid Prototyping Journal* 11(5), 278-286.

Shim, M.S., Park, J.J., 2001. The formability of aluminium sheet in incremental forming. *Journal of Materials Processing Technology* 113, 654-658.

Shi, X.F., Gao, L., Khalatbari, H., Xu, Y., Wang, H., Jin, L.L., 2013. Electric hot incremental forming of low carbon steel sheet: accuracy improvement. *International Journal of Advanced Manufacturing Technology* 68, 241-247.

Silva, M.B., Skjoedt, M., Martins, P.A.F., Bay, N., 2008a. Revisiting the fundamentals of single point incremental forming by means of membrane analysis. *International Journal of Machine Tools & Manufacturing* 48(1), 73-83.

Silva, M.B., Skjoedt, M., Atkins, A.G., Bay, N., Martins, P.A.F., 2008b. Single-point incremental forming and formability-failure diagrams. *Journal of Strain Analysis for Engineering Design* 43, 15-35.

Silva, M.B., Skjoedt, M., Bay, N., Martins, P.A.F., 2009. Revisiting single-point incremental forming and formability failure diagrams by means of finite elements and experimentation. *Journal of Strain Analysis for Engineering Design* 44(4), 221-234.

Silva, M.B., Nielsen, P.S., Bay, N., Martins, P.A.F., 2011. Failure mechanisms in single-point incremental forming of metals. *International Journal of Advanced Manufacturing Technology* 56, 893-903.

Skjoedt, M., Silva, M.B., Martins, P.A.F., Bay, N., 2010. Strategies and limits in multi-stage single-point incremental forming. *Journal of Strain Analysis for Engineering Design* 45, 33-44.

Suresh, K., Khan, A., Regalla, S.P., 2013. Tool path definition for numerical simulation of single point incremental forming. *Procedia Engineering* 64, 536-545.

Taguchi, G., Chowdhury, S., Wu, Y.I., 2005. *Taguchi's Quality Engineering Handbook*, Wiley, Michigan.

Taleb Araghi, B., Manco, G.L., Bambach, M., Hirt, G., 2009. Investigation into a new hybrid forming process: Incremental sheet forming combined with stretch forming. *CIRP Annals - Manufacturing Technology* 58, 225–228.

Taleb Araghi, B., Göttmann, A., Bambach, M., Hirt, G., Bergweiler, G., Diettrich, J., Steiners, M., Saeed-Akbari, A., 2011. Review on the development of a hybrid incremental sheet forming system for small batch sizes and individualized production. *Production Engineering* 5, 393-404.

Xu, D.K., Malhotra, R., Reddy, N.V., Chen, J., Cao, J., 2012. Analytical prediction of stepped feature generation in multi-pass single point incremental forming. *Journal of Manufacturing Processes* 14(4), 487-494.

Young, D., Jeswiet, J., 2004. Wall thickness variation in single-point incremental forming. *Proceedings of the Institution of Mechanical Engineers, Part B: Journal of Engineering Manufacture* 218, 1453-1459.

Zhang, C., Xiao, H.F., Yu, D.H., 2013. Incremental forming path-generated method based on the intermediate models of bulging simulation. *International Journal of Advanced Manufacturing Technology* 67, 2837-2844.

Zhu, H., Liu, Z.J., Fu, J.H., 2011. Spiral tool-path generation with constant scallop height for sheet metal CNC incremental forming. *International Journal of Advanced Manufacturing Technology* 54, 911-919.

Zhu, H., Li, N., 2013. A new STL model-based approach for tool path generation in CNC incremental forming. *International Journal of Advanced Manufacturing Technology* 69(1-4), 277-290.

Appendix I

TABLE 2 in **Paper G** is corrected as follows:

Material Property	Value
Density (kg/m ³)	2,800
Young's modulus (GPa)	70
Yield strength (MPa)	92.7
Ultimate tensile strength (MPa)	196
Strain hardening coefficient (MPa)	355
Power law coefficient	0.22

Appendix II

Paper L

Efficient force prediction for incremental sheet forming and experimental validation

Li, Y.L., **Liu, Z.B.**, Lu, H.B., Daniel, W.J.T., Liu, S., Meehan, P.A.

International Journal of Advanced Manufacturing Technology

2014, Volume: 73(1-4), Pages: 571-587.

Note that this paper is an additional publication by the author but not forming part of this thesis. It contains the further work for the tangential forming force prediction, in which the experimental validation work is part of the work in Papers A and B.

Efficient force prediction for incremental sheet forming and experimental validation

Yanle Li · Zhaobing Liu · Haibo Lu ·
W. J. T. (Bill) Daniel · Sheng Liu · Paul A. Meehan

Received: 16 September 2013 / Accepted: 21 January 2014 / Published online: 19 February 2014
© Springer-Verlag London 2014

Abstract Incremental sheet forming (ISF) has been attractive during the last decades because of its greater flexibility, increased formability and reduced forming forces. However, traditional finite element simulation used for force prediction is significantly time consuming. This study aims to provide an efficient analytical model for tangential force prediction. In the present work, forces during the cone-forming process with different wall angles and step-down sizes are recorded experimentally. Different force trends are identified and discussed with reference to different deformation mechanisms. An efficient model is proposed based on the energy method to study the deformation zone in a cone-forming process. The effects of deformation modes from shear, bending and stretching are taken into account separately by two sub-models. The final predicted tangential forces are compared with the experimental results which show an average error of 6 and 11 % in respect to the variation of step-down size and wall angle in the explored limits, respectively. The proposed model would greatly improve the prediction efficiency of forming force and benefit both the design and forming process.

Keywords Incremental sheet forming · Forming force · Formability · Prediction · Shear · Bending

Nomenclature

t_0	Initial sheet of the metal sheet
Δz	Vertical step-down size of the tool path
A	Wall angle of the cone part
f	Feed rate of the forming tool

r_t	The radius of the forming tool
r_i	The radius of the current tool position
r_o	The outer radius of the deformed zone
r	The radius of the flow line
θ_c, θ_t and θ_s	Dividing angles for the flow line
M and N	Parameters used for optimising dissipated power
Z_t	Vertical position of the tool head surface
Z_s	Vertical position of the sheet after previous tool path
$S(X)$	Shape function
Zf_c, Zf_s and Zf_s^f	Curve functions for the flow line
v_r, v_θ and v_z	Components of velocity in deforming zone
$\dot{\epsilon}_{ij}$	Components of strain rates in deforming zone
ϵ	Plastic strain
y_0	Average yield strength
E_h	Slope of the stress–strain curve
\dot{w}	Dissipated power
F_x, F_y and F_z	Force components in global orthogonal Cartesian coordinate system
F_{xp}, F_{yp} and F_{zp}	Peak values of the measured force
F_t	Average value of the converted tangential force at the steady state

1 Introduction

Incremental sheet forming (ISF) technology is an emerging forming process ideal for rapid prototype and small batch production. In an ISF process, a flat metal sheet is gradually formed into the designed 3D shape using computer numerical control (CNC)-controlled generic tool stylus. The process is highly flexible such that very complex shapes can be achieved with careful tool path programming and sometimes with the

Y. Li (✉) · Z. Liu · H. Lu · W. J. T. (B). Daniel · S. Liu · P. A. Meehan
School of Mechanical and Mining Engineering, The University of
Queensland, St Lucia, Brisbane, QLD 4072, Australia
e-mail: yanle.li@uq.edu.au

support of a die. Therefore, ISF was widely accepted as a promising forming process over conventional processes such as deep drawing and stamping [1, 2] for small batch production. Emmens et al. [3] comprehensively reviewed the history of the technology of ISF. Three development periods were clarified and an extensive list of patents was provided which directly reflects that ISF has received great attention particularly in the automotive industry. However, one of the dominant limits for the further development and commercialization of ISF technology is the limited geometrical accuracy of the final shape [4]. Essa and Hartley [5] investigated the effects of adding a backing plate, a supporting kinematic tool and modifying the final stage of the tool path on the improvement of the geometrical accuracy through a finite element (FE) model. It was found that the sheet bending near the initial tool contact location was minimised by the backing plate; the springback was reduced by the kinematic tool; and the pillow effect was eliminated by the modified tool path. Although various strategies [6] have been proposed to improve product accuracy, a systematic understanding of the local deformation mechanics and further investigation on the forming force are essential.

Over the past few years, forces during ISF have been intensively studied mainly experimentally due to its possible application in aspects including on-line control, failure prevention and process optimization. Duflou et al. [7] experimentally investigated the relationship of the forming forces with the four selected process parameters: the vertical step-down size, tool diameter, wall angle and the initial sheet thickness. It was concluded that the forming forces will increase with the increase of vertical step-down size, wall angle and sheet thickness. Filice et al. [8] worked on the force analysis and classified the force trends of tangential force into three types: steady-state force trends, polynomial force trends and monotonically decreasing force trends. Ambrogio et al. [9] concluded that the force gradient after the peak can be effectively considered as a critical indicator to detect and prevent workpiece fracture. Therefore, forming force is a potential indicator for forming limits identification. Petek et al. [10] proposed an autonomous on-line system for fracture identification and localization by analysing the reaction force with a skewness function. Another failure criterion presented by Fiorentino [11] is based on force monitoring during the forming process. This approach was achieved by comparing the stresses acting on the material calculated from forming forces with the ultimate strength of the material. Additionally, Ingarao et al. [12] investigated the use of recorded force data to evaluate the energy consumption required for the ISF process, which provides guidance for sustainable development of the process.

Prediction of forming forces in ISF provides understanding of the deformation mechanics, monitoring of the forming process, failure prediction, and a means of on-line control

and optimisation. The efficient prediction of the forming force is still one of the main limitations for the further development of ISF technology, although some authors attempted to bridge the existing gap. Even though FE models are commonly used to predict forming force for various forming processes, it is significantly time consuming for the ISF process. This is partly due to the fact that the deformation of the sheet during ISF is localised and continuously changing over the whole process. Smith et al. [13] reported a simulation time of 24 days for a single point incremental forming process for a truncated cone with a major diameter of 45 mm and wall angle of 40°. To overcome the above computational challenges of the FE approach, Raithatha and Duncan [14] developed a new model that is based on the numerical minimization of internal work within the material. In this method, the minimization of plastic work was formulated as a second-order cone programming (SOCP) optimization problem and was solved efficiently using primal dual interior point SOCP algorithms. The results showed that the computing time for a straight line indentation on a sheet with dimensions of 0.1×0.1 m is 5–9 min. However, the reduced computing time was achieved at a loss of model accuracy which results in considerable fluctuation at the roof of the groove. Iseki [15] obtained the forming forces for the incremental forming of a pyramid using an approximated deformation analysis. The analysis was based on a plane-strain deformation model, and the results were validated with experimental values. Aerens et al. [16] studied the incremental forming of truncated cones with different materials using experimental and statistical analyses. Regression formulae were proposed to predict the triple forming forces including axial, radial, and tangential components from input variables including wall angle, initial thickness, tool diameter, and vertical pitch. Finally, an approximate formula was deduced for predicting the axial component for forming any material based on the tensile strength only. Recently, Mirnia and Dariani [17] proposed a new approach to predict the tangential force on a truncated cone using an assumed deformation zone and an upper-bound analysis. It was reported that the forces were in good agreement with those from the experimental work of Aerens et al. [16]. Nevertheless, large errors can be expected for severe deformation conditions (e.g. $\Delta z > 0.5$ mm).

The above review of the recent studies shows that most of the previous work on forming force is investigated experimentally and very few models are available for the efficient prediction of the forming force. Although complex forming processes can be modelled through numerical methods, analytical study of the process still plays a pivotal role in understanding the mechanism of the process and developing efficient predictive modelling. This study will present an analytical method to analyse the deformation of the contact region

and also calculate the required forming force by taking into account two different deformation mechanisms. In particular, the main contributions of this paper are:

- The development and application of two efficient analytical sub-models for tangential force prediction in the ISF process. All three major deformation modes involved in ISF, shear, bending and stretching are taken into account.
- The generalisation and validation of an empirically combined efficient model. A comparison of the results obtained with a very efficient combined model with the experimental values to determine the validity of assumptions for three different deformation mechanisms.
- The experimental investigation and quantification of the effects of wall angle and step-down size on forming force and part formability in terms of failure depth.

To this end, the experimental set up and machine for the cone-forming process is firstly described in Section 2. Subsequently, Section 3 outlines the methodological approach including theoretical justifications and analytical techniques used for the proposed analytical force prediction model. The experimental force results with different forming parameters are then provided in Section 4. This section also provides the results for the tuning and validation of the models to the experimental results. Finally, conclusions and future work are presented in Section 5.

2 Experiments

To facilitate the study of the effect of product geometry and step-down size on the forming force and formability, truncated cones with different wall angles were selected as the target shapes.

2.1 Equipment setup

The forming tests were performed on a state-of-the-art machine dedicated for the multi-point ISF process designed by Amino Corporation as shown in Fig 1. The machine allows mould based forming for a maximum size of $2,100 \times 1,450 \times 550$ mm with a FANUC controller for precise control. The movement of the two horizontal axes (X and Y) can have a maximum speed of 60 m/min with a repeatability of ± 0.05 mm. The vertical (Z) axis is driven by an AC servo motor with the power of 1 kW that allows a maximum acting force of 3 kN. The hemispherical tool with a radius of 15 mm was used to deform the material. The tip of the tool is tungsten carbide and the body is made of K110 steel which was hardened and tempered to HRC60. The sheet material used in the present study was aluminium 7,075-O sheet with 1.6 mm in thickness and was cut into 300×300 mm in size.

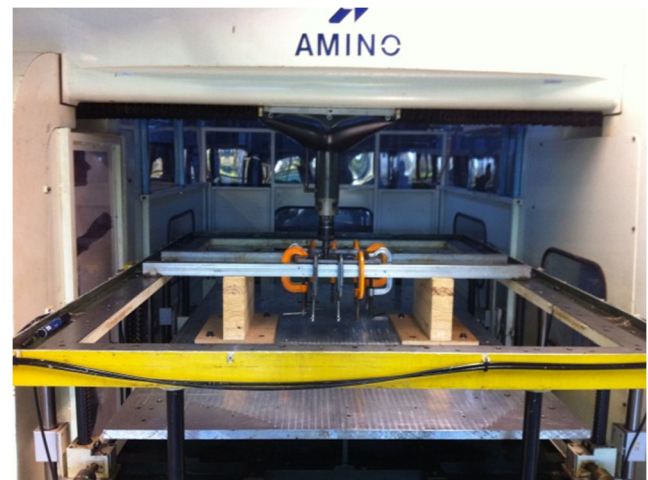


Fig. 1 Incremental sheet forming on amino machine

Figure 2 presents the true stress–strain curves for aluminium 7075-O sheets with 1.6 mm thickness derived from the tensile test for three different directions (rolling, diagonal and transverse). It shows that the deviations of the curves are quite small so the material can be assumed to be isotropic. Similar to r value averaging, the true stress values for three directions can be averaged as,

$$\bar{\sigma} = \frac{\sigma_0 + 2\sigma_{45} + \sigma_{90}}{4} \quad (1)$$

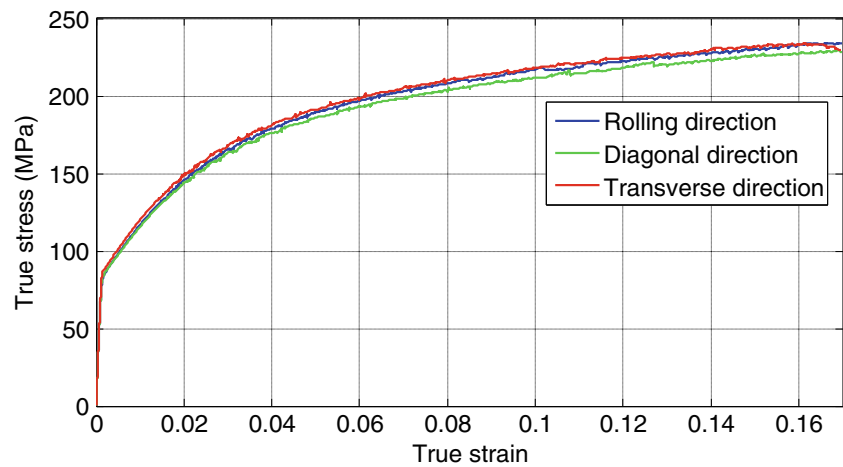
where σ_0 , σ_{45} and σ_{90} are the true stress values in rolling, diagonal and transverse direction, respectively. Then the stress–strain relation for the sheet can be fit by the Swift type work hardening power law,

$$\bar{\sigma} = K(\varepsilon_0 + \varepsilon)^n, \quad (2)$$

where ε is the plastic strain; K , ε_0 and n are material parameters listed in Table 1.

The forming forces acting on the forming tool have been measured continuously over time during the process. There are several ways to capture the forming force, such as the cantilever sensor designed by Jeswiet [18] and force dynamometer used by Duflou et al. [7]. In the present work, three full Wheatstone bridges configured by four strain gauges have been designed and mounted on the hemispherical tool. The three bridges were designed to measure the three orthogonal forces: two bending directions (F_x and F_y) and one axial direction (F_z), respectively. Those strain gauges were calibrated twice in all three directions by applying a series of known forces. The calibrated system shows a mostly linear relation between strain and output voltage.

Fig. 2 True stress–strain curves for 7075-O aluminium alloy sheets with 1.6 mm thickness



2.2 Experimental tests

Lubricant (Shell Tellus Oil 68) was sprayed liberally on the blank before forming to prevent excessive friction. A backing plate was placed underneath the sheet in order to increase the rigidity between the forming area and sheet flange. The feed rate of the forming tool was set to 4,000 mm/min. Figure 3 shows the experimental configuration and a case study of a truncated cone formed by Amino CNC machine.

For the tool path strategy, the Z-level tool path with different vertical step-down size (Δz , the increment between two successive passes) were utilised so the truncated cones are formed in a stepwise manner with many contours. All the cones were designed with the same major diameter of 140 mm but with a smaller cone height for smaller inclination of the wall due to the geometric constraint. The angle between the deformed sheet to the horizontal plan is defined as wall angle (α). The tests were conducted until fracture and the forming forces for all the three orthogonal components (F_x , F_y , and F_z) were recorded continuously during this process. Two sets of experiments have been designed and the detailed process parameters are listed in Tables 2 and 3. Specifically, wall

angles of the truncated cone have been set ranging from 30° to 70° while other parameters are constant (i.e. $\Delta z = 0.5$ mm, $t_0 = 1.6$ mm, $f = 4,000$ mm/min and $r_t = 15$ mm) to investigate the effect of wall angle on forming forces and formability. Similarly, in the second set of experiments, step-down sizes have been designed varying from 0.1 to 1.0 mm, whereas other parameters are fixed to study how step down affects the forming force and formability in the cone-forming process.

3 Modelling

In this model, the energy method [19] is used to analyse the deformation behaviour and predict the tangential force of the truncated cone during the ISF process. According to the theory of the energy method, the total power of the plastic deformation should have minimum value. Under this condition, the 3D-deformed shape of the metal sheet and the strain components with minimum dissipated power are recognised as the best approximation for those of actual deformation. This theory is employed to analyse the deformation mechanism and predict the forming force in the ISF process.

A concise block diagram of the procedure to analyse deformation of the deformed curved surface is presented in Fig. 4. Two sub-models based on different deformation mechanisms (shear and bending with stretching) are included in the present model to investigate how the deformation mode is affected by the variation of forming parameters. By making different assumptions of the deformed curved surface, the total dissipated power of the sheet because of the combination of shear, bending and stretching can be calculated and minimised. Once the minimum total power is determined, the detailed information of the deformed zone and tangential force can be calculated.

Table 1 Mechanical properties of Aluminium 7075-O sheets with 1.6 mm thickness

Material	7075-O
Density (t/mm^3)	2.81×10^{-9}
Young's modulus (GPa)	70
Poisson's ratio	0.33
Tensile Yield Strength (MPa)	92
Ultimate Tensile Strength	198
Plastic coefficient K	352.58
Hardening exponent n	0.221

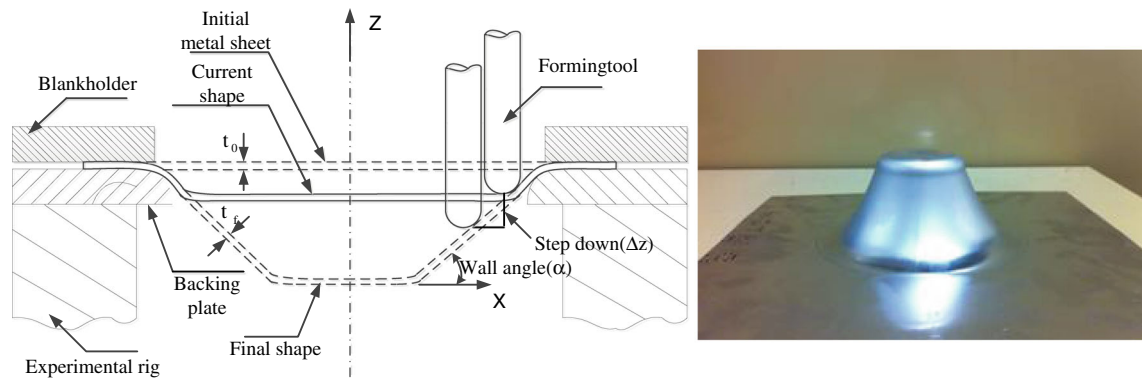


Fig. 3 Sketch of ISF experimental parameters and a case study made from Al 7075-O of 1.6 mm in thickness

The critical task is to construct a proper deformed curved surface for the local deformed area ahead of the forming tool to express the actual deformation. The metal sheet other than the deformed area is assumed rigid. Figure 5 sketches the deformation zone in ISF from different viewing aspects. Parameters used for the analytical formulation are marked in the figure. It is assumed that the deformation area induced by the current tool path is a circle within a radius of (r_o-r_i) ahead of the tool with the same centre of the hemispherical tool; where r_i is the current tool path radius and r_o is the outer radius of the deformed zone which can be obtained from the geometric relations between the current and previous forming path. Along the circumferential direction, a series of flow lines are assumed to express the surface at the centre of the metal sheet of the deformed sheet.

In the present model, as shown in Fig. 5c, the deformation zone is divided into three regions: I, contact region; II, non-contact region following the height of tool head; and III, non-contact region following the height of the formed sheet. One of the typical flow lines with a radius of r is depicted in Fig. 5b. The flow line is defined as three curves Zf_c, Zf_t and Zf_s which correspond to regions I, II and III, respectively (see Appendix 1 for calculation procedure of three deformation regions). Zf_c has the same geometric function with the tool head surface as it is the region contacting

with the tool but the conjunct point with Zf_t is unknown therefore is advisable to be determined as the following equation with an adjustable parameter M ,

$$Zf_c(r, \theta) = Z_c = M(Z_s - Z_o) + Z_o, \quad (0 \leq M \leq 1) \quad (3)$$

where Z_s and Z_o are the vertical position of the sheet formed in previous pass and the tool vertex with the radius of r . To represent the height variation of the non-contact surface of the sheet, a normalised shape function $S(X)$ is introduced. $S(X)$ is tentatively designed as two-second order Bezier curves with the following equation,

$$S(X) = \begin{cases} 1 - \left(\frac{\theta - \theta_c}{\theta_t - \theta_c}\right)^2 (1-N) \left(\frac{r_o - r}{r_o - r_i}\right) & \theta_c \leq \theta \leq \theta_t & 0 \leq N \leq 1 \\ 1 - \left(\frac{\theta - \theta_s}{\theta_s - \theta_t}\right)^2 (1-N) \left(\frac{r_o - r}{r_o - r_i}\right) & \theta_t \leq \theta \leq \theta_s & 0 \leq N \leq 1 \end{cases} \quad (4)$$

Here, N is another adjustable parameter which can be obtained through the optimisation of the dissipated power. The value of $S(X)$ changes from N to 1 corresponding to the variation of θ and r within their ranges. The calculated shape function $S(X)$ is presented in Fig. 6 with different values of N . As shown in the figure, the pattern of the shape function is significantly affected by the value of N which makes it

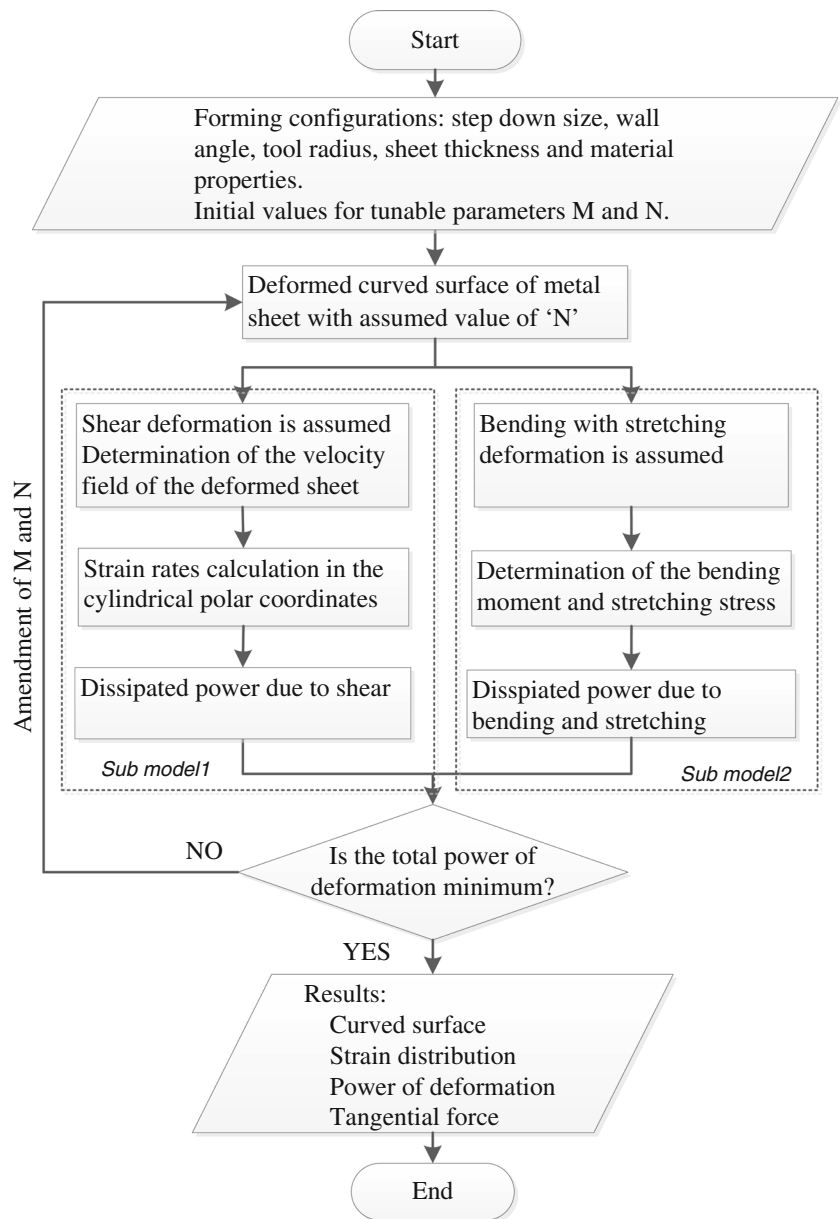
Table 2 Experimental design for different wall angles

Wall angle α (deg)	Step-down Δz (mm)	Tool radius (mm)	Thickness (mm)	Feed rate (mm/min)	Designed height (mm)
30	0.5	15	1.6	4,000	28
40	0.5	15	1.6	4,000	40
50	0.5	15	1.6	4,000	60
60	0.5	15	1.6	4,000	75
62	0.5	15	1.6	4,000	75
63	0.5	15	1.6	4,000	75
65	0.5	15	1.6	4,000	75
70	0.5	15	1.6	4,000	75

Table 3 Experimental design for different step-down sizes

Wall angle α (deg)	Step-down Δz (mm)	Tool radius (mm)	Thickness (mm)	Feed rate (mm/min)	Designed height (mm)
60	0.1	15	1.6	4,000	75
60	0.2	15	1.6	4,000	75
60	0.3	15	1.6	4,000	75
60	0.4	15	1.6	4,000	75
60	0.5	15	1.6	4,000	75
60	0.7	15	1.6	4,000	75
60	1.0	15	1.6	4,000	75

Fig. 4 Block diagram of the procedure to analyse deformation of the deformed curved surface



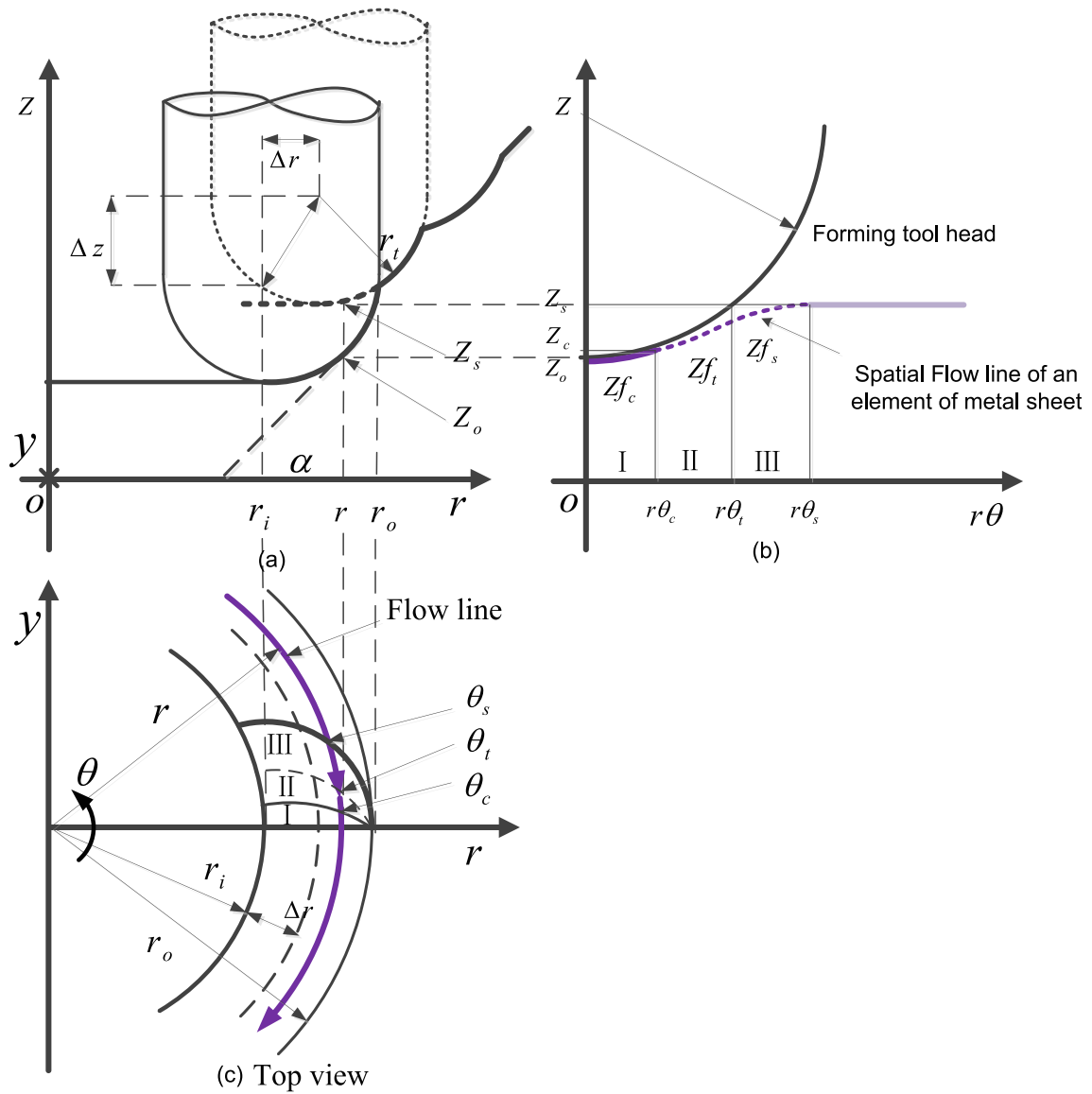
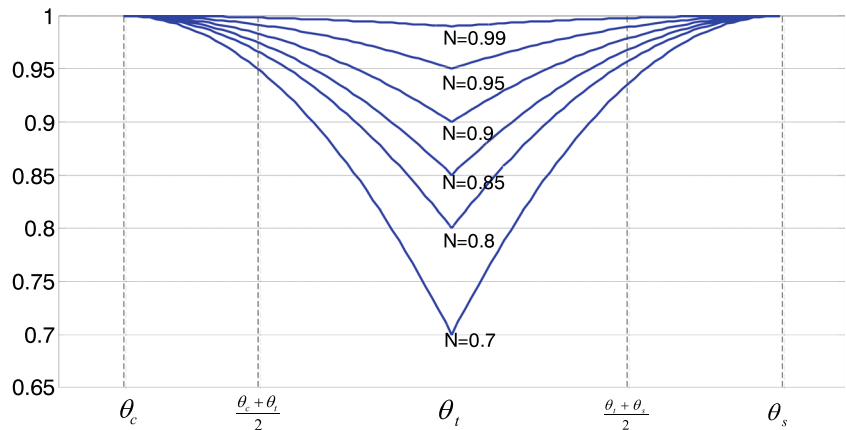


Fig. 5 Deformation zone in the cone-forming process: **a** $r-z$ view of the geometrical relations in incremental sheet forming during previous and current path, **b** $r\theta-z$ view and **c** $r-\theta$ view of a typical flow line for the deformed curved surface along the circumferential direction of the sheet ahead of the tool

Fig. 6 Calculated curves of shape function $S(X)$ with different values of parameter in N



effective to control the flow line. Another advantage of this definition is to satisfy the boundary condition and also to avoid the velocity discontinuity on the surface with θ_c and θ_s . However, a velocity discontinuity surface is introduced at the intersecting surface of the two shape functions. It should be noted that the dissipated power because of the discontinuity should also be included in subsequent calculation. Using the shape function, the flow line is defined by the following equation,

$$Zf = \left\{ \begin{array}{ll} Zf_c(r, \theta) = Z_i & (0 \leq \theta \leq \theta_c) \\ Zf_t(r, \theta) = S(X) * Z_t & (\theta_c \leq \theta \leq \theta_t) \\ Zf_s(r, \theta) = S(X) * Z_s & (\theta_t \leq \theta \leq \theta_s) \end{array} \right\} \quad (5)$$

Zf_t is defined following on the geometry of the tool surface Z_r , whereas Zf_s is based on the height of the sheet in previous pass (refer Fig. 5 for symbol definition). As a result, the flow line for the deformation zone is successfully defined using two adjustable parameters M and N and can be tailored by adjusting these presupposed parameters. In the following section, the detailed calculation procedure for two sub-models based on the assumed deformation zone and flow line is described.

$$\begin{aligned} \dot{\epsilon}_{rr} &= \frac{\partial v_r}{\partial r} & \dot{\epsilon}_{\theta\theta} &= \frac{\dot{u}_r}{r} + \frac{1}{r} \frac{\partial v_\theta}{\partial \theta} & \dot{\epsilon}_{zz} &= \frac{\partial v_z}{\partial z} \\ \dot{\epsilon}_{r\theta} &= \frac{1}{2} \left(\frac{1}{r} \frac{\partial v_r}{\partial \theta} + \frac{\partial v_\theta}{\partial r} + \frac{v_\theta}{r} \right) & \dot{\epsilon}_{\theta z} &= \frac{1}{2} \left(\frac{\partial v_\theta}{\partial z} + \frac{1}{r} \frac{\partial v_z}{\partial \theta} \right) & \dot{\epsilon}_{rz} &= \frac{1}{2} \left(\frac{\partial v_r}{\partial z} + \frac{\partial v_z}{\partial r} \right) \end{aligned} \quad (10)$$

By substituting the velocity field into above equations, the strain rates are obtained as,

$$\dot{\epsilon}_{\theta z} = \frac{f}{2rr_i} \frac{\partial^2 Zf}{\partial \theta^2} \quad (11)$$

$$\dot{\epsilon}_{rz} = \frac{f}{2r_i} \frac{\partial^2 Zf}{\partial \theta \partial r} \quad (12)$$

$$\dot{\epsilon}_{ij} = 0. \text{ (for strain rate in other directions)} \quad (13)$$

From the above calculation, it can be noticed that all the strain rate components are equal to zero except the shear components in vertical directions ($\dot{\epsilon}_{\theta z}$ and $\dot{\epsilon}_{rz}$). Since the dissipated power is calculated based on the value of strain rates, this sub-model is entirely due to the shear deformation mode.

3.1 Sub-model 1—shear deformation

3.1.1 Velocity field and strain rates

For a flow line at radius r , it only flows in the vertical and the circumferential directions, thus

$$v_r = 0 \quad (6)$$

In the circumferential direction, the sheet metal rotates at an angular velocity f/r_i round the centreline of the cone, thus

$$v_\theta = r \frac{f}{r_i} \quad (7)$$

The vertical component can be calculated from the flow line function as,

$$v_z = \frac{\partial Zf}{\partial r} v_r + \frac{\partial Zf}{\partial \theta} \dot{\theta} \quad (8)$$

Therefore, by substituting $v_r=0$ and $\dot{\theta} = f/r_i$,

$$v_z = \frac{f}{r_i} \frac{\partial Zf}{\partial \theta} \quad (9)$$

The strain rates in the cylindrical polar coordinates are defined as,

3.1.2 Dissipated power

As mentioned in the previous section, introduction of the shape function $S(X)$ results in a velocity discontinuity surface at the angle of θ . The dissipated power due to the discontinuity can be integrated along the discontinuity surface as,

$$w_{dis} = \iint_{dis} k |\Delta v| ds, \quad (14)$$

where k is the yield shear stress and its relation with average yield strength (refer Appendix 2) is express as,

$$k = \frac{y_0}{\sqrt{3}} \quad (15)$$

In the above equation, Δv is the velocity discontinuity in the vertical direction and can be computed in the following equation,

$$\Delta v = \Delta v_z = \frac{f}{r_i} \frac{\partial z f_s}{\partial \theta_{\theta=\theta_i}} - \frac{f}{r_i} \frac{\partial z f_t}{\partial \theta_{\theta=\theta_i}} \quad (16)$$

The dissipated power of the flow line during the cone-forming process, computed using strain rates, neglecting the velocity discontinuity can be expressed as,

$$\dot{w}_f = y_0 \iiint \left(\frac{2}{3} \dot{\epsilon}_{ij} \dot{\epsilon}_{ij} \right)^{\frac{1}{2}} dv = \frac{2y_0 t_0}{\sqrt{3}} \iiint (\dot{\epsilon}_{\theta z}^2 + \dot{\epsilon}_{rz}^2)^{\frac{1}{2}} ds \quad (17)$$

where t_0 is the initial thickness of the sheet. Accordingly, the total dissipated power due to shear deformation is obtained as,

$$\dot{w}_{\text{shear}} = \dot{w}_{\text{dis}} + \dot{w}_f. \quad (18)$$

The above equation for dissipated power is a function of two optimising parameters M and N . By minimising the dissipated power with varying M and N in their defined range (i.e. $0 \leq M, N \leq 1$), the deformed curved surface for the deformation zone closer to the experiment is obtained. It is reasonably assumed that the rate of plastic work due to the tangential force acting on the forming tool is,

$$\dot{w}_{\text{shear}} = F_t v_\theta \quad (19)$$

Now, by substituting the average radius of the deformed zone $(r_i + r_o)/2$ into equation (7) to obtain the angular velocity, the tangential force can be expressed as,

$$F_{\text{shear}} = \frac{r_i \dot{w}_{\text{shear}}}{f \cdot (r_i + r_o)/2} \quad (20)$$

3.2 Sub-model 2—bending with stretching

3.2.1 Bending moment and tensile stress

In the current analysis, the dissipated power is minimised through the optimisation of the flow line in the circumferential direction while neglecting the influence along the radial direction. This is based on the following considerations. Firstly, the bending moment and tensile stress could be more sensitive to the shape of the flow line in the forming direction than the radial direction. In addition, in radial direction, the sheet is already curved in the previous pass and the deformed curve is very close to the tool surface so the allowed optimising range is limited. Therefore, the current analysis can increase the calculating efficiency without significant sacrifice in terms of accuracy. Assume the flow line along the circumferential direction is mainly in the deformation mode of bending under stretching. The stress and strain distributions are shown in Fig. 7 in which the range of strain across the thickness is from just below the mid-surface strain ϵ_{1a} , to just above it. Since the sheet is completely yielded, a strain-hardening effect is assumed for the material sheet as a Swift type of power law. The stress–strain relation is then regarded to be linear across the thickness with constant value of E_h which corresponds to the slope of the stress–strain curve at a local strain value of

ϵ_{1a} . In ISF, the radius of curvature is assumed to be large compared with the thickness, so the bending strain can be approximated as,

$$\epsilon_b = \ln \left(1 + \frac{y}{\rho_0} \right) = \frac{y}{\rho_0}, \quad (21)$$

where y is the distance to the mid-surface and ρ_0 is the radius of the curved sheet. So the total strain at some distance y from the mid-surface is given by,

$$\epsilon_1 = \epsilon_a + \epsilon_b = \epsilon_{1a} + \frac{y}{\rho_0} \quad (22)$$

The stress is then given by,

$$\sigma_1 = \sigma_a + E_h \cdot \frac{y}{\rho_0} \quad (23)$$

The moment associated with the stress distribution is then computed as,

$$M = \int_{-t_0/2}^{t_0/2} \left\{ \sigma_a + E_h \cdot \frac{y}{\rho_0} \right\} y dy = \frac{E_h t_0^3}{\rho_0 12} \quad (24)$$

Also, the tensile stress is given as,

$$T = \sigma_a t_0 \quad (25)$$

3.2.2 Dissipated power

As shown in Fig. 7a, the local strain along the circumferential direction can be calculated according to Eq. (4) in [20],

$$\epsilon_{1a} = \frac{dl - d_0}{d_0} = \frac{\rho_0 d\varnothing - \rho_0 d\varnothing \cos\varnothing}{\rho_0 d\varnothing \cos\varnothing} = \frac{1}{\cos\varnothing} - 1 \quad (26)$$

The slope angle of the flow line can be approximated as,

$$\tan\varnothing = \frac{1}{r} \frac{\partial z f}{\partial \theta} \quad (27)$$

The above equation states the relation between the slope angle \varnothing and the tool travelling angle θ , thus the rate of plastic work for the deformation zone due to bending can be given as,

$$\dot{w}_b = \iint M d\varnothing ds = \iint \frac{E_h t_0^3}{\rho_0 12} \frac{d\varnothing d\theta}{d\theta dt} ds \quad (28)$$

Similarly, the rate of plastic work due to tension stress is,

$$\dot{w}_s = \iint T \epsilon_a dl ds = \iint \sigma_a t_0 \epsilon_a \rho_0 d\varnothing ds = \iint \sigma_a t_0 \epsilon_a \rho_0 \frac{d\varnothing}{d\theta} \frac{d\theta}{dt} ds \quad (29)$$

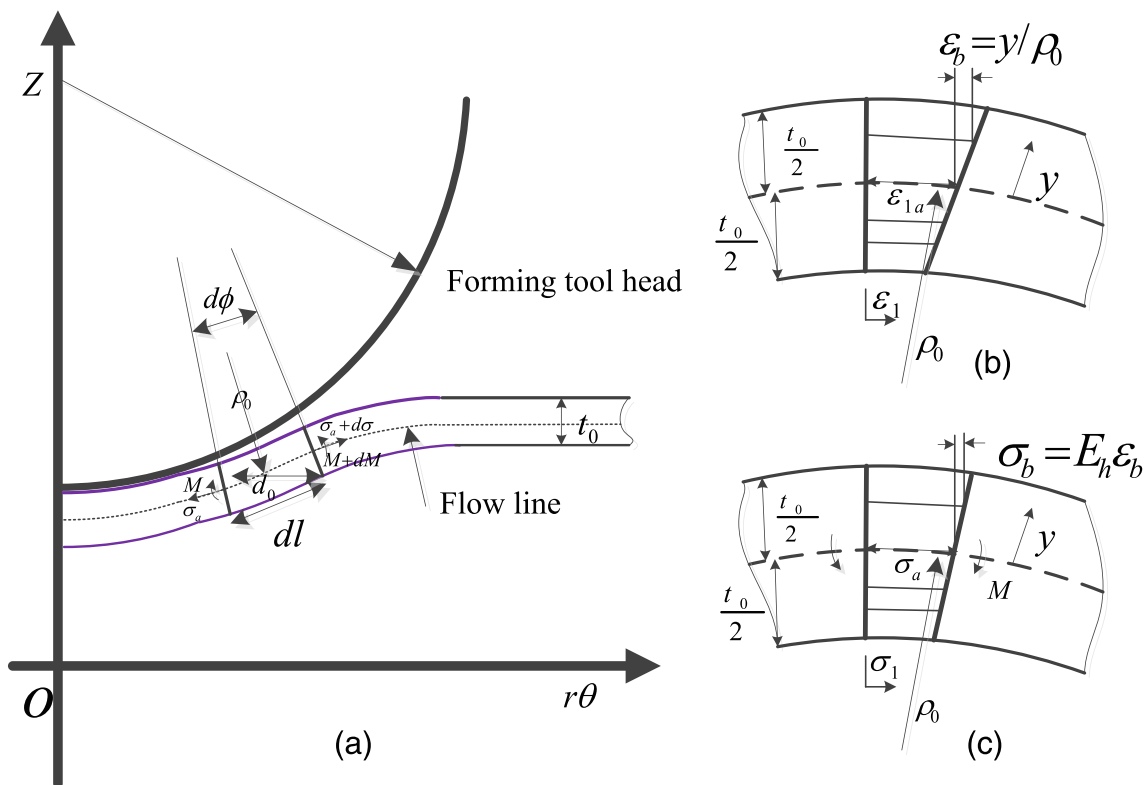


Fig. 7 a Deformed diagram showing the range of stress for the sheet bent and stretched to a mid-surface strain of ε_{1a} . b The strain distribution when bent over a tool of radius ρ_0 and c the stress distribution

Accordingly, the total dissipated power due to bending and stretching is,

$$\dot{w}_{bs} = \dot{w}_b + \dot{w}_s \quad (30)$$

Similar to Eq. (20), the tangential force is computed as,

$$F_{bs} = \frac{r_i \dot{w}_{bs}}{f \cdot (r_i + r_o) / 2} \quad (31)$$

4 Results

4.1 Force trend in ISF

Figure 8 presents the record of the three component of force over the process ($\alpha=60^\circ$, $\Delta z=0.5$ mm) versus time with a zoomed view. In one cycle, tangential forces (F_x and F_y) change in a sinusoidal way between their maximum and minimum values due to the current tool position relative to the global absolute axis around a contour of the truncated cone. In contrast with the horizontal forces, the vertical force shows small fluctuations in the final steps caused by the Z-level tool path. The amplitude of the forces

increases during the early phase of the process and tends to become steady for the rest of the process. This could be due to a number of reasons. Firstly, the initial development of the plastic deformation could result in the rapid increase in forming force according to the characteristic of the stress–strain curve. Previous studies [7, 9] suggest that bending deformation is the most relevant mechanism at this stage. In addition, with the build-up of the contact area between tool head and the sheet surface, the force required to deform the sheet is also increased. Additionally, the increase of the vertical force can be assigned to the continuous deforming of the material which combines bending, shear and stretching mechanisms [21, 22]. The further deformation would result in the increase of the forming force caused by the strain hardening of the material. However, thinning of the material would reduce the magnitude of the force. Therefore, the later contour loops of the forming force are determined by the combined effects of strain hardening and thinning.

4.2 Effect of wall angle

To study the effect of wall angles on the forming force, the vertical forces at wall angles varying from 30° to 70° are

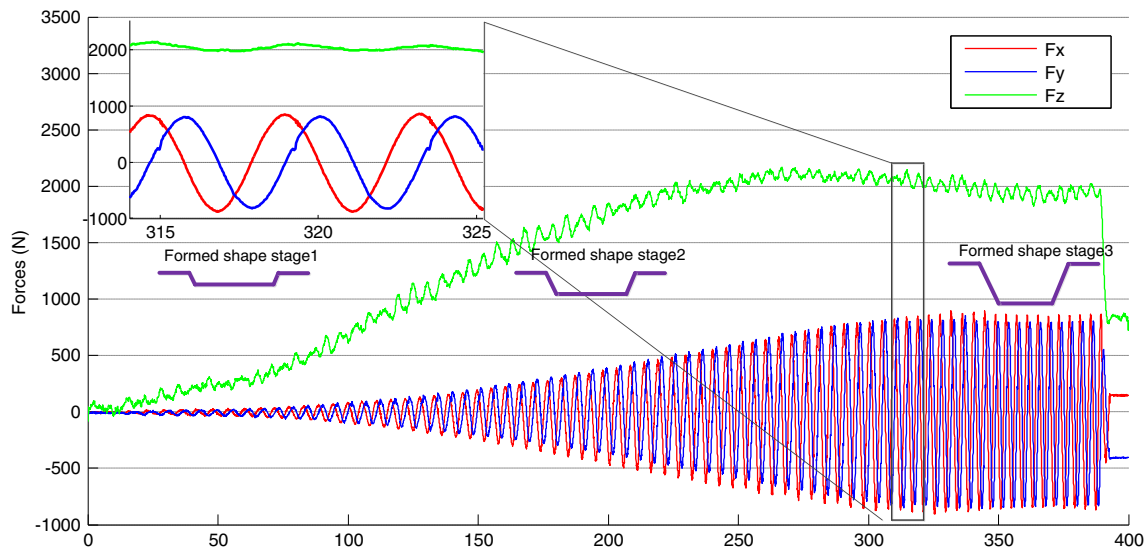


Fig. 8 Three force components (F_x , F_y and F_z) versus forming time and a detailed view for two cycles during forming a cone (with three cross-sectional diagrams of the formed shape)

plotted in Fig. 9. For small wall angles under 60° , the vertical forces reach the turning point at the forming depth of around 30 mm and then keep rising slowly until the end of the process. The magnitudes of F_z for these cases at the same depth approximately have the same value. On the contrary, the force trends are recorded in a different fashion for wall angles larger than 60° . The forces quickly register their peak values at a depth of around 12 mm and then decrease monotonically towards process completion/failure. The achievements of steady conditions are delayed with small wall angles. This is because with a smaller wall angle, the sheet undergoes

a longer bending process before the occurrence of strain hardening. It appears that the increase of F_z is caused by work hardening, while the decrease is due to the material thinning. From Fig. 9, it is demonstrated that a decrease of F_z is only found in cases with fracture. Therefore, if the material work hardening plays a dominant role to compensate sheet thinning, the force could remain steady and avoid fracture. Otherwise, if thinning prevails, the forces drop quickly which indicates the failure of the material. If appropriate statistical analysis can be performed to calculate the force gradient after the peak value, this could possibly be considered as an

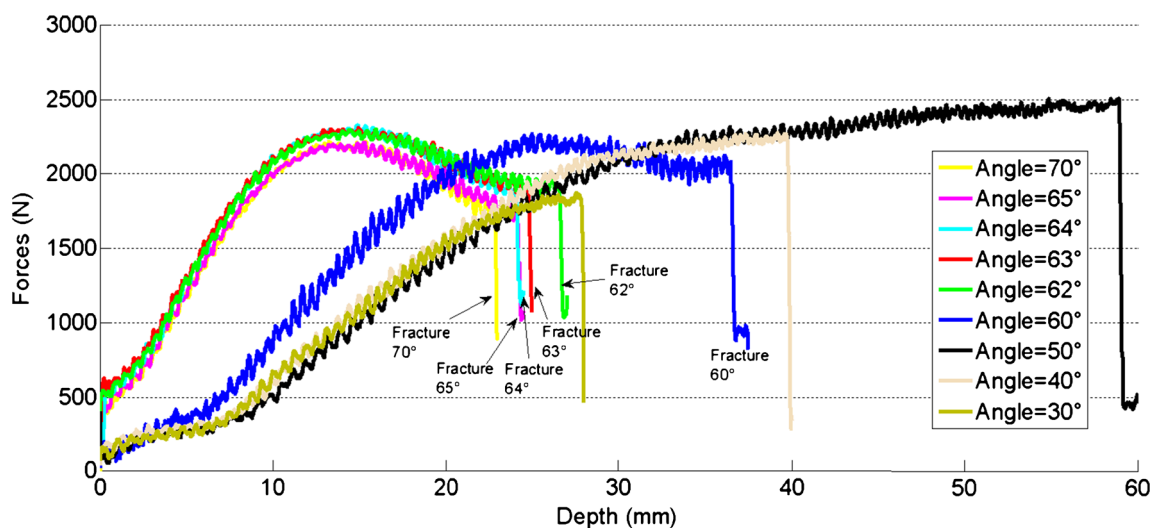


Fig. 9 Vertical force trend with the varying of wall angle (fracture parts are marked)

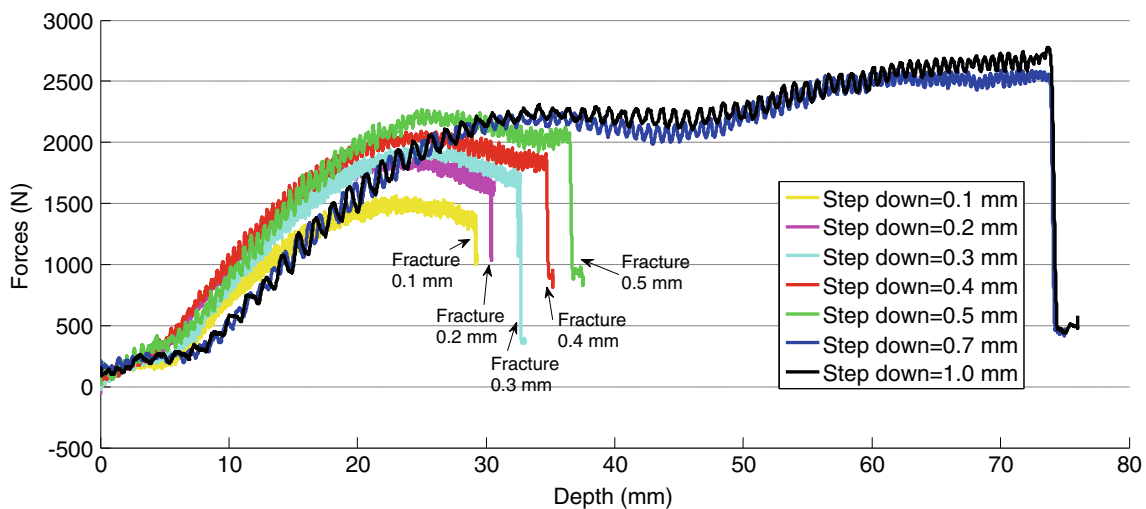


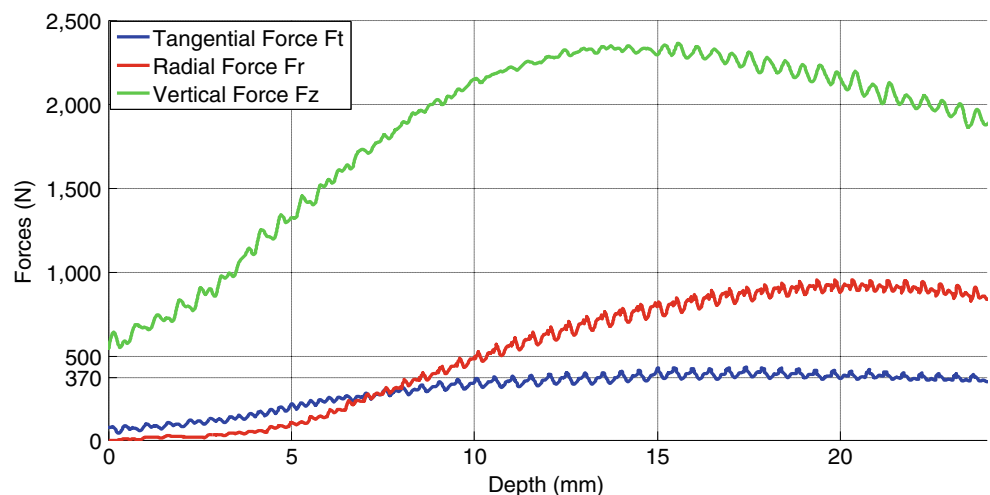
Fig. 10 Vertical force trend with the varying of step-down size (fracture parts are marked)

effective indicator for failure prediction. As listed in Table 2, the designed heights of the cones for 30° , 40° and 60° are 28, 40 and 60 mm because of the limits of minor diameter, respectively. These three parts are formed successfully without fracture because the thinning of the sheet is under the forming limit of the material. With the increase of the wall angle from 60° to 70° , the formability in terms of the achieved forming depth, as marked in Fig. 9 reduces slightly from 37.5 to 23 mm. According to the sine law ($t = t_0 * \sin(90 - \alpha)$) [23] which is based on the constancy of volume, the sheet thickness after deformation is decreases as wall angle increases. The literature also indicates that the local thinning determines the formability of the ISF process. Therefore, at the same forming depth, the thinning ratio of the material is higher for the parts with larger wall angle, resulting in a lower formability.

4.3 Effect of step down

A set of experiments has also been performed with different step-down sizes (Δz) ranging from 0.1 to 1.0 mm. The evolution histories of the vertical force F_z at the varying of step-down sizes are presented in Fig. 10. It can be noticed that at the former stage with depth from 0 to 20 mm, the vertical forces for large Δz (0.7 and 1.0 mm) show smaller values compared with forces with small step-down sizes. However, after a depth of 40 mm, the F_z values present a limited decrease and then increase until the part is successfully formed. It can also be seen from Fig. 10 that only the parts with Δz of 0.7 and 1.0 mm are formed successfully and the fracture occurs with smaller step-down size. This can be explained by the fact that smaller Δz leads to more tool contact overlaps. In particular, with small Δz , the

Fig. 11 Transposed tangential and radial forces versus forming depth for a cone with angle of 65°



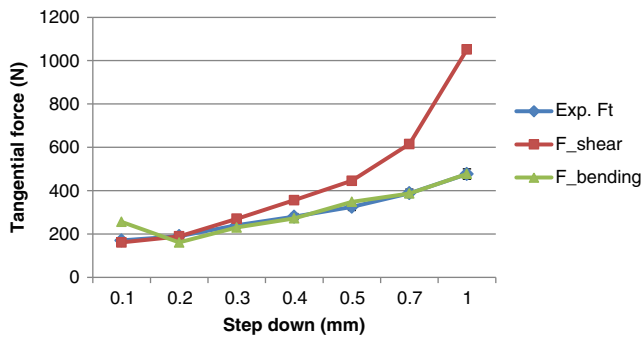


Fig. 12 Predicated tangential forces for two sub-models compared with experimental values with different step-down sizes (other parameters as standard setting: $\alpha=60^\circ, r_f=15$ mm, $t_0=1.6$ mm)

percentage of overlap between consecutive tool paths is higher which means the portion of hardened material deformed by the tool in each pass is larger. Therefore, the stress required for the deformation rises. As a result of the higher stress state induced in the material, the sheet formability is reduced while the required forming force is increased.

4.4 Comparison of the modelling and experimental results

Force components in vertical and global X and Y directions have been compared and analysed in previous sections. However, to better understand the mechanism of the deformation process and to make a comparison with the proposed model, forces in tangential direction are critical. Therefore, the horizontal forces (F_x and F_y) need to be converted to tangential (F_t) and radial components (F_r) to ensure the comparison is effective. The same methodology presented in [16] is used to determine the converted tangential and radial forces and the results for a 65° cone-forming process are plotted in

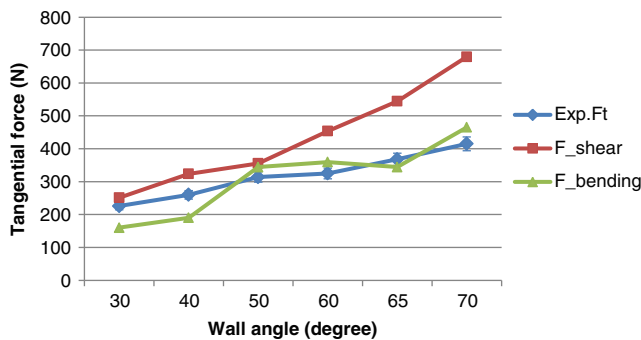


Fig. 13 Predicated tangential forces for two sub-models compared with experimental values with different wall angles (other parameters as standard setting: $\alpha=60^\circ, r_f=15$ mm, $t_0=1.6$ mm)

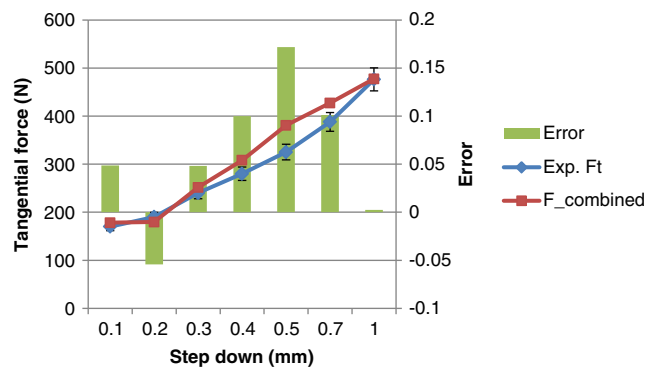


Fig. 14 Errors between predicted and measured tangential forces with different step-down sizes

Fig. 11. It is shown that the tangential force increases gradually until the forming depth of 10 mm and then reaches the steady state for the rest of the forming cycles where the forces remain reasonably constant. The average tangential force value in the steady state is recorded and used to compare with the proposed analytical model.

In order to validate the proposed efficient analytical model, the predicted tangential forces with different forming parameters were compared with the experimental results. Figure 12 presents the comparison of predicted tangential forces and experimentally measured values with variation of step-down size from 0.1 to 1 mm. By comparison, the sub-model 1 based on shear deformation can provide good agreement with experimental results for the cases with small step-down sizes (below 0.5 mm). With the increase of the step down, the difference between analytical and experimental results increases accordingly. Additionally, for step down larger than 0.5 mm, the error becomes significantly high. A similar error trend can be noticed for the tangential force prediction for sub-model 1 with the increase of wall angle values as shown in Fig. 13. The larger deviations for large step-down sizes as well as large wall angles may be due

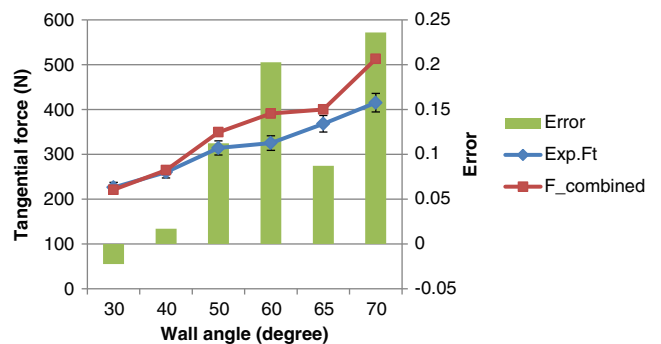


Fig. 15 Errors between predicted and measured tangential forces with different wall angles

to the following inherent limits of the deformation mechanics. Firstly, the sub-model 1 is based on the assumption that no material flow is taken into account in the radial direction. Therefore, the calculated dissipated power is totally due to the shear strain rates of the deformed elements. However, bending and stretching which cause plastic strains are also evident in some experimental tests [24] and FE simulations [22]. Secondly, with a large-step depth, the deformation zone which is represented by Bezier curves may contribute to a more severe deformation compared with that of the actual deformed area, resulting in the higher force value. Furthermore, the assumption that the non-contact regions of the sheet are considered as rigid material may also cause the over prediction of the force.

To provide further insight into these above limits, a sub-model 2 which takes into account bending and stretching effects was established. The predicted forces using the sub-model 2 are also compared with measured results in Figs. 12 and 13. It is noticed that the bending based prediction of tangential values is more accurate for larger step-down sizes. However, as shown in Fig. 13, the bending model alone cannot accurately predict the force trend across the range of wall angles. Therefore, a linear combination of these two sub-models has been constructed

to balance the contribution of shear and bending on the prediction of tangential force,

$$F_{\text{combined}} = \lambda F_{\text{shear}} + (1-\lambda)F_{bs} \quad (32)$$

where F_{shear} and F_{bs} are the predicted tangential force due to shear and bending deformation mechanism, respectively; λ is a normalised fraction taking into account parameters of wall angle and step-down size. The purpose of the parameter λ is to balance the contribution between the shear based model and the bending based model to provide a more accurate prediction of the tangential force. The shear-based model depends on λ and the bending-based model depends on $(1-\lambda)$ as given in Eq. (32). According to the experimental results as well as the mechanics of plastic deformation, the parameter λ has to meet the following requirements,

- The parameter of λ should be dimensionless,
- The value of λ should range from 0 to 1 in the experiments,
- The value of λ should decrease with the increase of wall angle,
- The value of λ should decrease with the increase of step-down size.

Considering the above conditions, an effective way to determine the value of λ can be achieved empirically by,

$$\lambda = \frac{\left(1 - \frac{\alpha}{90^\circ}\right) \left(1 - \frac{\Delta z}{\Delta z_{\max}}\right)}{\left(1 - \frac{\alpha}{90^\circ}\right) \left(1 - \frac{\Delta z}{\Delta z_{\max}}\right) + \frac{\alpha}{90^\circ} \frac{\Delta z}{\Delta z_{\max}}} = \frac{(90^\circ - \alpha)(\Delta z_{\max} - \Delta z)}{(90^\circ - \alpha)(\Delta z_{\max} - \Delta z) + \alpha \Delta z} \quad (0 < \Delta z \leq 1) \quad (33)$$

where α and Δz correspond to the values of wall angle and step-down size. The explored maximum step down Δz_{\max} in this study is 1 mm. According to the above equation, the contribution of the shear based model decreases proportionally with the increase of wall angle and step-down size while the significance of bending and stretching rises with more severe plastic deformation due to larger step-down sizes and higher wall angles. The choice of model for λ could be explained more deeply in future research to obtain model based prediction.

Figures 14 and 15 present the comparison between the predicted and experimental values of tangential forces with different configurations. The average error for the combined model is only 6 and 11 % in respect to the variation of step-down size and wall angle, respectively. As the prediction can be performed within only several minutes using the proposed

model, it would greatly improve the prediction efficiency of forming force.

5 Conclusions

In the present work, experimental measurement on forming forces in the truncated cone-forming process was conducted and the trend of forming force was also analysed. Efficient analytical models for tangential force prediction were proposed and validated through experimental data. The following was concluded.

- Forming forces have been successfully measured on a benchmark ISF case by means of strain gauges and provide useful information to understand the relationship

between the force and other forming parameters. It is concluded that the force trend may attributed to the bending effect of the sheet in the early phase of the process and the combined effects of sheet thinning and strain hardening in the second stage of the process.

- From the experimental results, tangential forces are nearly constant during the second stage of the process and the steady values demonstrate a growing trend with the increase of step-down size and wall angle. In the investigated range, a reasonably large step-down size should be selected to achieve a better formability in terms of forming depth.
- Major deformation modes including shear, bending and stretching are analytically considered in the proposed sub-models. The results from each model were analysed separately which suggest that the deformation mechanism in ISF is a combination of shear, bending and stretching.
- An empirical combined model has been constructed which can provide the prediction of tangential force with an average error less than 11 % for the experimental conditions employed in this study. The current work will be helpful to provide an efficient method for tangential force prediction.

The current model is based on the tool path for the cone-forming process. Nevertheless, it can be expected that using a modification of the presented model, tangential forces for different part geometries can be obtained as well. As the empirical relationship given herein for the two sub-models is valid for the experimental conditions employed in this study, a general empirical model able to predict forming force for any

process design needs to be investigated under a wider range of process conditions.

Acknowledgements The present work was supported by Australian Research Council (ARC) Linkage project, Boeing Research and Technology Australia and QMI Solutions in Australia. China Scholarship Council (CSC) is also acknowledged for the scholarship support.

Appendix 1

Calculation of critical angles

As we can see from Fig. 16, the deformation zone which is being formed in current path can be divided into six regions. In radial direction, the deformation zone is divided into two parts by the radius of $(r_i + \Delta r)$. In circumferential direction, three critical angles (θ_c , θ_t and θ_i) are used to define the assumed flow line. In Fig. 16, we can see that regions Ia, IIa and IIIa are undeformed areas during last pass so these are flat before the current forming pass, whereas regions Ib, IIb and IIIb are previously deformed in the last forming pass. Vertical positions for the sheet before the current forming pass are,

$$Z_{sa} = Z_t + \Delta z \quad (r_i \leq r \leq r_i + \Delta r) \tag{34}$$

$$Z_{sb} = Z_t + \Delta z + r_i - \sqrt{r_i^2 - (r - r_i - \Delta z \tan(90 - \alpha))^2} \quad (r_i + \Delta r \leq r \leq r_o) \tag{35}$$

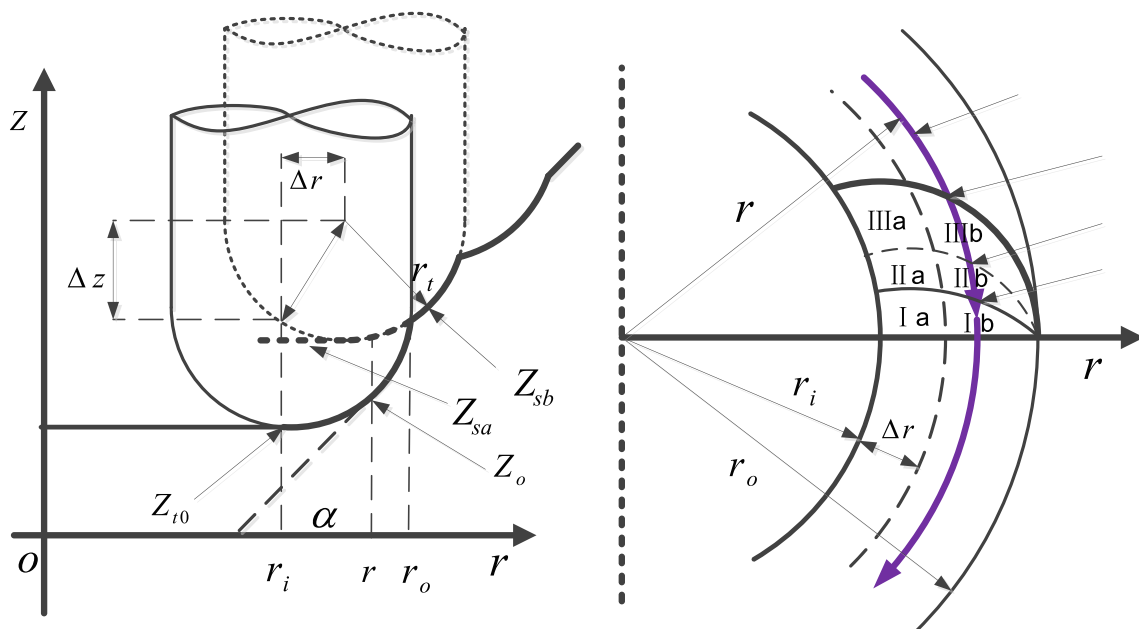


Fig. 16 Divided deformation zone in the cone-forming process

a) Calculation of θ_c

As previously defined, Z_c is the conjunct point for curve Zf_c and tool head surface, so θ_{ca} is calculated by solving the following two equations,

$$\begin{cases} Z_c = M(Z_{s1}-Z_o) + Z_o \\ Z_c = Z_{t0} + r_t - \sqrt{r_t^2 - (r \cos \theta - r_i)^2 - (r \sin \theta)^2} \end{cases} \quad (36)$$

According to the geometric relations of the tool head, we have,

$$\begin{cases} Z_o = Z_{t0} + (r_t - r_{tc}) \\ r_{tc} = \sqrt{r_t^2 - (r - r_i)^2} \end{cases} \quad (37)$$

The contact angle θ_{ca} can be solved from Eqs. (37) and (38) gives

$$\theta_{ca} = \cos^{-1} \frac{\left(\sqrt{r_t^2 - (r - r_i)^2} - M(Z_{sa} - Z_o) \right)^2 - r_t^2 + r^2 + r_i^2}{2rr_i} \quad (38)$$

Similarly, the contact angle θ_{cb} which separates regions Ib and IIb can be solved as,

$$\theta_{cb} = \cos^{-1} \frac{\left(\sqrt{r_t^2 - (r - r_i)^2} - M(Z_{sb} - Z_o) \right)^2 - r_t^2 + r^2 + r_i^2}{2rr_i} \quad (39)$$

b) Calculation of θ_t

When $r_i \leq r \leq r_i + \Delta r$, θ_{ta} is calculated to define regions IIa and IIIa,

$$\begin{cases} Z_{ta} = Z_{t0} + \Delta z \\ Z_t = Z_{t0} + r_t - \sqrt{r_t^2 - (r \cos \theta - r_i)^2 - (r \sin \theta)^2} \end{cases} \quad (40)$$

Let Z_{ta} equals Z_t , the angle θ_{ta} can be solved as,

$$\theta_{ta} = \cos^{-1} \frac{(r_t - \Delta z)^2 - r_t^2 + r^2 + r_i^2}{2rr_i} \quad (41)$$

Similarly, for calculation of θ_{tb} , we have

$$\begin{cases} Z_{tb} = Z_{t0} + \Delta z + r_t - \sqrt{r_t^2 - (r - r_i - \Delta z \tan(90 - \alpha))^2} \\ Z_t = Z_{t0} + r_t - \sqrt{r_t^2 - (r \cos \theta - r_i)^2 - (r \sin \theta)^2} \end{cases} \quad (42)$$

$$\theta_{tb} = \cos^{-1} \frac{\left(\sqrt{r_t^2 - (r - r_i - \Delta z \tan(90 - \alpha))^2} - \Delta z \right)^2 - r_t^2 + r^2 + r_i^2}{2rr_i} \quad (43)$$

c) Calculation of θ_s

The deformation zone is assumed to be a circle with the radius of $r_o - r_i$, so the following equations set can be given as,

$$\begin{cases} X^2 + Y^2 = r^2 \\ (X - r_i)^2 + Y^2 = (r_o - r_i)^2 \end{cases} \quad (44)$$

The angle θ_s can be solved as,

$$\theta_s = \sin^{-1} \frac{Y}{r} \quad (45)$$

Appendix 2

Calculation of average yield strength and equivalent strain

For each of the six regions, do the integral for equivalent strain. Take region Ia for example,

$$\bar{\varepsilon}_{I\alpha} = \iint_0^{\theta_{ca}} \frac{2}{\sqrt{3}} (\varepsilon_{\theta z}^2 + \varepsilon_{rz}^2) d\theta dr \quad (46)$$

On the velocity discontinuity surface,

$$\bar{\varepsilon}_{disa} = \frac{2}{\sqrt{3}} \varepsilon_{\theta z} = \frac{1}{\sqrt{3}} \frac{|\Delta v|}{v_\theta} \quad (47)$$

The average equivalent strain is given as,

$$\bar{\varepsilon}_{avg} = \frac{\bar{\varepsilon}_{total}}{r_o - r_i} = \frac{\bar{\varepsilon}_{Ia} + \bar{\varepsilon}_{Ib} + \bar{\varepsilon}_{II\alpha} + \bar{\varepsilon}_{IIb} + \bar{\varepsilon}_{III\alpha} + \bar{\varepsilon}_{IIIb} + \bar{\varepsilon}_{disa} + \bar{\varepsilon}_{disb}}{r_o - r_i} \quad (48)$$

By assuming the swift type work hardening law $\sigma_{eq} = K(\varepsilon_0 + \varepsilon)^n$ for a sheet metal, the average yield strength is obtained as,

$$y_0 = \frac{\int_0^{\bar{\varepsilon}_{avg}} \sigma_{eq} d\varepsilon}{\int_0^{\bar{\varepsilon}_{avg}} d\varepsilon} \quad (49)$$

where ε is the plastic strain. Also, K, n and ε_0 are the material parameters.

References

- Jeswiet J, Micari F, Hirt G, Bramley A, Dufloy J, Allwood J (2005) Asymmetric single point incremental forming of sheet metal. Ann CIRP—Manuf Technol 54(2):623–649
- Echraf SBM, Hrairi M (2011) Research and progress in incremental sheet forming processes. Mater Manuf Processes 26(11):1404–1414. doi:10.1080/10426914.2010.544817

3. Emmens WC, Sebastiani G, van den Boogaard AH (2010) The technology of incremental sheet forming—a brief review of the history. *J Mater Process Technol* 210(8):981–997. doi:10.1016/j.jmatprotec.2010.02.014
4. Micari F, Ambrogio G, Filice L (2007) Shape and dimensional accuracy in single point incremental forming: state of the art and future trends. *J Mater Process Technol* 191(1–3):390–395. doi:10.1016/j.jmatprotec.2007.03.066
5. Essa K, Hartley P (2011) An assessment of various process strategies for improving precision in single point incremental forming. *Int J Mater Form* 4(4):401–412. doi:10.1007/s12289-010-1004-9
6. Duflou JR, Verbert J, Belkassam B, Gu J, Sol H, Henrard C, Habraken AM (2008) Process window enhancement for single point incremental forming through multi-step toolpaths. *CIRP Ann - Manuf Technol* 57(1):253–256. doi:10.1016/j.cirp.2008.03.030
7. Duflou J, Tunçkol Y, Szekeres A, Vanherck P (2007) Experimental study on force measurements for single point incremental forming. *J Mater Process Tech* 189(1):65–72
8. Filice L, Ambrogio G, Micari F (2006) On-line control of single point incremental forming operations through punch force monitoring. *CIRP Ann—Manuf Technol* 55(1):245–248
9. Ambrogio G, Filice L, Micari F (2006) A force measuring based strategy for failure prevention in incremental forming. *J Mater Process Technol* 177(1–3):413–416
10. Petek A, Kuzman K, Suhač B (2009) Autonomous on-line system for fracture identification at incremental sheet forming. *CIRP Ann - Manuf Technol* 58(1):283–286. doi:10.1016/j.cirp.2009.03.092
11. Fiorentino A (2013) Force-based failure criterion in incremental sheet forming. *Int J Adv Manuf Technol* 68(1–4):557–563. doi:10.1007/s00170-013-4777-4
12. Ingarao G, Ambrogio G, Gagliardi F, Di Lorenzo R (2012) A sustainability point of view on sheet metal forming operations: material wasting and energy consumption in incremental forming and stamping processes. *J Cleaner Prod* 29–30(0):255–268. doi:10.1016/j.jclepro.2012.01.012
13. Malhotra R, Xue L, Belytschko T, Cao J (2012) Mechanics of fracture in single point incremental forming. *J Mater Process Technol* 212(7):1573–1590
14. Raithatha A, Duncan S (2009) Rigid plastic model of incremental sheet deformation using second-order cone programming. *Int J Numer Methods Eng* 78(8):955–979
15. Iseki H (2001) An approximate deformation analysis and FEM analysis for the incremental bulging of sheet metal using a spherical roller. *J Mater Process Technol* 111(1):150–154
16. Aerens R, Eyckens P, Van Bael A, Duflou JR (2010) Force prediction for single point incremental forming deduced from experimental and FEM observations. *Int J Adv Manuf Technol* 46(9):969–982
17. Mirnia MJ, Dariani BM (2012) Analysis of incremental sheet metal forming using the upper-bound approach. *Proceedings of the Institution of Mechanical Engineers, Part B: Journal of Engineering Manufacture*
18. Jeswiet J, Duflou JR, Szekeres A (2005) Forces in single point and two point incremental forming. *Adv Mater Res* 6–8:449–456
19. Halmos GT (2006) *Roll forming handbook*, vol 67, Book, Whole. CRC/Taylor & Francis, Boca Raton
20. Wang G, Ohtsubo H, Arita K (1998) Large deflection of a rigid-plastic circular plate pressed by a sphere. *J Appl Mech* 65(2):533–535. doi:10.1115/1.2789089
21. Allwood J, Shouler D, Tekkaya AE (2007) The increased forming limits of incremental sheet forming processes. *Key Eng Mater* 344: 621–628
22. Smith J, Malhotra R, Liu WK, Cao J (2013) Deformation mechanics in single-point and accumulative double-sided incremental forming. *The International Journal of Advanced Manufacturing Technology*: 1–17. doi:10.1007/s00170-013-5053-3
23. Avitzur B, Yang CT (1960) Analysis of power spinning of cones. *J Eng Ind* 82(3):231. doi:10.1115/1.3663052
24. Silva MB, Nielsen PS, Bay N, Martins PAF (2011) Failure mechanisms in single-point incremental forming of metals. *Int J Adv Manuf Technol* 56(9):893–903. doi:10.1007/s00170-011-3254-1

Erratum to: Efficient force prediction for incremental sheet forming and experimental validation

Yanle Li · Zhaobing Liu · Haibo Lu ·
W. J. T. (Bill) Daniel · Sheng Liu · Paul A. Meehan

Published online: 9 May 2014
© Springer-Verlag London 2014

Erratum to: Int J Adv Manuf Technol
DOI: 10.1007/s00170-014-5665-2

The first sentence in section 3 needs to be changed into:

In this model, the energy method [19] and upper bound theory [17] are used to analyse the deformation behaviour and predict the tangential force of the truncated cone during the ISF process.

The division of deformation zone in Figures 5 and 16 referred to Figure 2 in [17].

References

17. Mirnia MJ, Dariani BM (2012) Analysis of incremental sheet metal forming using the upper-bound approach. Proceedings of the Institution of Mechanical Engineers, Part B: Journal of Engineering Manufacture
19. Halmos GT (2006) Roll forming handbook, vol 67, Book, Whole. CRC/Taylor & Francis, Boca Raton

The online version of the original article can be found at doi:10.1007/s00170-014-5665-2.

Y. Li (✉) · Z. Liu · H. Lu · W. J. T. (B). Daniel · S. Liu · P. A. Meehan
School of Mechanical and Mining Engineering, The University of
Queensland, St Lucia, Brisbane, QLD 4072, Australia
e-mail: yanle.li@uq.edu.au